


For Reference

NOT TO BE TAKEN FROM THIS ROOM



Digitized by the Internet Archive
in 2023 with funding from
University of Alberta Library

<https://archive.org/details/Javed1970>

THE UNIVERSITY OF ALBERTA
COMPUTER-AIDED STUDY OF THE
ELECTRICAL BEHAVIOUR OF MICROWAVE VARACTORS

by



ALAUDDIN JAVED

A THESIS

SUBMITTED TO THE FACULTY OF GRADUATE STUDIES
IN PARTIAL FULFILMENT OF THE REQUIREMENTS FOR THE DEGREE
OF DOCTOR OF PHILOSOPHY

DEPARTMENT OF ELECTRICAL ENGINEERING

EDMONTON, ALBERTA

FALL, 1970

ABSTRACT

The electrical behaviour of microwave varactors under both steady-state and large-signal transient conditions is investigated. Numerical iterative methods are used to solve the one-dimensional two-carrier transport equations which are taken to describe the behaviour of these devices under both steady-state and transient conditions. The solutions for the steady-state and time-dependent cases are obtained by modifying and extending numerical methods, already available in the literature, to cover the present cases. Considerable attention is given to the numerical analysis of the steady-state and time-dependent cases in order to achieve a numerical algorithm sufficiently sound to cope with several severe difficulties of the problem. Two diodes, taken to represent two distinct kinds of microwave varactor, are considered. Results have been computed for four external excitations, namely: steady-state voltage excitation, "turn-on", "turn-off" and sinusoidal excitation in a broadband circuit. A slight charge accumulation in the vicinity of the $n - n^+$ space charge region during the "turn-off" transient in the $p^+ - n - n^+$ step-recovery diode, and an inductive behaviour of these devices under large-signal sinusoidal excitation, are two of the many interesting aspects revealed by the results. The microwave measurement techniques used for the varactor measurements made are also presented and discussed.

ACKNOWLEDGEMENTS

The work was carried out in the Department of Electrical Engineering during the period from September 1966 - July 1970 under the supervision of Dr. P. A. Goud, whom I wish to thank for his help and encouragement throughout the course of this work.

Sincere thanks are in order for Mr. J. E. Fearn for his skillful assistance in the experimental work. I also wish to thank Mr. E. Buck for his help in the fabrication of various components used in the experimental work.

The financial support provided by the Canadian International Development Agency and the Department of Electrical Engineering is gratefully acknowledged. I also wish to thank the Vice-Chancellor, West Pakistan University of Engineering and Technology, for granting me a leave of absence.

The patience of Mr. J. E. Fearn and his skillful typing of the manuscript are very much appreciated. Finally, I wish to thank Miss P. Stimpson for her help and patience in reading the manuscript.

TABLE OF CONTENTS

	Page
CHAPTER I: INTRODUCTION	1
CHAPTER II: MICROWAVE VARACTOR DIODES	7
2.1 Introduction	7
2.2 Design considerations	8
2.3 The fabrication process and its mathematical model	10
2.3.1 Fabrication process	10
2.3.2 The mathematical model	11
2.4 Physical description of the diodes selected	14
CHAPTER III: PHYSICAL MODELLING	18
3.1 Introduction	18
3.2 Important physical phenomena	19
3.2.1 Bulk generation-recombination	19
3.2.2 Mobility	21
3.2.3 Degeneracy	24
3.2.4 Surface recombination and the surface boundary condition	25
3.3 Assumptions for other physical phenomena	28
3.4 Validity of one-dimensional analysis	28
3.5 Synopsis	32
CHAPTER IV: MATHEMATICAL MODELLING	33
4.1 Introduction	33
4.2 Fundamental mathematical equations	34
4.2.1 Charge transport equation	34
4.2.2 Charge continuity equation	34
4.2.3 Poisson's equation	35
4.2.4 Total current continuity equation	35
4.2.5 Auxiliary relations	35
4.3 Normalised one-dimensional equations for steady-state conditions	36
4.4 Normalised one-dimensional equations for the time-dependent cases	38
4.5 Boundary conditions	39
4.5.1 Steady-state case	39

4.5.2	Time-dependent cases	40
4.6	Summary	42
CHAPTER V: ANALYTICAL FORMULATION AND NUMERICAL TECHNIQUES FOR SOLUTION OF STEADY-STATE CASE		43
5.1	Introduction	43
5.2	Derivation of reduced set of equations	44
5.3	Iterative procedure of solution	47
5.4	Numerical techniques	51
5.4.1	Numerical integration and differentiation	51
5.4.2	Solution of Poisson's equation	52
5.5	On the accuracy of numerical solution	53
5.6	Calculation of incremental capacitance and series resistance	55
5.6.1	Incremental capacitance	55
5.6.2	Series resistance	57
5.7	Summary	57
CHAPTER VI: ANALYTICAL FORMULATION AND NUMERICAL TECHNIQUES FOR TIME-DEPENDENT CASES		59
6.1	Introduction	60
6.2	Derivation of reduced set of equations	61
6.3	Boundary and initial conditions	63
6.4	Iterative method of solution	65
6.5	Selection of discretization scheme	66
6.6	Details of adopted procedure	71
6.7	On different forms of external excitations	85
6.7.1	Procedure for voltage-driven case	85
6.7.2	Outline of procedure when an equation relating terminal current and voltage is known	89
6.8	On the accuracy of the numerical solution for time-dependent cases	91
6.8.1	Truncation error in the time domain	92
6.8.2	Iteration error	94
6.8.3	Errors in the initial solution	95
6.8.4	Other sources of numerical error	96
6.8.5	Time step, iteration and truncation errors and numerical error growth in the time domain	97
6.9	Summary	99
CHAPTER VII: RESULTS FOR STEADY-STATE CASE		101
7.1	Introduction	101

7.2	Results for diode No. 1	102
7.3	Results for diode No. 2	127
7.4	Synopsis	150
CHAPTER VIII: LARGE-SIGNAL "TURN-ON" RESPONSE		153
8.1	Introduction	153
8.2	Results for diode No. 1	154
8.3	Results for diode No. 2	161
8.4	Conclusions	174
CHAPTER IX: LARGE-SIGNAL "TURN-OFF" RESPONSE		176
9.1	Introduction	176
9.2	Results for diode No. 1	177
9.3	Results for diode No. 2	183
9.4	Conclusions	199
CHAPTER X: LARGE-SIGNAL, SINUSOIDAL EXCITATION RESPONSE		201
10.1	Introduction	201
10.2	Results for diode No. 1	202
10.3	Results for diode No. 2	211
10.4	Conclusions	220
CHAPTER XI: MICROWAVE MEASUREMENTS OF THE STATIC CHARACTERISTICS OF A MICROWAVE VARACTOR		222
11.1	Introduction	222
11.2	Dielectric post approach	223
11.2.1	Equivalent circuit of the diode in a reduced-height waveguide	223
11.2.2	Measurements	229
11.2.3	Obtaining the series resistance from the measured terminal impedance	234
11.3	Results	238
11.4	Conclusions	243
CHAPTER XII: CONCLUSION		245
REFERENCES		248
APPENDIX A: AUTOMATICALLY ADJUSTABLE SELECTION OF DISCRETIZATION MESH SIZE IN THE TIME DOMAIN		253

LIST OF TABLES

	Page
TABLE 2.1 : Parameters selected for fabrication process of diode No. 1 and diode No. 2	17
TABLE 2.2 : Physical dimensions selected for diode No. 1 and diode No. 2	17
TABLE 3.1 : Numerical values of parameters required in Caughey's empirical expression for mobility	22
TABLE 4.1 : List of normalisation factors used	37
TABLE 11.1 : Terminal impedance of step-recovery diode (HP. No. 5082-0251) measured by the dielectric post approach	236
TABLE 11.2 : The values of series resistance R_s for step-recovery diode (HP. No. 5082-0251) as determined by the dielectric post approach	240

LIST OF FIGURES

	Page
FIGURE 2.1 : Net impurity concentration of diode No. 1 versus distance	15
2.2 : Net impurity concentration of diode No. 2 versus distance	16
FIGURE 3.1 : Exact dependencies of electron density upon $(E_F - E_C)$ and T compared with that given by the Boltzmann approximation ⁴⁰	26
3.2 : Enlarged cross-section of a doubly diffused mesa varactor (not to scale)	30
3.3 : Carrier zone in the diode substrate under steady- state, forward-bias operating conditions	30
3.4 : One-dimensional p-n junction model	30
FIGURE 5.1 : Overall iterative scheme for steady-state calculations of diode parameters	49
FIGURE 6.1 : Iterative scheme for calculating diode parameters for the current-driven transient case	67
6.2 : Detailed overall iterative procedure used for the current-driven transient case	80
6.3 : Prediction and interpolation stages as proposed by DeMari ⁵⁴ for computation of the voltage- driven transient case	87
6.4 : Overall scheme for computing diode parameters for the voltage-driven transient case	90
FIGURE 7.1 a: Spatial distribution of net doping and mobile carrier densities for diode No. 1 under steady- state conditions for $V_A = 0.0$ volt	103
7.1 b: Spatial distribution of net doping and mobile carrier densities for diode No. 1 under steady- state conditions for $V_A = 0.7$ volt	104
7.1 c: Spatial distribution of net doping and mobile carrier densities for diode No. 1 under steady- state conditions for $V_A = 0.9$ volt	105
7.1 d: Spatial distribution of net doping and mobile carrier densities for diode No. 1 under steady- state conditions for $V_A = 1.0$ volt	106

FIGURE 7.2 a:	Spatial distribution of electrostatic potential, and hole and electron quasi-Fermi levels for diode No. 1 under steady-state conditions for $V_A = 0.0$ volt	108
7.2 b:	Spatial distribution of electrostatic potential, and hole and electron quasi-Fermi levels for diode No. 1 under steady-state conditions for $V_A = 0.7$ volt	109
7.2 c:	Spatial distribution of electrostatic potential, and hole and electron quasi-Fermi levels for diode No. 1 under steady-state conditions for $V_A = 0.9$ volt	110
7.2 d:	Spatial distribution of electrostatic potential, and hole and electron quasi-Fermi levels for diode No. 1 under steady-state conditions for $V_A = 1.0$ volt	111
7.3 a:	Spatial distribution of net recombination rate for diode No. 1 under steady-state conditions for $V_A = 0.7$ volt	113
7.3 b:	Spatial distribution of net recombination rate for diode No. 1 under steady-state conditions for $V_A = 0.9$ volt	114
7.3 c:	Spatial distribution of net recombination rate for diode No. 1 under steady-state conditions for $V_A = 1.0$ volt	115
7.4 a:	Spatial distribution of carrier mobilities for diode No. 1 under steady-state conditions for $V_A = 0.0$ volt	116
7.4 b:	Spatial distribution of carrier mobilities for diode No. 1 under steady-state conditions for $V_A = 0.7$ volt	117
7.4 c:	Spatial distribution of carrier mobilities for diode No. 1 under steady-state conditions for $V_A = 0.9$ volt	118
7.4 d:	Spatial distribution of carrier mobilities for diode No. 1 under steady-state conditions for $V_A = 1.0$ volt	119
7.5 a:	Spatial distribution of electron and hole currents for diode No. 1 under steady-state conditions for $V_A = 0.7$ volt	120
7.5 b:	Spatial distribution of electron and hole currents for diode No. 1 under steady-state conditions for $V_A = 0.9$ volt	121
7.5 c:	Spatial distribution of electron and hole currents for diode No. 1 under steady-state conditions for $V_A = 1.0$ volt	122

FIGURE 7.6 :	Terminal current of diode No. 1 as a function of terminal voltage (steady-state conditions)	125
7.7 :	Incremental capacitance of diode No. 1 as a function of terminal voltage (steady-state conditions)	126
7.8 a:	Spatial distribution of net doping and mobile carrier densities for diode No. 2 under steady-state conditions for $V_A = 0.0$ volt	128
7.8 b:	Spatial distribution of net doping and mobile carrier densities for diode No. 2 under steady-state conditions for $V_A = 0.5$ volt	129
7.8 c:	Spatial distribution of net doping and mobile carrier densities for diode No. 2 under steady-state conditions for $V_A = 0.8$ volt	130
7.8 d:	Spatial distribution of net doping and mobile carrier densities for diode No. 2 under steady-state conditions for $V_A = 1.0$ volt	131
7.9 :	Spatial distribution of electric field for diode No. 2 under steady-state conditions for $V_A = 0.0$ volt	132
7.10a:	Spatial distribution of electrostatic potential and electron and hole quasi-Fermi levels for diode No. 2 under steady-state conditions for $V_A = 0.0$ volt	134
7.10b:	Spatial distribution of electrostatic potential and electron and hole quasi-Fermi levels for diode No. 2 under steady-state conditions for $V_A = 0.5$ volt	135
7.10c:	Spatial distribution of electrostatic potential and electron and hole quasi-Fermi levels for diode No. 2 under steady-state conditions for $V_A = 0.8$ volt	136
7.10d:	Spatial distribution of electrostatic potential and electron and hole quasi-Fermi levels for diode No. 2 under steady-state conditions for $V_A = 1.0$ volt	137
7.11a:	Spatial distribution of net recombination rate for diode No. 2 under steady-state conditions for $V_A = 0.5$ volt	139
7.11b:	Spatial distribution of net recombination rate for diode No. 2 under steady-state conditions for $V_A = 0.8$ volt	140
7.11c:	Spatial distribution of net recombination rate for diode No. 2 under steady-state conditions for $V_A = 1.0$ volt	141

FIGURE	7.12a:	Spatial distribution of carrier mobilities for diode No. 2 under steady-state conditions for $V_A = 0.0$ volt	143
	7.12b:	Spatial distribution of carrier mobilities for diode No. 2 under steady-state conditions for $V_A = 0.5$ volt	144
	7.12c:	Spatial distribution of carrier mobilities for diode No. 2 under steady-state conditions for $V_A = 0.8$ volt	145
	7.12d:	Spatial distribution of carrier mobilities for diode No. 2 under steady-state conditions for $V_A = 1.0$ volt	146
	7.13a:	Spatial distribution of electron and hole currents for diode No. 2 under steady-state conditions for $V_A = 0.5$ volt	147
	7.13b:	Spatial distribution of electron and hole currents for diode No. 2 under steady-state conditions for $V_A = 0.8$ volt	148
	7.13c:	Spatial distribution of electron and hole currents for diode No. 2 under steady-state conditions for $V_A = 1.0$ volt	149
	7.14 :	Terminal current of diode No. 2 as a function of terminal voltage (steady-state conditions)	151
	7.15 :	Incremental capacitance of diode No. 2 as a function of terminal voltage (steady-state conditions)	152
FIGURE	8.1 :	Turn-on voltage response of diode No. 1 for a large current step	155
	8.2 :	Turn-on voltage response of diode No. 1 for the initial phase of the turn-on transient	156
	8.3 :	Evolution of the electric field distribution in diode No. 1 during the turn-on transient (values of time instants indicated in Fig. 8.1)	158
	8.4 :	Evolution of the electron density distribution in diode No. 1 during the turn-on transient (values of time instants indicated in Fig. 8.1)	159
	8.5 :	Evolution of the hole density distribution in diode No. 1 during the turn-on transient (values of time instants indicated in Fig. 8.1)	160
	8.6 :	Injected hole-charge ratio as a function of time during the turn-on transient for diode No. 1	162

FIGURE 8.7	: Turn-on voltage response of diode No. 2 for a large current step	163
8.8	: Turn-on voltage response of diode No. 2 for the initial part of the turn-on transient	165
8.9	: Evolution of the electron density distribution in diode No. 2 during the turn-on transient	166
8.10	: Evolution of the hole density distribution in diode No. 2 during the turn-on transient	167
8.11a:	Evolution of the electric field distribution in diode No. 2 during the initial part of the turn-on transient	168
8.11b:	Evolution of the electric field distribution in diode No. 2 during the later part of the turn-on transient	169
8.12a:	Evolution of the displacement current distribution in diode No. 2 during the initial part of the turn-on transient	170
8.12b:	Evolution of the displacement current distribution in diode No. 2 during the later part of the turn-on transient	171
8.13	: Evolution of the electron drift current distribution in n^+ -region of diode No. 2 during the turn-on transient	172
FIGURE 9.1	: Circuit model used for the study of the large-signal turn-off response of the diodes	178
9.2	: Switching waveform applied to the diodes	178
9.3	: Terminal voltage as a function of time during the initial period of the reverse transient, for diode No. 1	179
9.4 a:	Evolution of the electric field in the vicinity of the junction during the initial period of the turn-off transient, for diode No. 1	181
9.4 b:	Evolution of the electric field throughout diode No. 1 during the initial period of the reverse transient	182
9.5	: Spatial distribution of hole and electron currents for a particular time instant ($= 0.55 \times 10^{-3}$) during the reverse transient, for diode No. 1	184
9.6	: Diode terminal voltage and current as a function of time during the reverse transient, for diode No. 1	185
9.7	: Hole density distribution at various instants of time during the reverse transient, for diode No. 1	186

FIGURE 9.8 a:	Electron density distribution at various instants of time during the reverse transient, for diode No. 1	187
9.8 b:	Electron density distribution at various instants of time during the reverse transient, for diode No. 1	188
9.9 :	Terminal voltage and current as a function of time during the initial period of the reverse transient, for diode No. 2	190
9.10 :	Electric field distribution at various instants of time (values indicated in Fig. 9.9) during the initial period of the reverse transient, for diode No. 2	191
9.11 :	Terminal voltage and current as a function of time during the reverse transient, for diode No. 2	193
9.12 :	Electric field distribution at various instants of time (values indicated in Fig. 9.11) during the reverse transient, for diode No. 2	194
9.13 :	Hole density distribution at various instants of time (values indicated in Fig. 9.11) during the reverse transient, for diode No. 2	195
9.14 :	Electron density distribution at various instants of time (values indicated in Fig. 9.11) during the reverse transient, for diode No. 2	196
9.15 :	Spatial distribution of hole and electron currents for a particular instant of time ($= 0.29 \times 10^{-4}$) during the reverse transient, for diode No. 2	198
FIGURE 10.1 :	Circuit model used for the study of the large-signal, sinusoidal excitation response of the diodes	203
10.2 :	Applied waveform in the circuit of Fig. (10.1)	203
10.3 :	Terminal voltage, applied voltage and terminal current versus time for the first five cycles after the signal is applied to diode No. 1	204
10.4 a:	Spatial distribution of hole and electron densities and of electric field at time instant t_1 (value indicated in Fig. 10.3) for diode No. 1	205
10.4 b:	Spatial distribution of hole and electron densities and of electric field at time instant t_2 (value indicated in Fig. 10.3) for diode No. 1	206

FIGURE 10.4 c:	Spatial distribution of hole and electron densities and of electric field at time instant t_3 (value indicated in Fig. 10.3) for diode No. 1	207
10.4 d:	Spatial distribution of hole and electron densities and of electric field at time instant t_4 (value indicated in Fig. 10.3) for diode No. 1	208
10.5 :	Spatial distribution of hole and electron densities at various instants of time during the fourth cycle (values indicated in Fig. 10.3), for diode No. 1	209
10.6 :	Terminal voltage and current versus time for about the first cycle of the applied signal for diode No. 2	212
10.7 a:	Spatial distribution of hole and electron densities and of electric field at time instant t_1 (value indicated in Fig. 10.6) for diode No. 2	213
10.7 b:	Spatial distribution of hole and electron densities and of electric field at time instant t_2 (value indicated in Fig. 10.6) for diode No. 2	214
10.7 c:	Spatial distribution of hole and electron densities and of electric field at time instant t_3 (value indicated in Fig. 10.6) for diode No. 2	215
10.7 d:	Spatial distribution of hole and electron densities and of electric field at time instant t_4 (value indicated in Fig. 10.6) for diode No. 2	216
10.7 e:	Spatial distribution of hole and electron densities and of electric field at time instant t_5 (value indicated in Fig. 10.6) for diode No. 2	217
10.7 f:	Spatial distribution of hole and electron densities and of electric field at time instant t_6 (value indicated in Fig. 10.6) for diode No. 2	218
10.8 :	Terminal voltage and current versus time for the initial transient period for diode No. 2	219
FIGURE 11.1 :	Sectional view of junction between a rectangular waveguide (TE_{10} mode) and coaxial line	224
11.2 :	Equivalent case of configuration shown in Fig. (11.1)	224
11.3 :	Equivalent circuit for the configuration shown in Fig. (11.2)	224
11.4 :	Complete equivalent circuit for waveguide shunted by a small-diameter dielectric post and an impedance Z_1 presented by a coaxial line	228

FIGURE 11.5	: Simplified equivalent circuit applicable for a centrally-mounted diode in the waveguide	228
11.6	: Cross-section of a typical packaged varactor diode	230
11.7	: The reduced-height rectangular waveguide diode mount	230
11.8	: Circuit arrangement used for measurements on waveguide mounted varactor diodes	233
11.9	: Slotted-line calibration curve at 6.757 GHz	235
11.10	: Packaged varactor diode equivalent circuit at microwave frequencies	237
11.11	: Simplified equivalent circuit of packaged varactor diodes at lower microwave frequencies	237
11.12	: Low-frequency terminal capacitance versus bias for the step-recovery diode measured (HP. No. 5082-0251)	239
11.13	: Step-recovery diode (HP. No. 5082-0251) impedance for various bias voltages derived by Harrison's method at 6 GHz	241
11.14	: Step-recovery diode (HP. No. 5082-0251) impedance for various bias voltages derived by Harrison's method at 7 GHz	242
11.15	: Calculated incremental capacitance of diode No. 2 and low frequency terminal capacitance of step-recovery diode (HP. No. 5082-0251) as functions of forward-bias voltage	244

CHAPTER I

INTRODUCTION

The varactor diode is a semiconductor device that is used as a variable-reactance circuit element. The variable reactance is provided by the junction capacitance, which is a nonlinear function of applied voltage^{1,2}. The varactor is therefore a nonlinear element, and this nonlinearity can produce substantially different effects. One of these is the switching or modulation of a microwave signal through variation of the reactance by means of an externally applied voltage. In a second usage, the nonlinearity causes the generation of harmonics of an applied microwave signal. In a third case, two microwave signals of different frequency may be applied, resulting in parametric amplification, up-conversion or down-conversion of one of the signals.

The purpose of the present work is to investigate both the static and dynamic behaviour of microwave varactors. The popular use of overdriven varactors³ necessitated the need of an analysis which covers forward-biased conditions in a relatively general form. Moreover, the response of a varactor driven by ideal steps of current and voltage is of considerable help in understanding its dynamic behaviour. In this study, four basically different forms of external excitations are chosen to be analysed. First is the behaviour of a varactor when a forward-biasing steady-state terminal voltage is specified. Second, the external excitation chosen is a large current step applied to the varactor initially in thermal equilibrium condition ('turn-on' transient). The third case deals with the situation that occurs when a reverse-biasing

potential is suddenly applied to a varactor initially in the steady-state forward-biased condition ('turn-off' transient). The fourth aspect that is selected to be analysed is the case of a reverse-biased varactor excited by a sinusoidal microwave signal (frequency in the GHz range) that is large enough to drive the varactor into forward-biased condition for a part of the cycle.

Basic concepts in the theory of p-n junctions were first presented by Shockley.⁴ Shockley's steady-state and small signal analysis was based upon the simplifying assumption that the space-charge layer of a p-n junction is completely depleted of mobile carriers. This assumption eliminates from Poisson's equation the distribution term for mobile holes and electrons and thereby reduces a difficult system of differential equations to a single, mathematically tractable differential equation. Despite this simplifying assumption, many conclusions derived from the depletion layer approximation are verified by laboratory experiments.

Shockley's depletion layer approximation contains severe restrictive features rendering it inapplicable to several modes of junction operation. In particular, to assume that the space-charge layer is free of mobile charge carriers implies that such a theoretical approximation is not applicable to forward-biased p-n junctions, nor to reverse-biased junctions containing a large electric current. Although these limitations have been recognised by many workers, no rigorous analytical treatment of the problem has been reported. Instead, other approaches^{5,6,7} have been used to simplify the mathematical equations characterising a semiconductor junction; each approach, however, has introduced a new set of uncertainties concerning the analytical

limitations arising from the use of simplifying assumptions.

A number of workers⁸⁻¹⁶ have studied the turn-on and turn-off transient in p-n junctions. These investigations have been conducted upon analytical models which neglected many physical mechanisms encountered in practical devices. Moreover, only highly asymmetrical p-n junctions were considered. Benda et al.¹⁷ gave a second order analytical treatment for p-i-n rectifiers. This analysis also neglected many physical mechanisms which are encountered in actual practice. To our knowledge, no comprehensive analytical treatment has been reported for a p-n junction excited by a sinusoidal signal large enough to forward-bias it for part of the cycle. The presence of the passive elements surrounding the p-n junction devices in the actual circuitry further complicates the already formidable mathematical problem.

Some of the assumptions generally adopted in almost all of the analytical work for the one-dimensional model (to which attention will be limited in this thesis) are the following:

- (a) Separation of the structure into regions with sharp boundaries, either fully depleted of mobile carriers, or space-charge neutral;
- (b) Postulation of explicit boundary conditions on relevant quantities in the interior of the device and at the interface between the depleted and neutral regions of assumption (a); limited choice of boundary conditions at the external contacts;

- (c) Limitation of the doping profile to very special cases (mostly step and linear distributions) and to particular quantitative values (mostly highly asymmetric impurity distributions);
- (d) Simplification of the dependence of carrier mobilities upon the electric field, doping and scattering phenomena;
- (e) Limitation of carrier recombination laws to the low-level linear case.

Numerical methods, with the aid of high-speed digital computers represent an alternate approach to the problem, the final aim being the achievement of a solution of the most general character without the conventional assumptions. Serious difficulties are also present in a numerical investigation, and have prevented most of the currently available numerical solutions from having the general character desired. The first comprehensive and general numerical procedure for the solution of the steady-state problem is presented by Gummel¹⁸ and is applied to the solution of transistors. DeMari¹⁹ later on exposed some of the limitations of Gummel's analytic formulation, slightly modified it and applied it to very short junction structures. Kennedy et al.²⁰ used numerical techniques to solve the zero-current model of the linearly-graded p-n junction. Later, DeMari²¹ reported a numerical method of solution of p-n junctions under arbitrary transient conditions and applied it to his simpler model having zero-recombination and constant mobilities to obtain solutions for the case of a highly asymmetrical step p-n junction. Another algorithm for time-dependent solutions of p-n

junction devices is reported by Scharfetter and Gummel²²; they applied it to solve for the large-signal behaviour of IMPATT diodes.

In this thesis numerical solutions for a relatively general physical model, considered sufficient for microwave varactors, are obtained to study the device behaviour under both static and dynamic conditions. The solutions for steady-state conditions are based on the algorithm furnished by Gummel¹⁸. The algorithm is slightly modified to make it more efficient at higher forward biases where Gummel's original algorithm tends to fail. The time-dependent solutions are based upon an extension of the algorithm furnished by DeMari²¹ for our more general physical model. Suitable numerical techniques are selected to deal with various critical situations inherent in the solution for our particular device. All the reported solutions are for one-dimensional cases. Microwave measurements of the static properties, particularly the series resistance, are also undertaken.

The presentation is divided into eleven sections. Chapter II discusses various design considerations for microwave varactors and describes the particular device structures chosen to represent two distinct types. Chapter III describes the important physical mechanisms included in the physical model adopted and discusses implications of the various assumptions made. Chapter IV describes the fundamental equations and boundary conditions that determine mathematically both the steady-state and time-dependent problems. Chapter V describes the details of the analytical formulation and the numerical techniques adopted for the steady-state case. Chapter VI presents the analytical formulation and numerical techniques suitable for the achievement of time-dependent solutions for the present physical model. It is an extension of the

numerical algorithm presented by DeMari²¹ for his simpler physical model. This chapter also discusses various sources of numerical error present in the algorithm and various trade-offs between different errors to decrease the overall error without increasing computation time. Chapter VII presents the results for the steady-state case: terminal properties and quantities in the interior of the device are displayed; the results are briefly discussed. Chapter VIII presents the results for the case when a large step of current is applied to the varactor initially in thermal equilibrium (turn-on transient). A brief discussion on the results is also offered. Chapter IX presents the results for the case when a reverse-biasing potential is applied to the varactor initially in the forward-biased condition (turn-off transient). The results are also discussed. Chapter X presents the internal and external behaviour of the varactor in a broad-band multiplier circuit. Chapter XI describes the various microwave techniques employed to measure the static characteristics of a varactor. Conclusions are given in Chapter XII; some of the several immediate applications for the analysis under more general conditions and the possibilities of extensions to more complex situations are briefly discussed.

CHAPTER II

MICROWAVE VARACTOR DIODES

This chapter describes the choice of physical structures representing the main categories of microwave varactor diodes. A simple mathematical model is formulated to predict the impurity distribution inside the diode structure. The parameters in the mathematical model are then chosen so that the desired impurity distribution is obtained. At the end of this chapter, the impurity distributions inside the diodes are displayed and various structural parameters of the diodes are tabulated.

2.1 Introduction

Microwave varactor diodes can be classified into two main categories. The diodes belonging to the first category have a varying capacitance in the reverse voltage direction. The movement of the potential wall in the depletion region uncovers charge continuously, and results in the capacitance change. This capacitance change in the reverse direction is used in varactor multipliers to obtain harmonic currents, which are related to the order of non-linearity in this capacitance. This class of microwave varactors will be mentioned as 'varactor diodes' in this thesis. The diodes belonging to the second category exhibit a relatively constant reverse-bias capacitance and a very large diffusion capacitance in the forward direction, resulting in a much greater variation of the total capacitance of a varactor. This class of microwave varactors will be mentioned as 'step-recovery diodes' in this thesis.

2.2 Design Considerations

Various useful varactor diode structures are described by Chang and Forster²³. They show that hyper-abrupt junctions, and "Pagoda" structures exhibit a relatively large capacitance variation. However, when compared to a step-junction having the same breakdown voltage, the improvement due to increased capacitance-voltage sensitivity is offset, or more than offset by the concomitant increase in the R-C product. Therefore a heavily doped step-junction can be taken to represent microwave varactors. It is almost impossible with the presently developed technology to construct a $p^+ - n^+$ diode with perfectly abrupt steps in the impurity concentration at the boundaries. Hence a doubly-diffused epitaxial diode in which the diffusion is very deep, i.e., the junction is formed by the impurities diffused in from the surface and substrate, is chosen as a typical microwave varactor. The impurity concentration at the substrate and at the surface are assumed to be very high to ensure low series resistance.

In the step-recovery diodes a constant reverse-bias capacitance and a very high diffusion capacitance are required. The diffusion capacitance is produced by the injection of minority carriers during the forward bias excursion of the varactor pump voltage and the subsequent withdrawal of this charge during the reverse bias portion of the waveform. In a step-recovery diode the following requirements must be met: Firstly, the junction must be capable of minority carrier injection, i.e., the injection of holes from a p-type region into an n-type region, and/or electrons in the other direction. The second basic requirement is that the injected charge be recoverable during the reverse-bias half of the cycle. In order for this to occur, two conditions are necessary; first,

the carriers must not recombine appreciably before they are withdrawn²⁴, and second, the carriers must not diffuse so far from the junction that they cannot be retrieved. The first condition is easily met by most silicon epitaxial microwave diodes, since the typical minority-carrier lifetime in such a material ranges from 10^{-8} to 5×10^{-6} seconds. Moreover, the diode can be subjected to higher lifetime²⁵ treatment to achieve still higher minority-carrier lifetime. Ga-As will fulfil this condition at higher microwave frequencies because minority-carrier lifetime is 10^{-9} seconds or less. Nearly all step-recovery diodes used at microwave frequencies below millimeter range are made of silicon. To satisfy the second of the above conditions, i.e., to prevent the minority-carriers from diffusing beyond the point of no return, large built-in electric fields on both sides of the junction are necessary. Also, because of the finite time required for the carriers to cross the depletion-region and current-limiting effects of the field produced by the injected carriers themselves, the depletion region must not be too wide. The ideal $p^+ - i - n^+$ diode is one with perfectly abrupt steps in impurity concentration at the boundaries with the i-layer, having a width between 0.5 and 4 microns. The epitaxial growth and diffusion occur in finite times at the diffusion temperature so that i-layer boundaries are graded. The device has to be fabricated such that the impurity profile is very steep. Moll et al.²⁶ have stated that if the width of the gradient region measured to an impurity concentration of 10^{18} cm^{-3} is less than 1/4 to 1/2 of the i-layer width, there is insignificant rounding-off and relatively little dependence of transient behaviour on the charge injection level. This criterion has been utilised in choosing

the impurity doping profile in this study. Undoped growth of silicon generally results in an n-type material. Thus the high-resistivity center region of the step-recovery diode analysed is assumed to be slightly donor doped (10^{15} cm^{-3}). The steep impurity profiles and the narrow junctions required for fast and complete recovery of the injected charge necessarily result in a lower breakdown voltage. The high-resistivity center region decreases the cut-off frequency of the device, since the effective series resistance¹ of a varactor is larger when its charge-storage capacitance is used than when operation is confined strictly to dielectric capacitance.

Another consideration which is important is the choice of junction area. We know that the junction capacitance and charge stored during forward-bias conditions²⁴ are proportional to the junction area. In step-recovery diodes the reverse-bias capacitance is undesirable²⁴; therefore, from this point of view, small junction area is desirable. As a result, a compromise has to be made between the charge-stored which decreases as the area is decreased and the reverse-bias junction capacitance which can be tolerated. The higher mobility of free electrons compared to that of the holes results in a lower resistivity for the same doping level. For this reason, the substrate in epitaxial mesa varactors is usually chosen to be n-type.

2.3 The Fabrication Process and its Mathematical Model

2.3.1 Fabrication Process

Fabrication steps²⁶ include epitaxial growth of the $i - n^+$ boundary and subsequent growth or diffusion of the $i - p^+$ boundary. These steps are followed by more or less conventional semiconductor

fabrication steps to shape it into a mesa-type structure. The diffusion time and temperature are chosen so as to yield the required impurity gradient. In the case of varactor diodes, deep diffusion is required, while in step-recovery diodes shallow diffusion is needed. In some cases the process is simplified and diffusion of donor impurities from the substrate and acceptor impurities from the surface are carried out simultaneously²⁷. Boron is one of the most useful p-type impurities and is chosen as the p-type impurity for our calculations. The substrate is taken to be phosphorous-doped. Phosphorous and boron have the same diffusion coefficient for 1000 - 1200°C, the most usual diffusion temperatures. For a varactor, where deep-diffusion is required, the substrate can be doped with arsenic (which has a diffusion coefficient whose value is 1/3 that of boron) to yield a deeper junction from the p-type impurity side. This in turn makes the ohmic contact to the surface easier to produce.

2.3.2 The Mathematical Model

Fick's first and second laws²⁸ are taken to govern the diffusion phenomenon.

$$f = -D \frac{\partial N}{\partial x} \quad \dots(2.1)$$

$$\frac{\partial N}{\partial t} = D \frac{\partial^2 N}{\partial x^2} \quad \dots(2.2)$$

where

f = particle flux through a plane parallel to the surface ($\text{cm}^{-2} \text{sec}^{-1}$),

D = diffusion coefficient ($\text{cm}^2 \text{sec}^{-1}$),

N = impurity concentration (cm^{-3}).

The first equation describes the rate of permeation of the diffusing impurities through a unit cross-sectional area of the host medium. The second equation specifies the rate of accumulation of diffusing impurities at different points in the host medium as a function of time.

The in-diffusion from the surface can be considered as if the epitaxial layer were of infinite thickness and its background impurity concentration negligible compared to the surface concentration. Then, for boundary conditions:

$$N(0,t) \Big|_{t \neq 0} = N_s; N(x,0) = 0 \quad \dots(2.3)$$

where

N_s = impurity concentration at the surface (cm^{-3}) and

x = distance from the surface (cm).

The solution²⁸ of Eq. (2.2) for a semi-infinite medium and boundary conditions of Eq. (2.3) yields the p-type impurity concentration-distribution:

$$N_a(x,t) = N_s \left(1 - \operatorname{erf} \frac{x}{2\sqrt{D_1 t}} \right) \quad \dots(2.4)$$

The n-type impurity distribution due to out-diffusion from the substrate can similarly be considered to occur as if the substrate and the epitaxial layer were of semi-infinite width; the background impurity concentration can be considered to be negligible compared to the substrate impurity concentration. Then, solving Eq. (2.2) for the boundary conditions:

$$N(x,0) = N_o \quad -\infty < x < 0$$

and

$$N(x,0) = 0 \quad 0 < x < +\infty ,$$

the donor impurity distribution can be expressed as follows (using the origin for x as in Eq. 2.4)

$$N_d(x,t) = \frac{N_o}{2} \left(1 - \operatorname{erf} \frac{x_e - x}{2\sqrt{D_2 t}} \right) \quad \dots(2.5)$$

where

x_e = epitaxial layer thickness,

N_o = impurity concentration of the substrate (cm^{-3}) and

$D_1, (D_2)$ = diffusion constant of p-type (n-type) impurity.

Detailed derivation of Eqs. (2.4) and (2.5) is given by Boltak²⁸. The net impurity distribution in the epitaxial layer after diffusion can be obtained from Eqs. (2.4) and (2.5) and its original impurity distribution. Thus:

$$N(x) = -N_s \left(1 - \operatorname{erf} \frac{x}{2\sqrt{D_1 t}} \right) + \frac{N_o}{2} \left(1 - \operatorname{erf} \frac{x_e - x}{2\sqrt{D_2 t}} \right) + N_b \quad \dots(2.6)$$

since the epitaxial layer is assumed to be uniformly doped with a density N_b . In this model we have neglected the following physical processes:

(1) The drift of the impurities due to electric field created during the diffusion process;

(2) The growth "tail" and out-diffusion of donor impurities from the substrate that may occur into the epitaxial layer during the epitaxial growth;

(3) The precipitation of the impurities that may occur during the diffusion process;

(4) The interaction of impurities with each other.

2.4 Physical Description of the Diodes Selected

Two basically different structures have been selected to represent the two distinct kinds of varactors. The choice of different structural parameters is based upon the discussion in Section 2.2. The doping profile is predicted by the mathematical model given in section 2.3. The diode chosen to represent varactor diodes is named 'diode No.1', and the diode chosen to represent step-recovery diodes is called 'diode No. 2'. Figures (2.1) and (2.2) display the doping profiles chosen for diode No. 1 and diode No. 2, respectively. Table (2.1) gives the description of the various parameters selected for our mathematical model to predict the doping profiles displayed in Figs. (2.1) and (2.2). Table (2.2) gives the description of the structural parameters of the diodes.

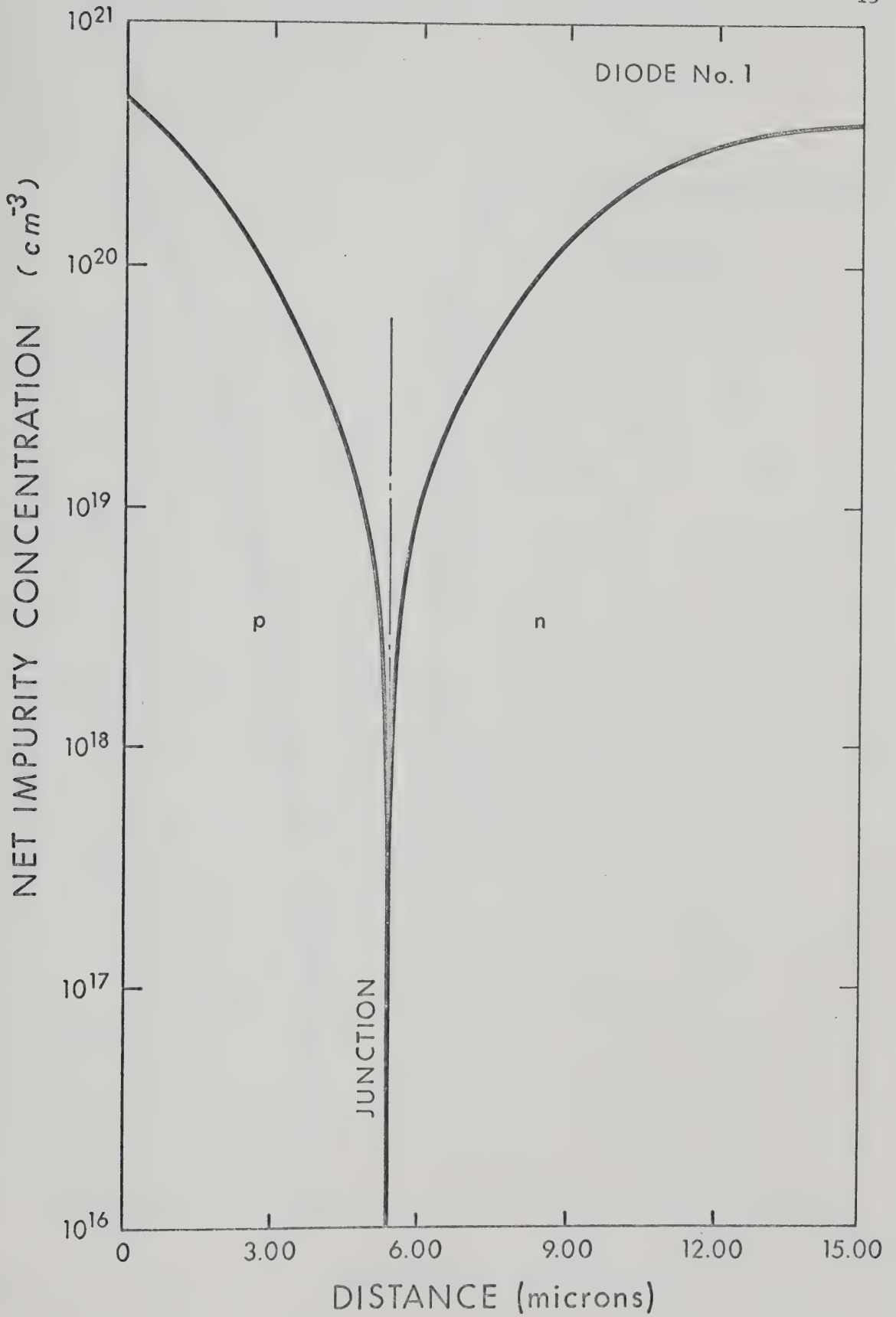


Fig. 2.1. Net impurity concentration of diode No. 1 versus distance.

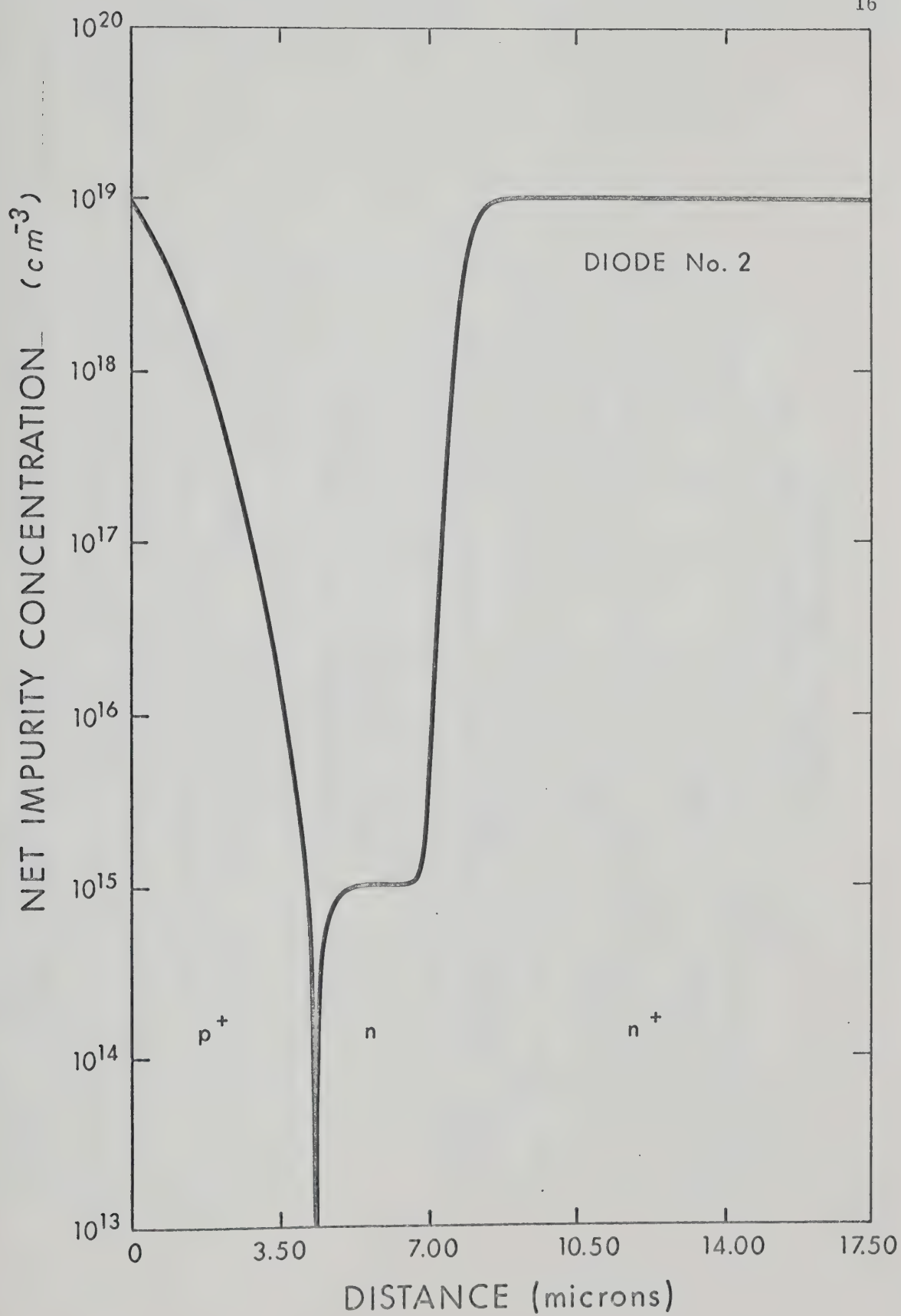


Fig. 2.2. Net impurity concentration of diode No. 2 versus distance.

Diode No.	Donor Material	Acceptor Material	Epitaxial Layer Doping	Diffusion Temperature	Diffusion Time
1	Phosphorous	Boron	10^{15} cm^{-3} Donor	1250°C	58 min.
2	Antimony	Boron	10^{15} cm^{-3} Donor	1200°C	35 min.

TABLE 2.1. PARAMETERS SELECTED FOR THE FABRICATION
PROCESS OF DIODE NO. 1 AND DIODE NO. 2.

Diode No.	Substrate Thickness	Epitaxial Layer Thickness	Cross-Section Area of Mesa (A)
1	20 Microns	10 Microns	$0.19 \times 10^{-4} \text{ cm}^2$
2	50 Microns	8 Microns	$0.19 \times 10^{-4} \text{ cm}^2$

TABLE 2.2. PHYSICAL DIMENSIONS SELECTED FOR
DIODE NO. 1 AND DIODE NO. 2.

CHAPTER III

PHYSICAL MODELLING

In this chapter, important physical processes occurring in the device are described. Various simplifications and assumptions are stated. Mathematical equations modelling the simplified physical processes are formulated. At the end of this chapter, the validity of the one-dimensional model is discussed.

3.1 Introduction

As stated earlier in Chapter I, numerical techniques have been preferred over analytical techniques to avoid most of the inherent limitations in the latter approach. With the aid of numerical techniques it is possible to include the various physical processes in their most general form. However, many serious difficulties are encountered in formulating a general numerical scheme. These difficulties arise from severe non-linearities inherent in the mathematical equations describing the problem. The other limiting factors which are to be taken into consideration are the availability of a limited computer memory and the need to keep the computation time within practical limits. In view of the above considerations, various assumptions have been made to simplify the problem mathematically. In the following sections, these simplifying assumptions are outlined and a qualitative discussion is offered on their validity in the present case.

3.2 Important Physical Phenomena

In this section, various assumptions made to simplify the mathematical problem are outlined. Mathematical equations to represent the simplified physical processes are formulated.

3.2.1 Bulk Generation - Recombination

The measured properties of silicon p-n junctions at room temperature deviate considerably from that predicted by Shockley's⁴ "ideal" theory. Later, Shah, Noyce and Shockley²⁹ improved the theory by taking into account the recombination and generation of the carriers in the space-charge region. They used a model of the single-level uniformly distributed Shockley, Read³⁰ and Hall³¹ recombination-generation centers to explain the p-n junction characteristics. According to Shockley and Read³⁰:

$$U = \frac{pn - n_i^2}{(n + n_1)\tau_{po} + (p + p_1)\tau_{no}} \quad \dots(3.1)$$

where

U = net recombination-generation rate ($\text{sec}^{-1} \text{ cm}^{-3}$)

p = density of holes (cm^{-3})

n = density of electrons (cm^{-3})

n_i = intrinsic concentration of carriers (cm^{-3})

τ_{po} = life time of excess holes in heavily doped n-type material (sec)

τ_{no} = life time of excess electrons in heavily doped p-type material (sec)

p_1 = density of holes when the Fermi-level is precisely at the trap level E_t (cm^{-3})

n_1 = density of electrons when the Fermi-level is precisely at the trap level E_t (cm^{-3}).

Recently Dolcan³² calculated the effects of the spatial dependence of recombination centers on the I-V characteristics of p-n junctions. He showed that these effects may explain the experimental deviations from Shockley's⁴ theory and from the theory of the carrier generation-recombination in the space-charge region. The 'gradual capture effect' is considered in his analysis by noting the possibility that the concentration of the capture centers tends to decrease when going inwards from the semiconductor surface and, therefore, for the carrier life time to increase in this direction.

Equation (3.1) is derived under the assumption that majority-carrier density is large compared to trap density so that we may neglect the change in charge density produced by changing concentrations in the traps. Two other assumptions made are non-degenerate conditions and that the readjustment time for a trapped electron is negligible compared to the average time for the trap to emit the electron and capture a hole. In order to use Eq. (3.1), we have to know trap level $E_t - E_i$ and carrier life times. Shockley²⁹ obtained them for his theoretical calculations by matching the theoretical formula, using linear-graded junction approximations, and the experimental data at three points. In this approach, however, no such elaborate effort is made. Rather, these parameters are chosen from empirical data in the literature. As the p-n junction is formed by diffusion of shallow impurities, phosphorous and boron, $E_t - E_i$ can be taken to be $10kT$ ²⁹. The life times of holes and electrons, τ_{po} and τ_{no} respectively, are assumed to be equal and equal to 10^{-6} sec. unless otherwise specified. A higher value, though not unrealistic², is used to decrease the effect of recombination which should be the case in the ideal step-recovery diode.²⁴ Moreover, we

treat carrier life-times independently of carrier densities, as the effect of such variation will be negligible in most devices³³.

3.2.2 Mobility

The dependence of mobility on doping density and field strength are well known^{33,34}. For simplicity, the carrier mobilities are often assumed invariant within a particular sample of semiconductor material. This, of course, is sometimes an unreasonable simplification. Experiments show that within a given sample of semiconductor material, the mobilities of holes and electrons undergo large changes³³. Such changes arise at large values of electric field and at impurity atom concentrations. For this reason, in this work, we consider the influence of both the electric field and impurity atom density upon mobility properties of holes and electrons.

In our analysis we have used analytic expressions³⁶ for hole and electron mobility dependence on doping density and field strength. Caughey et al.³⁶ derived these expressions empirically from published experimental data. Doping dependence of mobility is of the following form:

$$\mu = \frac{\mu_{\max} - \mu_{\min}}{1 + (N_{\text{gross}}/N_{\text{ref}})^{\alpha}} + \mu_{\min} \quad \dots(3.2)$$

where

$$N_{\text{gross}} = N_d + N_a .$$

Values of μ_{\max} , μ_{\min} , N_{ref} and α are given in Table (3.1), for silicon.

Parameter	Value		Units
	Holes	Electrons	
μ_{\max}	495.0	1330.	$\text{cm}^2/\text{V-S}$
μ_{\min}	47.7	65.0	$\text{cm}^2/\text{V-S}$
α	0.76	0.72	
N_{ref}	6.3×10^{16}	8.5×10^{16}	cm^{-3}

TABLE 3.1. NUMERICAL VALUES OF PARAMETERS
REQUIRED IN CAUGHEY'S EMPIRICAL
EXPRESSIONS FOR MOBILITY.

The field dependence of mobility is given by the following expression:

$$\mu = \frac{\mu_o}{1 + \frac{|E|}{E_{crit}}} \quad \dots(3.3)$$

where

μ_o = low field mobility

E_{crit} = critical field strength

= 20,000 V/cm for holes

= 8,000 V/cm for electrons

$|E|$ = absolute value of the electric field.

Another effect which is important is carrier-carrier collisions, which further decreases the mobility. This effect is only important at high injection levels. The possibility of a reduction in carrier mobility by carrier-carrier scattering at high concentrations has been discussed by Fletcher⁵, Hall³⁷ and Davies³⁸. They have found reasonable agreement between experimentally measured values obtained on germanium and the values obtained by the formula

$$\frac{1}{\mu} = \frac{1}{\mu_o} + \frac{1}{\mu_{np}} \quad \dots(3.4)$$

where μ_o is the low level mobility and μ_{np} is given by Eq. (3.5)

$$\mu_{np} = \left\{ \frac{3\epsilon^2 (kT)^{3/2} (m_n + m_p / m_n m_p)^{1/2}}{\pi^{1/2} 2^{5/2} q^3 n} \right\} \cdot \left[\ln \left\{ \frac{12\pi\epsilon (kT)^2}{h^2 q^2 n} \cdot \frac{m_n + m_p}{m_n m_p} \right\} \right]^{-1} \quad \dots(3.5)$$

where³⁹

ϵ = dielectric constant (11.7 for silicon)

m_n = effective mass of electron ($1.1m_o$ for silicon at 20°C)

m_p = effective mass of holes ($0.57m_o$ for silicon at 20°C)

h = Plank's constant

$n = p$ = carrier density.

Fletcher⁵ showed that hole-electron scattering is important at densities greater than 10^{17} cm^{-3} . Since for the dynamic conditions to which the diode is subjected, carrier concentration of this order will be restricted to a narrow region in the vicinity of the junction, we have neglected this effect to reduce the computation time.

3.2.3 Degeneracy

In this study, Boltzmann statistics are assumed to be valid. This assumption simplifies the mathematical problem in many ways; charge transport phenomena can be derived from Boltzmann's transport equation, validity of Einstein's relation can be assumed and Boltzmann's relation can be used.

As has been discussed by Shockley⁴⁰, the difference between Fermi and Boltzmann statistics is negligible when the predicted carrier concentrations are small compared to the effective numbers of states in the conduction and valence bands. The effective density of states in the conduction and valence bands is given by

$$N = 2.5 \times 10^{19} \left(\frac{m_{\text{eff}}}{m_o} \right)^{3/2} \left(\frac{T}{300\text{K}} \right)^{3/2} \dots (3.6)$$

So at $T = 300\text{K}$, using $m_{\text{eff}} = 0.49m_o$ for holes and $m_{\text{eff}} = 0.98m_o$ for electrons⁴¹

$$N_c \approx 2.4 \times 10^{19} \text{ cm}^{-3}$$

$$N_v \approx 8.5 \times 10^{18} \text{ cm}^{-3}$$

It is evident that degeneracy will first become apparent in the valence band. As discussed in detail by Shockley⁴⁰, the Boltzmann statistics are valid up to $0.1 N$, i.e., hole density of $0.85 \times 10^{18} \text{ cm}^{-3}$ and electron density of $0.24 \times 10^{19} \text{ cm}^{-3}$ for silicon. From Shockley's discussion, the error in Boltzmann statistics is less than a factor of two for predicted carrier densities less than about $4N$; a hole density of $3.8 \times 10^{19} \text{ cm}^{-3}$ and electron density of $9.6 \times 10^{19} \text{ cm}^{-3}$ for silicon. This point is further illustrated by Fig. (3.1). It shows that classical approximation always overestimates the carrier density in the valence and conduction bands.

3.2.4 Surface Recombination and the Surface Boundary Condition

Surface recombination is characterized by a parameter termed surface recombination velocity, just as the bulk recombination process is characterized by the life time of minority carriers. It defines the average velocity of carriers which maintain the recombination process by their flow to the surface. This parameter is dependent upon the carrier concentration and is constant only in the case of small deviations from the equilibrium concentration. The velocity S depends essentially on the treatment of the surfaces. Only by careful etching may a low value of surface recombination velocity be obtained. If it is high, injected carriers will be lost to the surface, and leakage current will be generated at the surface, the direction depending upon whether the operation of the device exposes the surface to a condition of minority carrier flooding or depletion. A value of 100 cm/sec is, in the opinion

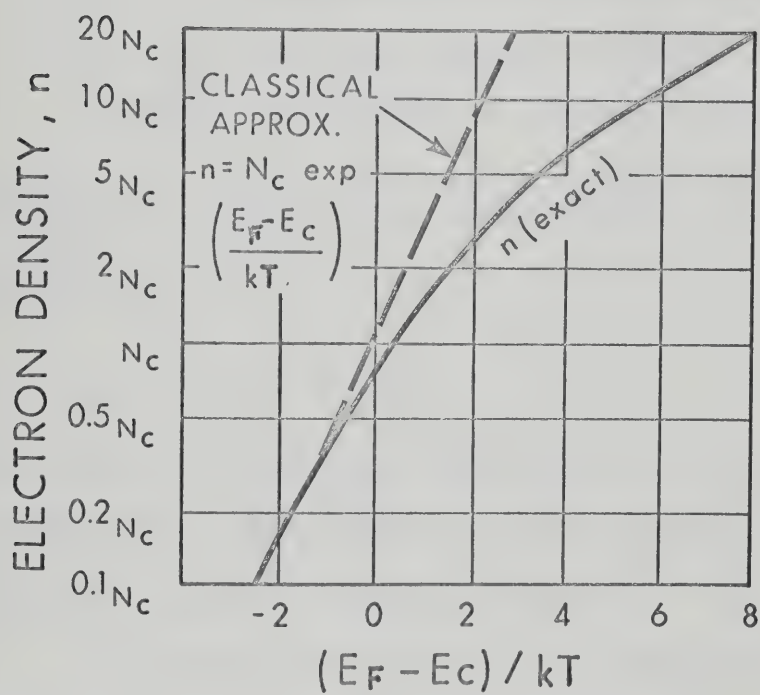


Fig. 3.1. Exact dependencies of electron density upon $(E_F - E_C)$ and T compared with that given by the Boltzmann approximation⁴⁰.

of the author, a reasonable value for carefully etched devices. It can be shown⁴² that

$$S = \frac{\bar{C}}{2} \frac{1 - R_o}{1 + R_o} \quad \dots(3.7)$$

where

S = surface recombination velocity

\bar{C} = the mean thermal speed

R_o = the probability that a single carrier in single collision with the surface will be sent back to the bulk rather than absorbed by recombination.

The boundary condition for minority carriers is given by⁴² (for a n-type specimen)

$$J_p = qS (p - p_n) \quad \dots(3.8)$$

where p and p_n are perturbed and equilibrium values of hole distribution, respectively. It is evident from Eq. (3.7) that the maximum value of velocity of surface recombination is $\bar{C}/2$.

In our analysis we have assumed that thermal equilibrium prevails at the contacts, i.e. carrier density at the contacts is constant and equal to its equilibrium value at all voltages of interest. Physically this means that terminal current on the p-side is totally carried by holes and terminal current on the n-side is totally carried by electrons. At low and medium forward-bias conditions, the minority carrier concentrations reaching the contacts (as given by Eq. (3.8)) are very small compared to the majority carrier concentrations; so it makes little difference in predicting the internal carrier distribution and the

terminal current if we use this assumption, which greatly simplifies the solution. However, at large forward-biases, the assumption that thermal equilibrium prevails at the contacts has to be modified according to Eq. (3.7), particularly on the p-side which is heavily doped and shorter in width compared to the n-side.

Along with the condition of thermal equilibrium, it is also assumed that charge neutrality prevails at the contacts. These two assumptions physically mean that the contacts are ohmic. Again the condition of neutrality will be violated at large forward-biases.

The assumption of thermal equilibrium at the contacts is augmented in step-recovery diodes by the fact that the doping profile is so chosen that the built-in electric field tends to localize the injected carriers near the junction and prevents them from reaching the contacts.

3.3 Assumptions for other Physical Phenomena

- (1) Temperature is assumed to be constant at 300°K .
- (2) Net doping density is independent of time.
- (3) Impurities are completely ionised.
- (4) Effect of radiation is negligible.
- (5) Tunnelling is negligible.
- (6) Skin effect is insignificant.
- (7) Frequency of the a.c. signal considered is low enough to allow the semiconductor to be collision dominated.

3.4 Validity of One-Dimensional Analysis

The fact that our analysis is one-dimensional should be looked into a little more deeply, to obtain some qualitative estimate of the effect it will have on our results. Many of the microwave varactors and

step-recovery diodes have a mesa structure, as shown in Fig. (3.2). At first glance, the validity of a one-dimensional analysis appears to be doubtful for both the static and dynamic cases. Let us start by considering the case when forward-bias is applied to the diode and steady-state conditions are allowed to prevail. The hole current will flow down through the substrate to the ohmic contact. Fig. (3.3) shows that the stationary forward current has a radial component. Its lateral spreading is, however, restricted by the fact that, at a constant voltage the current density rapidly decreases if the effective base width becomes too large compared to the ambipolar diffusion length. It is because of the bulk recombination and the longer the path that a carrier takes, the greater is the chance that it will recombine. We also see that the greater the recombination, the less will be the lateral spreading. At high forward biases, carrier mutual repulsion and non-uniformity of temperature will contribute further to lateral displacement, but again the bulk-recombination will tend to reduce this additional radial component by heavier recombination and hence reducing the current density and number of carriers that are laterally spread.

Moreover, in step-recovery diodes, the built-in electric field tends to localize the injected minority carriers in the vicinity of the intrinsic layer and thus tends to prevent the carriers from going deep into the substrate and from spreading there laterally.

Now let us go one step further and consider the situation where a diode, initially in forward-biased state, is suddenly reverse-biased. Conditions in the substrate are different particularly in the vicinity of the p-layer. Since initially charge neutrality is absent here, a stronger spreading can occur by mutual repulsion of holes. Besides, the

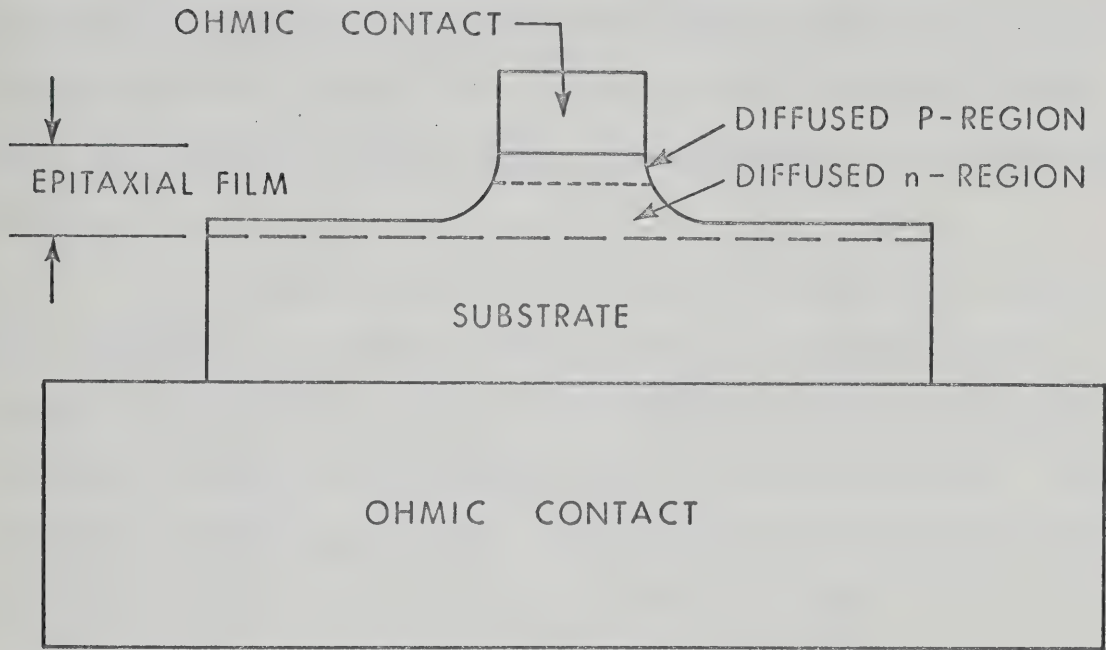


Fig. 3.2. Enlarged cross section of a doubly diffused mesa varactor (not to scale).

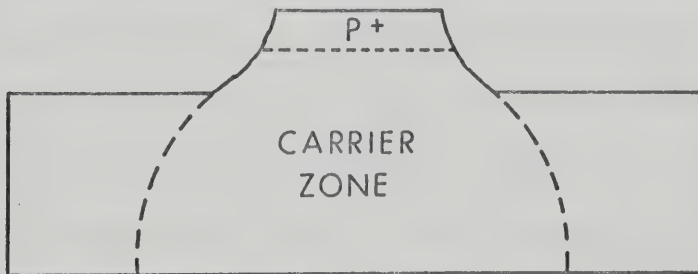


Fig. 3.3. Carrier zone in the diode substrate under steady-state, forward-bias operating conditions.

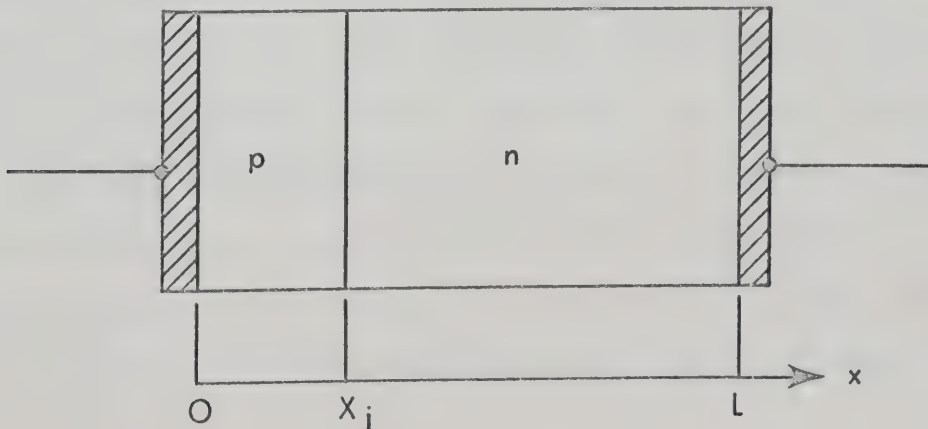


Fig. 3.4. One-dimensional p-n junction model.

current is flowing as a drift current and with relatively low recombination compared to the steady-state case; it can make good use of lateral spreading. Lateral spreading thus reduces the current density and a smaller voltage drop may result when compared to the one-dimensional model.

When a diode is turned-on by a high current pulse the displacement current will initially be dominant and then gradually particle current will take over and mobile carriers will be injected across the junction; in this case, recombination will be quite significant. Thus, the lateral displacement of the injected carriers will be checked in the later part of the transient as in the steady-state case.

However, the assumption of constant uniform temperature throughout the device when it is being subjected to high power operation is not valid. The temperature towards the center will be higher than that near the surface, because of imperfect cooling of the heat generated. Moreover, the surface recombination velocity has a finite value. This accumulation of charge at the contact when the diode is driven into high forward-bias condition will contribute to further degrade the one-dimensional model.

Thus, from the above qualitative arguments, it is obvious that the values of dynamic characteristics predicted by our model will be the least that may be expected. The performance of the device will be degraded by various effects (lateral spreading, non-uniform temperature distribution and finite recombination velocity at the surface, etc.) which are ignored in our present analysis. Moll et al.²⁶ give an empirical estimate of the allowance to be made to the recovery time in $p^+ - i - n^+$ diodes predicted by the uniform one-dimensional model. He

suggests that 10 picoseconds per micron of i-layer width adequately accounts for the discrepancy caused by various effects which the one-dimensional model ignores. It is obvious that for transition times of 0.5 ns or more this correction is relatively small (8% or less in our case).

3.5 Synopsis

The Shockley - Read - Hall single-level model is taken to characterize the carrier generation-recombination in our device. Carrier mobility dependence upon doping concentrations and electric field is considered. The empirical expressions given by Caughey et al.³⁶ are used. The validity of Boltzmann statistics is assumed. It is further assumed that thermal equilibrium and charge-neutrality prevail at the contacts. Constant temperature, time independent net doping concentrations, complete ionisation of impurities and no tunnelling are also assumed. Skin effect and radiation effects are neglected. Moreover, the semi-conductor is assumed to be collision-dominated. It is pointed out that the one-dimensional model fails to take into consideration various effects such as lateral spreading of carriers, non-uniform distribution of temperature etc.

CHAPTER IV

MATHEMATICAL MODELLING

In this chapter, the mathematical equations based upon the physical modelling discussed in Chapter III are set up. These equations are then normalised to avoid recurring factors. They are then simplified for both the time-independent (steady-state case) and time-dependent cases for the one-dimensional model. At the end of this chapter, the boundary conditions for these normalised equations are formulated.

4.1 Introduction

Having made the simplifying assumptions for the physical processes occurring inside the device, the next step is to outline various mathematical equations which are taken to govern the physical behaviour of the device. The system of equations used in this analysis was previously outlined by Van Roosbroeck⁴³ in connection with investigations of the flow of holes and electrons in semiconductor materials. Appropriate boundary conditions, necessary for the unique solution of the above mentioned equations, are easily obtained from the simplified physical model of Chapter III. This system of equations along with the appropriate boundary conditions form our mathematical model, which completely defines the mathematical problem. The solution of this mathematical problem will yield the behaviour of the device as originally desired.

4.2 Fundamental Mathematical Equations

4.2.1 Charge Transport Equation

The Boltzmann transport equation (our assumption of non-degenerate semiconductor makes the Boltzmann statistics valid) with various conventional approximations (Moll, pp. 62 - 67)⁴⁴ and supplemented by quantum mechanical restrictions (Pauli-exclusion principle) is taken to describe the transport phenomena in our model. It yields electron and hole currents as a sum of a diffusion component and a drift component representing Ohm's law. Such a simple form of current flow equation yields the following equation for holes and electrons, respectively:

$$\begin{aligned} J_p(\bar{r}, t) = & -q\mu_p(\bar{r}, t) p(\bar{r}, t) \nabla \Psi(\bar{r}, t) \\ & -qD_p(\bar{r}, t) \nabla p(\bar{r}, t) \end{aligned} \quad \dots(4.1)$$

$$\begin{aligned} J_n(\bar{r}, t) = & -q\mu_n(\bar{r}, t) n(\bar{r}, t) \nabla \Psi(\bar{r}, t) \\ & +qD_n(\bar{r}, t) \nabla n(\bar{r}, t) \end{aligned} \quad \dots(4.2)$$

4.2.2 Charge Continuity Equation

The continuity equations for holes and electrons are statements of conservation of charge and areas follows:

$$\frac{\partial p(\bar{r}, t)}{\partial t} = -U(\bar{r}, t) - \frac{1}{q} \nabla J_p(\bar{r}, t) + g_p, \quad \dots(4.3)$$

$$\frac{\partial n(\bar{r}, t)}{\partial t} = -U(\bar{r}, t) + \frac{1}{q} \nabla J_n(\bar{r}, t) + g_n, \quad \dots(4.4)$$

where

$U(\bar{r}, t)$ = net rate of change of injected charge carriers due to recombination and spontaneous generation

and

g_p' , (g_n') = rate of generation of holes (electrons) in the volume due to photon or other exciting agency. (not considered in our model)

4.2.3 Poisson's Equation

It relates the electrostatic potential to the net spatial electric charge in terms of mobile carrier densities and the fixed net impurity atom concentration N , which is the difference between the donor and acceptor distributions N_d and N_a , respectively.

$$\nabla^2 \Psi(\bar{r}, t) = \frac{q}{\epsilon} \left[n(\bar{r}, t) - p(\bar{r}, t) - N(\bar{r}) \right] \quad \dots (4.5)$$

where

$$N(\bar{r}) = N_d(\bar{r}) - N_a(\bar{r})$$

4.2.4 Total Current Continuity Equation

$$J_t(\bar{r}, t) = J_n(\bar{r}, t) + J_p(\bar{r}, t) - \epsilon \frac{\partial}{\partial t} \nabla \Psi(\bar{r}, t) \quad \dots (4.6)$$

$$\nabla \cdot J_t(r, t) = 0 \quad \dots (4.6a)$$

Equation 4.6 expresses the total current density as the sum of the electron and hole particle currents J_n and J_p , respectively, plus a displacement current term.

4.2.5 Auxiliary Relations

$$E(\bar{r}, t) = -\nabla \Psi(\bar{r}, t)$$

$$\left. \begin{aligned} D_n(\bar{r}, t) &= \mu_n(\bar{r}, t) \frac{kT}{q} \\ D_p(\bar{r}, t) &= \mu_p(\bar{r}, t) \frac{kT}{q} \end{aligned} \right\}$$

EINSTEIN RELATION

where

D_n and D_p = electron and hole diffusion constants
respectively

μ_n and μ_p = electron and hole mobilities respectively.

4.3 Normalised One-Dimensional Equations for Steady-State Conditions

It is very convenient at this stage to express the relevant quantities in normalised form; the set of normalization constants is chosen with the criteria of achieving the highest simplification in the relations of interest. The list of normalisation factors used is given in Table (4.1).

The fundamental equations may be written in normalised form for the steady-state case as follows:

$$J_p(x) = -\mu_p(x) \left[\frac{dp(x)}{dx} + p(x) \frac{d\Psi(x)}{dx} \right] \quad \dots(4.7)$$

$$J_n(x) = \mu_n(x) \left[\frac{dn(x)}{dx} - n(x) \frac{d\Psi(x)}{dx} \right] \quad \dots(4.8)$$

$$\frac{dJ_p(x)}{dx} = -U(x) \quad \dots(4.9)$$

$$\frac{dJ_n(x)}{dx} = U(x) \quad \dots(4.10)$$

$$\frac{d^2\Psi(x)}{dx^2} = (n(x) - p(x) - N(x)) \quad \dots(4.11)$$

$$J_t = J_p(x) + J_n(x) \quad \dots(4.12)$$

with the auxiliary relations:

$$E(x) = - \frac{d\Psi(x)}{dx}$$

NORMALISED QUANTITY		NORMALISATION FACTOR	
Description	Symbol	Symbol	Numerical Value
Spatial Co-ordinate	x	$L_D = \sqrt{\epsilon V_t / q n_i}$	$0.333481 \times 10^{-2} \text{ cm}$
Time Co-ordinate	t	L_D^2 / D_o	$0.111209 \times 10^{-4} \text{ sec}$
Electrostatic Potential	ψ	V_t	$0.258426 \times 10^{-1} \text{ volts}$
Quasi-Fermi Levels	ϕ_p, ϕ_n	V_t	$0.258426 \times 10^{-1} \text{ volts}$
Applied (or terminal) Voltage	V_a	V_t	$0.258426 \times 10^{-1} \text{ volts}$
Barrier Potential	V_d	V_t	$0.258426 \times 10^{-1} \text{ volts}$
Electric Field	E	V_t / L_D	$0.774937 \times 10^1 \text{ volts/cm}$
Carrier Densities	n, p	n_i	$0.15 \times 10^{11} \text{ cm}^{-3}$
Net Impurity, Donor and Acceptor Densities	N_t, N_d, N_a	n_i	$0.15 \times 10^{11} \text{ cm}^{-3}$
Total, Electron and Hole Currents	J_t, J_n, J_p	$q D_o n_i / L_D$	$0.720580 \times 10^{-6} \text{ amps/cm}^2$
Generation-Recombination Rate	U	$D_o n_i / L_D^2$	$0.134880 \times 10^{16} \text{ cm}^{-3} \text{ sec}^{-1}$
Carrier Mobilities	μ_p, μ_n	D_o / V_t	$0.386956 \times 10^2 \text{ cm}^2/\text{volt-sec}$
Conductivity	σ	$q D_o n_i / V_t$	$0.929856 \times 10^{-7} (\Omega \text{cm})^{-1}$
Capacitance / Unit Area	C	ϵ / L_D	$0.310089 \times 10^{-9} \text{ Farads/cm}^2$
Carrier Diffusion Constant	D_p, D_n	D_o	$0.1 \times 10^1 \text{ cm}^2/\text{sec}$

TABLE 4.1. LIST OF NORMALIZATION FACTORS USED.

$$N(x) = N_d(x) - N_a(x) \quad \dots (4.13)$$

$$n(x) = e^{\left[\Psi(x) - \Phi_n(x)\right]} \quad \dots (4.14)$$

$$p(x) = e^{\left[\Phi_p(x) - \Psi(x)\right]} \quad \dots (4.15)$$

$$\sigma(x) = \mu_n(x) n(x) + p(x) \mu_p(x) \quad \dots (4.16)$$

where Φ_n , and Φ_p are electron and hole fermi levels originally introduced by Shockley.

4.4 Normalised One-Dimensional Equations for the Time Dependent Case

$$J_p(x,t) = -\mu_p(x,t) \left[\frac{\partial p(x,t)}{\partial x} + p(x,t) \frac{\partial \Psi(x,t)}{\partial x} \right] \quad \dots (4.17)$$

$$J_n(x,t) = \mu_n(x,t) \left[\frac{\partial n(x,t)}{\partial x} - n(x,t) \frac{\partial \Psi(x,t)}{\partial x} \right] \quad \dots (4.18)$$

$$\frac{\partial p(x,t)}{\partial t} = -U(x,t) - \frac{\partial J_p(x,t)}{\partial x} \quad \dots (4.19)$$

$$\frac{\partial n(x,t)}{\partial t} = -U(x,t) + \frac{\partial J_n(x,t)}{\partial x} \quad \dots (4.20)$$

$$\frac{\partial^2 \Psi(x,t)}{\partial x^2} = (n(x,t) - p(x,t) - N(x)) \quad \dots (4.21)$$

$$J_t(x,t) = J_n(x,t) + J_p(x,t) + J_d(x,t) \quad \dots (4.22)$$

$$\frac{\partial J_t(x,t)}{\partial x} = 0 \quad \dots (4.23)$$

with the auxiliary relations:

$$E(x,t) = - \frac{\partial \Psi(x,t)}{\partial x} \quad \dots (4.24)$$

$$D_p(x,t) = \mu_p(x,t) \frac{kT}{q} \quad \dots (4.25)$$

$$D_n(x,t) = \mu_n(x,t) \frac{kT}{q} \quad \dots (4.26)$$

4.5 Boundary Conditions

4.5.1 Steady-State Case

Assumption of carrier equilibrium at the contacts yields the following equations:

$$\left. \begin{aligned} \phi_n(0) &= \phi_p(0) \\ \phi_n(L) &= \phi_p(L) \end{aligned} \right\} \quad \dots (4.27)$$

Assumption of charge-neutrality at the contacts gives equations (4.28).

$$\left. \begin{aligned} n(0) - p(0) - N(0) &= 0 \\ n(L) - p(L) - N(L) &= 0 \end{aligned} \right\} \quad \dots (4.28)$$

The most general relationships between the carrier and current boundary values may be specified; only their functional dependence will be indicated here:

$$\left. \begin{aligned} n(0) &= f_1 [J_n(0), J_p(0)] \\ p(0) &= f_2 [J_n(0), J_p(0)] \\ n(L) &= f_3 [J_n(L), J_p(L)] \\ p(L) &= f_4 [J_n(L), J_p(L)] \end{aligned} \right\} \quad \dots (4.29)$$

For contacts of the ohmic type as assumed in our model, equation (4.29) assumes the following simple form:

$$\left. \begin{aligned} n(0) &= n_n \quad ; \quad n(L) = n_p \\ p(0) &= p_n \quad ; \quad p(L) = p_p \end{aligned} \right\} \quad \dots(4.30)$$

where

n_n, p_n, n_p, p_p = equilibrium carrier densities at the external contacts.

According to Shockley's definition of quasi-Fermi levels, we can write the following equation:

$$\left. \begin{aligned} \phi_n(L) - \phi_n(0) &= V_a \\ \phi_p(L) - \phi_p(0) &= V_a \end{aligned} \right\} \quad \dots(4.31)$$

Condition of charge neutrality at the contacts can be rewritten in terms of quasi-Fermi levels and electrostatic potential as follows:

$$\psi(0) = \phi_p(0) - \ln \left[\sqrt{\left[\frac{N(0)}{2} \right]^2 + 1} - \frac{N(0)}{2} \right] \quad \dots(4.32)$$

$$\psi(L) = \phi_p(L) - \ln \left[\sqrt{\left[\frac{N(L)}{2} \right]^2 + 1} - \frac{N(L)}{2} \right] \quad \dots(4.33)$$

4.5.2 Time-Dependent Cases

Four boundary conditions on the mobile carrier densities for our device may be specified. These may be characterised by the same generality of relations, as given in Eq. (4.29), which are rewritten as:

$$\left. \begin{aligned}
 n(0,t) &= q_1 \begin{bmatrix} J_n(0,t), J_p(0,t) \end{bmatrix} \\
 p(0,t) &= q_2 \begin{bmatrix} J_n(0,t), J_p(0,t) \end{bmatrix} \\
 n(L,t) &= q_3 \begin{bmatrix} J_n(L,t), J_p(L,t) \end{bmatrix} \\
 p(L,t) &= q_4 \begin{bmatrix} J_n(L,t), J_p(L,t) \end{bmatrix}
 \end{aligned} \right\} \dots (4.34)$$

For ohmic-type external contacts as assumed in our model, the boundary condition as given in Eq. (4.34) assumes the simple form:

$$\begin{aligned}
 n(0,t) &= n_n \\
 p(0,t) &= p_n \\
 n(L,t) &= n_p \\
 p(L,t) &= p_p
 \end{aligned} \dots (4.35)$$

A dependent boundary condition on the slope of the electric field is furnished by Poisson's equation:

$$\left. \begin{aligned}
 \frac{\partial E(x,t)}{\partial x} \Big|_{x=0} &= p(0,t) - n(0,t) + N(0) \\
 \frac{\partial E(x,t)}{\partial x} \Big|_{x=L} &= p(L,t) - n(L,t) + N(L)
 \end{aligned} \right\} \dots (4.36)$$

For ohmic contacts, it reduces to the following form:

$$\frac{\partial E(x,t)}{\partial x} \Big|_{x=0,L} = 0 \dots (4.37)$$

As an aside, the electrostatic potential $\Psi(x,t)$ and terminal voltage $V_a(t)$ may be computed by subsidiary relations:

$$\Psi(x,t) = - \int_0^x E(x',t) dx' + \Psi(0,t) \quad \dots(4.38)$$

$$V_a(t) = - \int_0^l E(x,t) dx + V_d \quad \dots(4.39)$$

where

$$V_d = \left[\int_0^l E(x) dx \right] \quad \text{at thermal equilibrium} \quad \dots(4.40)$$

4.6 Summary

The simplified Boltzmann transport equation is assumed to describe charge transport phenomena in our model. The charge-continuity, charge-transport, total current continuity and Poisson's equations are taken to govern the device behaviour. Various physical considerations of Chapter III yield the necessary boundary conditions. All the equations are normalised and reduced to one-dimensional form.

CHAPTER V

ANALYTICAL FORMULATION AND NUMERICAL TECHNIQUES

FOR SOLUTION OF STEADY-STATE CASE

In this chapter the details of the numerical solution of the problem for the steady-state case are discussed. The mathematical simplifications employed to derive various equations are outlined. The iterative procedure for the solution is then given. Various numerical techniques used are also discussed. A procedure to estimate the consistency of the numerical solution is also given. At the end, the numerical algorithm is extended to compute the incremental capacitance and the series resistance of the diodes.

5.1 Introduction

Steady-state solutions are required in this thesis for two reasons:

- (1) To study the static behaviour of the device;
- (2) To furnish the initial values for the solutions of dynamic cases.

A self-consistent scheme for the solution of the junction device problem was presented first by Gummel¹⁸, who applied it to the steady-state solutions of junction transistors. This scheme has an inherent limitation (due to present limitations of available digital computers) in that it cannot be applied to the case where a large reverse-bias is applied. DeMari¹⁹ exposed some of the limitations of Gummel's scheme and modified it to a certain degree for a constant mobility, zero

recombination model.

In this thesis, steady-state results are derived for a relatively general model, as discussed in Chapter III, using basically the algorithm furnished by Gummel.¹ The algorithm is modified to make it more efficient at high forward-biases where Gummel's original algorithm tended to fail. (DeMari did not have this problem as his model did not include the recombination-generation term, though he claimed that the extension is straight-forward). At very high recombination-generation, however, the present algorithm also failed to converge. Expressions for the electron quasi-Fermi level, hole quasi-Fermi level and electrostatic potential, which are treated as independent variables (as in DeMari's¹⁹ derivation) rather than obtaining them through a set of identities (as done by Gummel¹⁸), are used.

5.2 Derivation of Reduced Set of Equations

Equations (4.7) and (4.8) can be written with the help of Boltzmann's equations (4.14) and (4.15) as

$$J_p(x) = -\frac{D_p(x)}{D_o} \left[\frac{d}{dx} e^{\Phi_p(x)} \right] e^{-\Psi(x)} \quad \dots(5.1)$$

and

$$J_n(x) = \frac{D_n(x)}{D_o} \left[\frac{d}{dx} e^{-\Phi_n(x)} \right] e^{\Psi(x)} \quad \dots(5.2)$$

Integrating Eqs. (5.1) and (5.2) w.r.t. x , we get:

$$e^{\Phi_p(x)} = - \int_0^x \gamma_p(x') J_p(x') e^{\Psi(x')} dx' + C_p \quad \dots(5.3)$$

and

$$e^{-\Phi_n(x)} = \int_0^x \gamma_n(x') J_n(x') e^{-\Psi(x')} dx' + C_n \quad \dots(5.4)$$

where

$$\gamma_p(x') = D_o/D_p(x') \quad \text{and} \quad \gamma_n(x') = D_o/D_n(x')$$

The constants of integration C_p and C_n are obtained by using the boundary condition of $\Phi_p(x)$ and $\Phi_n(x)$ at $x = L$. Substituting these values of C_p and C_n , we get:

$$e^{\Phi_p(x)} = \int_x^L \gamma_p(x') J_p(x') e^{\Psi(x')} dx' + e^{\Phi_p(L)} \quad \dots(5.5)$$

and

$$e^{-\Phi_n(x)} = - \int_x^L \gamma_n(x') J_n(x') e^{-\Psi(x')} dx' + e^{-\Phi_n(L)} \quad \dots(5.6)$$

Now to determine $J_p(x)$ and $J_n(x)$, we proceed as follows:

From Eqs. (4.9) and (4.10), we get,

$$J_p(x) = - \int_0^x U(x') dx' + K_p \quad \dots(5.7)$$

and

$$J_n(x) = \int_0^x U(x') dx' + K_n \quad \dots(5.8)$$

Substituting Eqs. (5.7) and (5.8) into Eqs. (5.5) and (5.6) and using the boundary value of $\Phi_p(x)$ and $\Phi_n(x)$ at $x = 0$, we obtain:

$$\begin{aligned} e^{\Phi_p(x)} &= - \int_x^L \gamma_p(x') e^{\Psi(x')} \left\{ \int_0^x U(x') dx' \right\} dx' \\ &+ \int_x^L \gamma_p(x') e^{\Psi(x')} \left[\frac{e^{\Phi_p(0)} - e^{\Phi_p(L)} + \int_0^L \gamma_p(x') e^{\Psi(x')} \left\{ \int_0^x U(x') dx' \right\} dx'}{\int_0^L \gamma_p(x') e^{\Psi(x')} dx'} \right] dx' \\ &+ e^{\Phi_p(L)} \end{aligned} \quad \dots(5.9)$$

and

$$\begin{aligned}
 e^{-\Phi_n(x)} &= - \int_x^L \gamma_n(x') e^{\Psi(x')} \left\{ \int_0^x U(x') dx' \right\} dx' \\
 - \int_x^L \gamma_n(x') e^{-\Psi(x')} &\left[\frac{-e^{-\Phi_n(0)} + e^{-\Phi_n(L)} - \int_0^L \gamma_n(x') e^{-\Psi(x')} \left\{ \int_0^x U(x') dx' \right\} dx'}{\int_0^L \gamma_n(x') e^{-\Psi(x')} dx'} \right] dx' \\
 + e^{-\Phi_n(L)} &\dots(5.10)
 \end{aligned}$$

The hole and electron currents are thus given by:

$$J_p(x) = - \int_0^x U(x') dx' + \frac{e^{\Phi_p(0)} - e^{\Phi_p(L)} + \int_0^L \gamma_p(x') e^{\Psi(x')} \left\{ \int_0^x U(x') dx' \right\} dx'}{\int_0^L \gamma_p(x') e^{\Psi(x')} dx'} \dots(5.11)$$

and

$$J_n(x) = + \int_0^x U(x') dx' + \frac{-e^{\Phi_n(0)} + e^{\Phi_n(L)} - \int_0^L \gamma_n(x') e^{-\Psi(x')} \left\{ \int_0^x U(x') dx' \right\} dx'}{\int_0^L \gamma_n(x') e^{-\Psi(x')} dx'} \dots(5.12)$$

Equations (5.9) and (5.10) give the values of the hole quasi-Fermi level and electron quasi-Fermi level respectively, in terms of electrostatic potential, carrier mobility, and generation-recombination rate. The electrostatic potential is furnished by the solution of Poisson's equation (4.11). The carrier mobility and generation-recombination rate, which are a function of the above three parameters and are treated as independent parameters, are given by Eqs. (3.3), (3.4)

or

$$\frac{d^2 \delta^{(j+1)}(x)}{dx^2} - \delta^{(j+1)} \left[e^{\left\{ \psi^{(j)}(x) - \phi_n^{(j)}(x) \right\}} + e^{\left\{ \phi_p^{(j)}(x) - \psi^{(j)}(x) \right\}} \right] \\ = - \frac{d^2 \psi^{(j)}(x)}{dx^2} + e^{\left\{ \psi^{(j)}(x) - \phi_n^{(j)}(x) \right\}} - e^{\left\{ \phi_p^{(j)}(x) - \psi^{(j)}(x) \right\}} - N(x) \dots (5.16)$$

if the terms of order $\delta^{(j+1)}(x)^2$ and higher are neglected.

Equation (5.16) represents a second-order linear differential equation in the unknown $\delta^{(j+1)}(x)$, with boundary conditions of Eq. (5.14) if the remaining quantities are available after the completion of the $(j)^{\text{th}}$ iteration.

The complete iteration scheme is shown in Fig. (5.1). The applied voltage V_A is specified, a trial potential distribution is chosen, and the absence of recombination is assumed to start the first cycle of the main iteration loop (labelled "j"). The electric field $E(x)$ and carrier mobilities $\mu_p(x)$ and $\mu_n(x)$ are computed as a function of position. From Eqs. (5.9) and (5.10), the values of $e^{\phi_p(x)}$ and $e^{\phi_n(x)}$ are then calculated. Knowing these values, Eq. (5.16) is solved to yield corrections $\delta(x)$ for electrostatic potential. After obtaining the corrected value of the electrostatic potential, the $(j)^{\text{th}}$ cycle is repeated until the correction $\delta(x)$ becomes sufficiently small. Then we include the computation of generation-recombination rate $U(x)$. This change in algorithm proves to be useful for the computation for high forward-bias conditions where in the presence of a large generation-recombination term, any significant discrepancy in the values of the starting values of electrostatic potential from the true values tends to

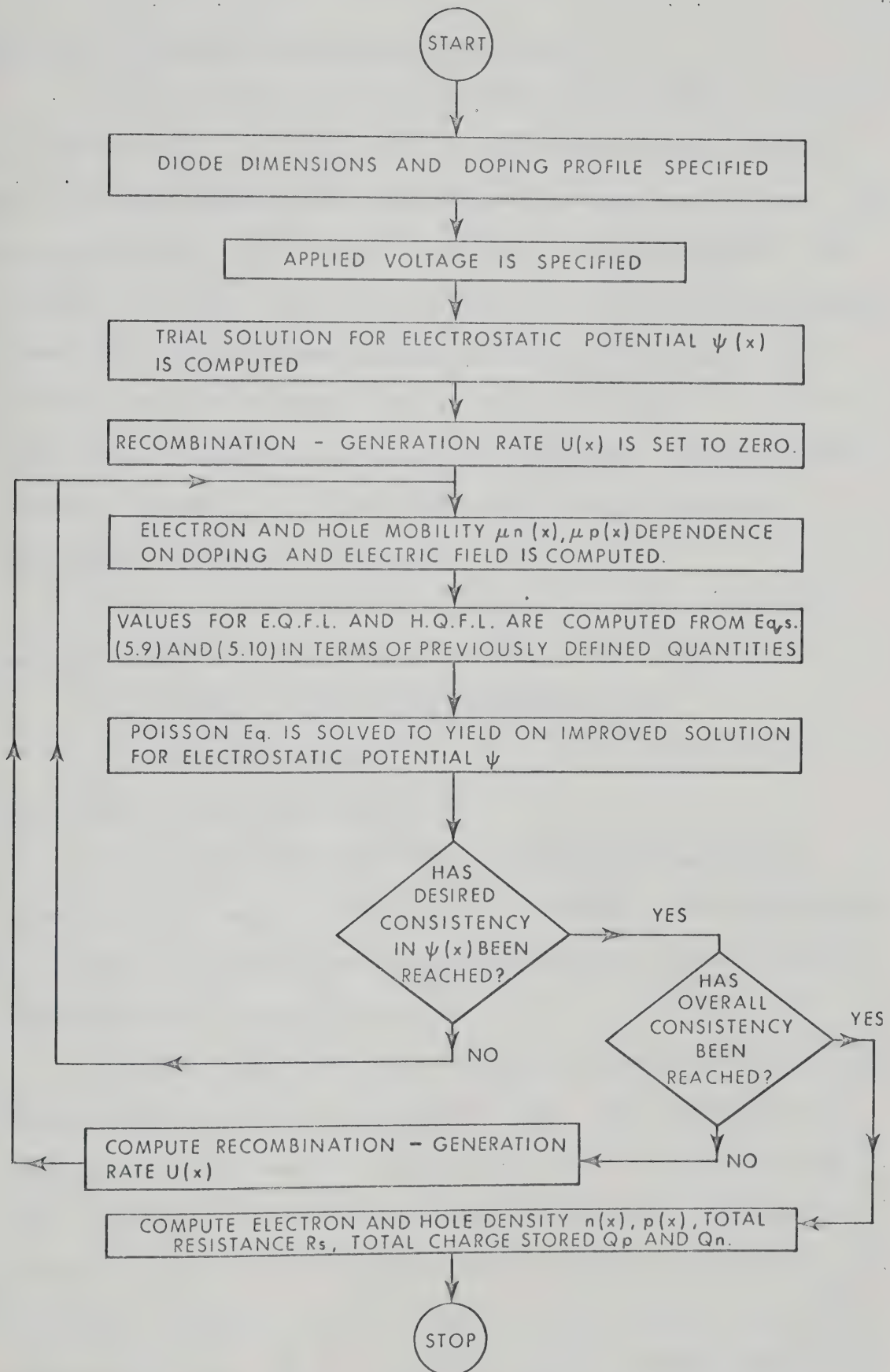


Fig. 5.1. Overall iterative scheme for steady-state calculations of diode parameters.

be amplified, hence endangering the convergence.

As is obvious, the success of this iteration scheme is dependent upon the choice of the trial solution of the electrostatic potential. If the discrepancy between the values of the true solutions and chosen trial solution is small, the solution converges to its final value in a few iterations and thus consumes less computer time. For step junctions and asymmetrical linearly-graded junctions, first-order expressions are available which can be safely used to start the solution.¹⁹ But, for doping profiles which are neither step nor asymmetric linearly-graded, analytical theory is of no great help. Some general approximate expressions based upon the assumptions:

- (1) the device consists of completely neutral and completely depleted regions,
- (2) absence of generation-recombination and
- (3) constant mobility

are worked out and solved numerically.

Overstratten and Nyuts⁴⁵ also recently published similar expressions to be used as starting values. However, under high forward bias conditions, these expressions did not help and a choice based on experience seemed to work out better.

For very high generation-recombination terms, the starting value of $U(x) = 0$ failed to be a satisfactory value. The solution did not converge, but rather went into oscillation. Though several starting values were tried, no satisfactory answer was obtained. This feature, however, did not limit our analysis, as due to higher carrier life times assumptions, we did not hit the region of critical values of generation-recombination term. But this feature is another limiting factor which

was omitted by Gummel¹⁸ and DeMari¹⁹.

5.4 Numerical Techniques

5.4.1 Numerical Integration and Differentiation

For the steady-state algorithm, suitable numerical techniques need to be chosen to approximate the numerical integrations and differentiations of interest. In the numerical execution of such operations, an error is usually introduced which often arises from truncating an infinite series at a convenient point. The differentiation and integration formulae adopted here are based on the Lagrange interpolation scheme. The first impression here is to use higher-order interpolation schemes to reduce truncation errors. But, we have to remember that higher-order interpolation may give misleading results when used with functions that are not well behaved. Such functions have higher derivatives having large magnitudes which fluctuate quite rapidly. For such functions a linear interpolation between the known values would have provided a better approximation than a third-order polynomial.⁴⁶ Unless the higher derivatives being approximated are well behaved and small in magnitude, it is wise to use linear interpolation. Various functions in our analysis vary very abruptly in the vicinity of metallurgical junctions. Their higher derivatives are not well-behaved and possess large magnitudes.

When an effort was made to use mixed formulae for integration using different orders of polynomials, completely unrealistic results were obtained which showed an oscillatory pattern. So, as a general rule linear interpolation was preferred in the vicinity of the junction, so long as a proper density of points, into which diode length was divided, was kept at a 'safe' level (determined experimentally).

5.4.2 Solution of Poisson's Equation

Poisson's equation rearranged in the form of Eq. (5.16) is to be solved in terms of the correction for the electrostatic potential distribution. To solve this second-order linear differential equation (Eq. 5.16) in the unknown $\delta^{(j+1)}(x_i)$, with boundary conditions

$$\delta^{(j)}(0) = 0 \quad \text{and} \quad \delta^{(j)}(L) = 0, \quad \dots(5.17)$$

a straight forward technique of approximating the analytical derivative with a finite difference scheme, followed by the solution of the linear algebraic equations is adopted to solve Eq. (5.16). Rewriting Eq. (5.16) after discretization, we obtain the following system of linear algebraic equations.

$$T\delta = A \quad \dots(5.18)$$

where

$$\delta = \begin{bmatrix} \delta_2 \\ \delta_3 \\ \vdots \\ \delta_n \end{bmatrix}$$

$$A = \begin{bmatrix} A_2 \\ A_3 \\ \vdots \\ A_n \end{bmatrix}$$

A_i is given by the following expression:

$$A_i = -\psi_i + e^{\left\{ \psi(i) - \phi_n(i) \right\}} - e^{\left\{ \phi_p(i) - \psi(i) \right\}} - N(i)$$

$$T = \begin{bmatrix} -B_2 + \frac{2}{H^2} & \frac{1}{H^2} & 0 & 0 & 0 & \dots \\ \frac{1}{H^2} & -B_3 + \frac{2}{H^2} & \frac{1}{H^2} & 0 & 0 & \dots \\ 0 & \frac{1}{H^2} & -B_4 + \frac{2}{H^2} & \frac{1}{H^2} & 0 & \dots \\ \vdots & \vdots & \vdots & \vdots & \vdots & \ddots \\ 0 & 0 & 0 & \dots & \frac{1}{H^2} & -B_n + \frac{2}{H^2} \end{bmatrix}$$

where

$$B_i = e^{\left\{ \Psi(i) - \Phi_n(i) \right\}} + e^{\left\{ \Phi_p(i) - \Psi(i) \right\}}$$

n = number of sections into which the diode is divided.

H = spatial mesh size.

To solve this system (Eq. 5.18), which contains a tri-diagonal matrix, a direct method using Gauss elimination and back-substitution is used, though indirect methods such as solution by iteration could also be used. Though pivoting is recommended to enhance the accuracy of the solution of the system, the nature of our tri-diagonal matrix in which the main diagonal is large in magnitude compared to the other two diagonal terms, pivoting is not required. Thus the above technique yielded a fast solution of the system of equations.

5.5 On the Accuracy of Numerical Solution

One of the most important questions about any numerical solution is its accuracy. In our case, though an estimate of truncation errors can be made at each step, yet estimating the overall accuracy picture is

rather complex because of the various other errors resulting from different sources and mixing with each other in a rather complicated way. Instead of evaluating the net overall error, we used the approach of DeMari¹⁹, i.e., to test the consistency of the solution, various analytical expressions, whose numerical counterparts display very different errors both in nature and magnitude (i.e. errors arising from the subtraction of large quantities of nearly equal magnitude, truncation error etc.) are employed to calculate the same quantity and the results are compared. To test this consistency the following set of relations are derived.

(1) Electric Field

$$E(x) = - \frac{d\Psi(x)}{dx} \quad \dots(5.19)$$

$$E(x) = \int_0^x \left\{ p(x') - n(x') + N(x') \right\} dx' + E(0) \quad \dots(5.20)$$

$$E(x) = \int_x^L \left\{ p(x') - n(x') + N(x') \right\} dx' + E(L) \quad \dots(5.21)$$

(2) Electric Currents

$$J_n(x) = \int_0^x U(x') dx' + \frac{-e^{\frac{\Phi_n(0)}{kT}} + e^{\frac{\Phi_n(L)}{kT}} - \int_0^L \gamma_n(x') e^{-\Psi(x')} \left\{ \int_0^x U(x') dx' \right\} dx'}{\int_0^L \gamma_n(x') e^{-\Psi(x')} dx'} \quad \dots(5.22)$$

$$J_n(x) = \mu_n(x) \left\{ \frac{dn(x)}{dx} - n(x) \frac{d\Psi(x)}{dx} \right\} \quad \dots(5.23)$$

$$J_n(x) = \gamma_n(x) \frac{d}{dx} \frac{e^{-\phi_n(x)}}{e^{\psi(x)}} \dots (5.24)$$

$$J_p(x) = - \int_0^x U(x') dx' + \frac{e^{\phi_p(0)} - e^{\phi_p(L)} + \int_0^L \gamma_p(x') e^{\psi(x')} \left\{ \int_0^x U(x') dx' \right\} dx'}{\int_0^L \gamma_p(x') e^{\psi(x')} dx'} \dots (5.25)$$

$$J_p(x) = - \mu_p(x) \left\{ \frac{dp(x)}{dx} + p(x) \frac{d\psi(x)}{dx} \right\} \dots (5.26)$$

$$J_p(x) = -\mu_p(x) \left\{ \frac{d}{dx} \frac{e^{\phi_p(x)}}{e^{\psi(x)}} \right\} e^{-\psi(x)} \dots (5.27)$$

So, we see that the final consistency of ψ , p , and n can be evaluated first by comparing results obtained for the electric field from Eqs. (5.19), (5.20) and (5.21). The discrepancies can further be exposed by comparing the results for hole and electric currents obtained by Eqs. (5.23) and (5.24) and (5.26) and (5.27) with equations (5.22) and (5.25), respectively. (These equations are used to evaluate the distribution of current throughout the analysis). The last comparison also shows the overall effect of the various internal inconsistencies on the terminal properties.

5.6 Calculation of Incremental Capacitance and Series Resistance

5.6.1 Incremental Capacitance

The numerical algorithm developed in Sections 5.1 - 5.5 is extended to compute the incremental capacitance and series resistance of the diode. If Q is the total charge (of holes or electrons) in the device, the incremental capacitance is defined at $V = V_a$ as

$$C \Big|_{V=V_a} = \frac{dQ}{dV} \Big|_{V=V_a} \quad \dots(5.28)$$

Writing Poisson's equation in integral form in terms of electric field at the contact, we get,

$$\int \{p(x) - n(x) + N(x)\} dx = E(L) - E(0)$$

When the above expression is differentiated w.r.t. voltage (V), we get,

$$\frac{d}{dV} \left\{ \int_0^L p(x) dx \right\}_{V=V_a} - \frac{d}{dV} \left\{ \int_0^L n(x) dx \right\}_{V=V_a} = \frac{d}{dV} \left\{ E(L) - E(0) \right\}_{V=V_a} \quad \dots(5.29)$$

The r.h.s. is the contribution of the surface charge at the terminal, to the total incremental capacitance. This term is neglected here, as it is only significant at very high injection levels. Hence:

$$\begin{aligned} C \Big|_{V=V_a} &= \left\{ \frac{d}{dV} \int_0^L p(x) dx \right\}_{V=V_a} \\ &= \left\{ \frac{d}{dV} \int_0^L n(x) dx \right\}_{V=V_a} \end{aligned} \quad \dots(5.30)$$

or, writing in terms of incremental quantities

$$\begin{aligned} C \Big|_{V=V_a} &= \int_0^L \frac{p'(x) - p(x)}{V_a' - V_a} dx \\ &= \int_0^L \frac{n'(x) - n(x)}{V_a' - V_a} dx \end{aligned} \quad \dots(5.31)$$

It is seen that, to determine the value of the incremental capacitance at any bias voltage, two solutions are to be obtained for two slightly different values of applied bias.

5.6.2 Series Resistance

The value of series resistance is generally defined¹ as the resistance offered to the flow of conduction current external to the space-charge region. For the case of epitaxial varactors, series resistance in the epitaxial layer is predominant and is given by

$$R_s = \frac{1}{A} \left\{ \int_0^{x_1} \rho_p(x) dx + \int_{x_2}^l \rho_n(x) dx \right\} \quad \dots(5.32)$$

ρ_p and ρ_n are the p-type and n-type resistivities which are functions of carrier concentrations and their mobilities. x_1 and x_2 are the boundaries of the space-charge region. As stated earlier, our physical model provides no well defined boundaries for transition region. Kennedy and O'Brien²⁰ in their numerical investigations on p-n junctions provide a definition of space-charge region which is in substantial agreement with other investigations of the linearly-graded junction problem. They assumed that the space-charge region is terminated at locations where the electrostatic charge density is one half its maximum value on each side of the structure. This definition is used in present investigations to define space-charge region for the calculation of series resistance.

5.7 Summary

In this chapter, the analytical formulation of the equations ((4.5) & (4.12)), describing the behaviour of the varactor diode under

steady-state conditions (as discussed in the previous chapter) have been outlined. The electron quasi-Fermi level ϕ_n , hole quasi-Fermi level ϕ_p and electrostatic potential Ψ have been chosen as independent parameters (as in Gummel's¹⁸ work). The generation-recombination and mobility dependence on electric field, impurity concentration and carrier-carrier interactions has been considered. Equations (5.9), (5.10) and (5.16) are the final equations solved according to the flow chart given in Fig.

(5.1). Equations (5.9) and (5.10) are derived independently (as done by DeMari¹⁹). Equation (5.16) is written in terms of correction in the trial solution of electrostatic potential Ψ . The overall algorithm was changed slightly to suit the cases where the recombination and regeneration term is quite dominant. But, for very high generation-recombination values, the overall scheme fails as the starting value of zero for the generation-recombination rate is found to be highly unsatisfactory. A criteria to test the accuracy of the final results is also given. At the end, the numerical algorithm is extended to compute the incremental capacitance and the series resistance of the diodes.

CHAPTER VI

ANALYTICAL FORMULATION AND NUMERICAL TECHNIQUES

FOR TIME-DEPENDENT CASES

In this chapter, we will discuss details of the numerical solution for various time-dependent excitations applied to the terminals of the diode. Three cases are discussed:

- (1) the terminal current as a function of time is known;
- (2) the terminal voltage as a function of time is known;
- (3) an equation relating the terminal current to the terminal voltage is known.

The mathematical manipulations employed to derive a reduced set of equations from the fundamental equations, Eqs. (4.17) to (4.22), are outlined. The boundary conditions needed to solve the reduced set of equations are derived. Then, the overall iterative procedure used to solve the reduced set of equations is outlined. The discretization scheme is selected from various available discretization schemes. After selecting the discretization scheme, details of the iterative procedure for a current-driven transient are discussed. Then algorithms for solution of the other two forms of external excitations are outlined. In the next section, various sources of numerical error and their effect on the accuracy of overall results are discussed. At the end of the chapter, various trade-offs between different errors, to decrease the overall error without increasing computation time, are also briefly discussed.

6.1 Introduction

Results are required for time-dependent excitations applied across the diode terminals with and without some passive elements connected to the diode to study the internal and external properties of the diode under dynamic conditions. Various forms of excitations are necessary to study different phenomena. To study the injection of charge when a diode is turned on from an initial condition of thermal equilibrium, a large step of current is a good choice of external excitation. Similarly to study the details of the reverse transient, a reverse voltage step large enough to sufficiently reverse bias the diode is applied to the diode initially biased in the forward direction. To study the device behaviour under large signal operating conditions, a sinusoidal excitation is employed. To study the terminal and internal properties of the diode when driven by the above mentioned excitations, an accurate numerical solution of Eqs. (4.17) to (4.23) along with boundary conditions (4.35 and 4.36), which are taken to govern the behaviour of our device, is required. DeMari²¹ has reported a numerical algorithm for the solution of these equations for a simpler model of zero-recombination and constant mobilities. He successfully applied it to the simple case of a highly asymmetrical step p-n junction. Another form of solution of this system of equations is furnished by Scharfetter and Gummel²², they applied this approach to the solution of the large signal behaviour of IMPATT diodes. In our case, DeMari's²¹ algorithm is extended to our relatively general model which includes the generation-recombination rate, and the mobility dependence upon electric field, the net doping density and the mobile carrier concentration. This extended scheme is then successfully applied to our selected two types of diode

structures, namely: $p^+ - n^+$ and $p^+ - i - n^+$ structure.

6.2 Derivation of Reduced Set of Equations

The fundamental equations (4.17) to (4.23) with the auxiliary relations Eqs. (4.24) to (4.26), which are taken to govern the behaviour under time-dependent excitation conditions, may be rearranged to a form more appropriate for numerical solution. If the expressions (4.17) and (4.18) for electron and hole current densities are inserted into Eq. (4.22), and use is made of the auxiliary relation of Eq. (4.24), the displacement term may be explicitly written as:

$$\begin{aligned} \frac{\partial E(x,t)}{\partial t} = & - \left\{ \mu_p(x,y) p(x,t) + \mu_n(x,t) n(x,t) \right\} E(x,t) \\ & + \mu_p(x,y) \frac{\partial p(x,t)}{\partial x} + \mu_n(x,t) \frac{\partial n(x,t)}{\partial x} \\ & + J_t(t) \end{aligned} \quad \dots (6.1)$$

Moreover, if the expressions (4.17) and (4.18) for hole and electron current densities are inserted into equations (4.19) and (4.20), respectively, we get:

$$\begin{aligned} \frac{\partial p(x,t)}{\partial t} = & \mu_p(x,t) \frac{\partial^2 p(x,t)}{\partial x^2} + \left\{ \frac{\partial \mu_p(x,t)}{\partial x} - E(x,t) \mu_p(x,t) \right\} \\ & \frac{\partial p(x,t)}{\partial x} - \left\{ \frac{\partial \mu_p(x,t)}{\partial x} E(x,t) - \frac{\partial E(x,t)}{\partial x} \mu_p(x,t) \right\} \\ & p(x,t) - U(x,t) \end{aligned} \quad \dots (6.2)$$

and

$$\begin{aligned} \frac{\partial n(x,t)}{\partial t} = & \mu_n(x,t) \frac{\partial^2 n(x,t)}{\partial x^2} + \left\{ \frac{\partial \mu_p(x,t)}{\partial x} - E(x,t) \mu_p(x,t) \right\} \frac{\partial p(x,t)}{\partial x} \\ & - \left\{ - \frac{\partial \mu_p(x,t)}{\partial x} E(x,t) + \frac{\partial E(x,t)}{\partial x} \mu_n(x,t) \right\} n(x,t) \\ & - U(x,t) \end{aligned} \quad \dots (6.3)$$

and, with the help of Poisson's Eq. (4.21),

$$\begin{aligned} \frac{\partial p(x,t)}{\partial t} = & \mu_p(x,t) \frac{\partial^2 p(x,t)}{\partial x^2} + \left\{ \frac{\partial \mu_p(x,t)}{\partial x} - E(x,t) \mu_p(x,t) \right\} \frac{\partial p(x,t)}{\partial x} \\ & + \left[- \frac{\partial \mu_p(x,t)}{\partial x} E(x,t) + \left\{ n(x,t) - p(x,t) - N(x) \right\} \mu_p(x,t) \right] p(x,t) \\ & - U(x,t) \end{aligned} \quad \dots (6.4)$$

and

$$\begin{aligned} \frac{\partial n(x,t)}{\partial t} = & \mu_n(x,t) \frac{\partial^2 n(x,t)}{\partial x^2} + \left\{ \frac{\partial \mu_n(x,t)}{\partial x} + \mu_n(x,t) E(x,t) \right\} \frac{\partial n(x,t)}{\partial x} \\ & + \left[\frac{\partial \mu_n(x,t)}{\partial x} E(x,t) - \mu_n(x,t) \left\{ n(x,t) - p(x,t) - N(x) \right\} \right] n(x,t) \\ & - U(x,t) \end{aligned} \quad \dots (6.5)$$

The reduced set of Eqs. (6.1), (6.4) and (6.5) with appropriate boundary conditions and initial conditions and external excitation $J(t)$, as discussed in the following sections, represents a complete formulation of the problem. In this formulation, the electric field E , the electron density n and the hole density p are chosen as the independent quantities

and represent the unknowns of the reduced set of equations.

6.3 Boundary and Initial Conditions

For a two-contact device, four boundary conditions on the mobile carrier densities may be specified.

$$\left. \begin{aligned} n(0,t) &= q_1 \begin{bmatrix} J_n(0,t), & J_p(0,t) \end{bmatrix} \\ p(0,t) &= q_2 \begin{bmatrix} J_n(0,t), & J_p(0,t) \end{bmatrix} \\ n(L,t) &= q_3 \begin{bmatrix} J_n(0,t), & J_p(0,t) \end{bmatrix} \\ p(L,t) &= q_4 \begin{bmatrix} J_n(L,t), & J_p(L,t) \end{bmatrix} \end{aligned} \right] \quad \dots(6.6)$$

A dependent boundary condition on the slope of electric field is given by Poisson's equation (4.21)

$$\left. \begin{aligned} \frac{\partial E(x,t)}{\partial x} \Big|_{x=0} &= p(0,t) - n(0,t) + N(0) \\ \frac{\partial E(x,t)}{\partial x} \Big|_{x=L} &= p(L,t) - n(L,t) + N(L) \end{aligned} \right] \quad \dots(6.7)$$

For external contacts of ohmic type, the boundary conditions of (6.6) assume the simple form:

$$\left. \begin{aligned} n(0,t) &= n_n \\ p(0,t) &= p_n \\ n(L,t) &= n_p \\ p(L,t) &= p_p \end{aligned} \right] \quad \dots(6.8)$$

where n_n , p_n , n_p and p_p are the equilibrium carrier densities at the external contacts. The dependent boundary conditions become then

$$\left. \frac{\partial E(x,t)}{\partial x} \right|_{x=0}^{x=L} = 0 \quad \dots(6.9)$$

and are a consequence of the charge neutrality condition of the ohmic contacts.

Moreover, the electrostatic potential $\Psi(x,t)$ and terminal voltage $V_a(t)$ may be computed by the subsidiary relations:

$$\Psi(x,t) = - \int_0^x E(x,t) dx + \Psi(0,t) \quad \dots(6.10)$$

$$V_a(t) = - \int_0^L E(x,t) dx + V_d \quad \dots(6.11)$$

where $\Psi(0,t)$ may be taken as reference value for electrostatic potentials and V_d is the diffusion potential defined by

$$V_d = \int_0^L E(x) dx \quad \text{thermal equilibrium} \quad \dots(6.12)$$

The electric field and mobile carrier density distributions throughout the interior of the device at the initial time $t=0$:

$$\left. \begin{array}{l} E(x,t) \\ n(x,t) \\ p(x,t) \end{array} \right| \text{ for } 0 < x < L, \text{ at } t=0 \quad \dots(6.13)$$

may be specified as independent initial conditions. If the evolution of

the time dependent solutions starts at steady-state condition, as in our case, the initial conditions are available from the steady-state solutions obtained with the method described in Chapter 5.

6.4 Iterative Method of Solution

Equations (6.1), (6.4) and (6.5) describe a system of three partial differential equations in terms of three unknowns; the electric field E , the electron density n and the hole density p . The equations are in two-dimensions namely time t and position x . Equations (6.4) and (6.5) are non-linear second order partial differential equations of the parabolic type.^{47, 48} Finite difference methods are chosen to achieve the solution of these two equations. The first step towards a numerical solution requires a discretization of relevant quantities at a finite number of points in both time and space. Appropriate numerical techniques are then to be devised to determine the spatial distributions of unknowns that satisfy the set of equations for assigned boundary conditions at each instant of time. An alternate approach of simultaneously determining the unknowns in both time and spatial domains first for broad mesh size and then gradually refining the mesh size till desired accuracy is reached, could be used. Because of heavier memory requirements in this approach, it is not considered feasible.

The discretization problem for the partial differential equation of the parabolic type is quite extensively discussed in the next section. In this section a numerical method of the solution is sketched schematically. For our model Eqs. (6.1), (6.4) and (6.5), boundary conditions (6.8) and (6.9), initial conditions (6.13) and external excitation $J(t)$ give the mathematical formulation of the problem. The

expressions for mobility dependence on electric field, doping density and carrier density and the net rate of generation-recombination, as discussed in Chapter III, are also needed. The highly non-linear character of the equations requires an iterative procedure at each instant of time to reach desired consistency. From the knowledge of the spatial distributions at $t=t_0$, it is desired to determine the unknowns at the next instant of time $t=t_1$. An educated "guess" for the electron and hole density spatial distributions at t_1 is made and these are inserted in Eq. (6.1) to solve for preliminary electric field spatial distribution at t_1 , which in turn may be inserted together with the "guess" for the hole density distribution, in Eq. (6.5) to solve for the electron density spatial distribution at $t=t_1$. These improved distributions may be inserted in Eq. (6.4) and the iteration cycle at the instant of time t_1 may be repeated until the desired consistency is reached, at t_1 . The distributions at time t_1 are then taken as initial conditions and the whole procedure is repeated to determine the distributions at time t_2 . The process terminates when the final stage is reached. The scheme is summarised in Fig. (6.1).

6.5 Selection of Discretization Scheme

In general, the continuous quantities appearing in the analytical formulations are discretized at a finite number of points in both position and time co-ordinates; the ensemble of these points constitutes a "grid" or "mesh". Finite difference schemes are then employed to approximate the analytical differentiations and reduce the problem to the solution of a system of finite difference equations, which represents the discretized formulation.

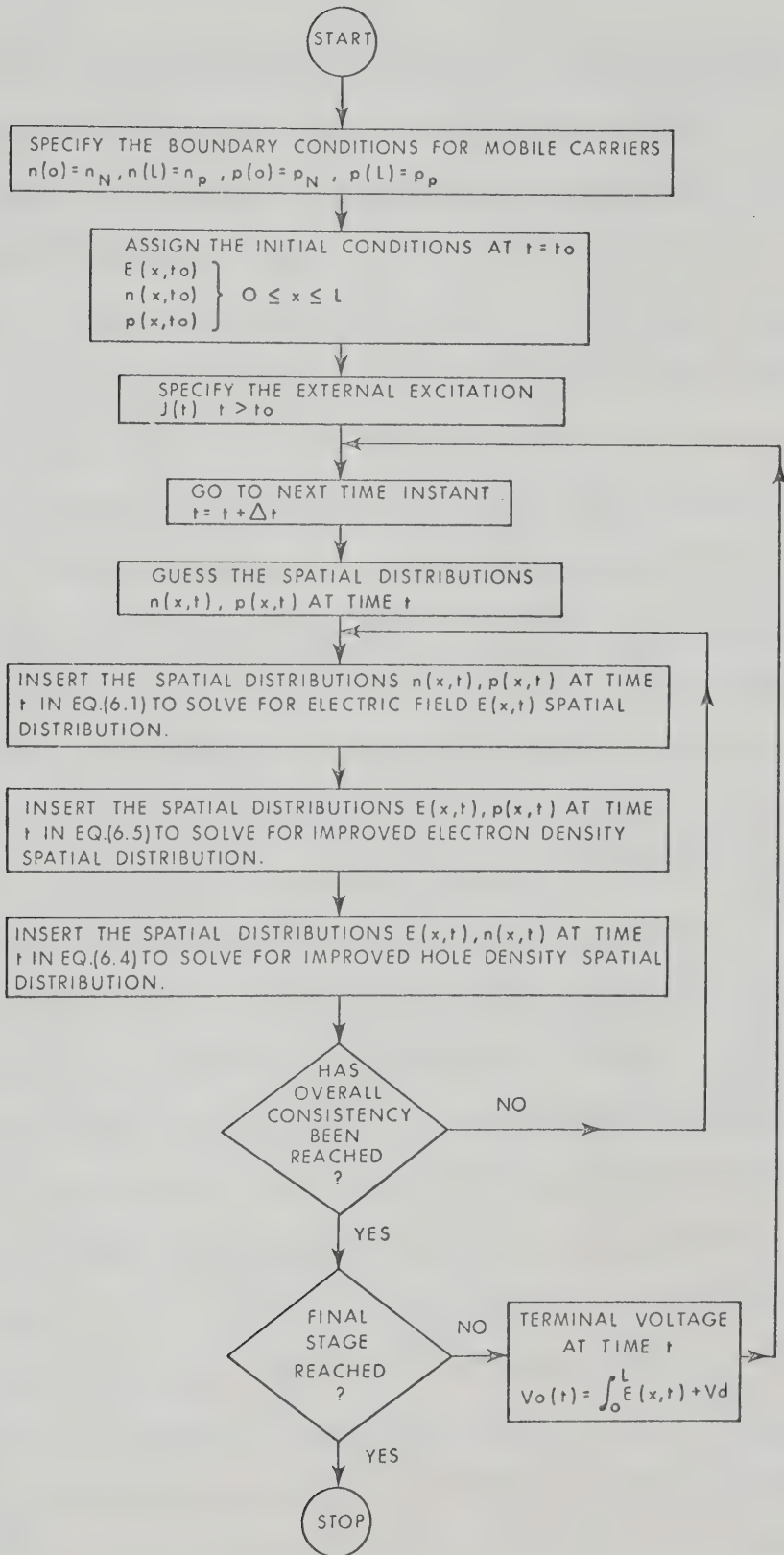


Fig. 6.1. Iterative scheme for calculating diode parameters for the current-driven transient case.

The basic problem here is the selection of a discretization scheme featuring both convergence and stability, together with a satisfactory degree of efficiency of computation. Convergence is defined as the discrepancy between the exact solution of the original analytical formulation and the exact solution of the system of difference equations. The theory of convergence deals with the conditions under which the discretization error becomes equal to zero in the limit of vanishing distance between adjacent position and time points. In addition, the actual numerical results obtained as a result of computations on the basis of the discretized formulation, differs from the exact solution of the system of difference equations by an amount equal to "numerical error". The problem of "stability" deals with conditions under which the numerical error is small throughout the entire range of the solution.

The available theory of numerical analysis^{47,48,49,53} furnishes several discretization schemes, the convergence and stability of which is proven for simpler cases. The theory is only complete for the case of linear equations with constant coefficients; for linear equations with non-constant coefficients, theory is still far from satisfactory. For non-linear equations, the conditions of convergence and stability are only available for a few special solutions and discretization schemes.⁴⁹ Hence the only guide line available to us is the solution of the simpler cases from which conclusions are extrapolated for more complex systems of non-linear differential equations such as ours.

Various discretization schemes available to us are discussed in literature.^{47,53} As we see there, in general two types of discretization schemes are available: explicit schemes and implicit schemes. Stability and convergence requirements for certain types of discretization schemes

are dependent upon restrictions on mesh size. For a linear differential equation with non-constant coefficients, the stability and convergence are proven in Ref. 47 (pp. 107) for the simplest explicit scheme. The restriction on mesh size is

$$\frac{\Delta t}{(\Delta x)^2} < \frac{1}{2a_o(x,t)} \quad \dots(6.13)$$

where

$$a_o(x,t) = \text{coefficient of the } \frac{\partial^2 f(x,t)}{\partial x^2} \text{ term.}$$

When applied to our case of Eqs. (6.4) and (6.5), we get:

$$\frac{\Delta t}{(\Delta x)^2} < \frac{1}{2\mu_p(x,t)} \quad \dots(6.14a)$$

$$\frac{\Delta t}{(\Delta x)^2} < \frac{1}{2\mu_n(x,t)} \quad \dots(6.14b)$$

Since $\mu_n(x,t)$ is greater than $\mu_p(x,t)$, the greatest value of $\mu_n(x,t)$ will determine the critical relationship between space and time mesh sizes. For

$$\Delta x = 10^{-3}$$

$$\Delta t \approx 2.5 \times 10^{-7} \approx 2.9 \times 10^{-12} \text{ sec.} \quad \dots(6.15)$$

This is the least value necessary to ensure convergence and stability. The value of Δt furnished by Eq. (6.15) is highly undesirable because of the huge number of points required for the time co-ordinate, resulting in a huge amount of computer time.

If we look at the implicit discretization schemes, we see that for the simpler case, unconditional convergence and stability without any constraints on the mesh size are guaranteed. This is proved in Ref. 47 (pp. 102) for linear equations with constant coefficients. However, as is obvious a partial differential equation of the parabolic type, discretized with an implicit scheme, requires the simultaneous solution of difference equations (one for each spatial point) at each instant of time, not required for the discretization generated by explicit schemes. But the freedom available in the selection of mesh size in both position and time co-ordinates appears to enable us to choose a reasonable number of points on the time co-ordinate and thus enable us to save computing time rather than increasing it. This is later verified in actual numerical computation. Due to this salient feature of the implicit discretization scheme, they are chosen over explicit schemes. The generalized implicit discretization has been employed ($\theta=1$), though the Crank - Nicholson discretization schemes ($\theta=1/2$) and other implicit discretization schemes ($0 < \theta < 1$) could also be employed. The Crank - Nicholson scheme has been demonstrated to be very sensitive to any numerical errors (errors in initial solution, truncation and round-off errors) and its stability is endangered even though the numerical errors are not severe from practical considerations.

After selecting the discretization scheme, the derivatives are approximated by finite-difference expressions derived from Lagrange's interpolation scheme. We have to be careful in choosing the finite difference expressions used to discretize the derivatives. If the order of the difference scheme is higher than original differential equation, the approximate solution may contain extraneous solutions which are not

at all related to the true solution. These extraneous solutions severely affect the convergence and stability conditions. The case of an ordinary linear differential equation with variable coefficients has been treated in reference 51 and the presence of extraneous solutions is found to be very hazardous. Although higher order interpolation schemes seemed to improve the accuracy of the numerical solution, their use is avoided in this work due to their highly uncertain stability and convergence conditions.

6.6 Details of Adopted Procedure

After choosing the generalised pure implicit scheme for discretization for the solution of Eqs. (6.4) and (6.5), we proceed to discuss the details of the iterative procedure outlined in Section 6.4. Equations (6.1), (6.4) and (6.5), when discretized on the basis of the above scheme, generate the following system of difference equations.

$$\begin{aligned} \frac{k_i^E - k_{i-1}^E}{\Delta t} = & - \left(k_{pi}^\mu k_{pi}^p + k_{ni}^\mu n_i \right) k_i^E \\ & + \left\{ k_{pi}^\mu k \left(\frac{\partial p}{\partial x} \right)_i - k_{ni}^\mu k \left(\frac{\partial n}{\partial x} \right)_i \right\} \\ & + k_t^J \end{aligned} \quad \dots(6.16)$$

$$\begin{aligned} \frac{k_i^p - k_{i-1}^p}{\Delta t} = & k_{pi}^\mu k \left(\frac{\partial^2 p}{\partial x^2} \right)_i + k_{i-1}^A k \left(\frac{\partial p}{\partial x} \right)_i \\ & + \left\{ k_{i-1}^{B1} + \left(k_i^n - k_i^p - N_i \right) k_{pi}^\mu \right\} k_i^p \end{aligned} \quad \dots(6.17)$$

where

$$k^{A1}_i = \left(\frac{\partial \mu_p}{\partial x} \right)_i - k^E_i k^{\mu}_{pi}$$

$$k^{B1}_i = - k^{\mu}_{pi} k^E_i$$

$$\frac{k^n_i - k^{n-1}_i}{\Delta t} = k^{\mu}_{ni} \left(\frac{\partial^2 p}{\partial x^2} \right)_i + k^{A2}_i k \left(\frac{\partial n}{\partial x} \right)_i$$

$$- \left\{ k^{B2}_i + \left(k^n_i - k^p_i - N_i \right) k^{\mu}_{ni} \right\} k^n_i$$

... (6.18)

where

$$k^{A2}_i = \left(\frac{\partial \mu_n}{\partial x} \right)_i + k^E_i k^{\mu}_{ni}$$

$$k^{B2}_i = - k^{\mu}_{ni} k^E_i$$

The left hand index ($k = 1, 2, 3, \dots, f$) represents the time instant in the discretization scheme. The right hand index ($i = 1, 2, 3, \dots, \ell$) represents the position in the discretization scheme. Quantities at instants of time $t < {}_k t$, and at any spatial point $0 < x_i < L$, are supposedly known and the solutions for the next instant of time ${}_k t$ are sought. According to the method briefly outlined in Section 6.4, an iterative procedure is employed at each instant of time to determine the unknown quantities. To start the iteration at each instant of time, trial solutions have to be selected. The values of hole density, electron density and electric field computed at the previous instant are

found to be satisfactory to serve as the starting solution.

It is convenient for us to introduce the corrections Δn and Δp for the electron and hole densities, respectively, defined as the difference between densities corresponding to two successive iterations

$$\left. \begin{aligned} k \Delta n_i^{(j)} &= k n_i^{(j)} - k n_i^{(j-1)} \\ k \Delta p_i^{(j)} &= k p_i^{(j)} - k p_i^{(j-1)} \end{aligned} \right] \quad \dots (6.19)$$

where

$$k = 0, 1, 2, 3, \dots f$$

$$i = 1, 2, 3, \dots \ell$$

$$j = 0, 1, 2, \quad (\text{number of iterations})$$

If the convergence of the approximate spatial distribution occurs during the iterative procedure at each instant of time, the following relations are readily verified with the aid of definition (6.19).

$$\lim_{\substack{j \rightarrow \infty \\ 1 \leq i \leq \ell \\ 0 \leq k \leq f}} k \Delta n_i^{(j)} = 0 \quad ; \quad \lim_{\substack{j \rightarrow \infty \\ 1 \leq i \leq \ell \\ 0 \leq k \leq f}} k \Delta p_i^{(j)} = 0 \quad \dots (6.20)$$

In addition, the time dependent property of the boundary conditions in Eq. (6.8) yields:

$$\left. \begin{aligned} k \Delta n_{i=1}^{(j)} &= 0 \\ k \Delta n_{i=\ell}^{(j)} &= 0 \\ k \Delta p_{i=1}^{(j)} &= 0 \\ k \Delta p_{i=\ell}^{(j)} &= 0 \end{aligned} \right] \quad \begin{array}{l} \text{for } 0 < k < f \\ \text{and any } (j) \end{array} \quad \dots (6.21)$$

If the quantities labelled k in equation (6.17) and (6.18) are identified with the subscript $(j+1)$ (with the exception of the terms $k-1^p_i$ and $k-1^n_i$), the relations in Eq. (6.19) becomes:

$$k^n_i^{(j+1)} = k^{\Delta n}_i^{(j+1)} + k^n_i^{(j)} \quad \dots (6.22)$$

$$k^p_i^{(j+1)} = k^{\Delta p}_i^{(j+1)} + k^p_i^{(j)} \quad \dots (6.23)$$

When inserting these into equations (6.17) and (6.18), one obtains:

$$\begin{aligned} k^{\mu p}_i^{(j)} \left(\frac{\partial^2 \Delta p}{\partial x^2} \right)_i^{(j+1)} + k^{\Delta 1}_i^{(j)} \left(\frac{\partial \Delta p}{\partial x} \right)_i^{(j+1)} \\ + k^{C1}_i^{(j)} \left(\Delta p \right)_i^{(j+1)} = k^{FP}_i^{(j)} \end{aligned} \quad \dots (6.24)$$

where

$$\begin{aligned} k^{\Delta 1}_i^{(j)} &= \left(\frac{\partial \mu_p}{\partial x} \right)_i^{(j)} - \left(\frac{E}{k} \right)_i^{(j)} \left(\frac{\mu_p}{k} \right)_i^{(j)} \\ k^{B1}_i^{(j)} &= - \left(\frac{\partial \mu_p}{\partial x} \right)_i^{(j)} \left(\frac{E}{k} \right)_i^{(j)} \\ k^{C1}_i^{(j)} &= \left\{ k^{B1}_i^{(j)} + \frac{\mu_p}{k} \left(k^n_i^{(j)} - 2k^p_i^{(j)} - N_i \right) - \frac{1}{k \Delta t} \right\} \\ k^{FP}_i^{(j)} &= \frac{\mu_p}{k} \left(\frac{\partial^2 p}{\partial x^2} \right)_i^{(j)} - k^{\Delta 1}_i^{(j)} \left(\frac{\partial p}{\partial x} \right)_i^{(j)} \\ &\quad - \left\{ k^{B1}_i^{(j)} + \frac{\mu_p}{k} \left(k^n_i^{(j)} - k^p_i^{(j)} - N_i \right) \right. \\ &\quad \left. - \frac{1}{k \Delta t} \right\} k^p_i^{(j)} - \frac{k-1^p_i}{\Delta t} + k^U_i \end{aligned}$$

and

$$\begin{aligned} & k^{\mu_{n_i}}(j) \left(\frac{\partial^2 \Delta n}{\partial x^2} \right)_i^{(j+1)} + k^{A2_i}(j) \left(\frac{\partial \Delta n}{\partial x} \right)_i^{(j+1)} \\ & + k^{C2_i}(j) \left(\Delta n \right)_i^{(j+1)} = k^{FN_i}(j) \end{aligned} \quad \dots (6.25)$$

where

$$\begin{aligned} k^{A2_i}(j) &= \left(\frac{\mu_n}{k} \right)_i(j) + k^{E_i}(j) \left(\frac{\mu_n}{k} \right)_i(j) \\ k^{B2_i}(j) &= - \left(\frac{\mu_n}{k} \right)_i(j) k^{E_i}(j) \\ k^{C2_i}(j) &= - \left\{ k^{B2_i}(j) + \left(2k^{n_i}(j) - k^{p_i}(j) - N_i \right) k^{\mu_{n_i}}(j) + \frac{1}{k \Delta t} \right\} \\ k^{FN_i}(j) &= - k^{\mu_{n_i}}(j) \left(\frac{\partial^2 n}{\partial x^2} \right)_i^{(j)} - k^{A2_i}(j) \left(\frac{\partial n}{\partial x} \right)_i^{(j)} \\ &+ \left\{ k^{B2_i}(j) + \left(k^{n_i}(j) - k^{p_i}(j) - N_i \right) k^{\mu_{n_i}}(j) + \frac{1}{k \Delta t} \right\} k^{n_i}(j) \\ &- \frac{k-1}{\Delta t} k^{n_i} + k^{U_i} \end{aligned}$$

Moreover, the electric field at the instant $(k+1)$, may be explicitly recovered from Eq. (6.16) and rewritten as:

$$\begin{aligned} k^{E_i}(j+1) &= \frac{\frac{k-1}{\Delta t} k^{E_i} + k^{\mu_{p_i}}(j) \left(\frac{\partial p}{\partial x} \right)_i^{(j)} - k^{\mu_{n_i}}(j) \left(\frac{\partial n}{\partial x} \right)_i^{(j)} - k^{J_t}}{k^{\mu_{p_i}} k^{p_i}(j) + k^{\mu_{n_i}} k^{n_i}(j) + \frac{1}{k \Delta t}} \\ &\dots (6.26) \end{aligned}$$

If the second order terms $(\Delta p)^2$ and $(\Delta n)^2$ are neglected and the three point formulae are used for numerical computation of derivatives of Δn and Δp in Eqs. (6.18) and (6.19), these assume the final form:

$$\begin{aligned} & k^{D1}_i^{(j)} k^{(\Delta p)}_{i-1}^{(j+1)} + k^{E1}_i^{(j)} k^{(\Delta p)}_i^{(j+1)} \\ & + k^{F1}_i^{(j)} k^{(\Delta p)}_{i+1}^{(j+1)} = k^{G1}_i^{(j)} \end{aligned} \quad \dots (6.27)$$

where

$$i = 2, 3, \dots, \ell-1$$

$$k = 1, 2, \dots, f$$

$$j = 1, 2, 3, \dots$$

$$k^{D1}_i^{(j)} = 2 \mu_{kP_i}^{(j)} - k^{A1}_i^{(j)} \Delta x_i$$

$$k^{E1}_i^{(j)} = -4 \mu_{kP_i}^{(j)} + 2(\Delta x)_i^2 k^{C1}_i^{(j)}$$

$$k^{F1}_i^{(j)} = 2 \mu_{kP_i}^{(j)} + k^{A1}_i \Delta x_i$$

$$k^{G1}_i^{(j)} = 2(\Delta x)_i^2 k^{(FP)}_i^{(j)}$$

and

$$\begin{aligned} & k^{D2}_i^{(j)} k^{(\Delta n)}_{i-1}^{(j)} + k^{E2}_i^{(j)} k^{(\Delta n)}_i^{(j+1)} \\ & + k^{F2}_i^{(j)} k^{(\Delta n)}_{i+1}^{(j+1)} = k^{G2}_i^{(j)} \end{aligned} \quad \dots (6.28)$$

where

$$i = 2, 3, \dots, \ell-1$$

$$k = 1, 2, \dots, f$$

$$j = 1, 2, 3, \dots$$

$$k^{D2}_i(j) = 2 \mu_{n_i}(j) - k^{A2}_i(j) \Delta x_i$$

$$k^{E2}_i(j) = -4 \mu_{n_i}(j) + 2(\Delta x)_i k^{C2}_i(j)$$

$$F2_i(j) = 2 \mu_{n_i}(j) + k^{A2}_i(j) \Delta x_i$$

$$k^{G2}_i(j) = 2(\Delta x)_i k^{(FN)}_i(j)$$

The numerical derivatives of the electron and hole densities in the expressions FP and FN are computed from the two-point differentiation formula, since, due to the steep gradient at the metallurgical junction of the relevant quantities, numerical derivative formulae based upon higher order interpolation formulae yield highly inaccurate values in the vicinity of the metallurgical junction and in some cases exhibited an oscillatory pattern for the distribution of internal quantities. The general rule followed in Chapter V; that for a function which does not exhibit well behaved higher order derivatives, lower order interpolation yielded better results, is observed. The only point about which we need to be very careful is that we choose a high enough density of points in the space co-ordinate so that truncation errors are bounded to ensure numerical stability.

Equations (6.27) and (6.28) may, with the help of boundary conditions of Eq. (6.21), also be written in the vector form as follows:

$$k^{(T_p)}(j) \quad k^{(\Delta p)}(j) = k^{(G1)}(j) \quad \dots (6.29)$$

$${}_k(T_n)^{(j)} {}_k(\Delta n)^{(j)} = {}_k(G2)^{(j)} \quad \dots (6.30)$$

where

T_p and T_n are tri-diagonal matrices

$$T_p = \begin{bmatrix} (E1)_2 & (F1)_2 & & & \\ (D1)_3 & (E1)_3 & (F1)_3 & & \\ & \dots & & & \\ & & (D1)_i & (E1)_i & (F1)_i \\ & & \dots & & \\ & & & (D1)_{\ell-2} & (E1)_{\ell-2} & (F1)_{\ell-2} \\ & & & & (D1)_{\ell-1} & (E1)_{\ell-1} \end{bmatrix} \quad \dots (6.31)$$

$$T_n = \begin{bmatrix} (E2)_2 & (F2)_2 & & & \\ (D2)_3 & (E2)_3 & (F2)_3 & & \\ & \dots & & & \\ & & (D2)_i & (E2)_i & (F2)_i \\ & & \dots & & \\ & & & (D2)_{\ell-2} & (E2)_{\ell-2} & (F2)_{\ell-2} \\ & & & & (D2)_{\ell-1} & (E2)_{\ell-1} \end{bmatrix} \quad \dots (6.32)$$

and Δn , Δp and $G1$, $G2$ are vectors:

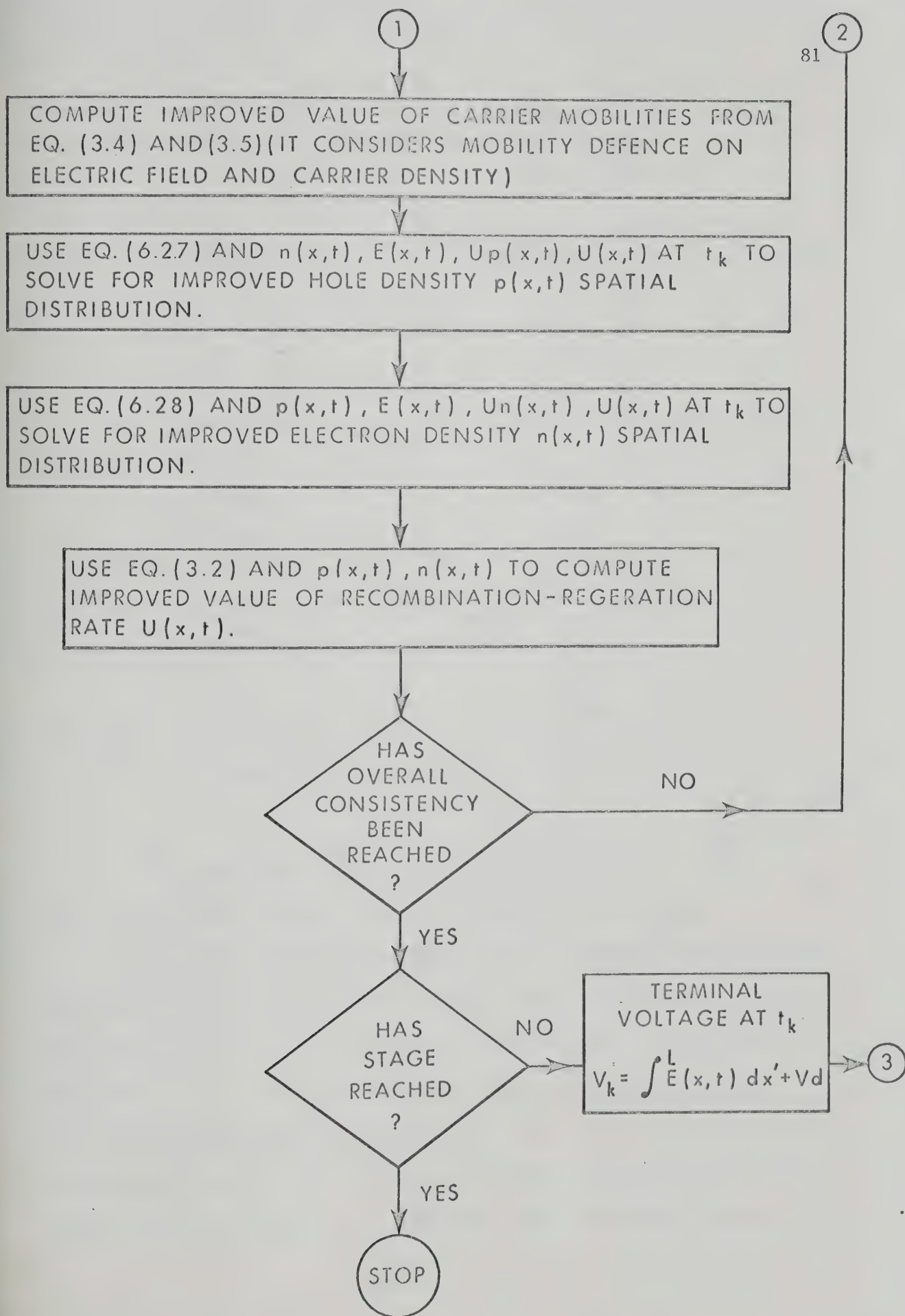


Fig. 6.2. Continued.

$$\Delta p = \begin{bmatrix} p_2 \\ p_3 \\ \dots \\ p_i \\ \dots \\ p_{\ell-2} \\ p_{\ell-1} \end{bmatrix}, \quad \Delta n = \begin{bmatrix} n_2 \\ n_3 \\ \dots \\ n_i \\ \dots \\ n_{\ell-2} \\ n_{\ell-1} \end{bmatrix} \quad \dots (6.33)$$

$$G1 = \begin{bmatrix} (G1)_2 \\ (G1)_3 \\ \dots \\ (G1)_i \\ \dots \\ (G1)_{\ell-2} \\ (G1)_{\ell-1} \end{bmatrix}, \quad G2 = \begin{bmatrix} (G2)_2 \\ (G2)_3 \\ \dots \\ (G2)_i \\ \dots \\ (G2)_{\ell-2} \\ (G2)_{-1} \end{bmatrix} \quad \dots (6.34)$$

As we see, Eqs. (6.26), (6.27) and (6.28) are our final equations on which our whole iteration scheme is to be based.

First the structure parameters: diode thickness, junction area and doping profile are specified. Carrier mobility dependence on net doping density and electric field is then incorporated (given by Eqs. (3.3) and (3.4)). Then the formula for calculating the rate of net generation-recombination is added (given by Eq. (3.2) in our case). The steady-state distributions obtained in Chapter V are specified as the initial spatial distributions of electric field, and mobile carrier

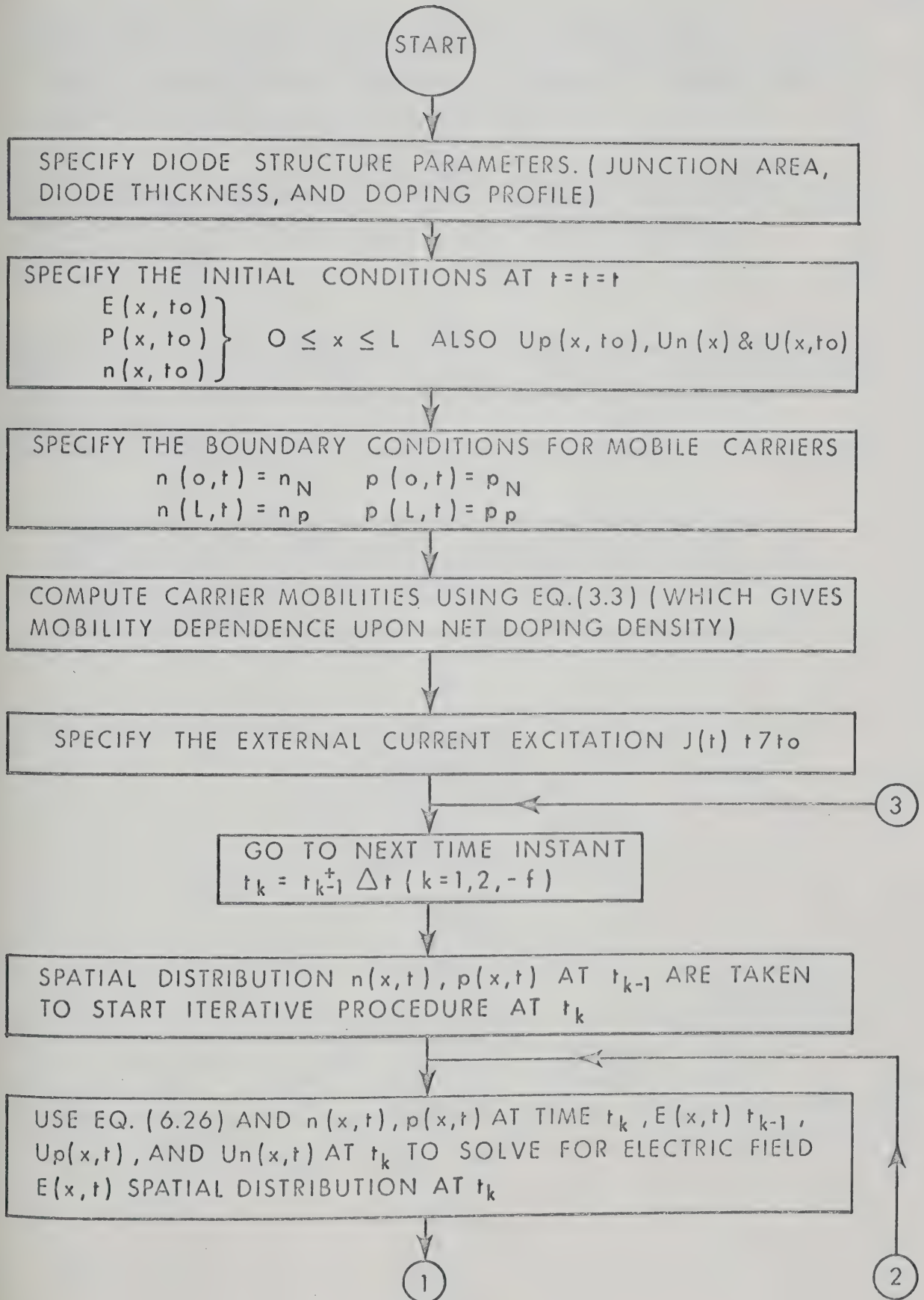


Fig. 6.2. Detailed overall iterative procedure used for the current-driven transient case.

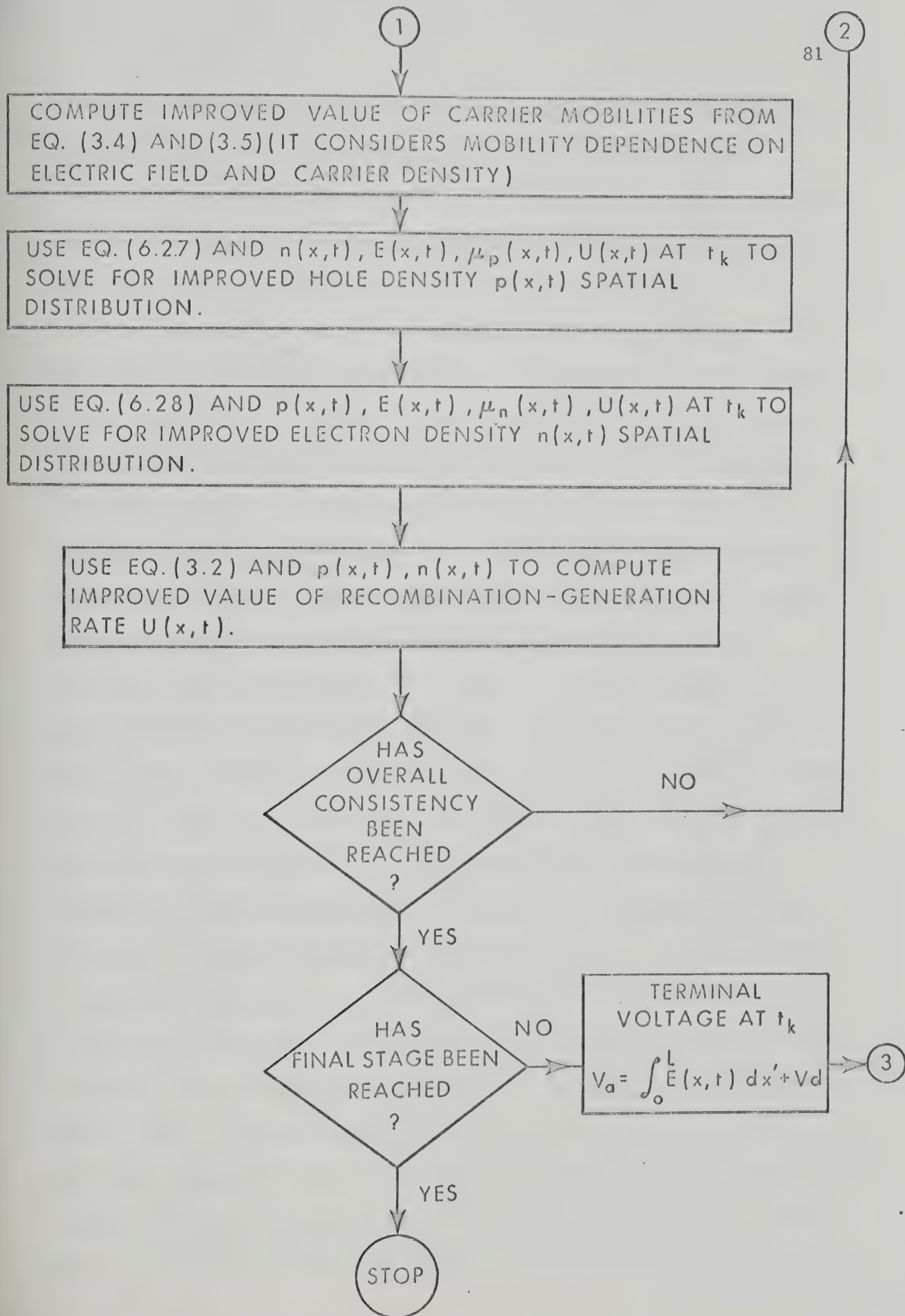


Fig. 6.2. Continued.

densities at the instant $k=0$. An external excitation of total current as a function of time is specified to drive the evolution of the transient. The spatial distributions of E , n , and p , the unknown of the problem, are sought at the first time instant $k=1$ and will be obtained with the use of an iterative successive approximation scheme. The iteration index (j) is set to zero and the spatial distributions of the mobile carrier densities available at the previous instant $k=0$ are taken as trial functions to start the iteration at the instant $k=1$. Equation (6.26) yields the spatial distribution of the electric field which may be inserted in the implicit system of Eqn. (6.27) to solve for the corrections ${}_k\Delta p_i^{(j+1)}$ ($i = 2, 3, \dots, \ell-1$) for hole density. Equation (6.23) then yields an improved hole density distribution which, together with the electric field distribution last obtained from Eq. (6.26) solves for the corrections ${}_k\Delta n_i^{(j+1)}$, so that Eq. (6.22) yields an improved electron distribution. Then, Eqs. (3.4) and (3.5) are used to yield an improved value of mobility based upon electric field and carrier densities. Equation (3.2) is used to yield an improved value of the net generation-recombination rate. The terminal voltage is obtained by integration of the electric field. Then over-all consistency tests are performed. A negative outcome of these tests at the considered instant of time ($k=1$) increases the iteration index by unity and restarts the cycle with the insertion of the improved mobile carrier distributions in Eq. (6.26) for an improved electric field distribution at the same time instant ($k=1$). A positive outcome of the consistency test accepts the quantities obtained by last iteration as 'the' solution at the time instant considered. Unless the final state ($k=f$) is reached, the time index is increased by unity, the iteration index (j) is set to zero and

the solution at the next time instant ($k=2$) is sought. The iteration is restarted by taking the mobile carrier distributions and mobilities available from the previous instant ($k=1$) as the trial function and inserted into Eq. (6.26). The same iteration procedure is repeated to achieve 'the' solutions at the instant ($k=2$) and the subsequent instants of time until the final state ($k=f$) is reached.

The tri-diagonal matrix system is solved by the same techniques successfully employed in Chapter V for the solution of the tri-diagonal system generated by the discretization of Poisson's equation in the steady-state scheme and is described in reference 47 (pp. 103 - 105).

The overall consistence, between the unknowns E , n and p and the system of equations determining them, may be tested at each iteration cycle for each instant of time by considering the magnitude of the corrections Δn , and Δp and the difference of the electric field distributions obtained by two successive iterations. If the magnitudes of these quantities are smaller than any specified value (iteration error at each instant of time), achievement of overall consistency at that instant is assumed. The final state ($k=f$) is reached when the external excitation has reached the final state, and the unknowns E , n and p are unchanged for an increase of time.

A most demanding requirement for the success of the described method is the convergence of the iteration procedure to the overall consistent solutions from a set of approximate trial distributions at each instant of time. In all the cases tested for various structures (two more than reported here) and external excitations, convergence was always obtained, though under certain conditions stability was

endangered (weak stability). The rate of convergence was quite fast in situations in which significant variations (in time) of the total current occurs, so that the electric field (given by Eq. 6.26) becomes the quantity driving the variations of mobile carrier distributions (Eqs. 6.27 and 6.28) and is essentially responsible for the evolution of the transient. A slower convergence rate was observed under conditions, opposite to those just described, i.e., when total terminal current remains constant. The rate of convergence for such cases was found to be well within practical limits except for conditions arising towards the termination of the transient, when the quantities approach the final steady-state distributions. The final distributions could be obtained from the steady-state schemes using current as the driving quantity. However, this was not the limitation in our case, as we aim to see the phenomena for comparatively shorter times. These effects were comparatively similar to that obtained by DeMari⁵⁴ for his less general model of constant mobility, and zero-recombination. But, the convergence was not that fast in the case of the 'electric field driven' transient because of the dependence of the carrier mobilities upon the electric field, which therefore had to be adjusted to reach overall consistency.

It is clear from the method and formulation described that complete freedom is available in the selection of both the spatial and time steps. Their selection depends upon the total error that can be tolerated. The time-step distributions may be conveniently chosen and automatically adjusted by the computer during the evolution of time. This is discussed in Appendix A.

6.7 On Different Forms of External Excitations

One of the following three possibilities is always known at the terminals of the diode:

- (1) The terminal current as a function of time (current-driven case);
- (2) The terminal voltage as a function of time (voltage-driven case);
- (3) An equation relating the terminal current to the terminal voltage.

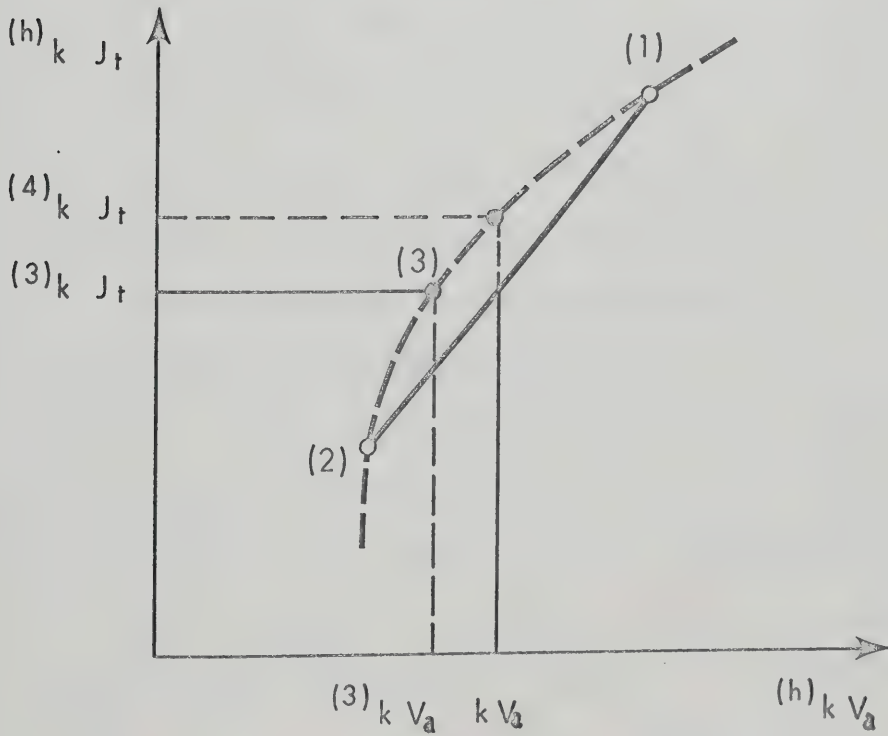
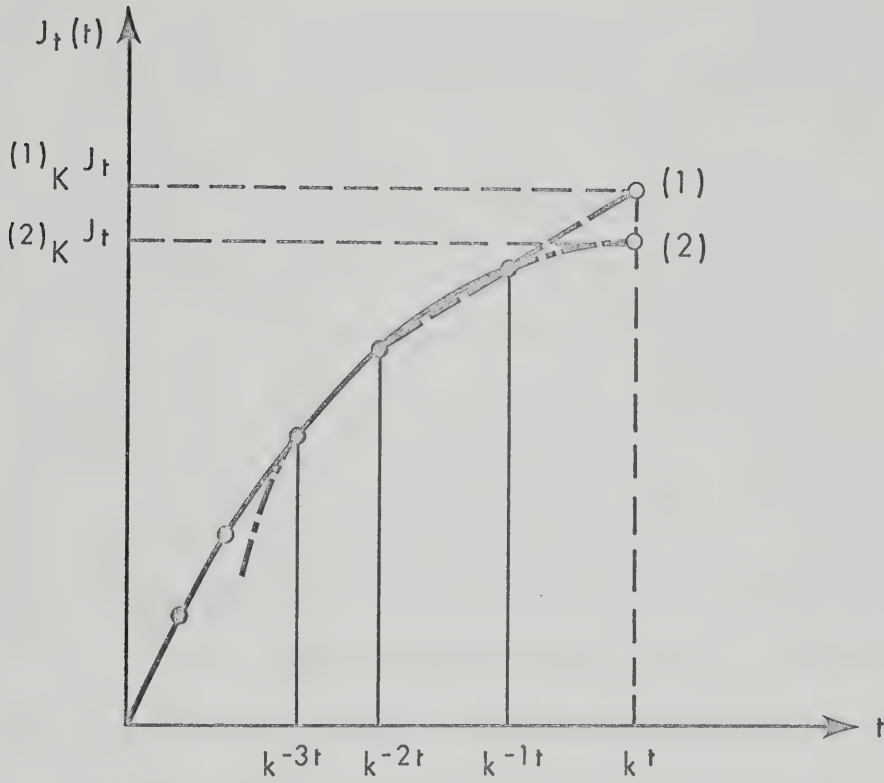
6.7.1 Procedure for Voltage-Driven Case

So far we have discussed the current-driven case. Now if the applied voltage as a function of time is specified at the terminals of the device, we need to substitute Eq. (6.26), expressing the variation of the electric field in terms of total current, by Poisson's equation (Eq. 4.21), which is written in terms of electrostatic potential $\Psi(x,t)$. The applied voltage then appears explicitly as a boundary condition for Ψ in the solution of the second-order differential Eq. (4.21). Now Eqs. (6.4) and (6.5), along with Eq. (4.21), rewritten in terms of the variables Ψ , n , and p , comprise a new set of fundamental equations. Eqs. (6.4) and (6.5) are treated just as for the current-driven transient case. Equation (4.21), the new equation of the set, is discretized and solved by the same method as was used in the solution of Poisson's equation for the steady-state case. An iteration procedure of the same type as described for the current-driven transient is used to reach the desired consistency between Ψ , n , p and Eqs. (6.4), (6.5) and (4.21) at each instant of time. A slower rate of convergence of the iterative procedure was observed in this case compared to that of the current-

driven transient case. This is expected, since the 'error' due to the variation of the electrostatic potential at the boundaries is contained at the boundary (at one contact) at the beginning of the iteration scheme at each instant of time and propagates throughout the whole interior before the solution is allowed to proceed to the following time instant. Moreover, the solution of this system of equations requires a heavier computation load, since it involves the solution of an additional tri-diagonal matrix necessitated by the solution of Poisson's equation.

An alternate approach is to use the method suggested by DeMari²¹ for his simpler model. In this method, the current-driven transient solution i.e., specifying the total current $J(t)$ and determining the terminal voltage V_a at each instant of time, is used as an integral part of the solution for the voltage-driven transient. The solutions for total current and internal distributions are assumed to be known for times $t < {}_k t$, and quantities at the following time instant are sought. If the total current ${}_k J$ were known, the iterative procedure described in Section 6.6 could be applied to obtain the unknown distributions at the instant ${}_k t$. The problem now consists of searching for a particular value of current ${}_k J$ that will yield the specified terminal voltage ${}_k V_a$. This is achieved in two stages using the current-driven transient algorithm at the specified instant of time. A "prediction" stage initially furnishes two estimates of the total current ${}_k^{(1)} J$ and ${}_k^{(2)} J$ close to the 'correct' value ${}_k J$, which is to be determined. This is achieved by using linear (two-point) and parabolic (three-point) extrapolations on the current responses as a function of time which furnishes, in general, two estimates for the current ${}_k J$. Two independent applications of the current-driven transient algorithm yields for the

(a) FIRST STAGE: PREDICTION



(b) SECOND STAGE: INTERPOLATION

Fig. 6.3. Prediction and interpolation stages as proposed by DeMari⁵⁴ for computation of the voltage-driven transient case.

two currents $^{(1)}_k J$ and $^{(2)}_k J$ the corresponding values of terminal voltages $^{(1)}_k V_a$ and $^{(2)}_k V_a$ which, in general, differ from the specified terminal voltage V_a . A second stage based on interpolation of the curve $^{(h)}_k V_a$ ($h = 1, 2, 3, \dots$) as a function of $^{(h)}_k J$ at the same time k , may now be started to obtain an improved estimate of the total current that generates a terminal voltage within an assigned tolerance about the specified value. A linear interpolation on the graph of $^{(1)}_k J$, $^{(2)}_k J$ versus $^{(1)}_k V_a$ and $^{(2)}_k V_a$ yields a third estimate $^{(3)}_k J$, corresponding to the specified terminal voltage V_a . A third application of the current-driven transient algorithm at the instant k for the current $^{(3)}_k J$ furnishes a third point $^{(3)}_k J$, $^{(3)}_k V_a$ on the current-voltage graph, so that a parabolic interpolation may be used to further improve, if necessary, the estimate of the total current. The procedure continues for higher-order interpolation schemes until values $^{(h)}_k J$, that generates the voltage $^{(h)}_k V_a$ sufficiently close to the specified V_a , is determined. Solutions at the instant k are then available and the overall procedure may be restarted at the following instant $k+1$ with the prediction stage. For a few initial time points ($k = 1, 2$) the prediction stage may not be performed as described; an arbitrary estimation procedure may be employed equally well, if the time step is kept small enough, in order to obtain a quasi-linear current-voltage characteristic in the interpolation stage. For a large voltage step, this procedure tended to fail, due to the large variation of current; the interpolation and extrapolations may fail to give proper values, unless an extremely small time-step is employed. In this case the first procedure using the electrostatic potential, the hole density and the electron density as independent variables is recommended

as there is no chance of failing. However, for small voltage driven transients, the 'extrapolation-interpolation' procedure is very efficient. The overall scheme, using this procedure is outlined in Figure (6.4).

6.7.2 Outline of Procedure When an Equation Relating Terminal Current and Voltage is Known

When a general two-port network, composed of ideal current and/or voltage sources and passive circuit elements, is connected to the terminal of the diode (two-contact device), both the total current density $J(t)$ of the device and terminal voltage $V_a(t)$ are quantities dependent upon the properties of both the diode and the network. At a particular time instant k , the two unknowns ${}_k J$ and ${}_k V_a$ are determined by the system:

$${}_k V_a = f_1 ({}_k J) \quad \dots(6.45)$$

$${}_k J = f_2 ({}_k V_a) \quad \dots(6.46)$$

The above equations are the discretized current-voltage relationships at the time instant k of the diode and the network respectively. These equations can be directly incorporated into the iterative procedures described previously. For a reasonable number of elements, the time required for the solution of this system is insignificant compared to the time required to compute one iterative cycle for the diode. The undesirable effect is the resulting slower convergence rate, so that more iterations are needed to achieve overall consistency at each instant of time.

For the simpler case in which only a resistance R in series with

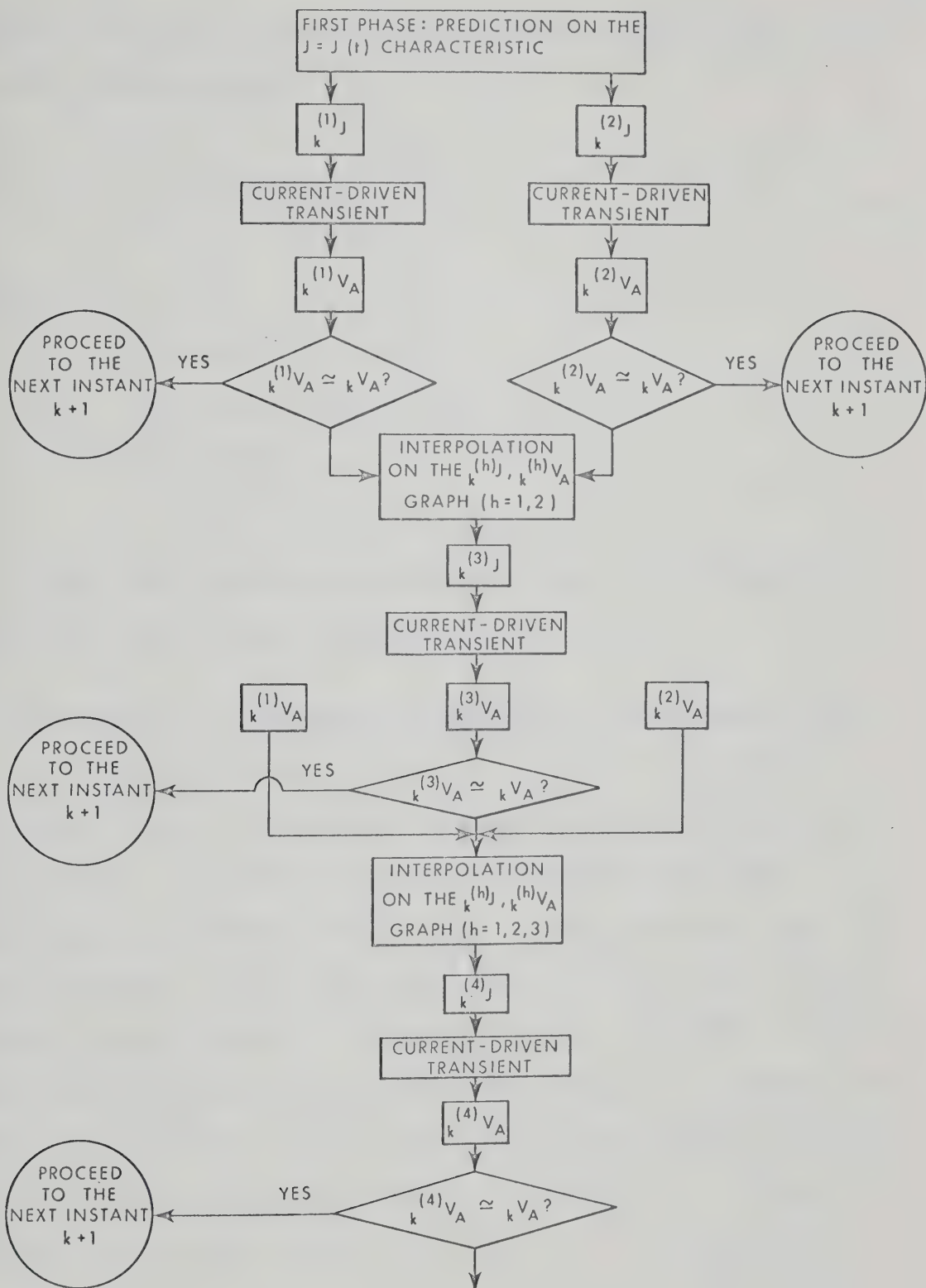


Fig. 6.4. Overall scheme for computing diode parameters for the voltage-driven transient case.

a time-dependent voltage source $V_G(t)$ is present in the external circuit, equation (6.46) results in:

$$k^J(j+1) = \frac{k^V_G - k^V_a(j) V_t}{R A J_o} \quad \dots(6.47)$$

where

A = area of the device

V_t = thermal voltage kT/q

$$J_o = \frac{q D_o n_i}{LD}$$

and voltages and currents are in normalised form. Results have been computed for both step and sinusoidal voltage sources.

6.8 On the Accuracy of the Numerical Solution for Time-Dependent Cases

In the time-dependent solution discussed in the previous sections, truncation errors both in the spatial and time domains are to be considered. In addition, the interaction between the errors introduced at the different time instants becomes a dominant factor for overall accuracy. The discretization error in the time domain and the growth of numerical error for increasing time are responsible for this interaction and consequently determine the conditions of convergence and stability, respectively. Due to this fact, the conditions of convergence and stability for different external excitations will be different and will have to be tested separately for each case. In the following subsections, the principal sources of error arising in the time dependent solution (besides the inaccuracies in the spatial domain), together with techniques considered suitable to evaluate and control the influence of

such errors on the final results, are briefly discussed.

6.8.1 Truncation Error in the Time Domain

In the formulation adopted for either the current-driven or the voltage-driven transient, the time derivatives are approximated by a discretization scheme, resulting in discretization error. This approximation is often achieved by truncating a Taylor expansion at a convenient point to obtain simple finite difference expressions. This truncation error depends upon the values of the higher derivatives, on the size of the time step, and on the order of the finite-difference equation used. The magnitude of the higher order time derivatives of the functions to be numerically differentiated is very much related to the abruptness of the time variation of the unknowns, directly dependent upon the time variation of the external excitation, for a given time step. For a decreasing time step, the variation of the electric field is more emphasized, if compared to the variation of the mobile-carrier densities. This is a consequence of the physical properties of the mobile carrier densities (and therefore the particle currents) requiring a finite time for a significant variation, where as the electric field (and therefore the displacement current) may respond immediately to any external excitation.

Time-mesh size compression when the external excitation varies more abruptly during the transient (resulting in larger values of the higher derivatives) to keep the truncation error constant and within limits can be employed and is discussed in detail in Appendix A.

One tempting idea is to employ higher order finite difference schemes to approximate the time derivative, to reduce the truncation errors. However, the stability and convergence may not be guaranteed

for each case. In some particular cases of linear parabolic equations with constant coefficients even the use of a three-point formula to approximate the first derivative, yielded unstable solutions (Reference 47pp. 125 - 131). Though higher-order finite difference schemes can be employed, their stability and convergence may not be present, and due to the lack of availability of any comprehensive theoretical work for a non-linear system of equations with variable coefficients such as under discussion, their convergence and stability must be tested individually by actual numerical computation.

For the cases of ideal excitations, such as a large step of current and voltage considered here, an overall control of the truncation error is not possible, since higher-order derivations are either infinite or discontinuous. Step functions are represented in the discretized context as ramps since only non-zero step sizes can be used. The smallest mesh size can be determined by the usual limitations on the permissible range of the computer model. When the results for the cases of step functions were considered for different time-mesh sizes (within limits which guarantee stability), it has been observed that they are relatively insensitive to the variation of time step size (within limits) except for the points in the very vicinity of the discontinuity, where higher time derivatives exhibit large magnitudes. The considerable error introduced at these singular points may be restricted to very short time intervals by the use of very small time steps. A valuable feature consistently observed is that the error introduced in the neighbourhood of the singular points does not affect significantly the response at later times. To sum up, it may be said that the discretization error of the solution obtained by the formulation described in previous

sections, may be considered sufficiently small for any practical purposes even for step functions (numerically worst case) if the proper choice of time step-size is made. The choice of time step-size is governed by the abruptness of the variation of the external excitation, and its effect on the time-variation of the unknowns, and is confirmed by testing on the actual numerical calculations for the evolution of the transients.

6.8.2 Iteration Error

The iterative procedure used at each instant of time, and described in the previous sections, are used to resolve the nonlinearities of the problem by achieving consistency between the spatial distribution of the unknowns and the system of the discretized equations. When the estimated discrepancy between the computed distributions at the completion of an iterative cycle, at a given instant of time, and the 'true' distributions, is less than a specified amount (determined by the conditions of convergence, and stability) the procedure restarts at the next time instant. This discrepancy represents the iteration error at a given time. The estimation of the stage, when overall consistency has been reached, can be made by either of the following criteria (depending upon the external excitations):

(1) This estimation may be obtained by an appropriate extrapolation of the corrections for the distributions available from the previous cycles at the same instant of time.

(2) A constant fraction of the maximum excursion (overall spatial points) of each unknown, at each instant of time, may be conveniently specified as the iteration error.

(3) The estimation may be made by considering only the consistency of the terminal response at each instant of time which

which reflects sufficiently well the behaviour of internal distributions (except at singular points).

(4) A more accurate evaluation of the consistency at a given time instant may be performed with the aid of a set of test relations derived from fundamental Eqs. (4.18) and (4.22). (The principle is the same as was used in the steady-state case). Due to heavy computation load, this technique is not suitable to test consistency at each iteration cycle, but may be used to refine the accuracy of the solution at a particular instant of time, for which spatial distribution of dependent quantities (such as particle current and net charge densities) are also required.

6.8.3 Errors in the Initial Solution

When the time dependent case is initiated from a steady-state condition, initial spatial distributions of unknowns must be furnished. These results are obtained from the solution for the steady-state case as described in Chapter V. The inaccuracy of these steady-state distributions represents a contribution to the numerical error of the transient solution. As such, it may generate unstable solutions, and therefore must be contained to sufficiently small values. It is the reason for taking all the precautionary steps we took to improve the accuracy of the steady-state solution.

There is still another aspect to be considered. The analytical and discretized formulations adopted for both the steady-state case and the time-dependent cases are not 'compatible' to each other, in the sense that the steady-state distributions feature truncation errors different from those introduced by the algorithm that generates transient solutions. Ideally, if a transient solution is initiated from a steady-

state condition in the absence of an external excitation, the internal distributions and terminal properties should remain unchanged. Instead, as a consequence of the above mentioned incompatibility, a "drift" of the original steady-state distributions is observed throughout the fictitious transient solution. The drift continues until compatibility between the spatial distributions and the new discretization scheme is achieved. Although the magnitude of the total shift is relatively small (of the order of the truncation error), it is enough to yield incorrect results for the initial period of the transient for the dependant quantities (such as particle and displacement currents spatial distribution). For the later part of the transient, this incompatibility did not affect the results significantly.

As a general rule, we can say that when initial conditions incompatible with the time-dependent formulation are used, a preliminary computation phase in the absence of external conditions is required, before initiating the actual transient solution to achieve overall compatibility. In our own case we followed this rule to avoid the errors arising from 'incompatibility' of the initial solution.

6.8.4 Other Sources of Numerical Error

(1) Round-off error is always present in a numerical solution dealing with quantities represented by a finite number of digits. It is minimized by using double-precision arithmetic in numerical computations which carry sixteen decimal places as in the IBM 360/67 model on which we performed our computations.

(2) Small differences between nearly equal numbers also contribute to the numerical error and are present in the expression for net charge density.

It may be stated that these two sources of error are not responsible for significant inaccuracies in the final results, since other contributions to the numerical errors (truncation and iteration errors) are dominant.

6.8.5 Time Step, Iteration and Truncation Errors and Numerical Error Growth in the Time Domain

A dominant factor, governing the rate of convergence at a given instant of time, is the magnitude of the time step at that instant. Larger steps are always responsible for slower convergence rates. The time step size, directly related to truncation error in the time domain, becomes a determining parameter very much affecting also the magnitude of the iteration error if the computations have to be completed within a certain amount of time. In such cases, iteration error may become dominant over the truncation error in the time domain, so that it is quite advantageous to select the time step size on the basis of the requirements dictated by a minimization of the iteration error. The total number of spatial points used also affects the convergence rate of the iterative procedure. This phenomenon is related to the propagation of the inconsistencies of the approximate distributions throughout the length of the device during the execution of an iterative cycle at a given time. A smaller number of spatial points with certain limits (chiefly dictated by the truncation error in the spatial domain) usually increases the convergence. In light of the above arguments a larger truncation error in the spatial domain is tolerated to decrease the number of spatial points, increase the convergence rate and consequently reduce the iteration error and thus save computation time. The abruptness of the doping profile is indirectly responsible for a

larger iteration error in the vicinity of the metallurgical interface. This is a consequence of the larger truncation error (in the spatial domain), occurring near the interface when we choose large spatial steps to increase the convergence. In actual practice, when this principle was applied to the structures considered, the results obtained were found to be satisfactory from any practical consideration.

The accumulation, throughout the evolution of the transient solution, of the iteration error introduced at each instant of time is of great importance. When a constant fraction of the excursion of the unknowns within a time-step is specified as the iteration error, a transient solution featuring a monotonic pattern is affected by the same relative error if the single iteration errors are accumulative. In the case of diode No. 1, a considerably more favourable situation has been observed. The iteration error at a given time instant is partially compensated for by a larger excursion of the unknowns at the next instant of time, so that the resulting error is less than the sum of the iteration errors introduced at the previous instant. DeMari⁵⁴ also observed this effect in his calculations on highly asymmetrical abrupt germanium p-n junctions for his simpler model and he attributes it to the consequence of the deviation from the "exact" condition of dynamic equilibrium at a given time caused by the iteration error, and he regarded it as an automatic feature inherent in the formulation adopted for the solution. However, in the case of diode No. 2, iterative errors exhibited an accumulative behaviour, and thus endangered the stability at later parts of the transients, unless certain precautions were taken. Moreover, due to the nature of the time variation of the independent variables, truncation errors in the time domain were found to be much

worse compared to the case of diode No. 1. As a consequence, we were forced to choose a much smaller time step size (of the order of 10) in the case of diode No. 2 compared to the case of diode No. 1. This allowed us to keep the truncation error in the time domain and the iteration error at a given instant of time well within limits of numerical instability.

6.9 Summary

An iterative method of the solution of the fundamental equations (Eqs. (4.18) - (4.23)) taken to govern the behaviour of the varactors under a time-dependent excitation has been presented in this chapter. The fundamental set of equations have been rearranged to a more convenient equivalent set of three non-linear partial differential equations (Eqs. 6.1, 6.4 and 6.5). Equations (6.4) and (6.5) are of the parabolic type, non-linear partial differential equations. Extrapolation from the simpler cases, treated by the theory of the numerical analysis lead to the choice of a generalised pure implicit discretization scheme; since restrictions on the discretization mesh inherent in explicit discretization scheme and sensitivity of generalised Crank-Nicholson discretization scheme to the numerical errors are not desirable. Gauss elimination and backward substitution method has been used to solve the system of linear algebraic equations generated as a result of the discretization. Details of the iterative procedure employed to resolve the various non-linearities inherent in the mathematical equations under consideration, has been presented. Then the numerical algorithm has been extended to cover the voltage-driven case and the case when an equation relating the terminal voltage and current is known. Various

sources of numerical error have been outlined and briefly discussed. It has been postulated that truncation error in the time domain and iteration error are mainly responsible for the overall accuracy of the results in the time domain. Therefore, the iteration and truncation errors have to be kept small. In view of the above requirement, a larger truncation error has been tolerated in the spatial domain by choosing a smaller number of points into which the diode is divided. This enabled us to keep the time mesh size small without consuming too much computation time. It is pointed out that due to the nature of the time derivatives of the various quantities inside the device, diode No.2 requires a smaller time-mesh size compared to diode No. 1 and hence diode No. 2 consumes more computation time.

CHAPTER VII

RESULTS FOR STEADY-STATE CASE

In this chapter, the computed results for both the internal and external properties of diode No. 1 and diode No. 2, when the forward steady-state terminal voltage of the diodes is specified, are presented and briefly discussed.

7.1 Introduction

The mathematical equations which are taken to govern the behaviour of the diodes under steady-state conditions are outlined in Chapter IV. The numerical solution of these equations is discussed in detail in Chapter V. The internal distribution of the independent variables of the mathematical formulation (electrostatic potential, electron quasi-Fermi level and hole quasi-Fermi level) and of the dependent variables (electron density, hole density, electron current density and hole current density) are useful in explaining the terminal behaviour. They are thus indirectly helpful in device design. The mobility and the generation-recombination rate distribution inside the device expose the validity of the physical model in which they are assumed constant. Moreover, the internal distributions of the hole density, the electron density and electrostatic potential are required for time-dependent solutions initial values, as already discussed in Chapter VI. The static characteristics of varactors and of step-recovery diodes, such as terminal current and incremental capacitance as a function of terminal voltage are very significant, though not sufficient

to characterize them. All the results are displayed in normalised units, unless otherwise specified (see Table 4.1).

7.2 Results For Diode No. 1

Detailed results for the internal distributions for both the independent and dependent variables are displayed in this section for terminal voltages of 0.0, 0.7, 0.9 and 1.0 volts. These results were stored on magnetic tape and were plotted directly by means of the Calcomp plotter attached to the IBM 360/67 system. The results displayed are electron density distribution, hole density distribution, net doping profile, electrostatic potential (E.S. Potential) distribution, electron quasi-Fermi level (E.Q.F.L.) distribution, hole quasi-Fermi level (H.Q.F.L.) distribution, electron current distribution, hole current distribution and generation-recombination rate distribution throughout the interior of the device.

Figures (7.1a), (7.1b), (7.1c) and (7.1d) give the electron and hole density distributions along with the net doping concentration distribution. These results reaffirm the inequality between the hole-electron density product and externally applied voltage V_a : $p(x) n(x) \leq e^{V_a}$. This is in agreement with Gummel's⁵⁵ and DeMari's¹⁹ recent numerical results for highly asymmetrical p-n junctions. The concentrations of minority-carriers near the external contacts is of interest as we have assumed ohmic contacts in our model. The concentration of minority-carriers increases as forward-bias is increased. Even at 1.0 volt forward-bias, the accumulation of minority-carriers near the ohmic contact at the substrate is relatively insignificant. On the other hand, at the ohmic contact at the end of

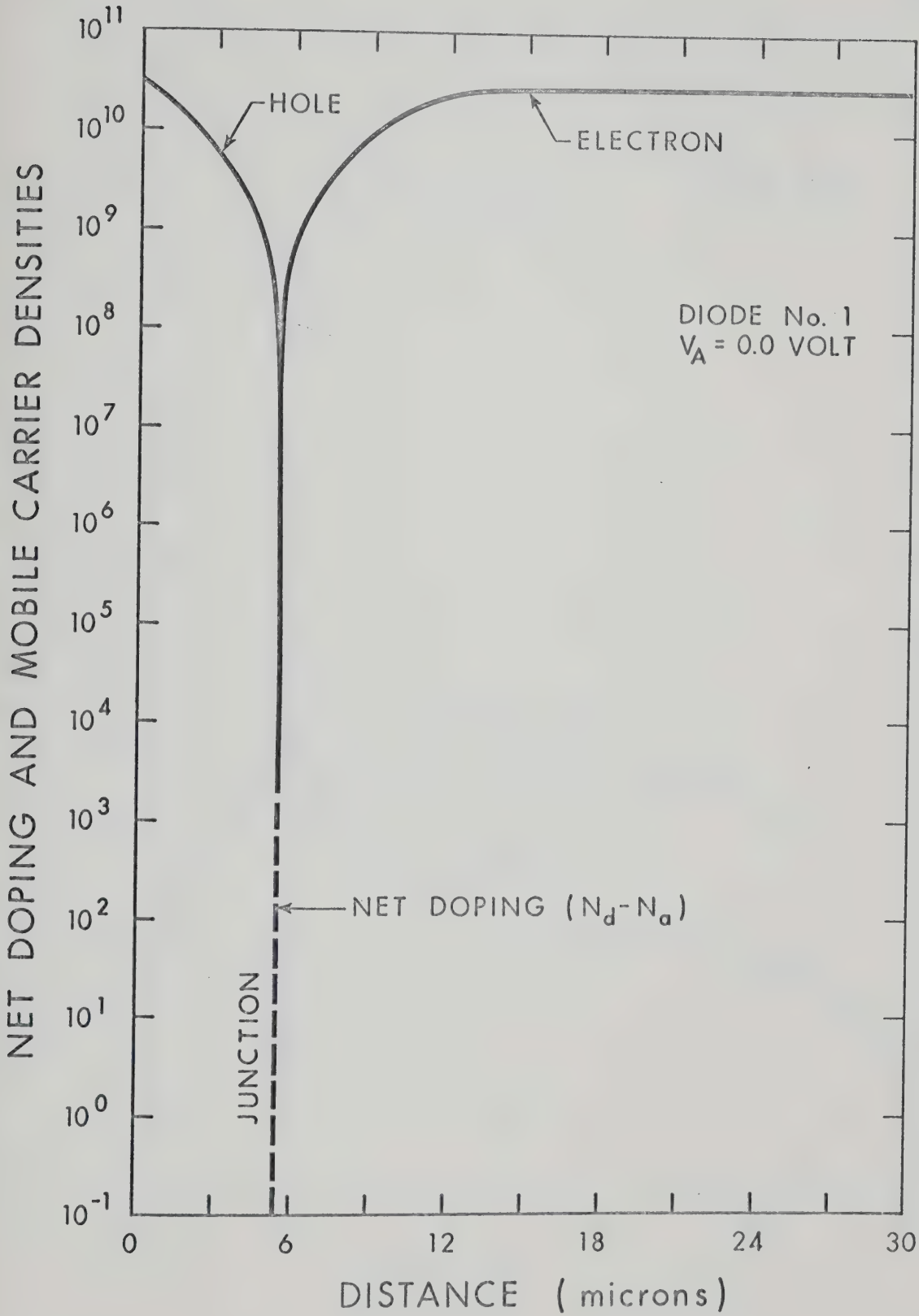


Fig. 7.1a. Spatial distribution of net doping and mobile carrier densities for diode No. 1 under steady-state conditions for $V_A = 0.0$ volt.

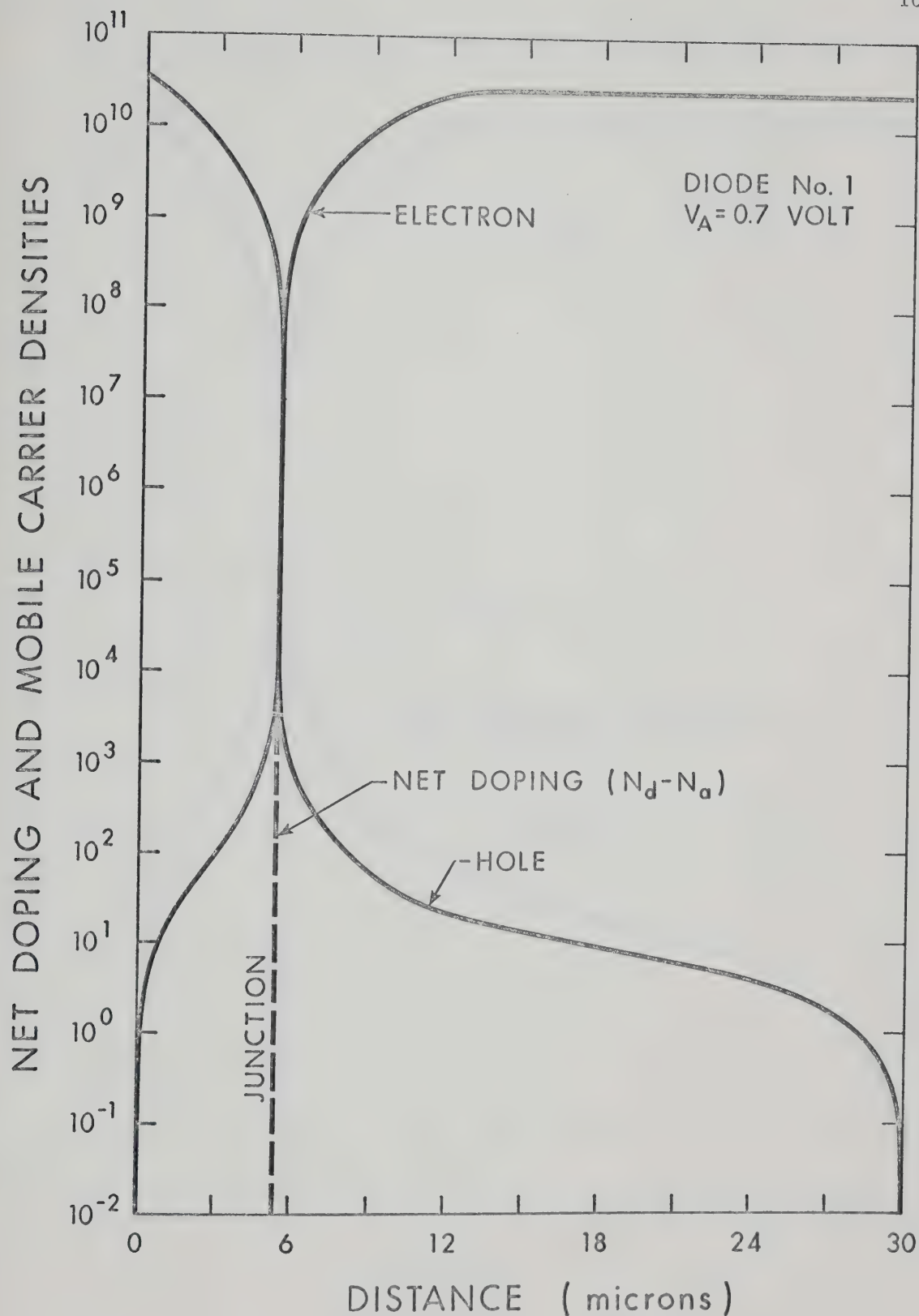


Fig. 7.1b. Spatial distribution of net doping and mobile carrier densities for diode No. 1 under steady-state conditions for $V_A = 0.7$ volt.

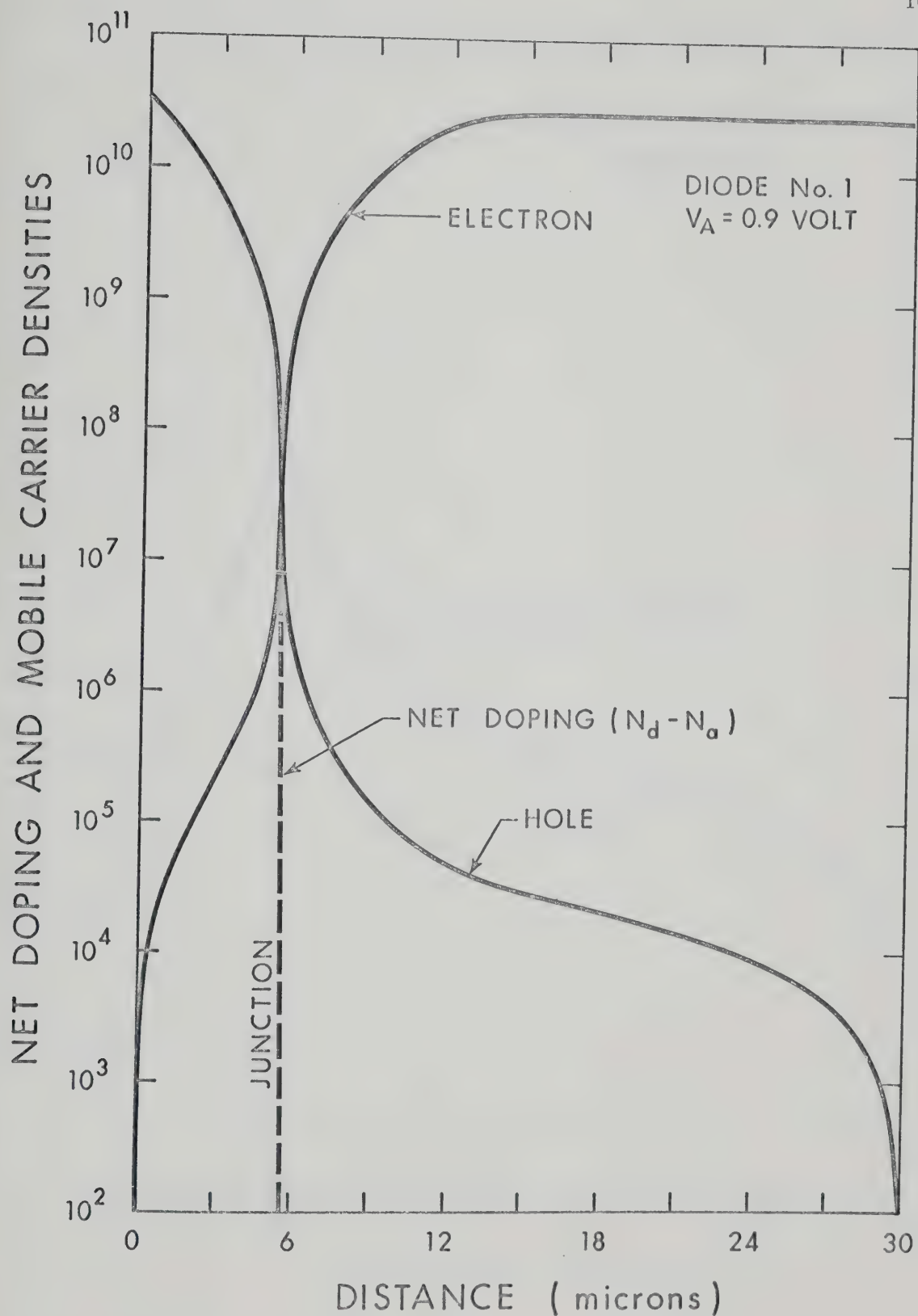


Fig. 7.1c. Spatial distribution of net doping and mobile carrier densities for diode No. 1 under steady-state conditions for $V_A = 0.9$ volt.

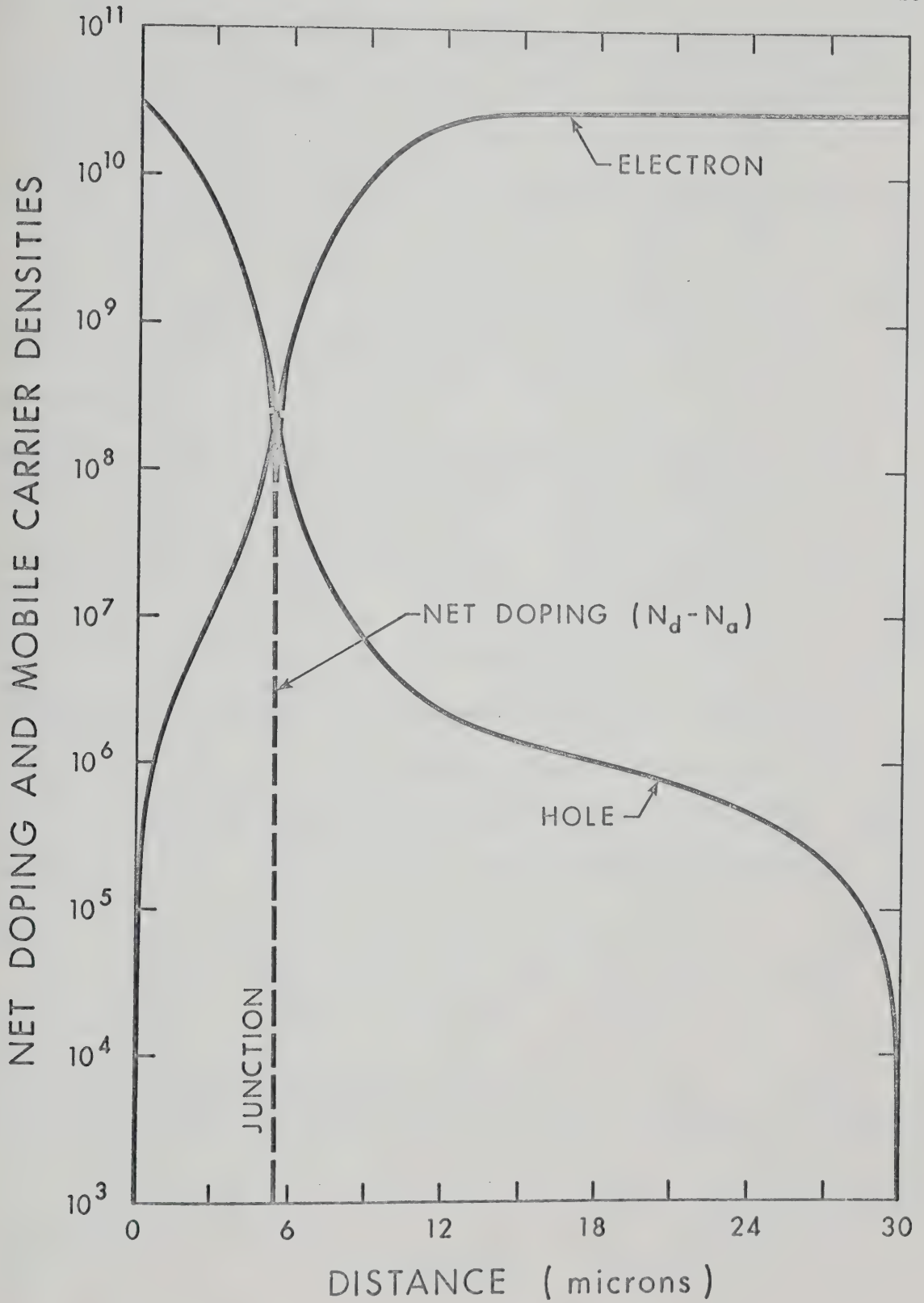


Fig. 7.1d. Spatial distribution of net doping and mobile carrier densities for diode No. 1 under steady-state conditions for $V_A = 1.0$ volt.

the narrow p-region, there is a greater accumulation of the minority-carriers (≈ 10 times more than on the n side). But this concentration of minority-carriers is small enough compared to the concentration of majority-carriers to significantly alter the charge neutrality near the external contacts on both the p- and n-side. It may be pointed out that at very high injection levels, when the minority-carrier concentrations become comparable to the majority-carrier concentrations, neutrality will be absent in a narrow region near the external contacts. Since the assumption of ohmic contacts will prevent the conductivity of such a region from being significantly modulated, a large current will cause a high voltage drop or, in equivalent terms, a strong electric field near the contacts to be built up. This electric field will, in turn, tend to expel the majority-carriers and attract the minority-carriers, thus resulting in a local alteration of neutrality balance. Conductivity modulation effects due to the minority-carrier injection, are absent till 0.9 V and start showing their presence for 1.0 Volt forward-bias. The narrow region near the metallurgical junction shows accumulation of the minority-carrier densities greater than the majority-carriers densities.

Figures (7.2a), (7.2b), (7.2c) and (7.2d) display the E.S. potential, E.Q.F.L. and H.Q.F.L. distribution throughout the interior of the device. These illustrations show that the assumption of constant Fermi levels in the transition region is a valid assumption for moderate forward-bias levels. Due to the injection of carriers across the junction, the abruptness of the E.S. Potential distribution at the metallurgical junction decreases gradually as the forward bias is increased. The E.S. Potential distribution for 1.0 volt forward bias (Fig. 7.2d) shows a small slope in the substrate. It shows that the

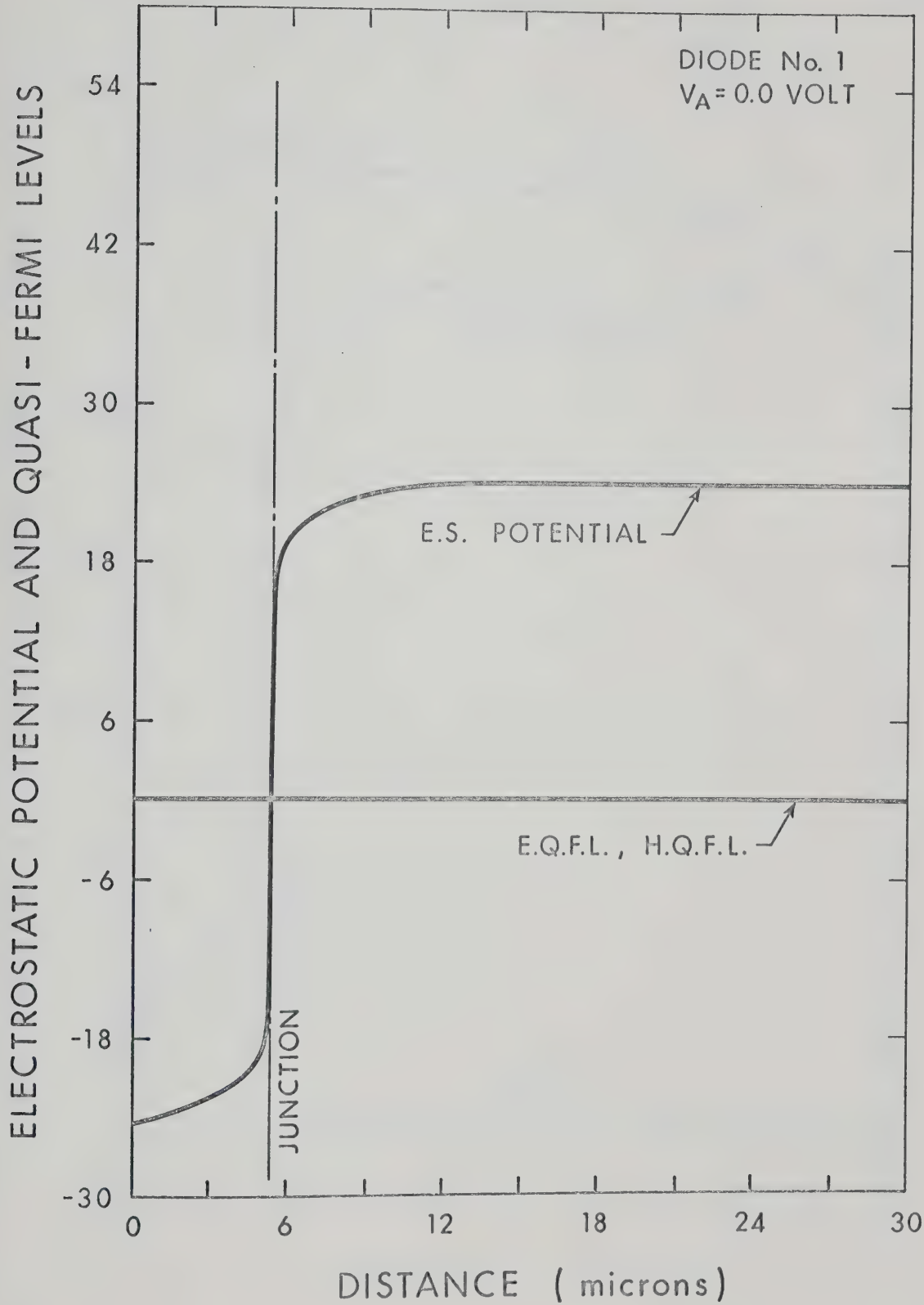


Fig. 7.2a. Spatial distribution of electrostatic potential and hole and electron quasi-Fermi levels for diode No. 1 under steady-state conditions for $V_A = 0.0$ volt.

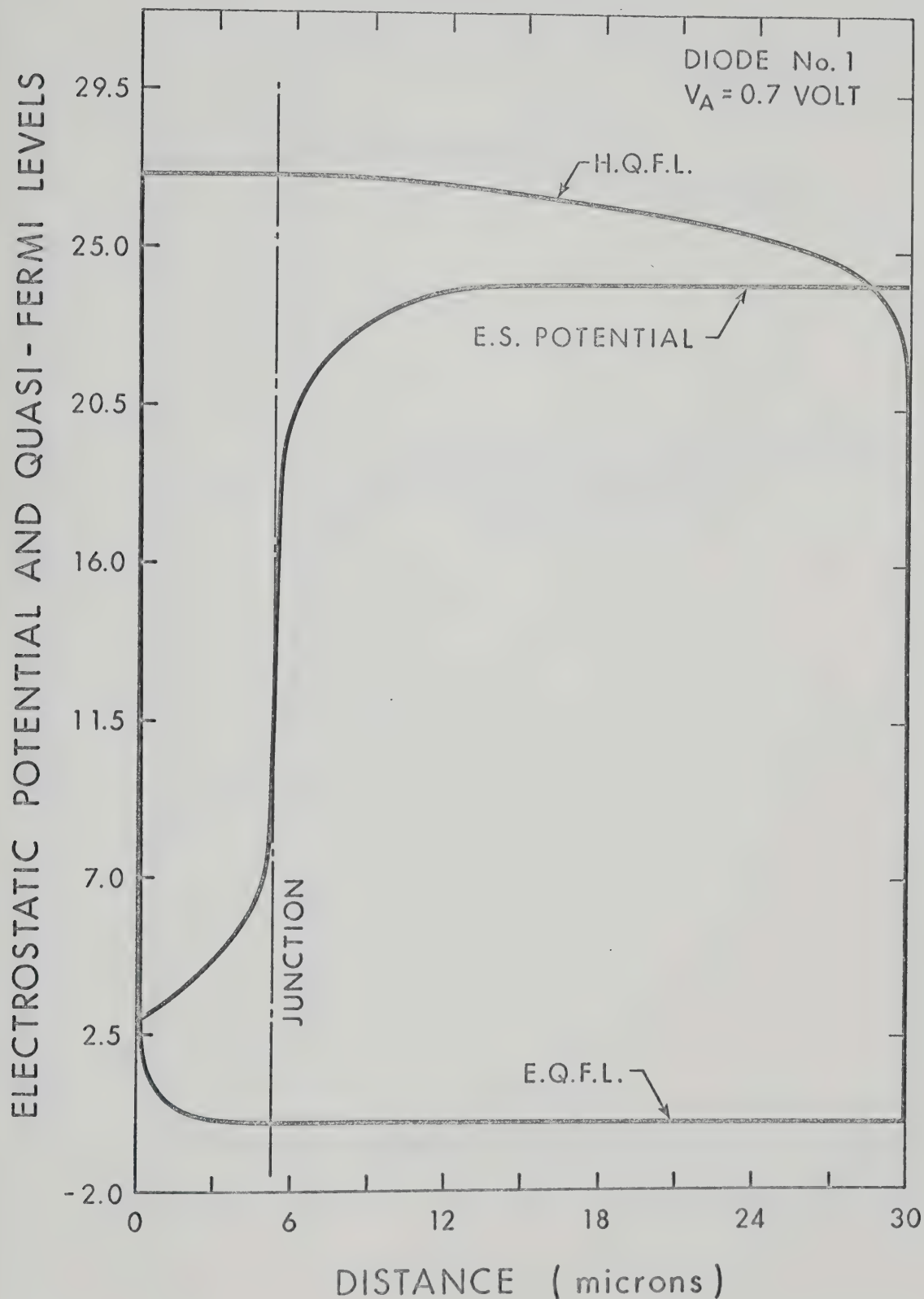


Fig. 7.2b. Spatial distribution of electrostatic potential and hole and electron quasi-Fermi levels for diode No. 1 under steady-state conditions for $V_A = 0.7$ volt.

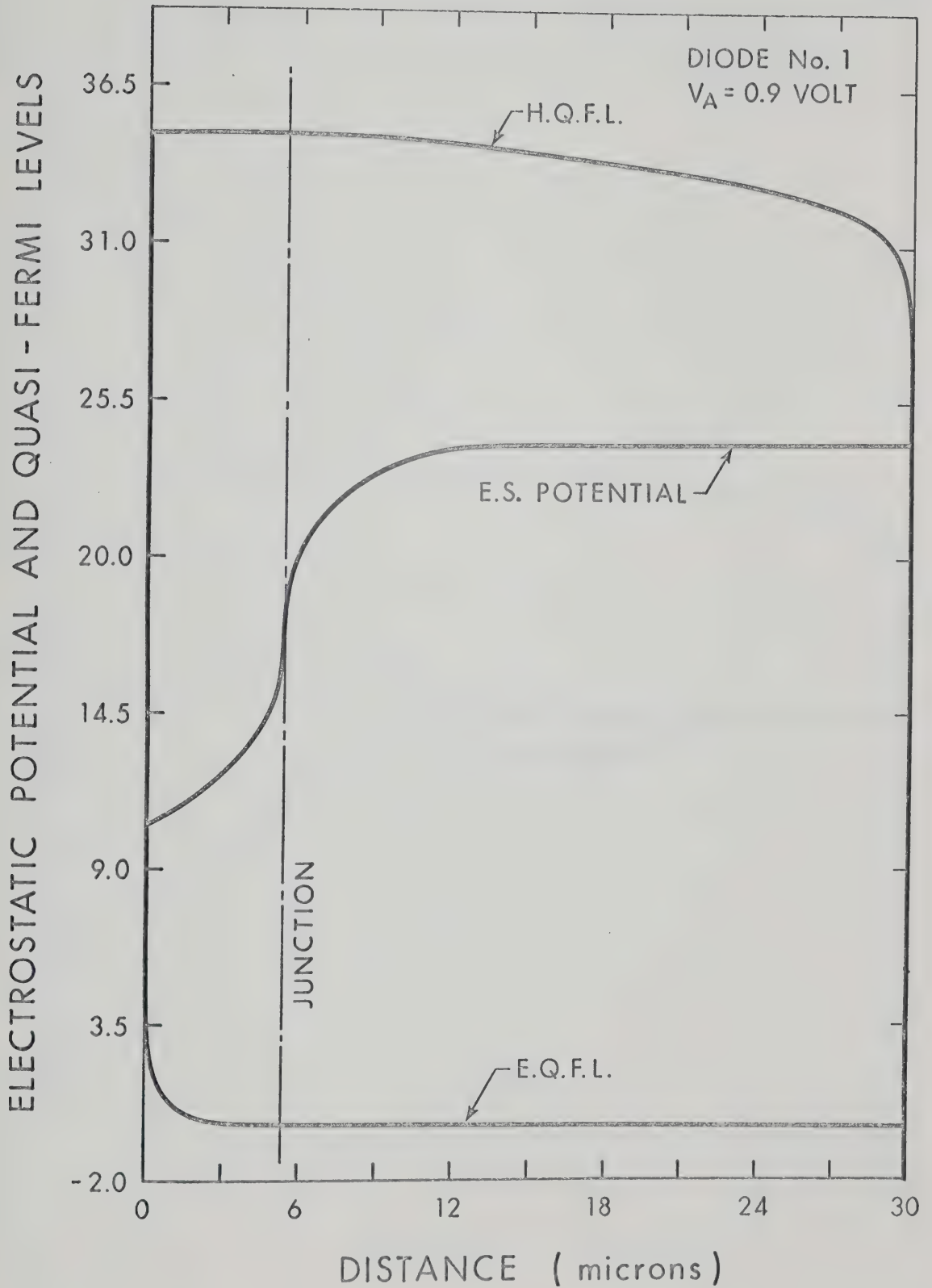


Fig. 7.2c. Spatial distribution of electrostatic potential and hole and electron quasi-Fermi levels for diode No. 1 under steady-state conditions for $V_A = 0.9$ volt.

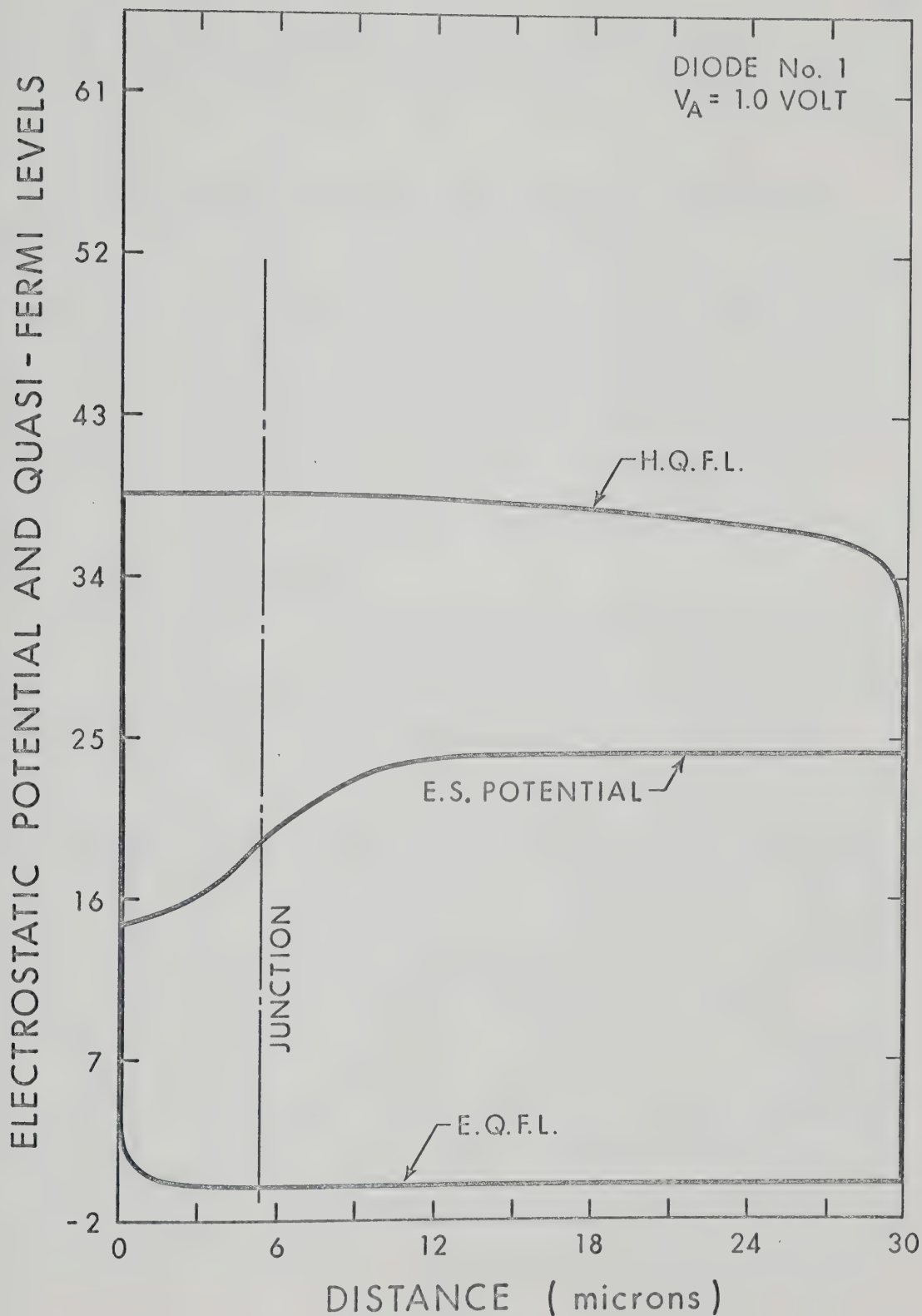


Fig. 7.2d. Spatial distribution of electrostatic potential and hole and electron quasi-Fermi levels for diode No. 1 under steady-state conditions for $V_A = 1.0$ volt.

presence of the minority-carriers in the substrate has become significant enough to cause a slight shift in the neutrality condition present before.

Figures (7.3a), (7.3b) and (7.3c) show the net generation-recombination rate for 0.7, 0.9 and 1.0 volts forward bias, respectively. Initially, most of the recombination is confined near the metallurgical junction (Fig. 7.3a), but as the forward bias is increased, recombination in the quase-neutral region of the diode becomes more and more important. For 1.0 volts forward bias, (Fig. 7.3c) shows that recombination is significant not only in the transition layer, but also in the quasi-neutral regions of the diodes.

Figures (7.4a), (7.4b), (7.4c) and (7.4d) show the mobility distribution throughout the interior of the device for 0.0, 0.7, 0.9 and 1.0 volts forward bias. These figures show that the assumption of constant mobilities (as assumed in most of the theoretical work) is highly inaccurate in the vicinity of the metallurgical junction, where it is a strong function of position due to the presence of the electric field and to the variation of net doping density. The electron mobility is about 1.5 times greater than the hole mobility, as expected.

Figures (7.5a), (7.5b) and (7.5c) show the spatial distribution of electron and hole currents^{*} for 0.7, 0.9, and 1.0 volts forward-bias. This shows an interesting feature in that, though the doping density of the p-side is higher (5×10^{20}) than that of the n-side (4×10^{20}), the electron current is the dominant current flowing in the substrate and

* For simplicity, in the following text, the term "current" will be consistently used to denote current density.

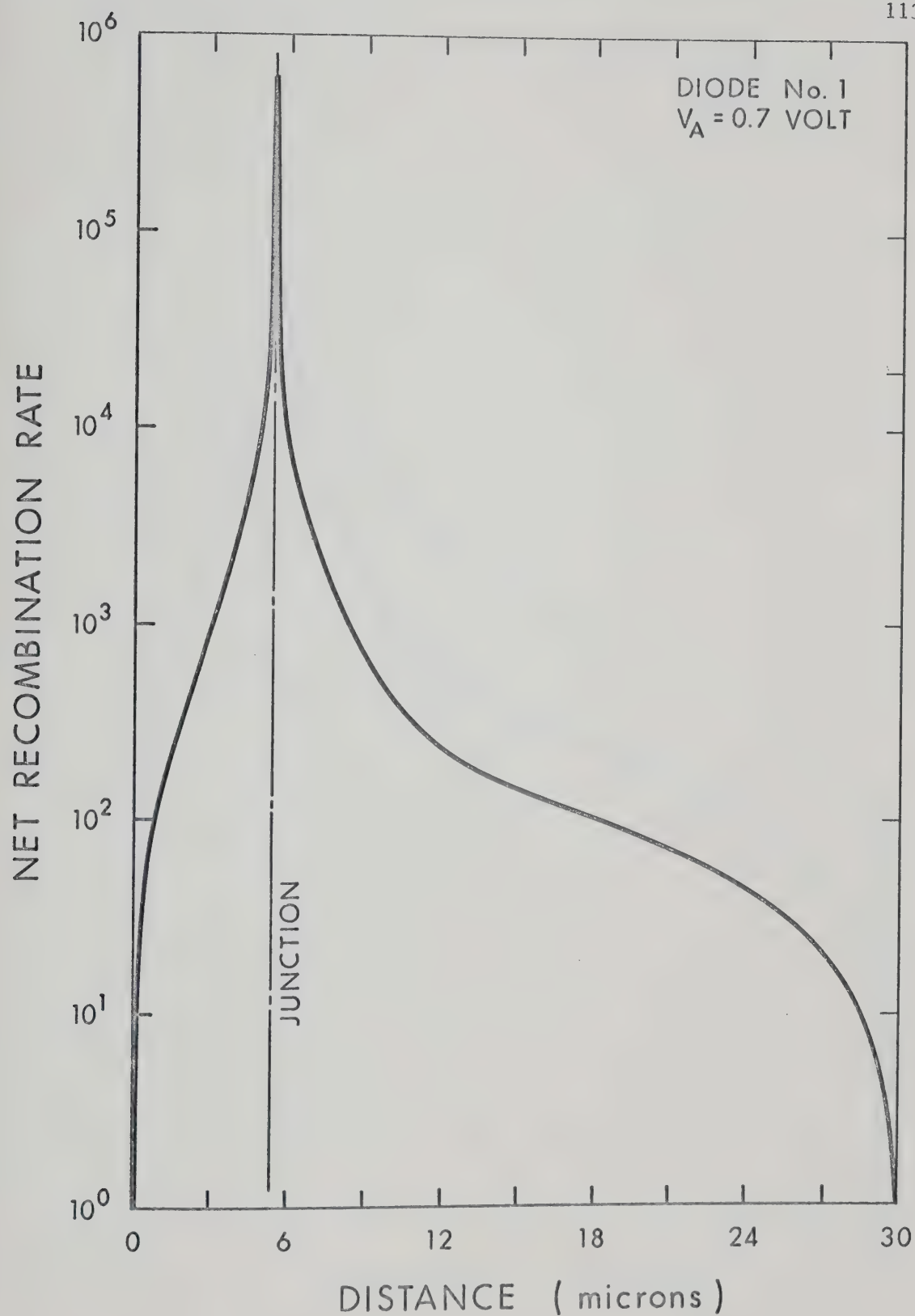


Fig. 7.3a. Spatial distribution of net recombination rate for diode No. 1 under steady-state conditions for $V_A = 0.7$ volt.

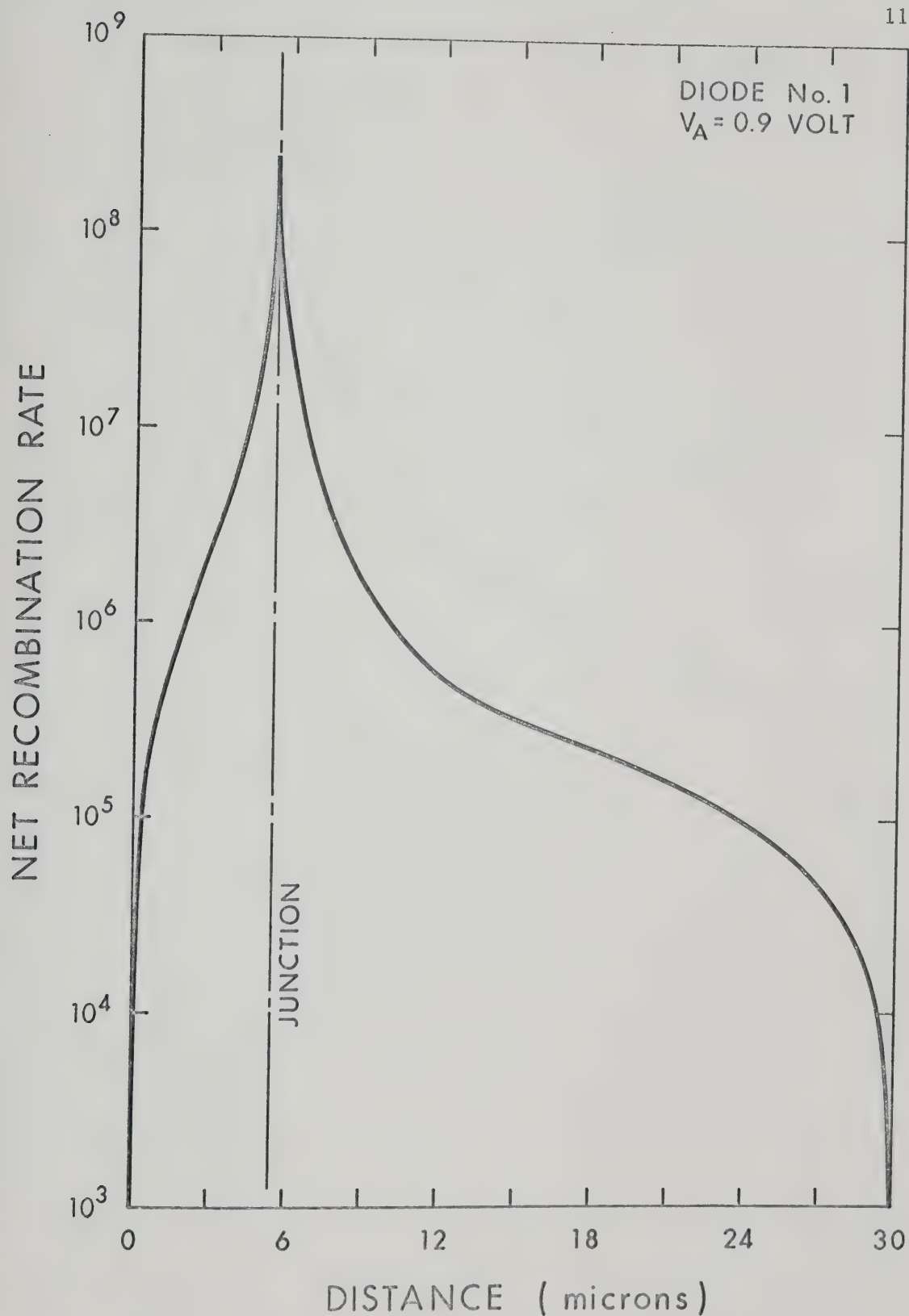


Fig. 7.3b. Spatial distribution of net recombination rate for diode No. 1 under steady-state conditions for $V_A = 0.9$ volt.

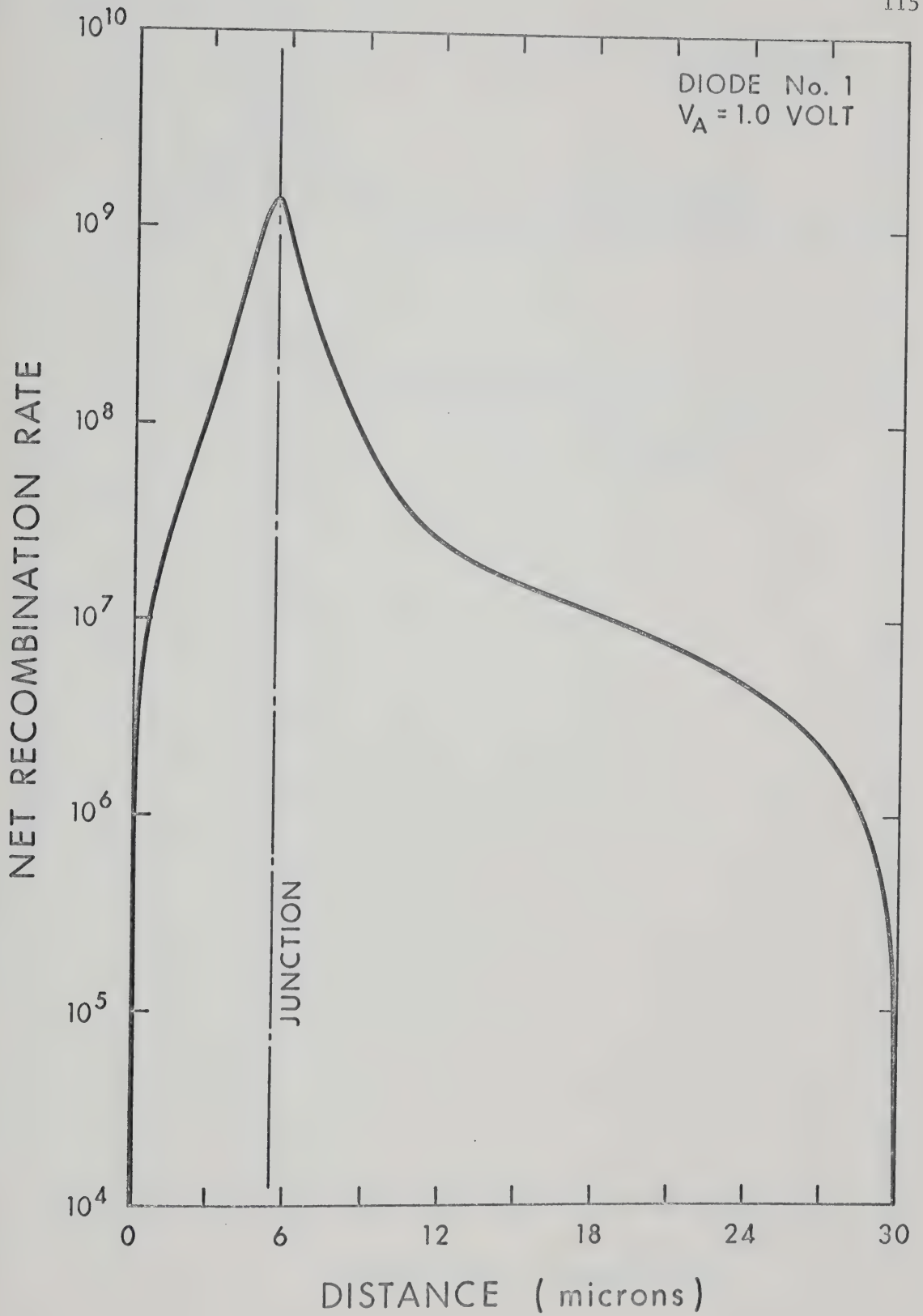


Fig. 7.3c. Spatial distribution of net recombination rate for diode No. 1 under steady-state conditions for $V_A = 1.0$ volt.

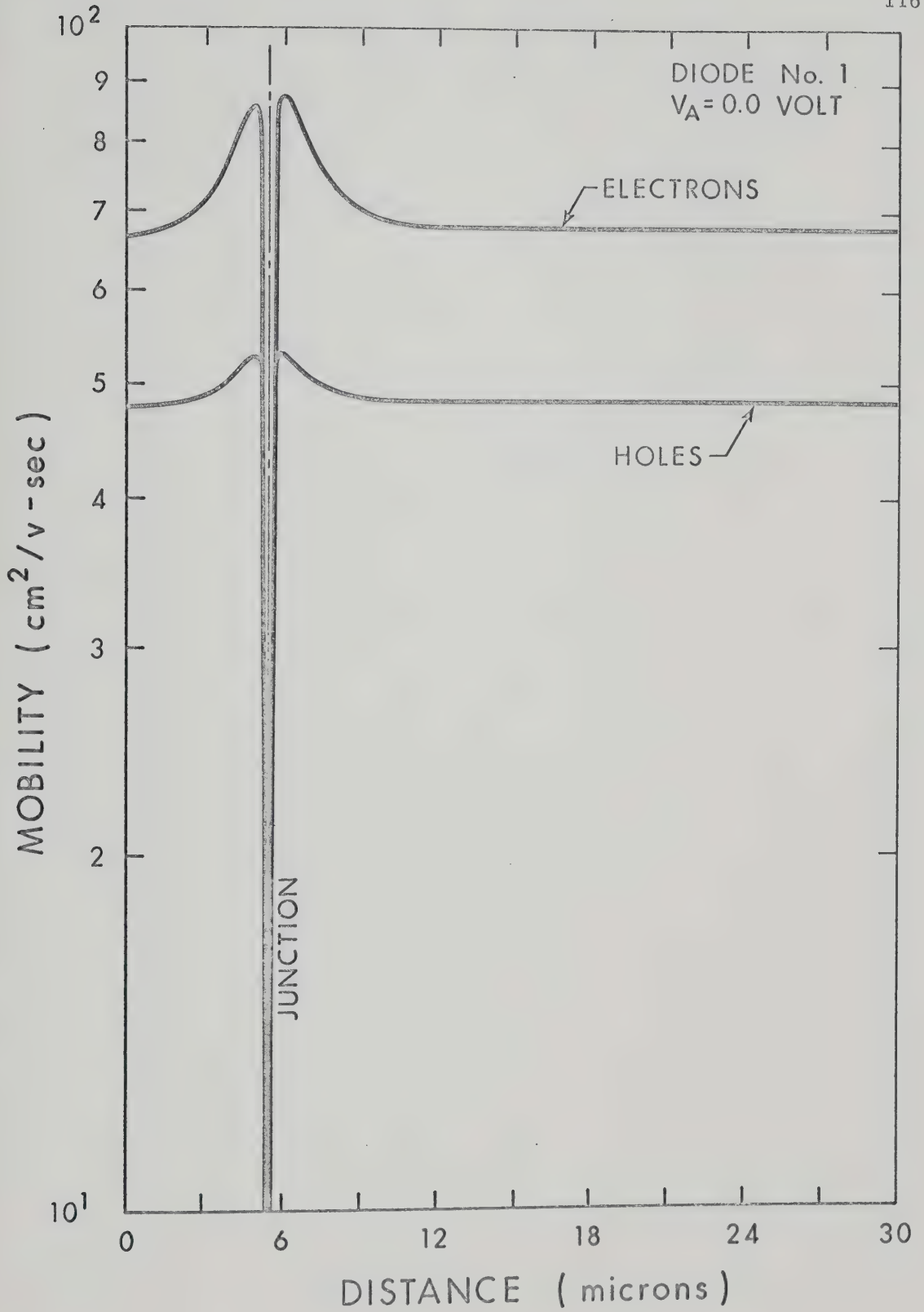


Fig. 7.4a. Spatial distribution of carrier mobilities for diode No. 1 under steady-state conditions for $V_A = 0.0$ volt.

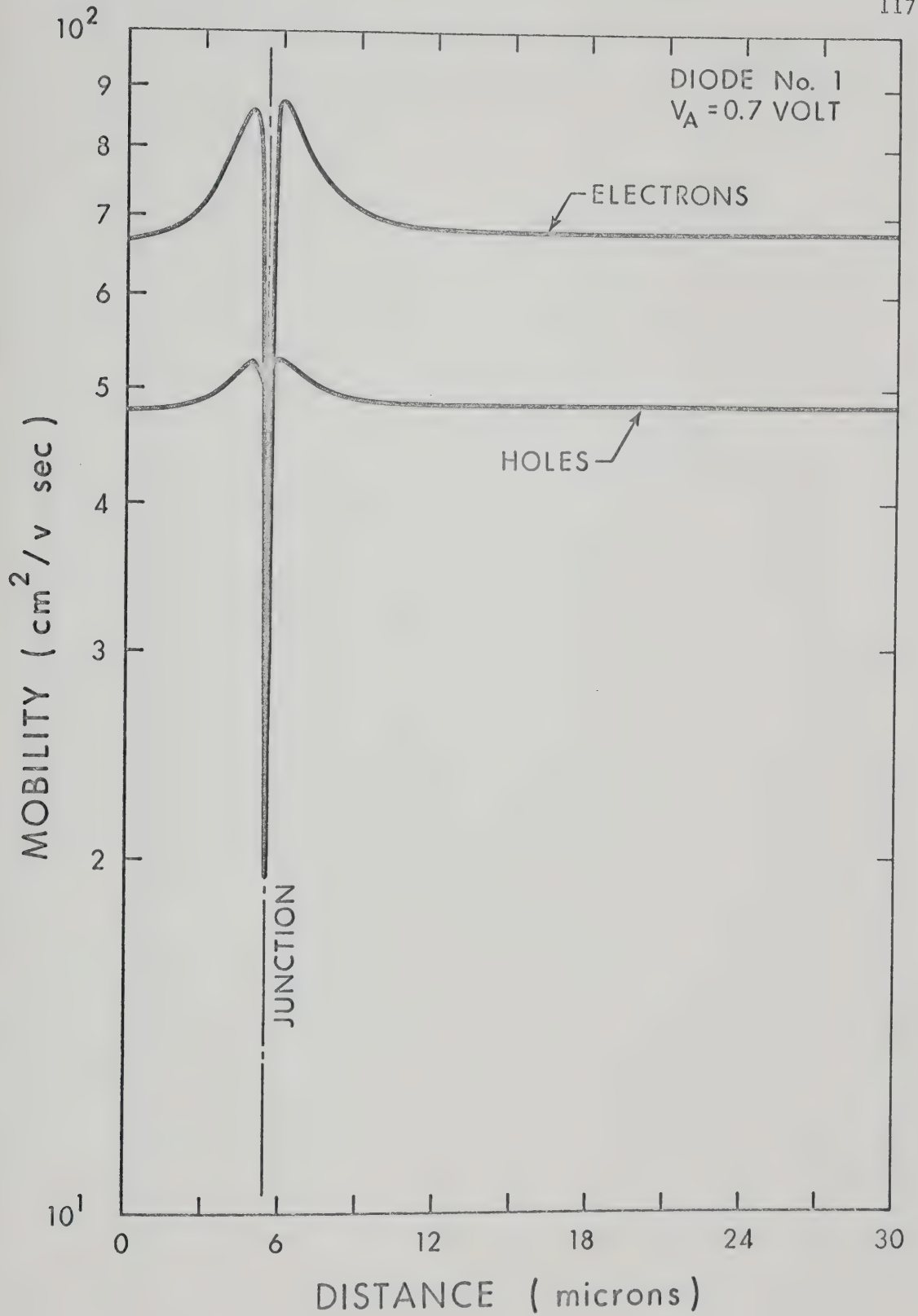


Fig. 7.4b. Spatial distribution of carrier mobilities for diode No. 1 under steady-state conditions for $V_A = 0.7$ volt.

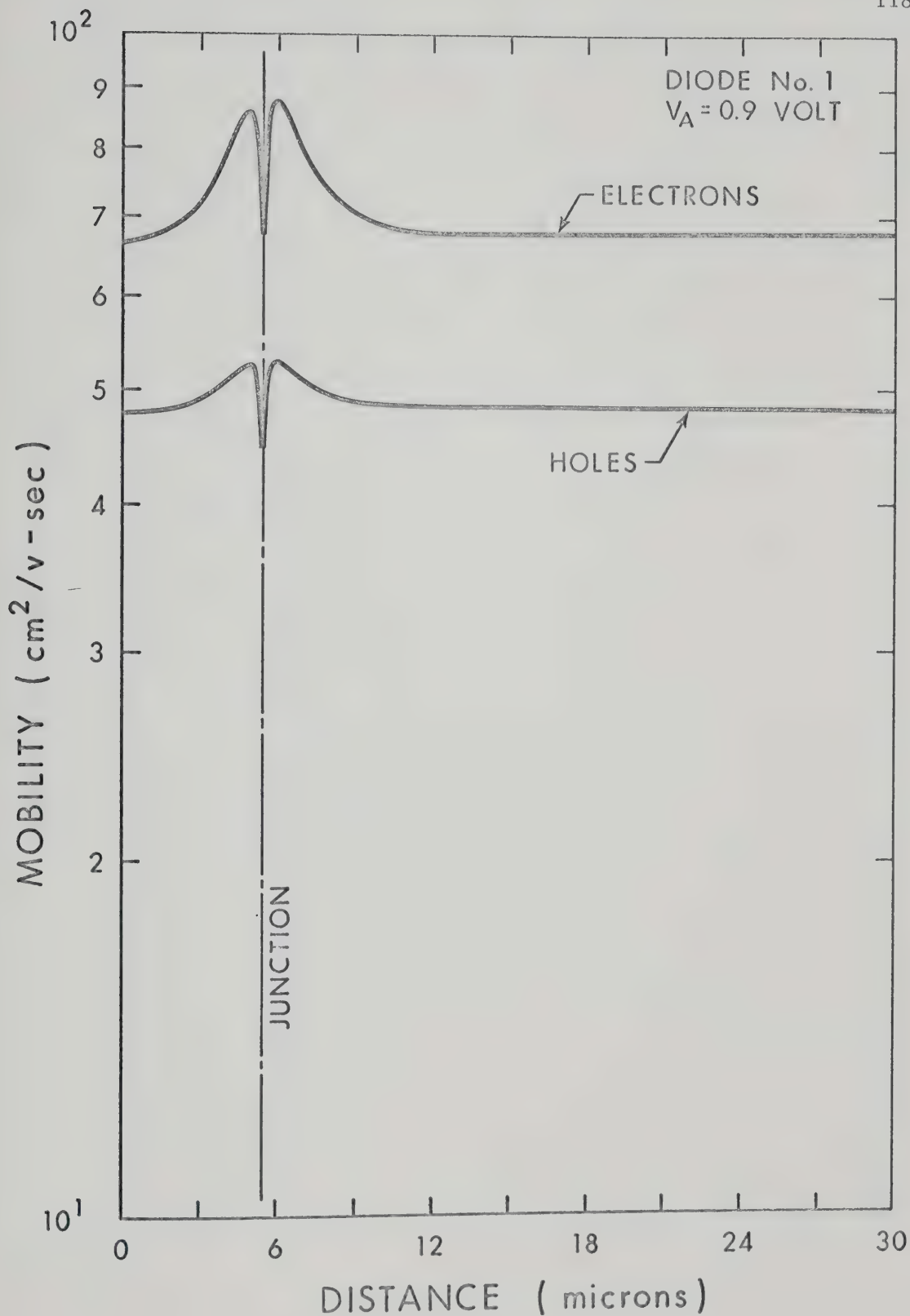


Fig. 7.4c. Spatial distribution of carrier mobilities for diode No. 1 under steady-state conditions for $V_A = 0.9$ volt.

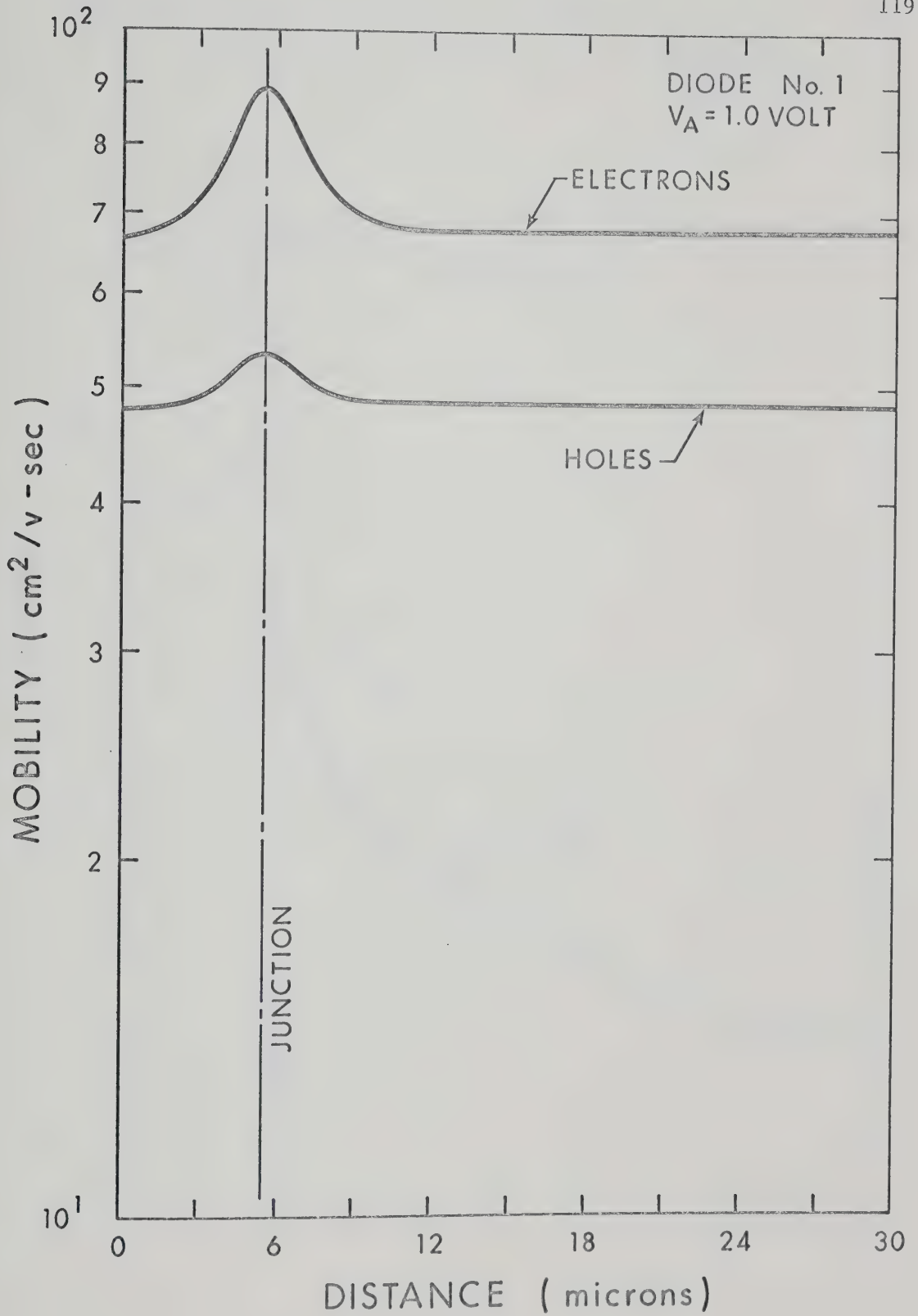


Fig. 7.4d. Spatial distribution of carrier mobilities for diode No. 1 under steady-state conditions for $V_A = 1.0$ volt.

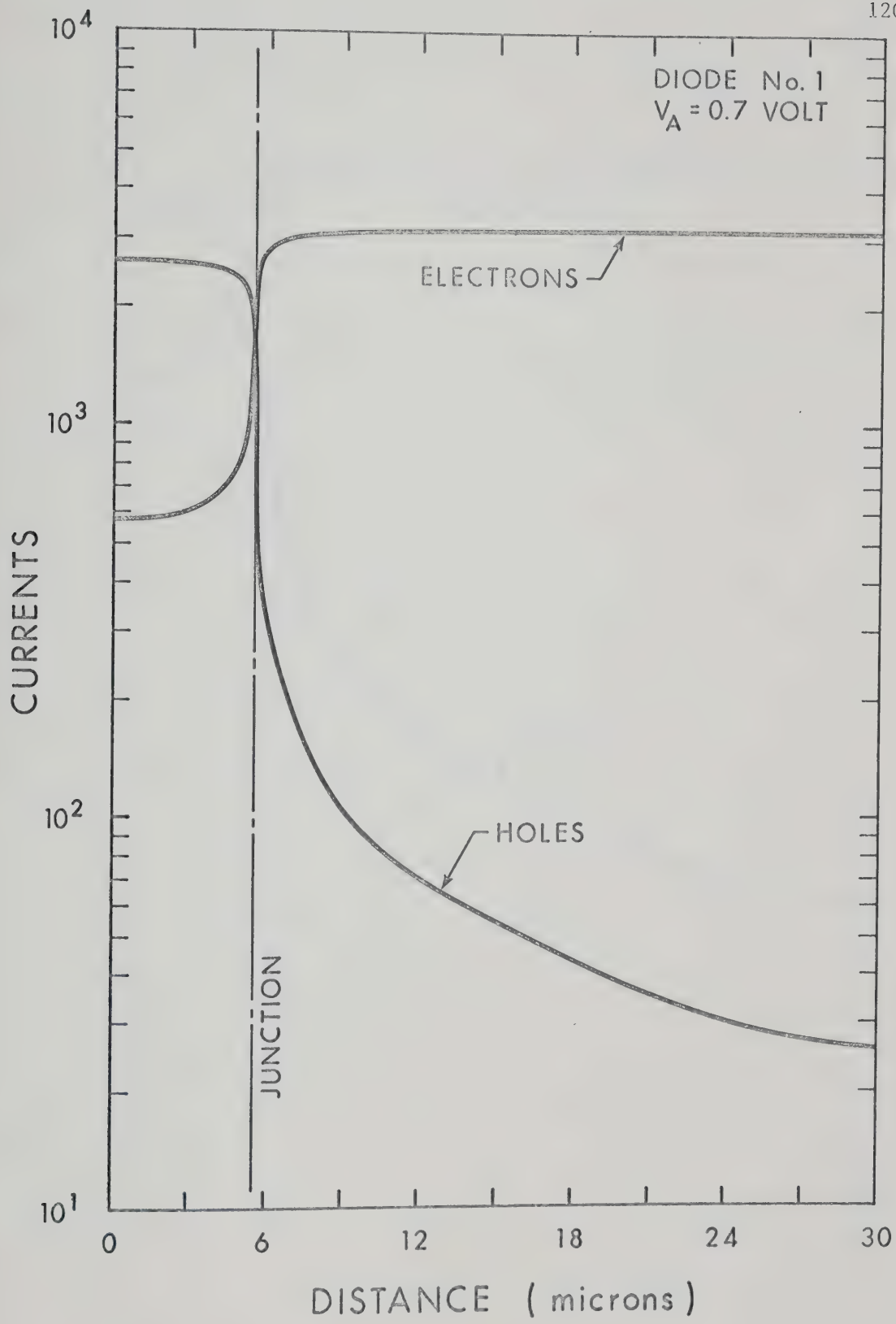


Fig. 7.5a. Spatial distribution of electron and hole currents for diode No. 1 under steady-state conditions for $V_A = 0.7$ volt.

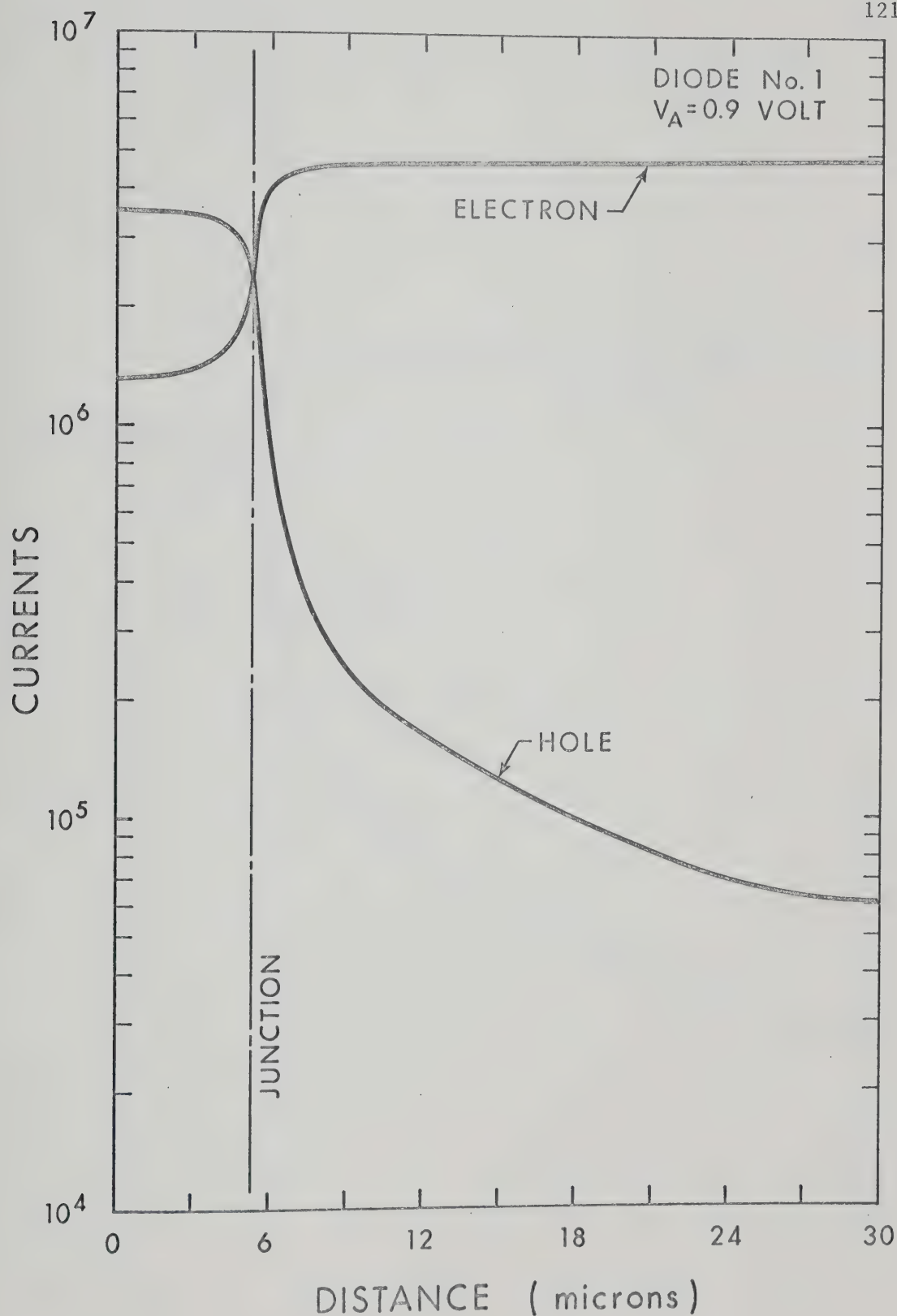


Fig. 7.5b. Spatial distribution of electron and hole currents for diode No. 1 under steady-state conditions for $V_A = 0.9$ volt.

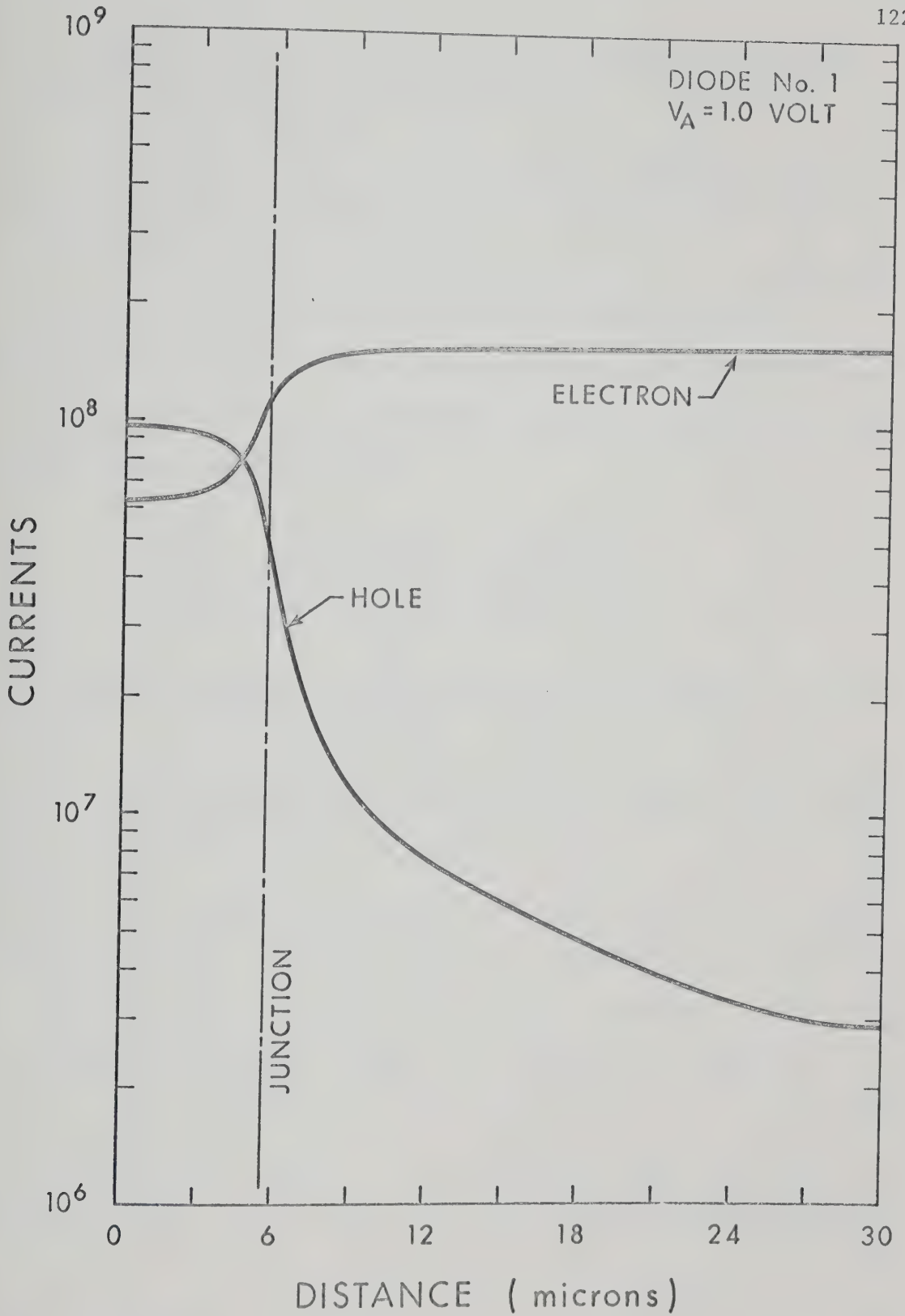


Fig. 7.5c. Spatial distribution of electron and hole currents for diode No. 1 under steady-state conditions for $V_A = 1.0$ volt.

makes a significant contribution to the total current in the p-side.

The hole current in the p-region makes a decreasing contribution to the total current as the forward-bias is increased; it contributes 81.7% of the total current in the p-region for 0.7 V bias compared to 72.5% and 60.5% for 0.9 V and 1.0 V forward bias, respectively. The contribution of the electron current to the total current in the p-region is increasing as the forward bias is increased. This may be explained in the following way: In our assumed model, the ratio of hole current to electron current can be written as

$$\frac{J_p(x)}{J_n(x)} = \frac{J_{p \text{ diffusion}}(x) - J_{p \text{ drift}}(x)}{J_{n \text{ diffusion}}(x) + J_{n \text{ drift}}(x)} \quad \dots(7.1)$$

In the case under discussion, $\frac{J_p(x)}{J_n(x)}$ decreases in the p-region. As the forward bias is increased, the electric field in the p-region also increases, which gives rise to a large increase in the hole drift current (holes are majority carriers, and therefore their concentration is very high and a small change in the electric field will cause a large change in the drift current). It seems that as the forward-bias is increased, the increment change in the hole drift current is greater, compared to that of the hole diffusion current. As a consequence of the above reasoning, we see that the hole current contribution to the total current will decrease in the p-region as the forward-bias is increased. The argument that the electron mobility is greater than the hole mobility is not relevant to this case, as their ratio is almost constant in the p-region for the biases considered (except in the transition region). The contribution of the hole current to the total current in the quasi-

neutral n-region increases slightly as the forward bias is increased (0.8, 1.27, 1.81% near the external contact at 0.7, 0.9 and 1.0 Volts, respectively). In this region, the diffusion component is increased more than the drift component as the terminal voltage is increased, since the electric field is either absent or has a very small value.

The terminal properties of the diode, namely the terminal current and the incremental capacitance as a function of the diode terminal voltage, are plotted in Figs. (7.6) and (7.7). The incremental capacitance starts showing a large variation at a forward-bias of 0.7 volts, and increases very rapidly to a value approximately 10^5 times the value at zero volts. The value of the series resistance at zero volts bias calculated from the definition given in Eq. (5.32) is 0.81 ohms. Cut-off frequency, the static figure of merit, is defined as follows¹:

$$f_{cv} = \frac{1}{2\pi R_{sv} C_{jv}} \quad \dots(7.2)$$

where

f_{cv} = cut-off frequency at the specified voltage (v).

R_{sv} = diode series resistance at the specified voltage (v).

C_{jv} = diode junction capacitance at the specified voltage (v).

The cut-off frequency for diode No. 1 at zero volts bias, calculated from Eq. (7.2), is 261 GHz. It is to be noted that the above calculation of the cut-off frequency did not include the package capacitance and the contact resistance.

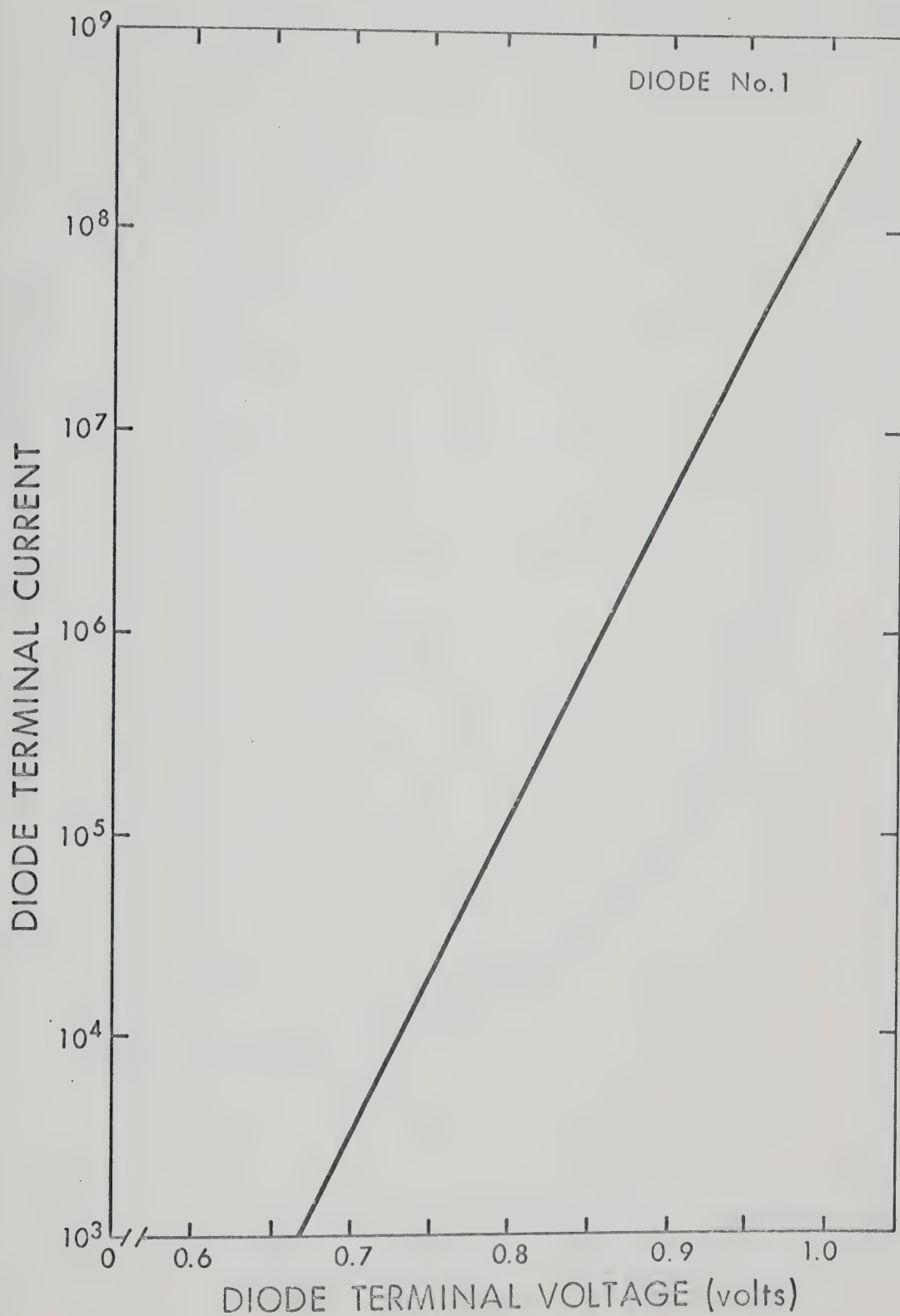


Fig. 7.6. Terminal current of diode No. 1 as a function of terminal voltage (steady-state conditions).

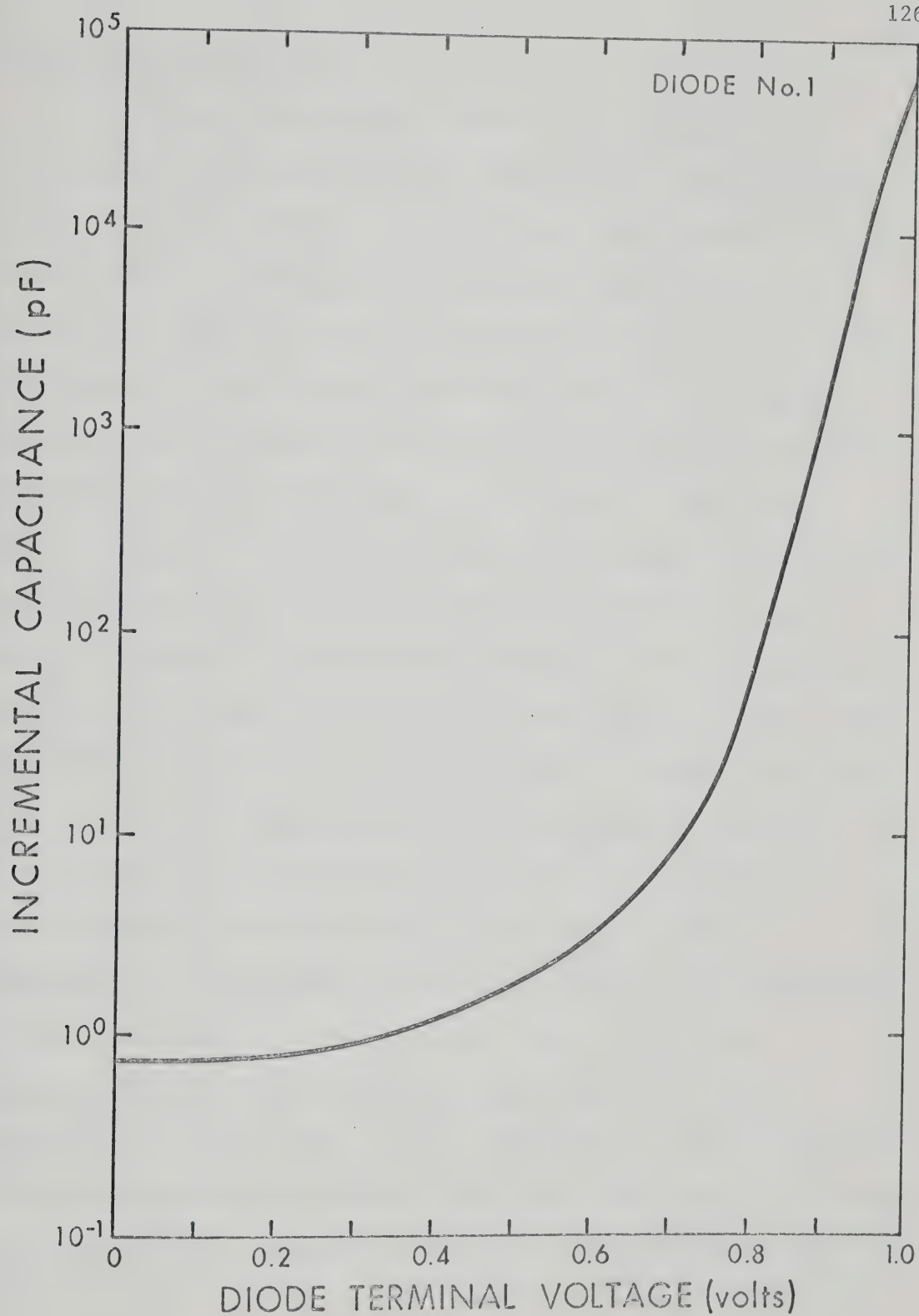


Fig. 7.7. Incremental capacitance of diode No. 1 as a function of terminal voltage (steady-state conditions).

7.3 Results For Diode No. 2

The results displayed are hole and electron density distributions, electrostatic potential, hole and electron quasi-Fermi level distributions, hole and electron current distributions, hole and electron mobility distributions and generation-recombination rate distribution. These quantities are displayed for 0.0, 0.5, 0.8 and 1.0 volts. Figures (7.8a), (7.8b), (7.8c) and (7.8d) give the hole and electron density distribution along with the net doping concentration distribution throughout the interior of the device. These results affirm the inequality between the electron-hole density product and the externally applied voltage V_a : $p(x) n(x) < e^{V_a}$, which was earlier pointed out by Gummel⁵⁵ for simple p-n junctions, and was reaffirmed by our results on diode No. 1 as mentioned in the previous section. This result shows that in our $p^+ - n - n^+$ structure, the electron and hole density distributions obey the same law as for simple p-n junctions. The hole and electron concentrations show that a great number of the injected minority carriers are stored in the middle n-region. Consequently the concentration of minority carriers in the quasi-neutral n^+ region is far less (by a factor of more than ten) than the concentration in the middle high resistivity layer. This may be explained with the help of Fig. (7.9), which displays the electric field in the neighbourhood of the middle n-region, when the diode is in thermal equilibrium. On both edges of the n-region, there is an appreciable negative electric field present. At the $p^+ - n$ junction the field is about 5 times higher than that at the $n - n^+$ edge. The electric field at the center of the n-region is zero. Due to the presence of this electric field, the flow of injected carriers into the n^+ and p^+ regions

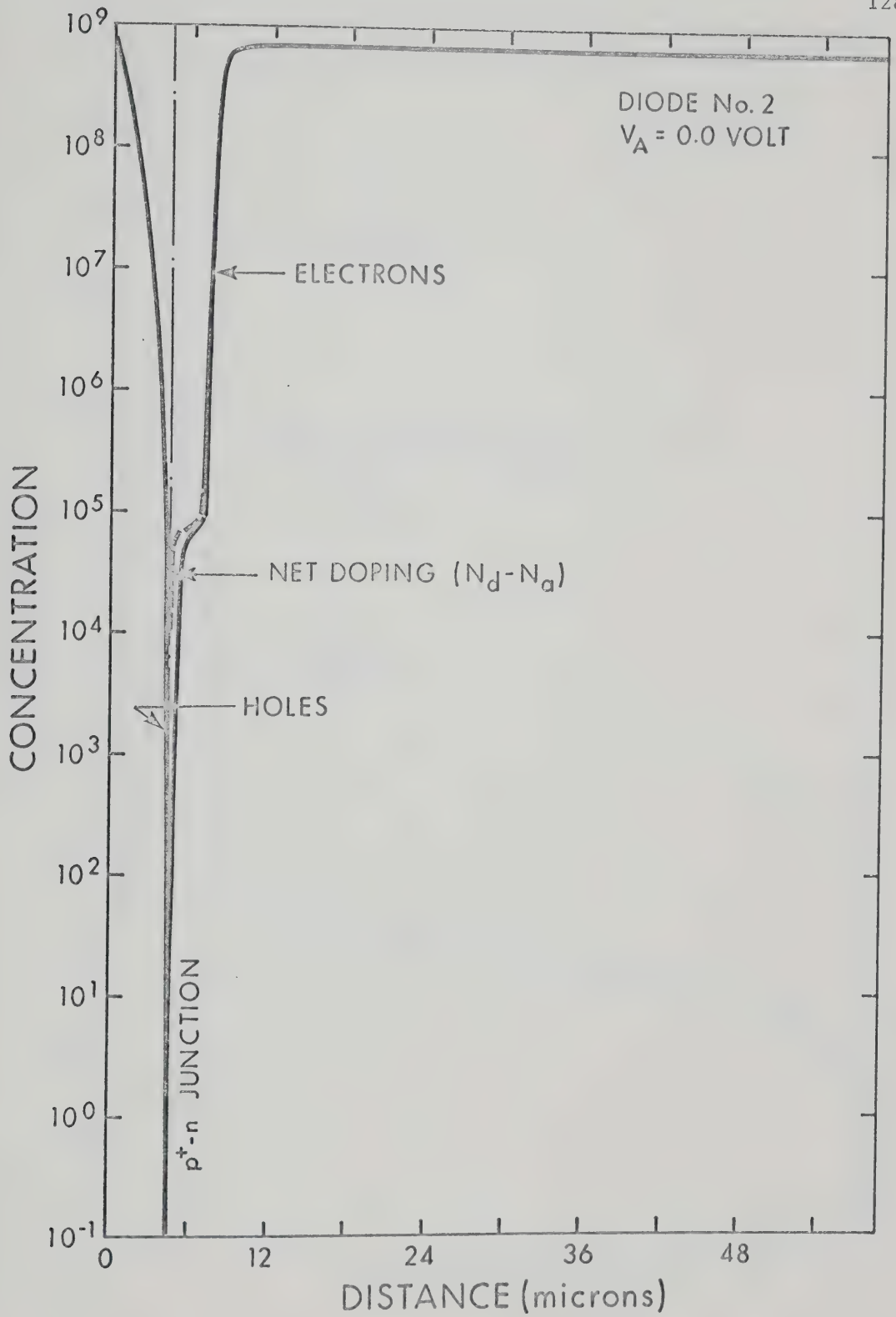


Fig. 7.8a. Spatial distribution of net doping and mobile carrier densities for diode No. 2 under steady-state conditions for $V_A = 0.0$ volt.

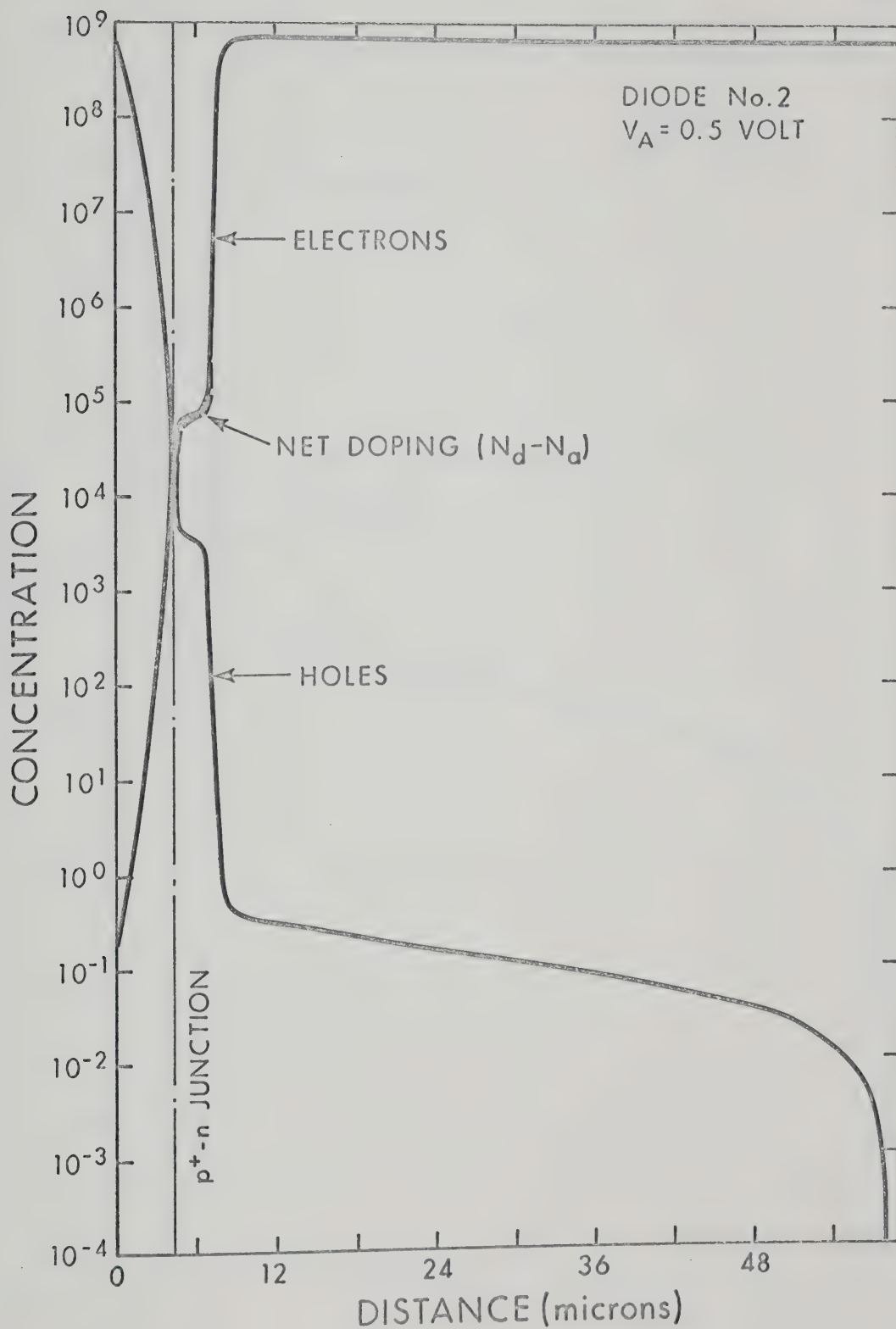


Fig. 7.8b. Spatial distribution of net doping and mobile carrier densities for diode No. 2 under steady-state conditions for $V_A = 0.5$ volt.

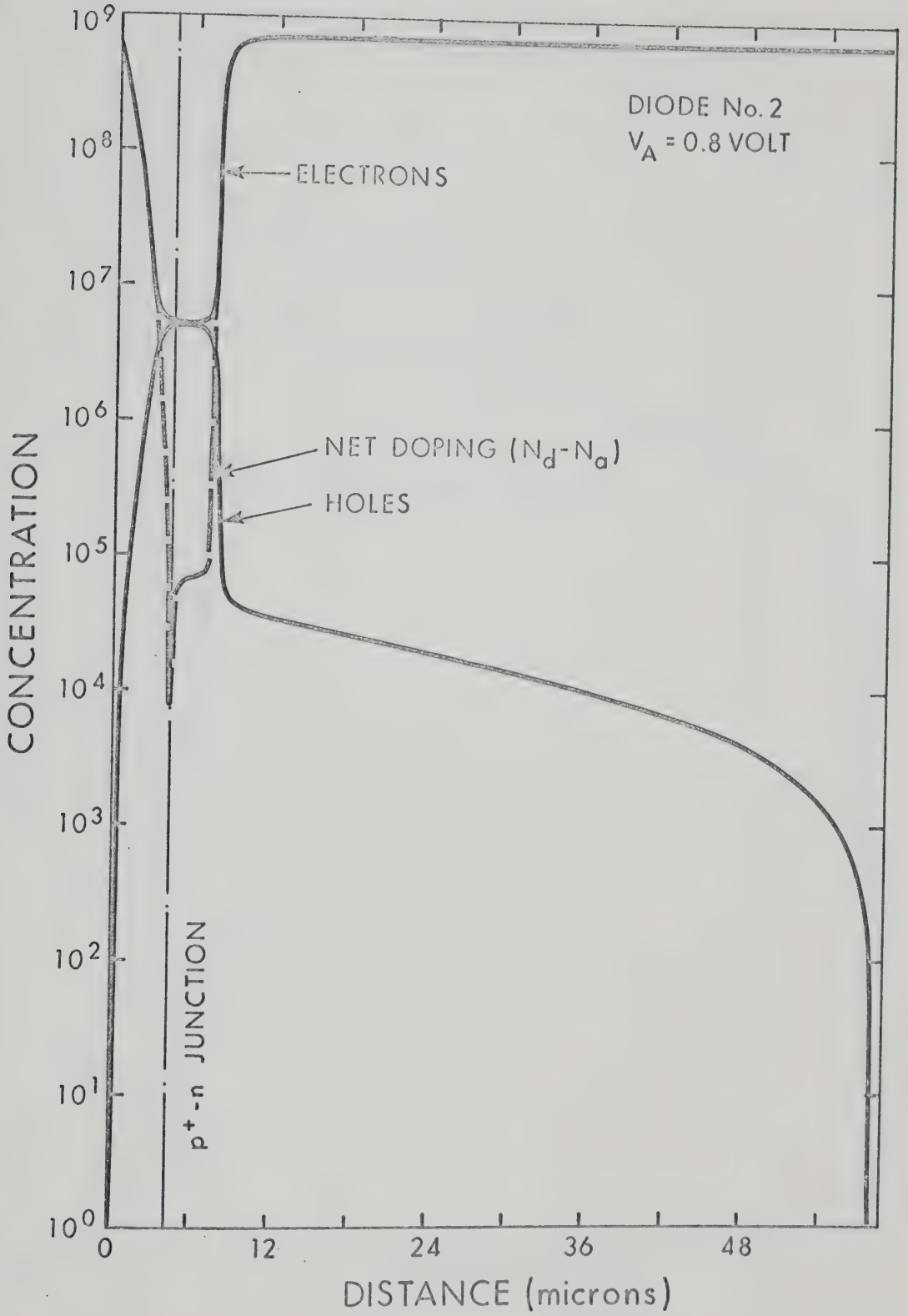


Fig. 7.8c. Spatial distribution of net doping and mobile carrier densities for diode No. 2 under steady-state conditions for $V_A = 0.8$ volt.

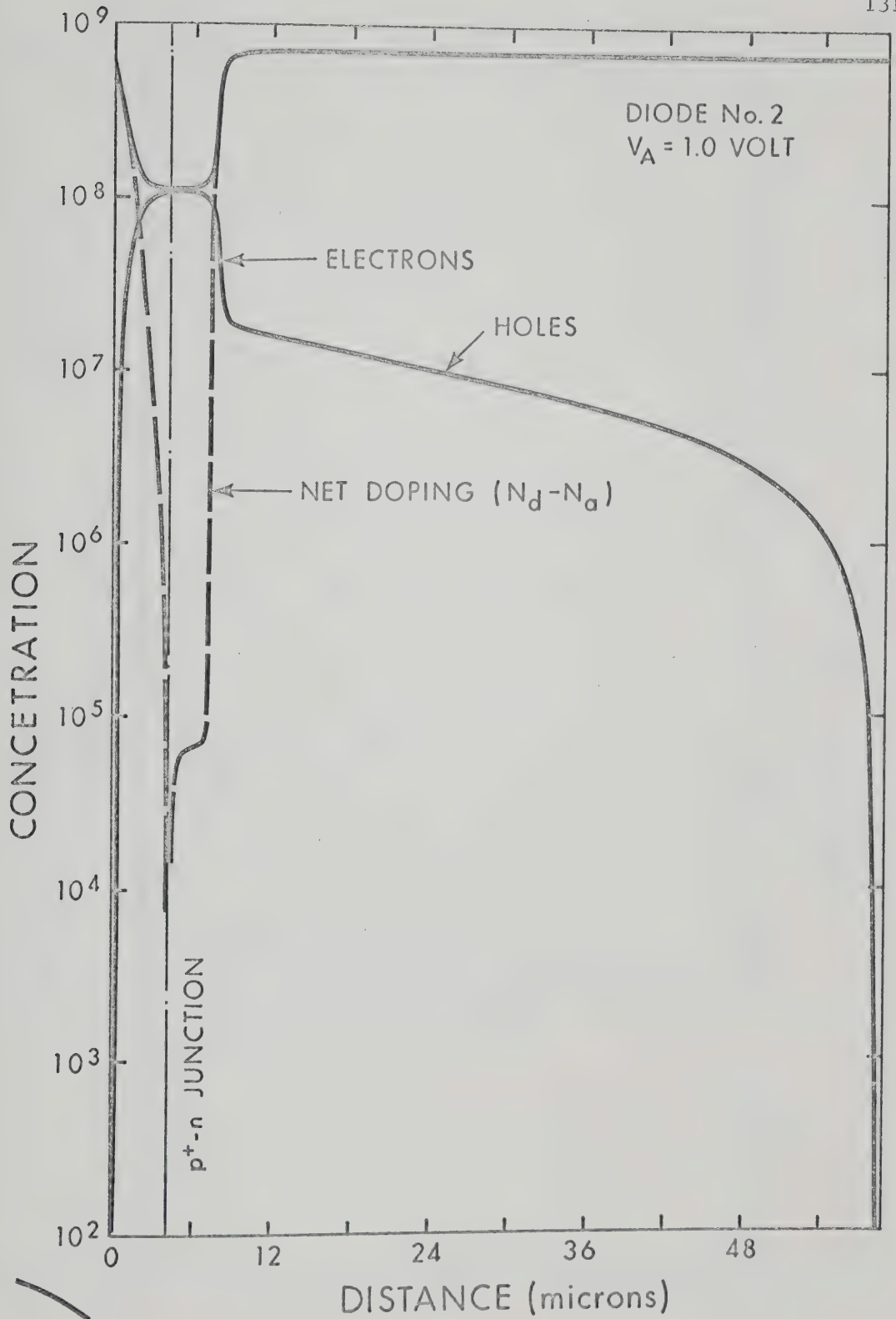


Fig. 7.8d. Spatial distribution of net doping and mobile carrier densities for diode No. 2 under steady-state conditions for $V_A = 1.0$ volt.

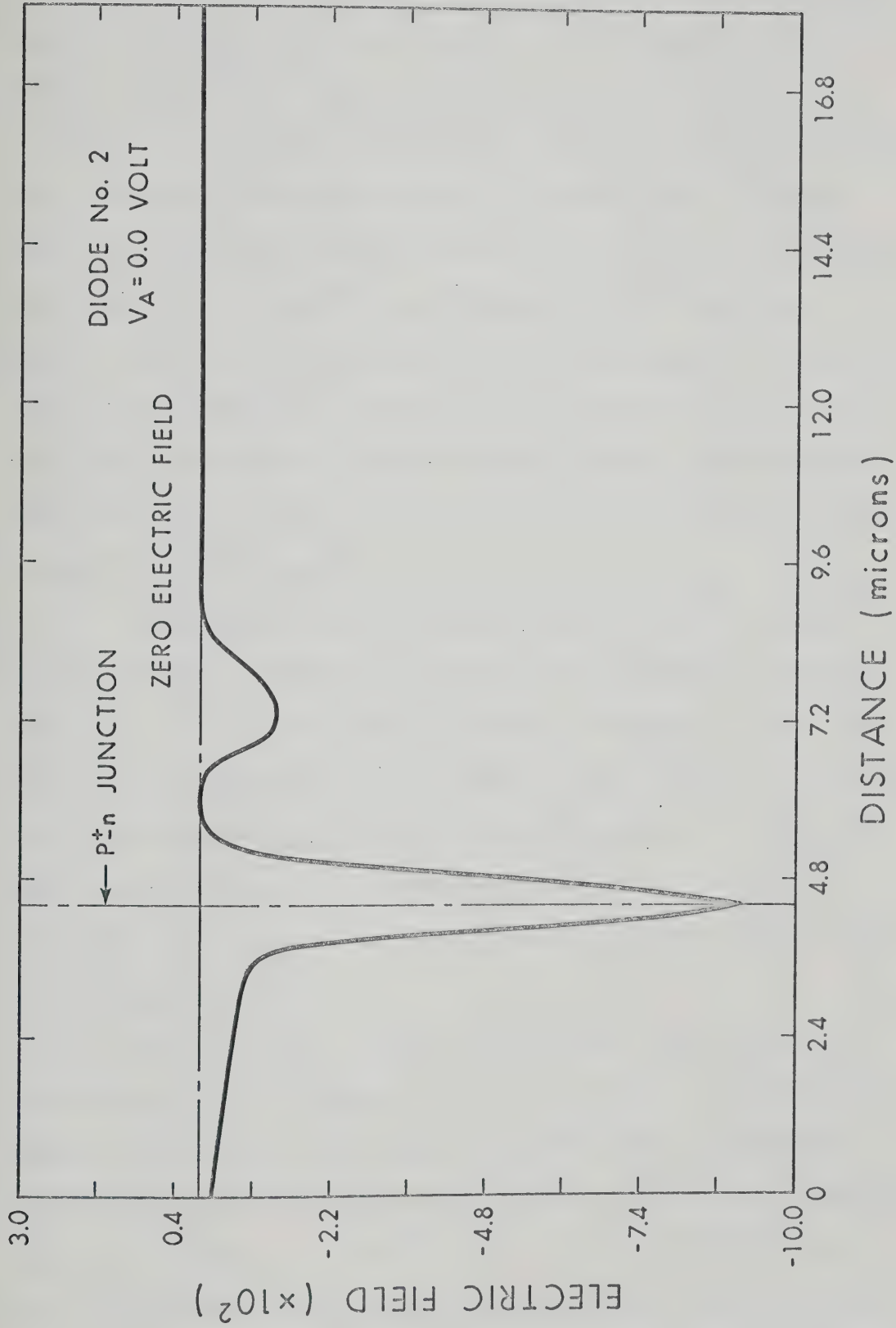


Fig. 7.9. Spatial distribution of electric field for diode No. 2 under steady-state conditions for $V_A = 0.0$ volt.

is retarded, resulting in an accumulation of injected charge in and around the n-region. This is a desirable effect since it tends to localize the injected charge in the vicinity of the junction, thus allowing it to be recovered in a shorter time when the diode is driven into reverse-bias (discussed in detail in Chapter IX). It may be pointed out that due to the presence of the electric field in a quite wide region, more energy will be dissipated in the diode during the transit times and will contribute another loss component to the total loss. The accumulation of the charge in the center n-region causes conductivity modulation, since the injected carrier concentration is much higher (of the order of 10^3 times for 1.0 volts) than the doping density ($1.0 \times 10^{15} / \text{cm}^3$).

The concentration of minority carriers near the external contacts exhibits a behaviour similar to that observed in diode No. 1. The carrier concentration near the contacts increases as the terminal voltage is increased and is much greater (of the order of 10^2 times) on the p^+ -side than on the n^+ -side. The concentration is observed to be less than that in diode No. 1, for the same current. It may be attributed to the presence of a large negative electric field, spread over a larger distance.

Figures (7.10a), (7.10b), (7.10c) and (7.10d) display the distribution of E.S. Potential, E.Q.F.L. and H.Q.F.L. throughout the interior of the device. The figure shows that the E.S. Potential distribution has a large slope (hence electric field) at the junctions between the regions of different doping. This slope (hence electric field) decreases as the forward bias is increased. Another important feature observed is the zero slope of the E.S. Potential (zero electric

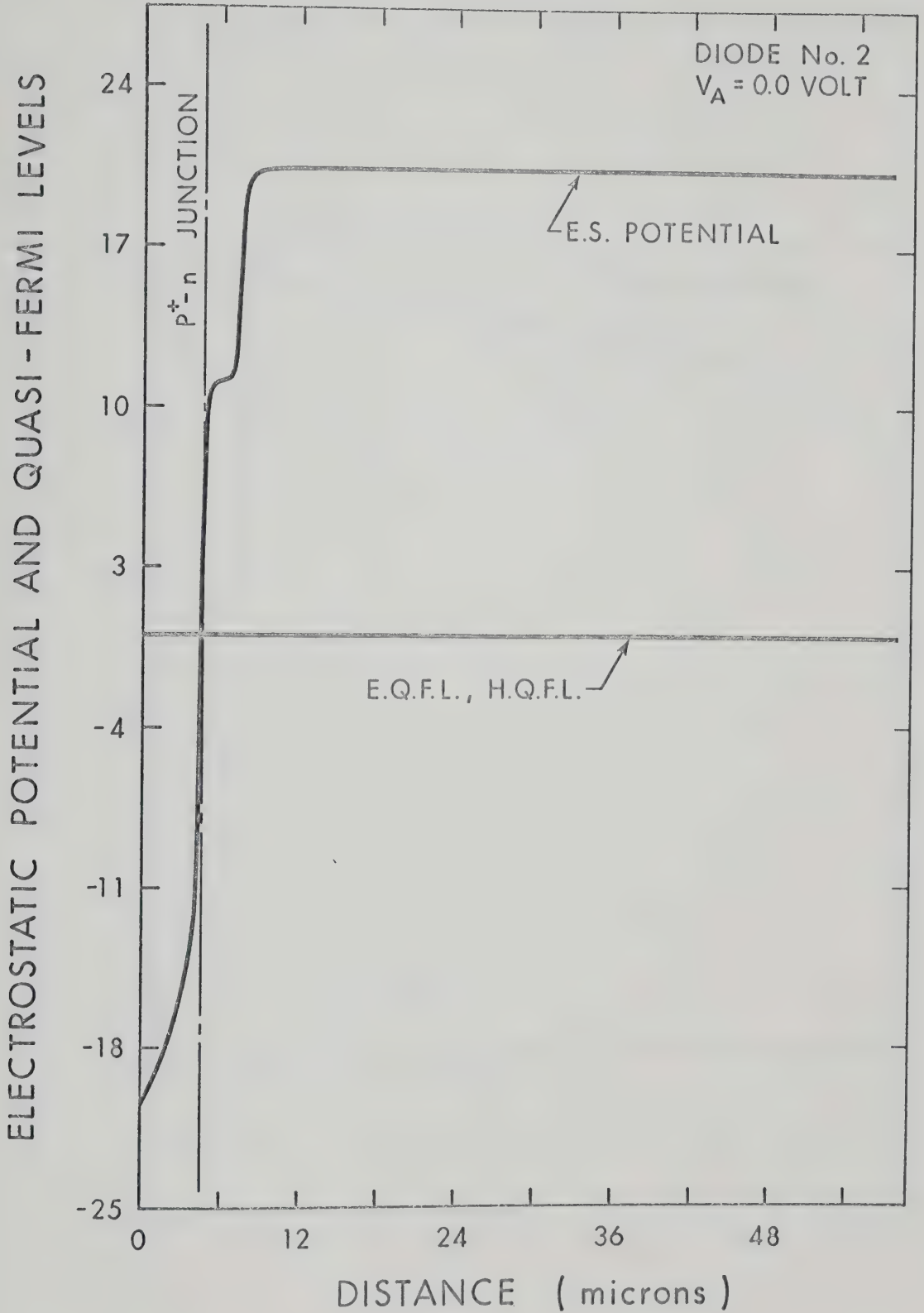


Fig. 7.10a. Spatial distribution of electrostatic potential and electron and hole quasi-Fermi levels for diode No. 2 under steady-state conditions for $V_A = 0.0$ volt.

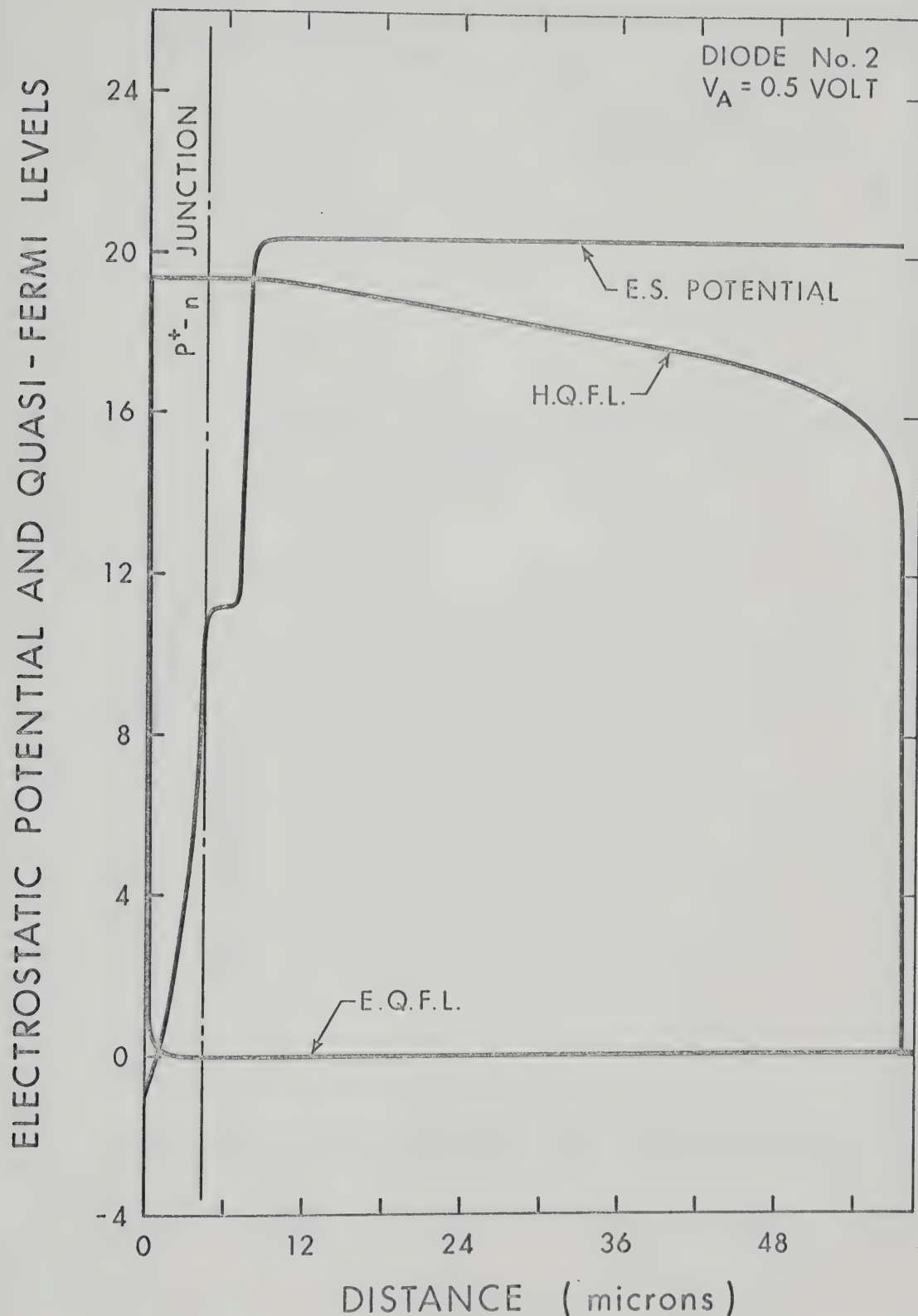


Fig. 7.10b. Spatial distribution of electrostatic potential and electron and hole quasi-Fermi levels for diode No. 2 under steady-state conditions for $V_A = 0.5$ volt.

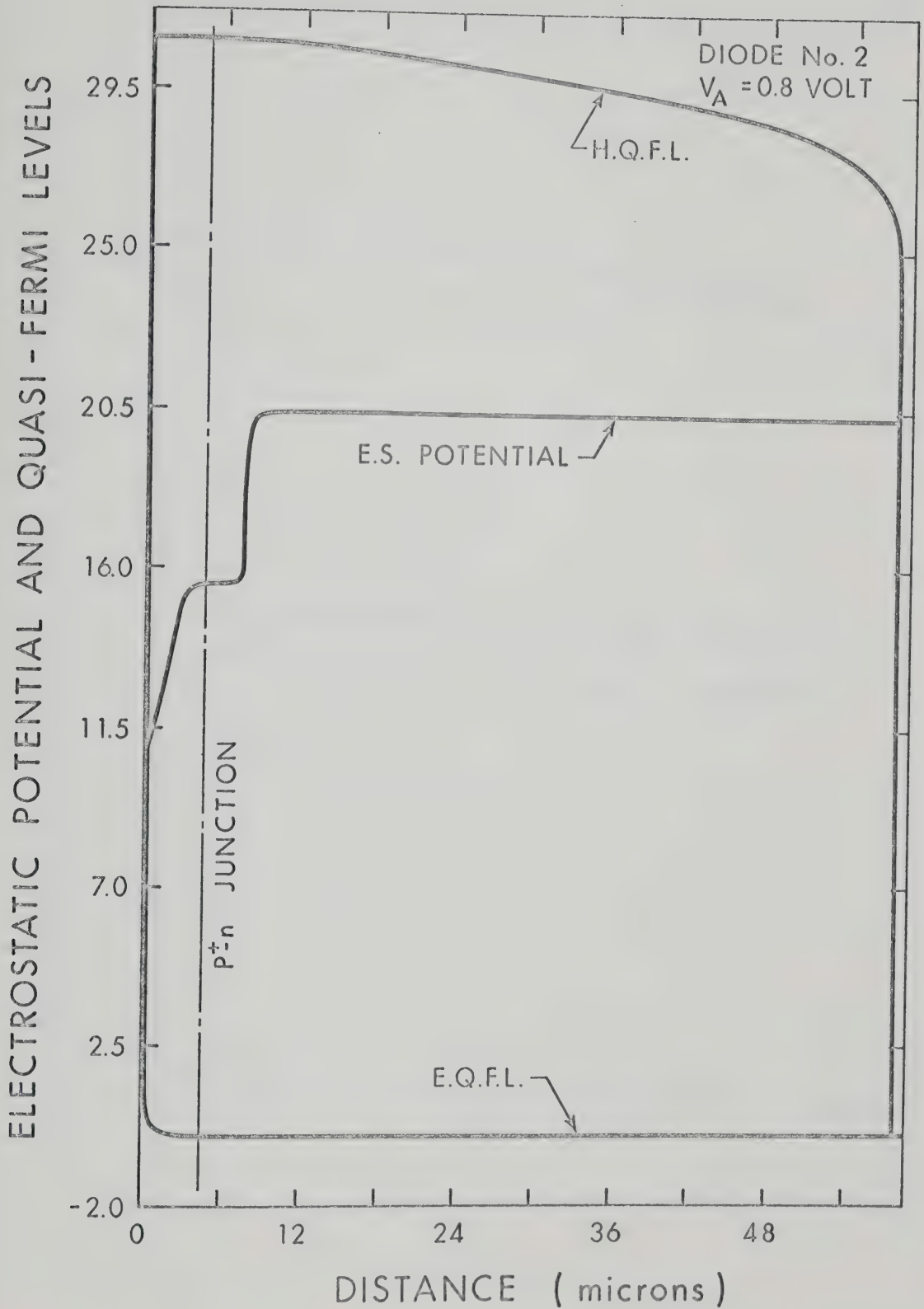


Fig. 7.10c. Spatial distribution of electrostatic potential and electron and hole quasi-Fermi levels for diode No. 2 under steady-state conditions for $V_A = 0.8$ volt.

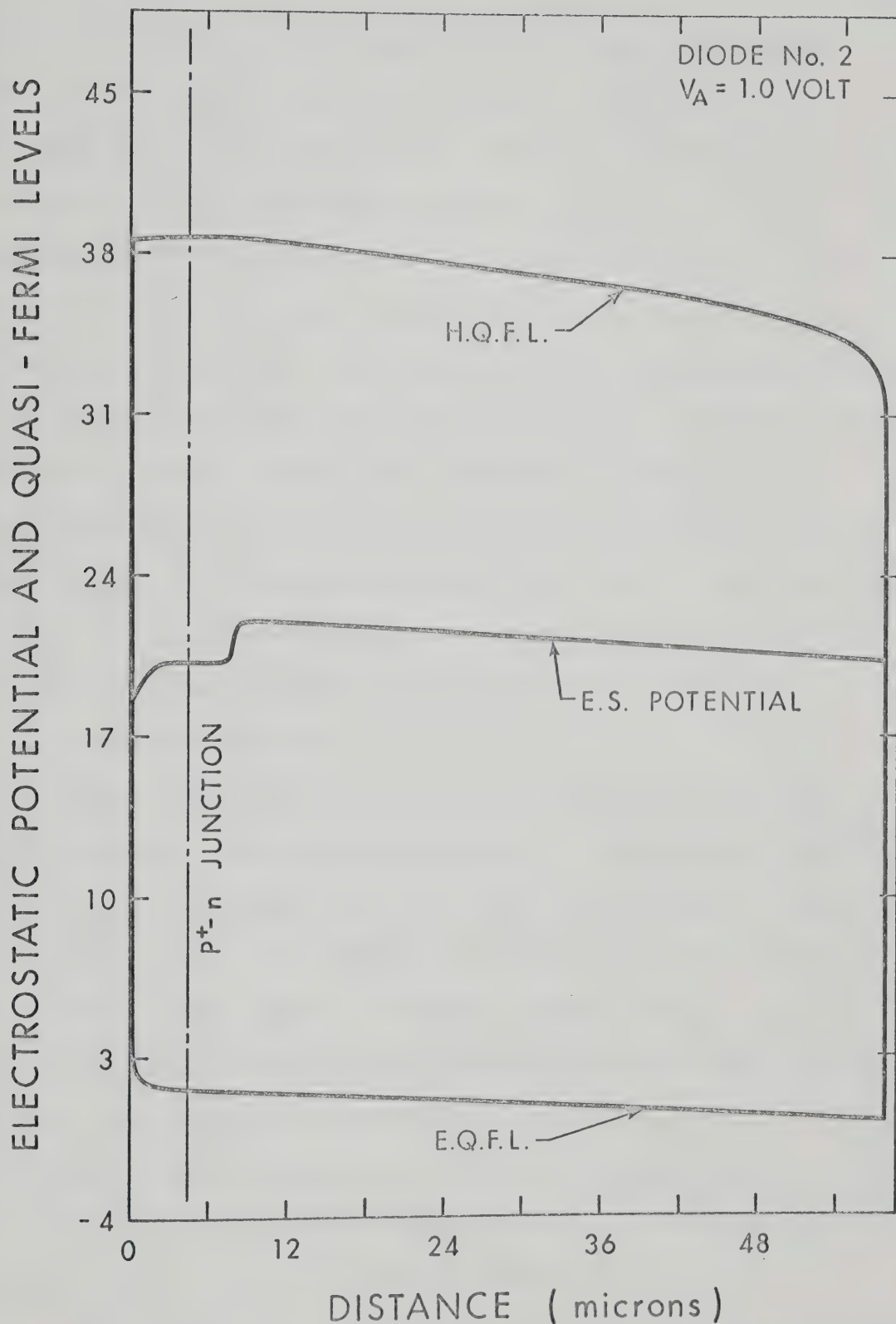


Fig. 7.10d. Spatial distribution of electrostatic potential and electron and hole quasi-Fermi levels for diode No. 2 under steady-state conditions for $V_A = 1.0$ volt.

field) in the vicinity of the center of the n-region. This charge-neutral region expands towards the p^+ -region as the forward bias is increased. If we look at Figs. (7.8a), (7.8b), (7.8c) and (7.8d), we see that the mobile charge density of both the hole and electrons injected into the n-region is equal (the doping concentration of the n-region is very low compared to that of the injected carriers), hence charge-neutrality prevails. The expansion of the central charge-neutral region towards the p^+ -region shows that the injection of the electrons becomes more and more dominant with increasing forward-bias. This argument is supported by the results for the electron and hole current distributions. At 1.0 volts forward-bias (Fig. 7.10d), a small positive electric field is present throughout the n^+ -region. Hole quasi-Fermi level also shows an appreciable slope in this region, which indicates the heavy injection of holes.

These results of the E.S. Potential, the E.Q.F.L. and H.Q.F.L. distributions expose various inconsistencies in the analytical model.^{39,56} The analytical model divides the diode into charge-neutral and space-charge regions, where space-charge is confined to the narrow layers at the junctions between regions of different doping. The E.Q.F.L. and H.Q.F.L. are assumed constant throughout both the space-charge regions. This model seems to fail at high forward-bias, where the electric field in both the n^+ - and p^+ -regions is no longer a negligible quantity, and the E.Q.F.L. and H.Q.F.L. are no longer constant in the vicinity of the junctions between regions of different doping.

The distribution of the generation-recombination rate throughout the interior of the device is plotted in Figs. (7.11a), (7.11b) and (7.11c). For low forward bias most of the recombination takes place in

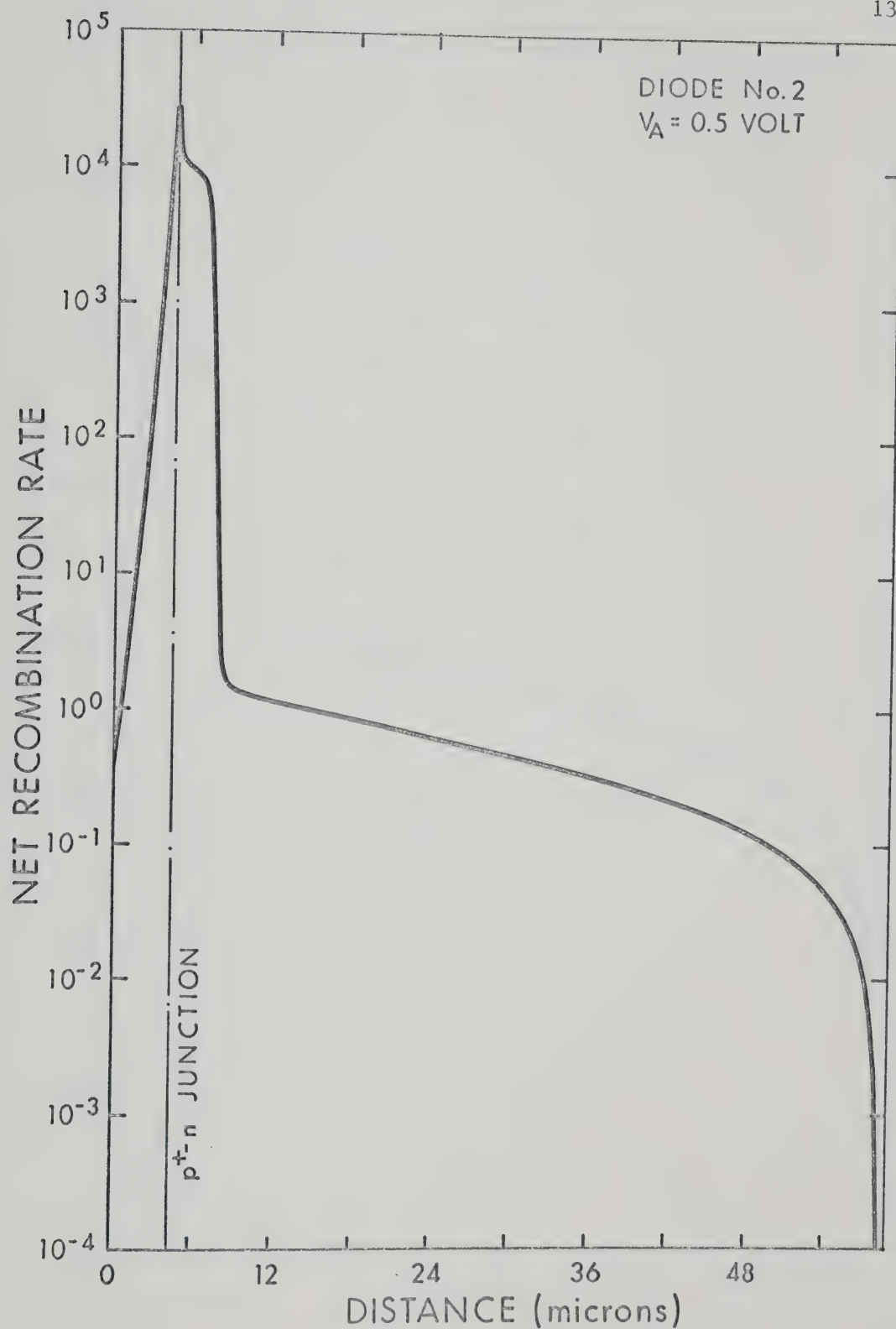


Fig. 7.11a. Spatial distribution of net recombination rate for diode No. 2 under steady-state conditions for $V_A = 0.5$ volt.

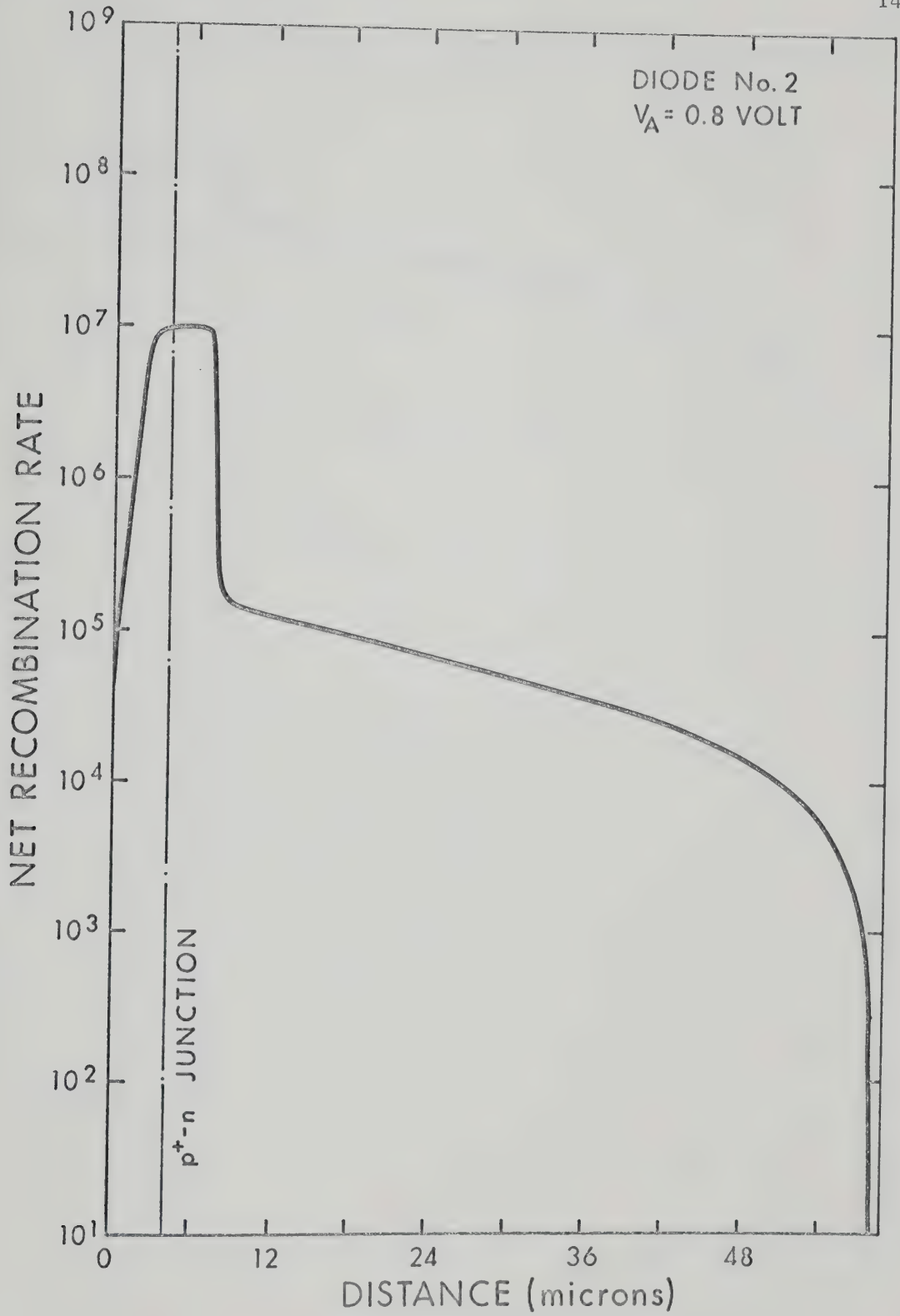


Fig. 7.11b. Spatial distribution of net recombination rate for diode No. 2 under steady-state conditions for $V_A = 0.8$ volt.

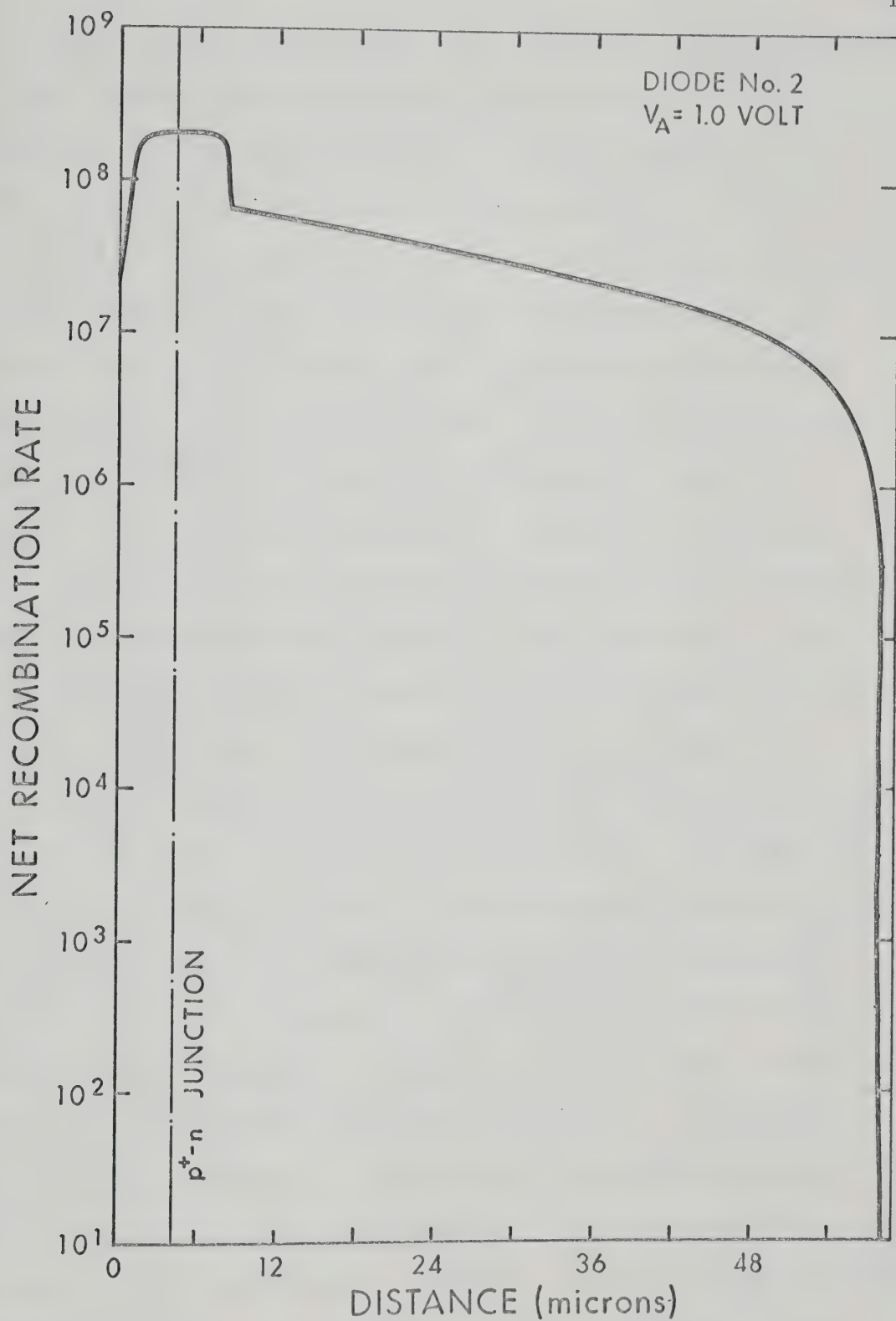


Fig. 7.11c. Spatial distribution of net recombination rate for diode No. 2 under steady-state conditions for $V_A = 1.0$ volt.

the n-region. As the forward bias is increased, the n-region is still the region having greater recombination, but the region of greater recombination expands further into the p^+ -region. Figures (7.12a), 7.12b), (7.12c) and (7.12d) display the hole and electron mobility distributions. The mobilities of both the hole and electron are about nine times greater in the n-region than in the quasi-neutral p^+ and n^+ regions. This is due to the fact that the n-region is very lightly doped compared to the p^+ - and n^+ -regions. Moreover, at low forward-biases, the high electric field at the p^+ -n junction causes the mobilities to decrease appreciably in the vicinity of the junction.

Figures (7.13a), (7.13b) and (7.13c) show the hole and electron current distribution for 0.5, 0.8 and 1.0 volts respectively. Initially, the hole and electron currents dominate the total current in the p^+ and n^+ regions, respectively. As the forward bias is increased, the electron current exhibits a marked increase in all three regions, until it becomes the major contributor of the total current throughout the diode (more than 90% at 1.0 volt). The contribution of the hole current in the p^+ -region for 0.5 V forward-bias is about 96%, decreasing to about 76% at 0.8 V. At high current densities (1.0 V forward-bias), it reduces to 5.16%. This marked decrease of the hole current contribution to the total current may be explained in the same way as explained in Section (7.2) for diode No. 1. The diffusion and drift components of the hole current are opposite in direction. As the forward bias is increased, the diffusion component increases, but as it appears that the drift components have a larger increment (holes are majority carriers in the p^+ and a small electric field is enough to give a large electric current) than the diffusion component, particularly at high forward-bias,

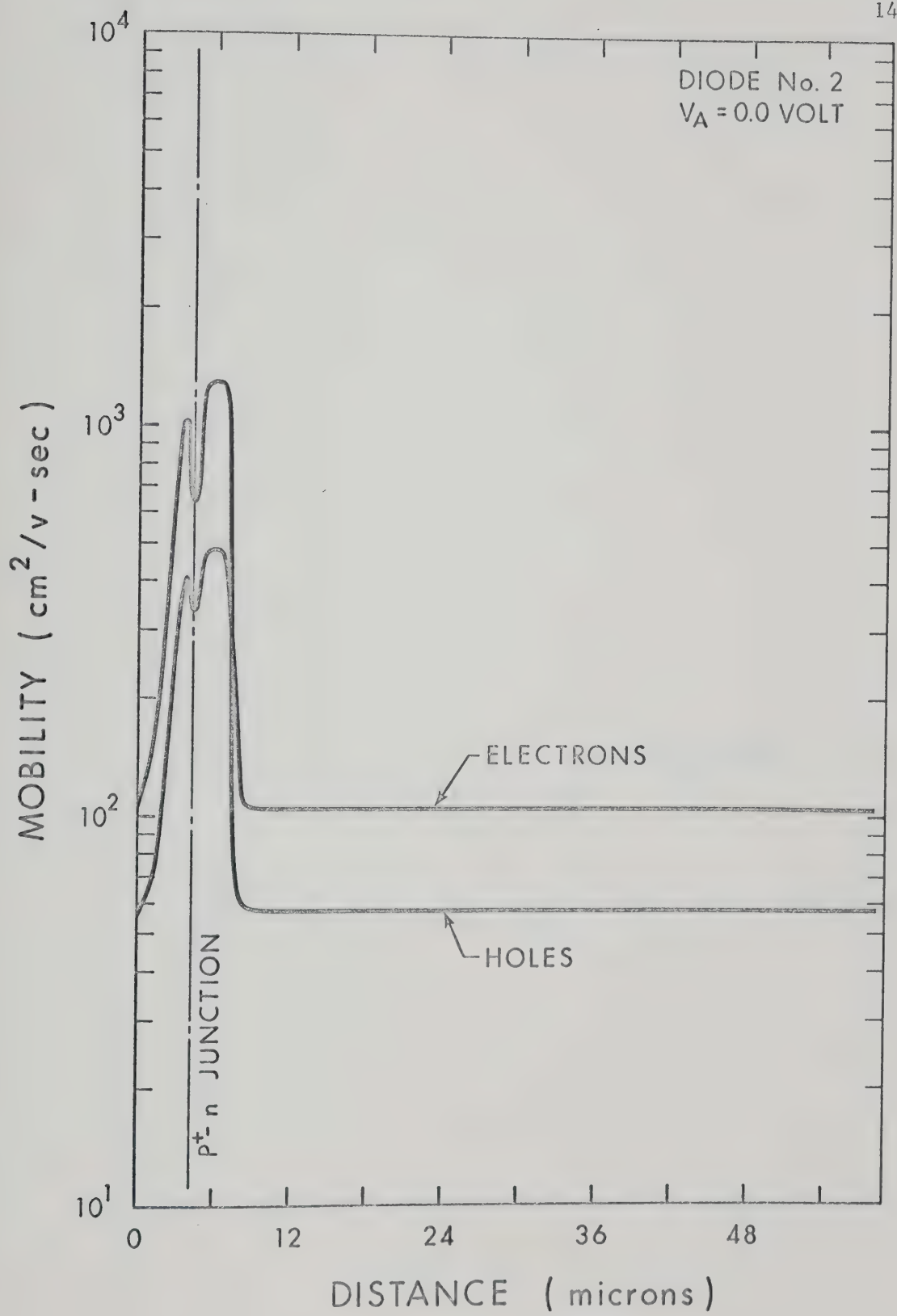


Fig. 7.12a. Spatial distribution of carrier mobilities for diode No. 2 under steady-state conditions for $V_A = 0.0$ volt.

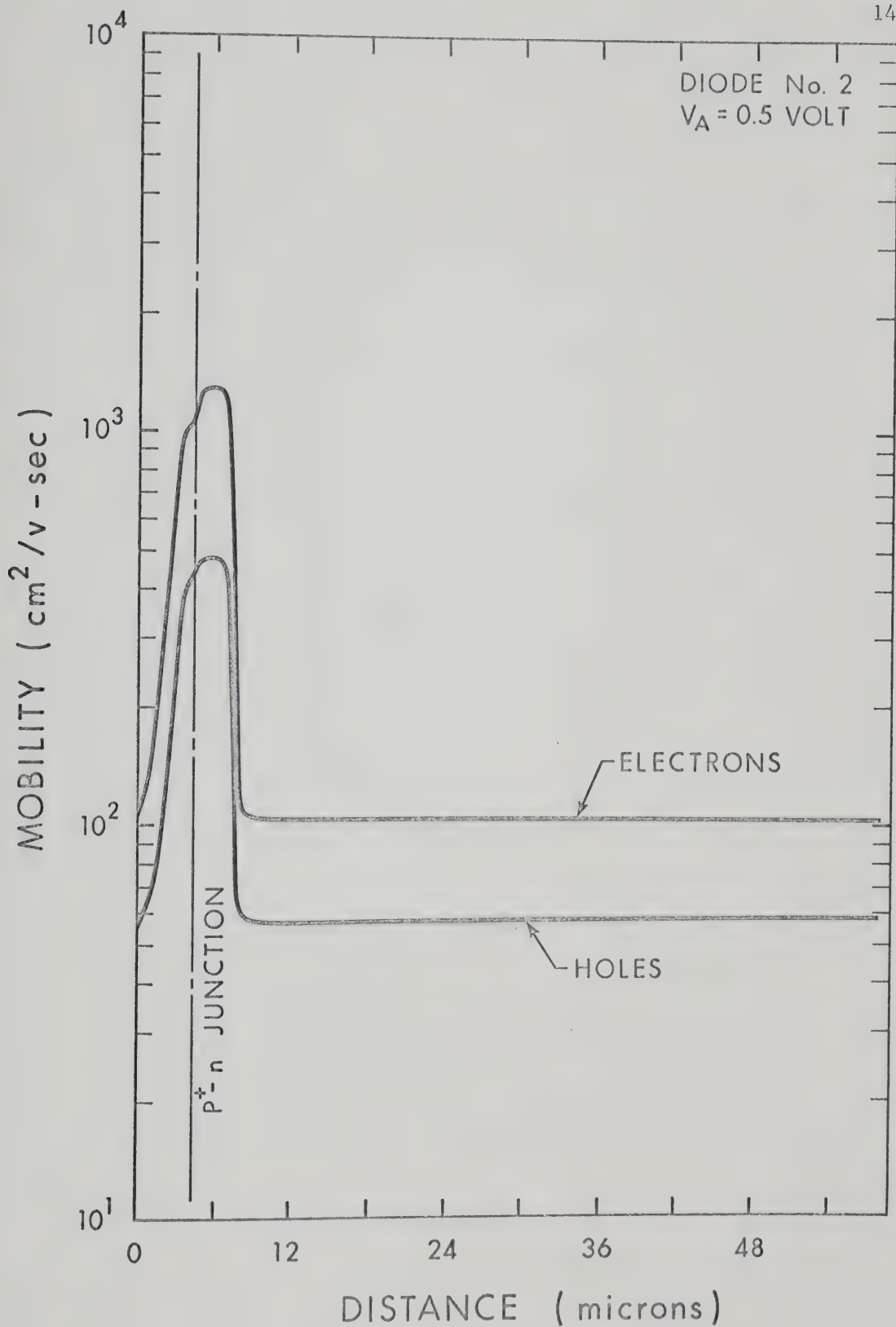


Fig. 7.12b. Spatial distribution of carrier mobilities for diode No. 2 under steady-state conditions for $V_A = 0.5$ volt.

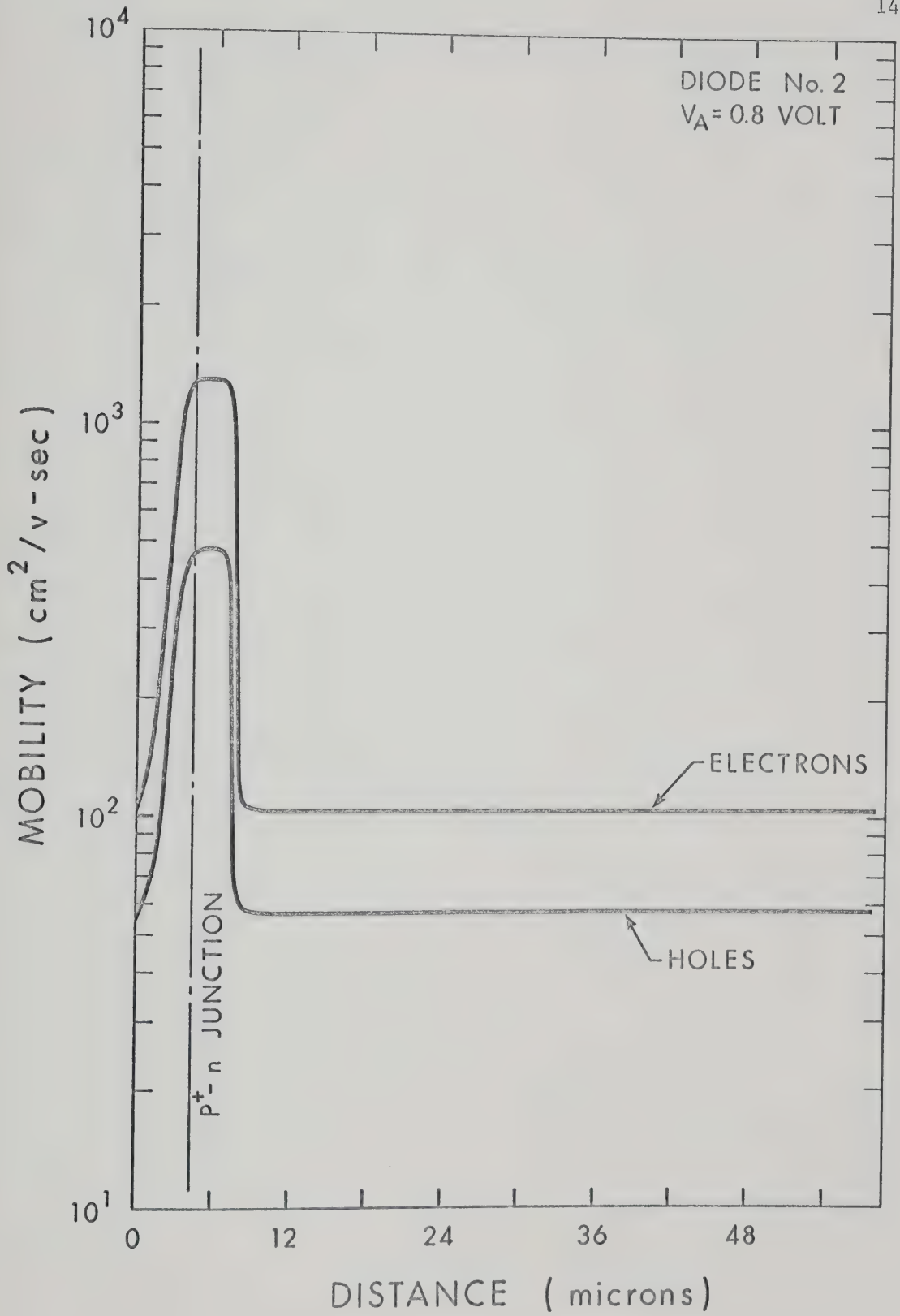


Fig. 7.12c. Spatial distribution of carrier mobilities for diode No. 2 under steady-state conditions for $V_A = 0.8$ volt.

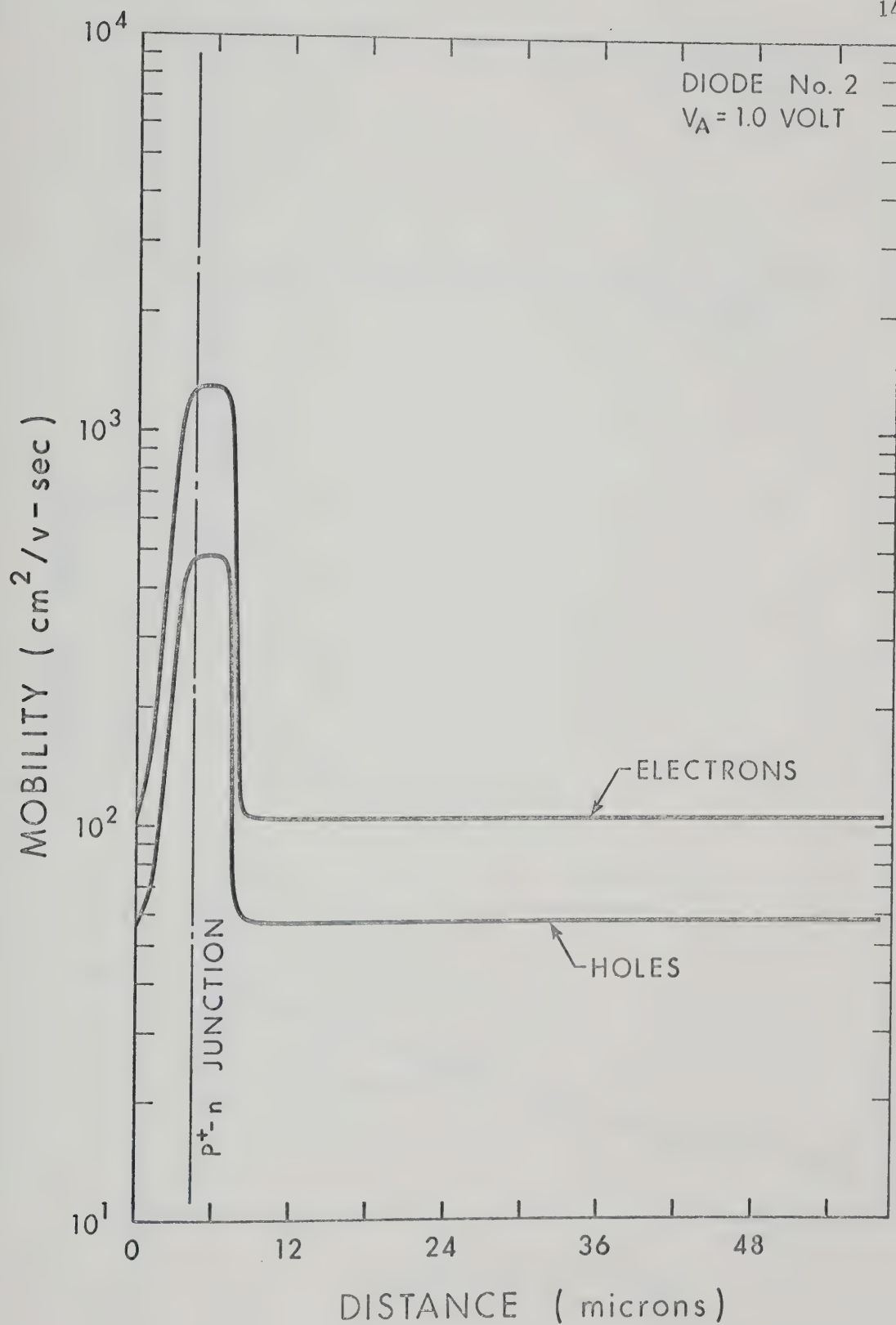


Fig. 7.12d. Spatial distribution of carrier mobilities for diode No. 2 under steady-state conditions for $V_A = 1.0$ volt.

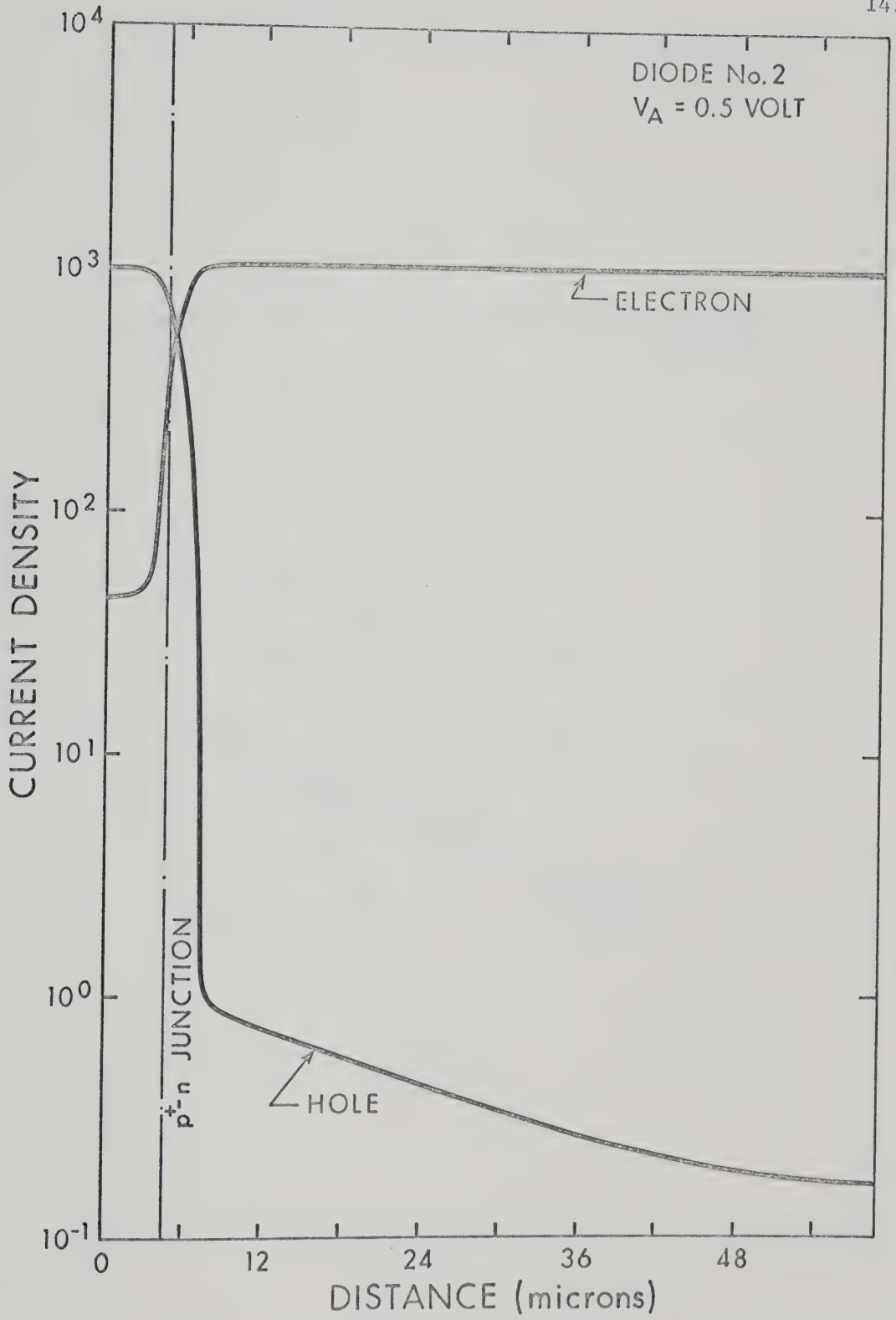


Fig. 7.13a. Spatial distribution of electron and hole currents for diode No. 2 under steady-state conditions for $V_A = 0.5$ volt.

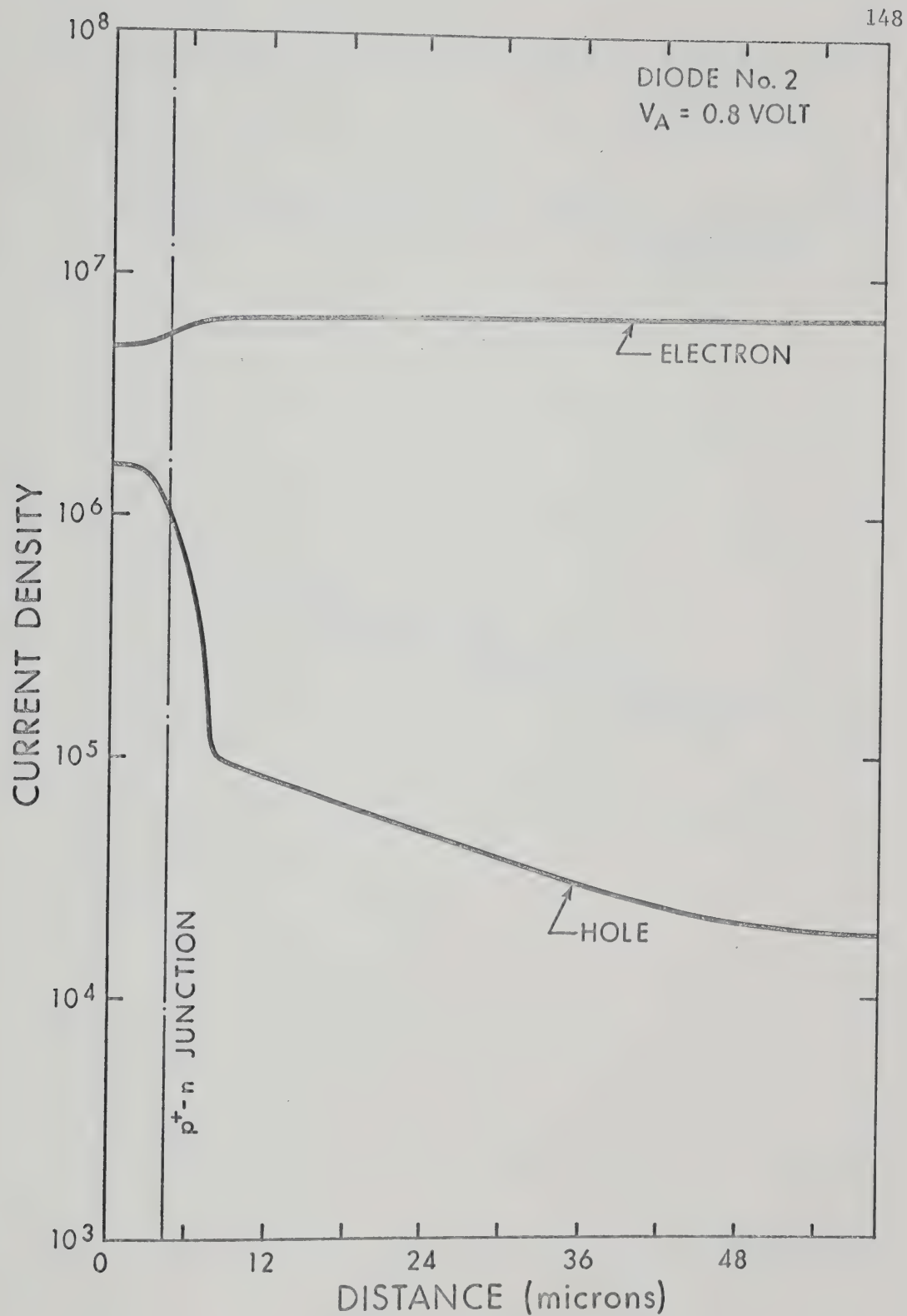


Fig. 7.13b. Spatial distribution of electron and hole currents for diode No. 2 under steady-state conditions for $V_A = 0.8$ volt.

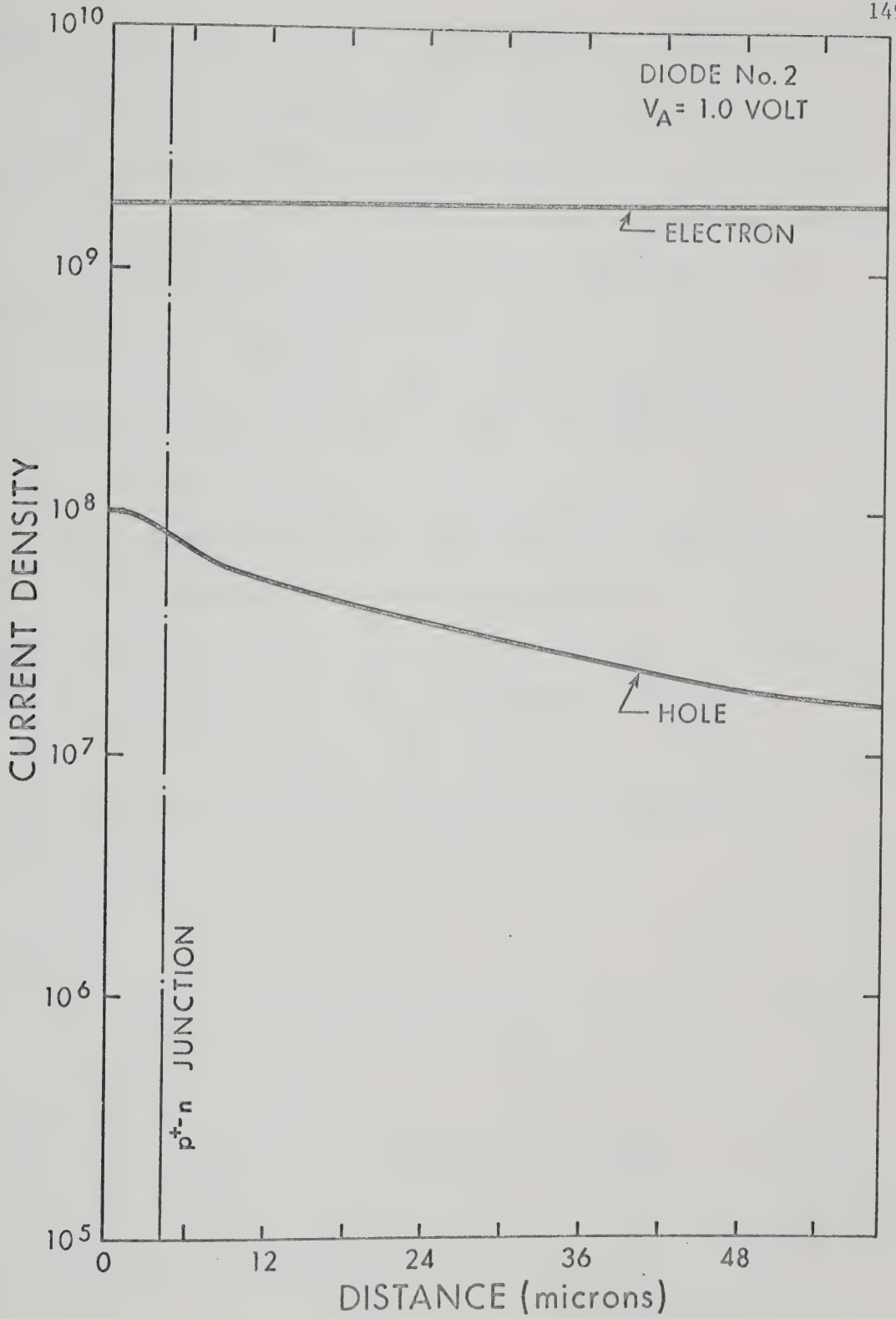


Fig. 7.13c. Spatial distribution of electron and hole currents for diode No. 2 under steady-state conditions for $V_A = 1.0$ volt.

when the electric field in the p^+ -region becomes more and more significant. It results in less and less hole current contribution to the total current as the forward-bias is increased. At low and moderate forward-biases, most of the decrease, in the hole and electron currents takes place in the central n-region. It may be attributed to the presence of high negative electric fields present at both ends of the n-region. At high forward-bias, when the space-charge regions at the junctions of the regions of different doping are partly neutralized, no such abrupt variation takes place at the ends of the n-layers.

The terminal properties of the diode, namely the terminal current and the incremental capacitance as a function of the diode terminal voltage, are plotted in Figs. (7.14) and (7.15). The value of the cut-off frequency at zero bias calculated from Eq. (7.2), is 52.6 GHz. It is to be noted that this value of the cut-off frequency is the upper limit that may be expected, since we did not include the package capacitance and contact resistance.

7.4 Synopsis

The internal and external behaviour of diode No. 1 and diode No. 2, for steady-state voltage excitation, has been presented. The results, displayed in graphical form as a function of position and of applied terminal voltage, give a thorough understanding of the devices' behaviour. A brief discussion of the results has indicated a number of interesting features and has demonstrated the usefulness of this computer simulation method in making a wealth of information available.

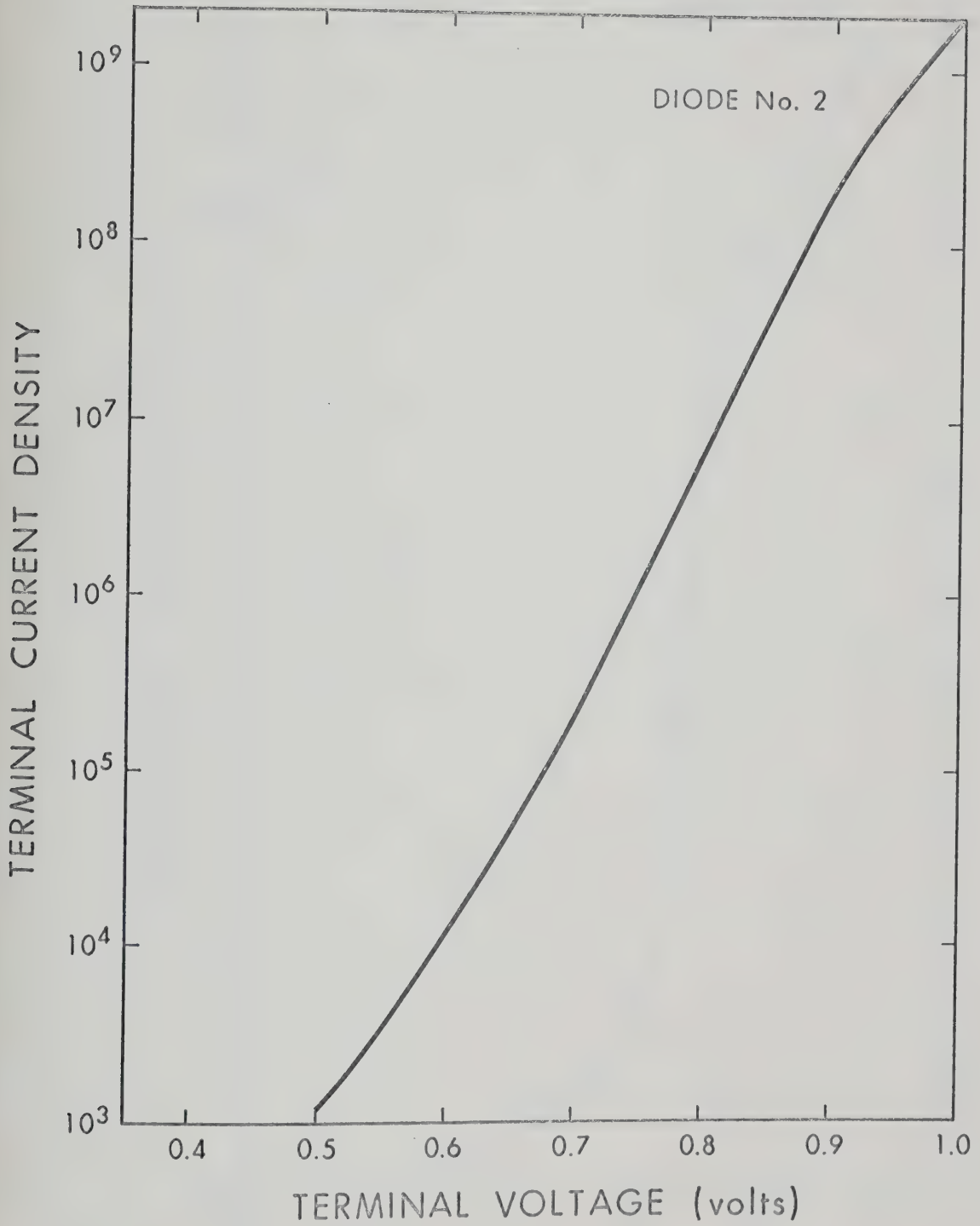


Fig. 7.14. Terminal current of diode No. 2 as a function of terminal voltage (steady-state conditions).

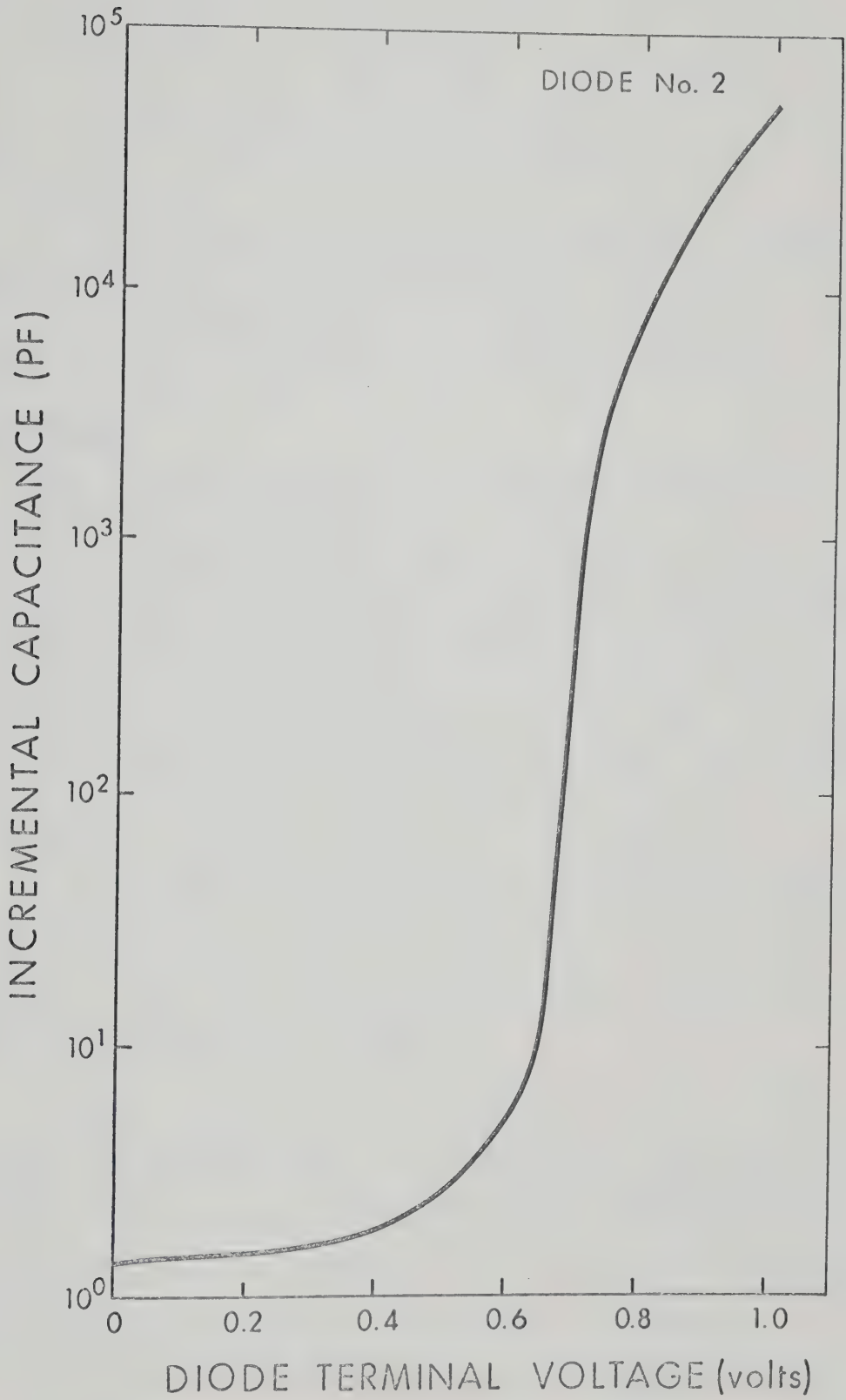


Fig. 7.15. Incremental capacitance of diode No. 2 as a function of terminal voltage (steady-state conditions).

CHAPTER VIII

LARGE-SIGNAL "TURN-ON" RESPONSE

In this chapter, the computed results for both the internal and external properties of diode No. 1 and diode No. 2, when "turned-on" by a large step of current, are presented and briefly discussed.

8.1 Introduction

When the bias of a diode is switched from either the reverse or the equilibrium state to a forward state, the behaviour of the diode under the condition is termed the "turn-on" response. From the point of view of charge-storage behaviour, this phenomenon is important. Unless a sufficient amount of charge is injected and stored during the forward part of the a.c. cycle, efficient use of the device as a step-recovery diode, inspite of a very fast recovery process, is impaired.

It is the purpose of this chapter to examine in detail and to explain quantitatively the forward transient behaviour of diode No. 1 and diode No. 2, which are taken to represent the two distinct kinds of varactor diodes as discussed in Chapter II.

A number of workers have studied this problem for a highly asymmetrical step junction diode.⁸ The reported characteristics serve as the guideline in this chapter, though our case is "doubly-injecting" and both carriers are to be considered. The two important results which are reported in the literature may be summarised as follows:

(1) The initial condition of the diode, either in the reverse state or in thermal equilibrium, has little effect on the observed

forward transient behaviour. But, if the diode is initially biased slightly in the forward direction, the maximum deviation between the initial value and the final value (voltage or current) can be greatly reduced;

(2) The diode forward transient is considered to consist of two components; one behaves in a manner similar to an inductive circuit, and the second in a manner similar to a capacitive circuit. For large currents, the inductive character dominates, while for small currents, it is the capacitive behaviour that dominates. Between these two extremes the transient exhibits an oscillatory behaviour.

The case discussed in this chapter is the behaviour of the diodes when a large step of current is suddenly applied across the diode terminals. All the results are plotted in normalised units, unless otherwise specified. (See Table 4.1)

8.2 Results for Diode No. 1

A current step having a value

$$J_t = 0 \quad t \leq 0$$

$$J_t = 0.16 \times 10^9 \quad t > 0$$

is applied directly to the terminals of diode No. 1, initially in thermal equilibrium condition. This value of current corresponds to 1.0 volts forward bias under steady-state conditions. The overall terminal voltage response is shown in Fig. (8.1). Figure (8.2) displays the response for the initial part of the transient. It is governed by the ohmic drop build-up and the charging of the depletion layer capacitance. The build-

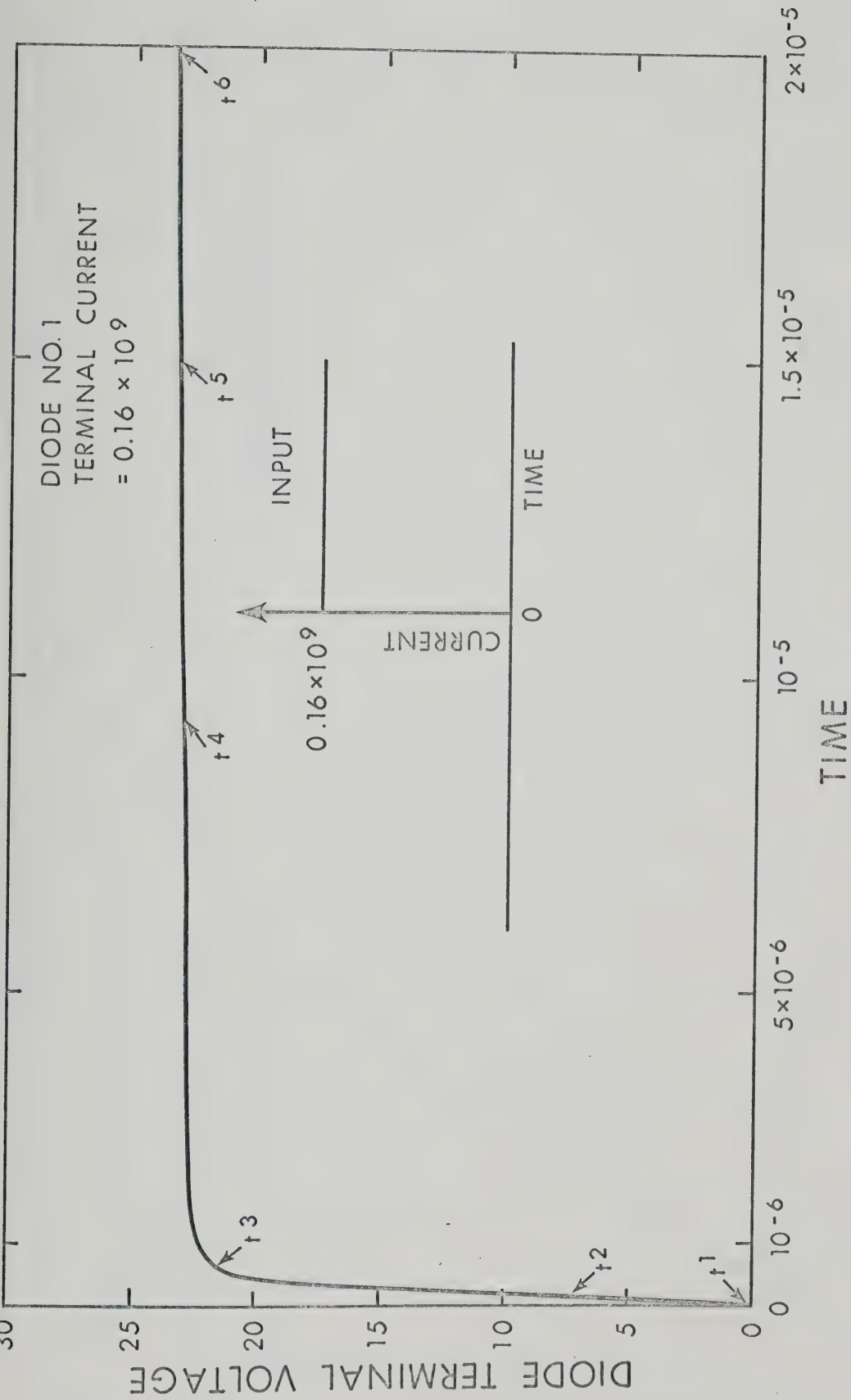


Fig. 8.1. Turn-on voltage response of diode No. 1 for a large current step.

SHORT TIMES
DIODE NO. 1
TERMINAL CURRENT
 $= 0.16 \times 10^9$

DIODE TERMINAL VOLTAGE

TIME

0 10^{-8} 5×10^{-8} 10^{-7} 1.5×10^{-7} 2.0×10^{-7}

Fig. 8.2. Turn-on voltage response of diode No. 1 for the initial phase of the turn-on transient.

up of the ohmic drop takes place in a time of the order of two times the dielectric relaxation time (1.1×10^{-16} sec. for the substrate having 0.4×10^{-3} ohm-cm. resistivity). Since the resistivity is so low, the ohmic-drop build-up is very small and very fast. Therefore, its influence on the overall transient is insignificant.

The overall transient may be taken to consist of two components: the junction voltage transient and the diode resistance transient. The former increases with time and the latter decreases with time. In our case, charging of the depletion layer capacitance in the initial stages and of the diffusion capacitance at later times dominate the overall transient response. The conductivity modulation which results in a decrease in the diode resistance has little effect even at latter times when a large number of the minority-carriers have been injected across the junction. It is due to the facts that this diode is very heavily doped and for any conductivity modulation to take place, the injected carrier density is to be comparable to the majority-carrier concentrations.

Figure (8.3) displays the electric field distribution for various time instants during the evolution of the transient. Figures (8.4) and (8.5) display the electron and hole density distributions for several time instants (the same as chosen for the display of the electric field) during the evolution of the transient. As is obvious from Fig. (8.3), the displacement current which is initially the major current component throughout the diode, becomes negligible in the quasi-neutral regions within a short time of the order of $2 \times T_{rn}^+$ (T_{rn}^+ is the dielectric relaxation time of the n^+ -region), but is still significant in the transition layer. However, it gradually decreases even in the

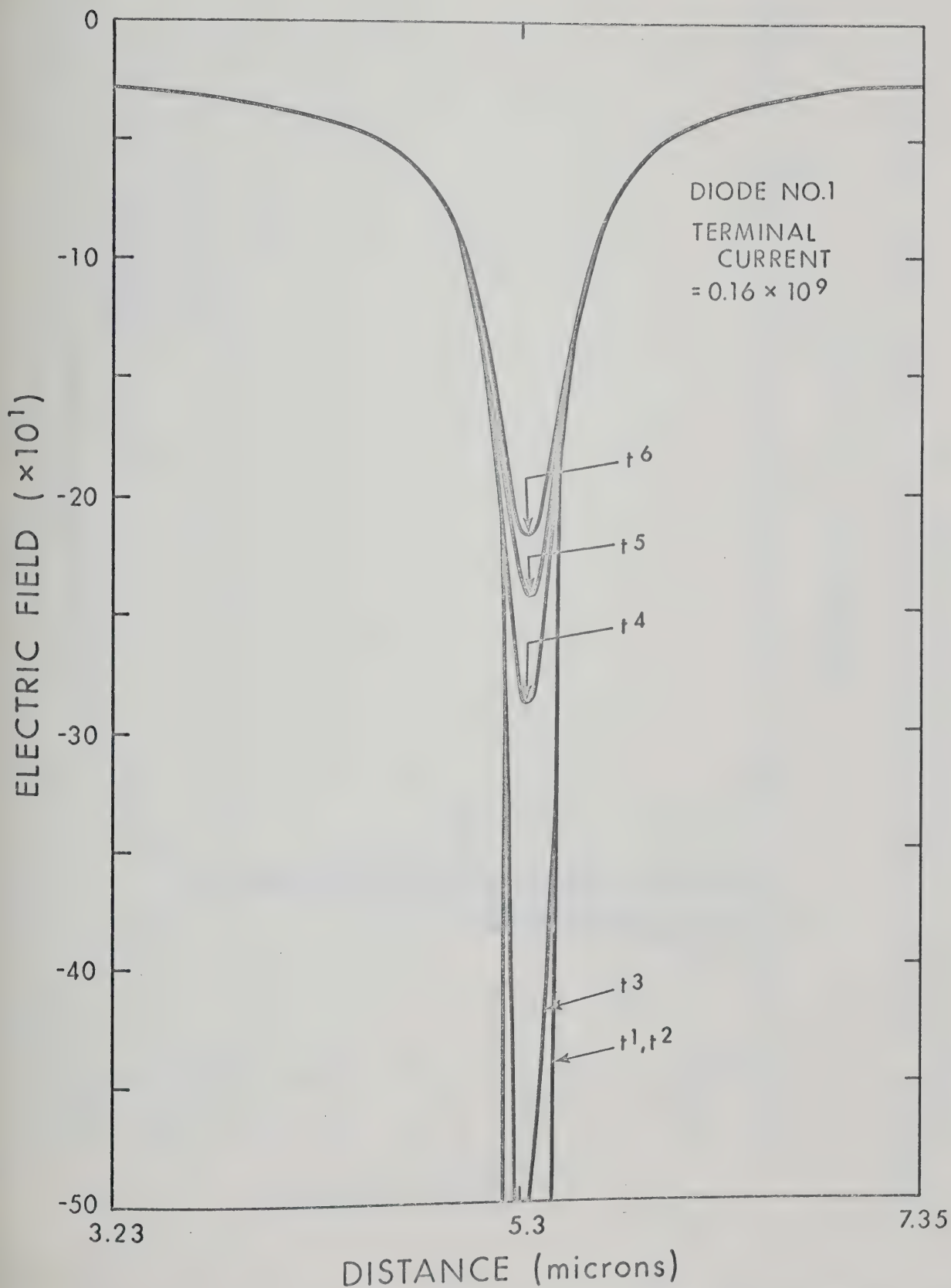


Fig. 8.3. Evolution of the electric field distribution in diode No. 1 during the turn-on transient (values of time instants indicated in Fig. 8.1).

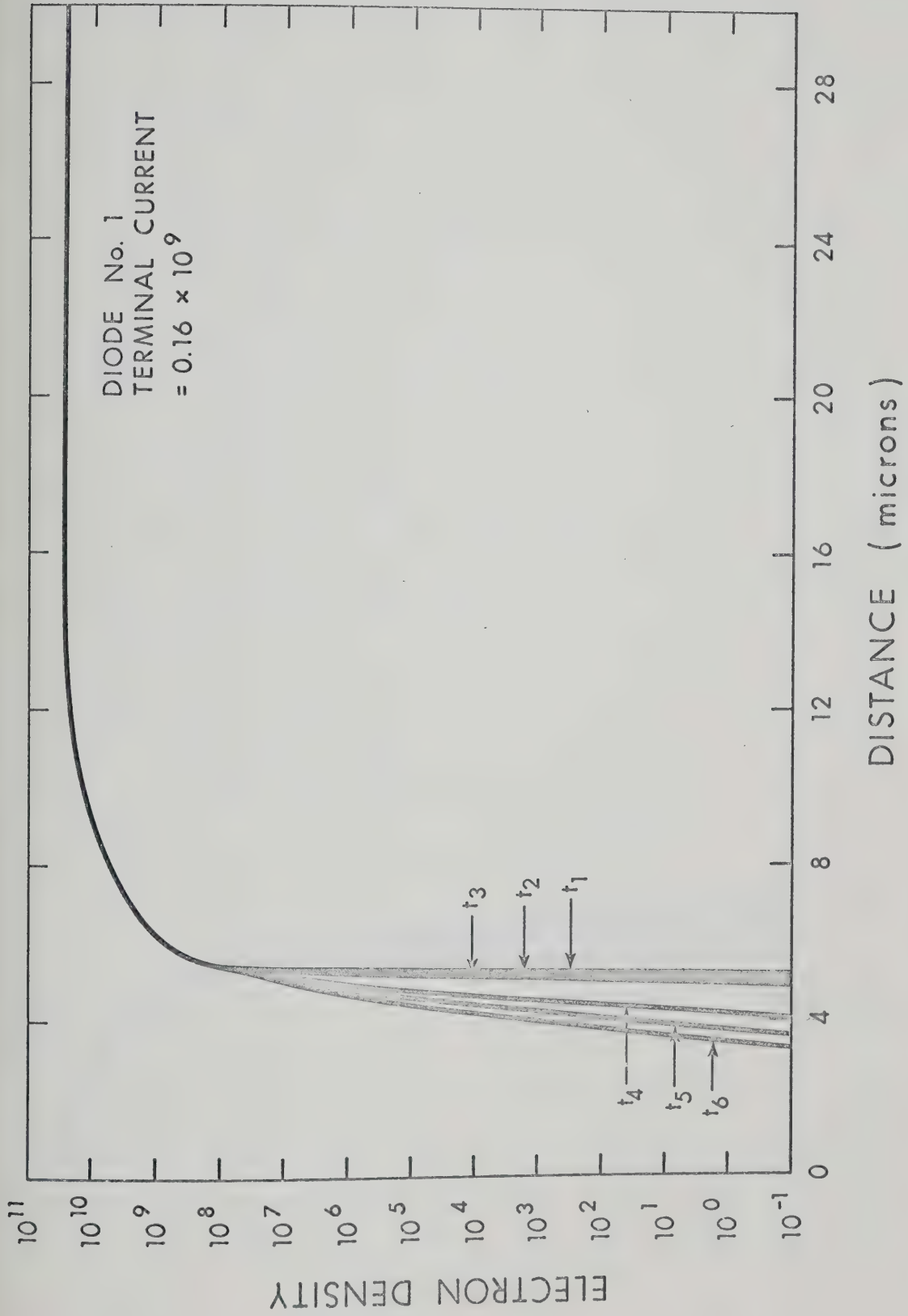


Fig. 8.4. Evolution of the electron density distribution in diode No. 1 during the turn-on transient (values of time instants indicated in Fig. 8.1).

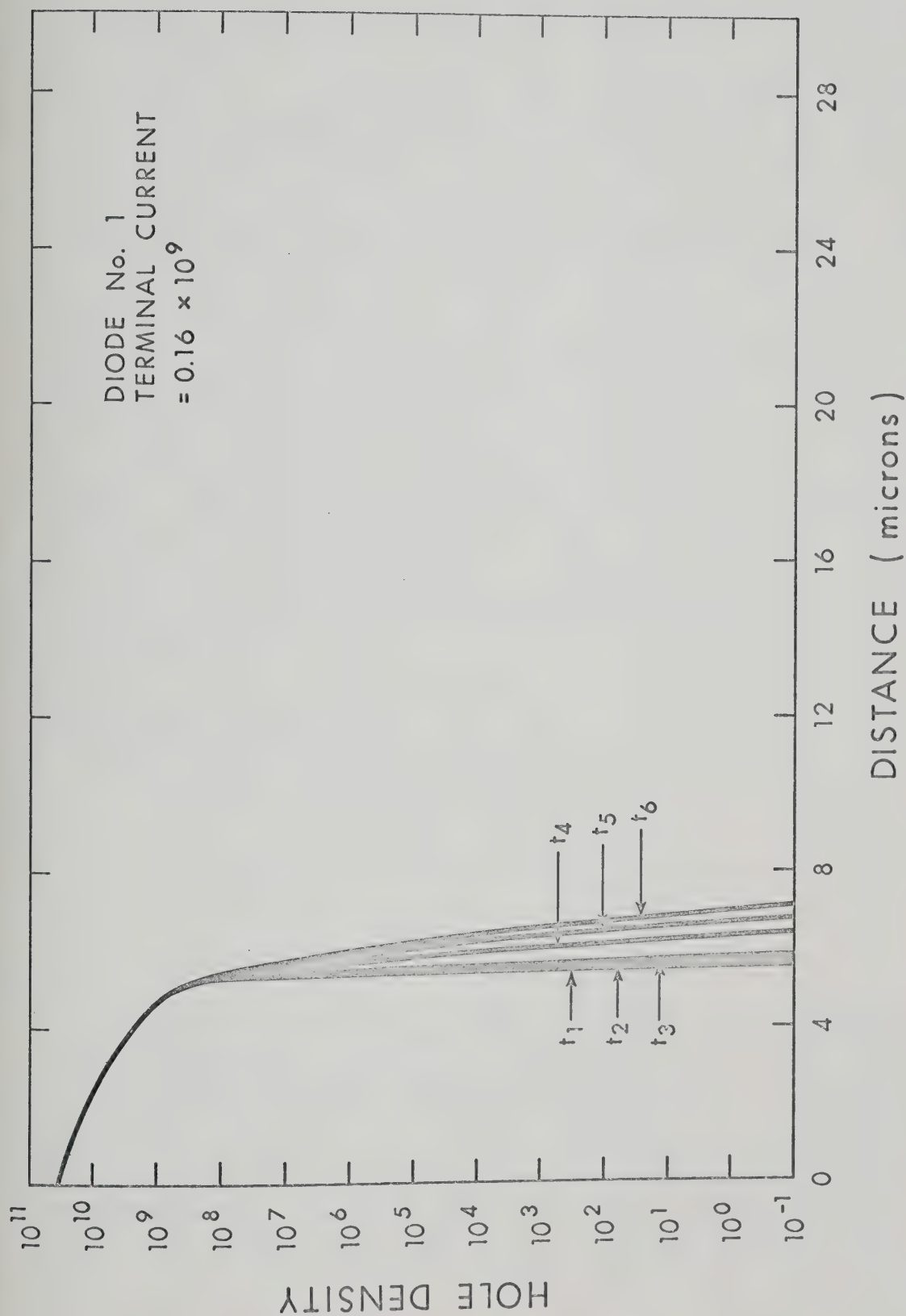


Fig. 8.5. Evolution of the hole density distribution in diode No. 1 during the turn-on transient (values of time instants indicated in Fig. 8.1).

transition layer towards its steady-state value of zero as the transient evolves in time. At this stage the transient is governed by the motion of the minority-carriers, and hence becomes slow in time. The diode will approach the steady-state conditions with a time constant of the order of the transit time of the holes in the substrate ($\approx 1.25 \times 10^{-6}$ sec.).

Figure (8.6) displays the ratio of the hole charge injected across the junction into the n-region to the holes stored in the n-region under the steady-state conditions for the same terminal current. It is to be noted that less than 5% of the charge is injected in a time of 2×10^{-5} . This time is comparable to the time period of a 4 GHz. signal. Moreover, this ratio will approach its final value of 1.0 with a time constant of the order of the transit time of the holes in the n-region ($\approx 1.5 \times 10^{-6}$ sec.).

8.3 Results for Diode No. 2

A current step having a value

$$J_t = 0 \quad t \leq 0$$

$$J_t = 0.75 \times 10^9 \quad t > 0$$

is applied directly to the diode. The diode is assumed to be in the thermal equilibrium before the current step is applied. The value of the current corresponds to 0.915 volts forward-bias under the steady-state conditions. The overall voltage response is displayed in Fig. (8.7). There is a overshoot present in the voltage response. The initial part of the transient ($t < 1.1 \times 10^{-11}$ sec.) mainly represents the build-up of ohmic drop in the quasi-neutral regions of the diode and

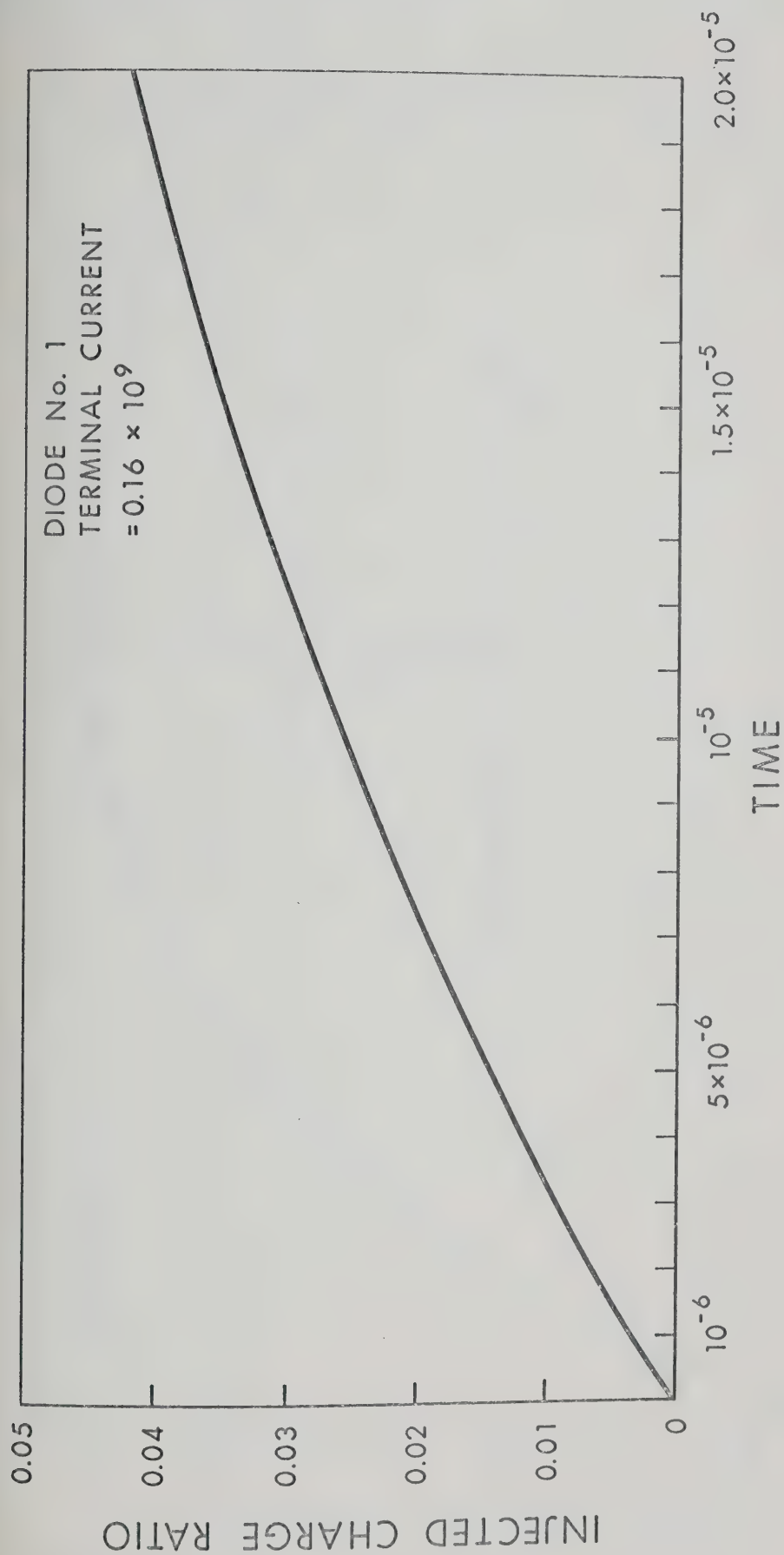


Fig. 8.6. Injected hole charge ratio as a function of time during the turn-on transient for diode No. 1.

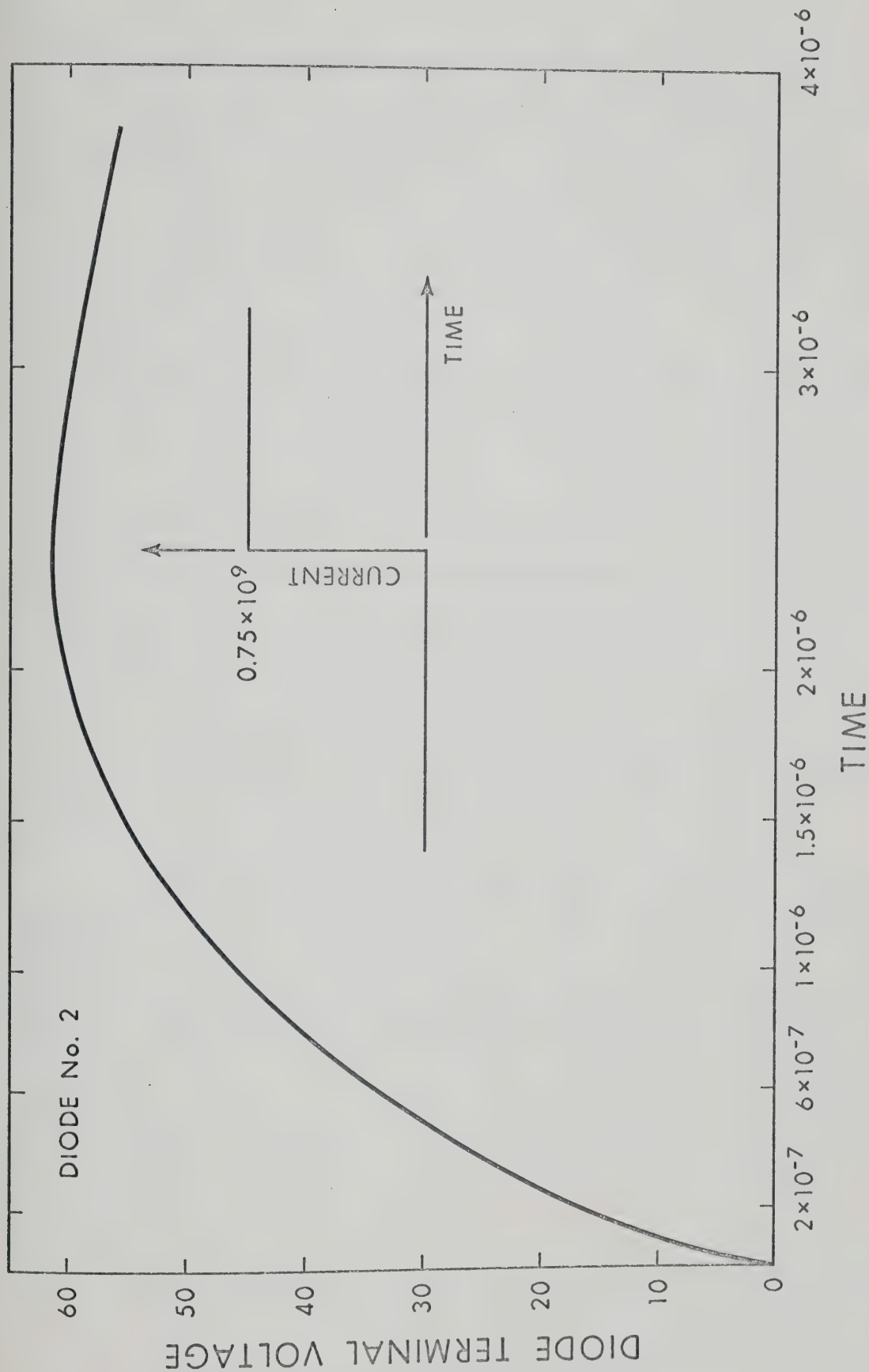


Fig. 8.7. Turn-on voltage response of diode No. 2 for a large current step.

the charging of the transition region capacitance. This phenomenon is ruled by dielectric relaxation properties of the high-resistivity region, and occurs within a period approximately equal to the dielectric relaxation time. T_{rn} , as a consequence of the dielectric relaxation times of the surrounding low resistivity regions (p^+ and n^+) are very small compared to T_{rn} . At later times (particularly $t > 0.24 \times 10^{-5}$), the conductivity modulation effects, comparatively small in the initial part of the response, are dominant, so that the diode terminal voltage decays to its final steady-state value. This decay is mainly governed by the conductivity modulation of the high-resistivity n-region, since in the substrate, the effect is far less because of its initial lower-resistivity and the fact that the injected carriers have to pass through the n-region before they reach the n^+ -region. Thus the time constant of the decay is essentially given by the transit time of the holes in the n-region ($\approx 6.0 \times 10^{-5}$)*. Note that the transit time for electrons is smaller due to their higher mobility. (≈ 2 times that of holes)

Figures (8.9) and (8.10) display the hole and electron densities during the evolution of the transient. In Figs. (8.11a) and (8.11b), the electric field as a function of distance is plotted for various instants of time. Figures (8.12a) and (8.12b) give the displacement current as a function of distance for various instants of time during the evolution of the transient. The electron drift current component in the n^+ -region as a function of distance is displayed in Fig. (8.13) for various

* This estimation is made from the expression $T_t = \frac{W^2}{4D_p}$, where W is the estimated width of the n-region and D_p is the average diffusion constant of holes in this region.

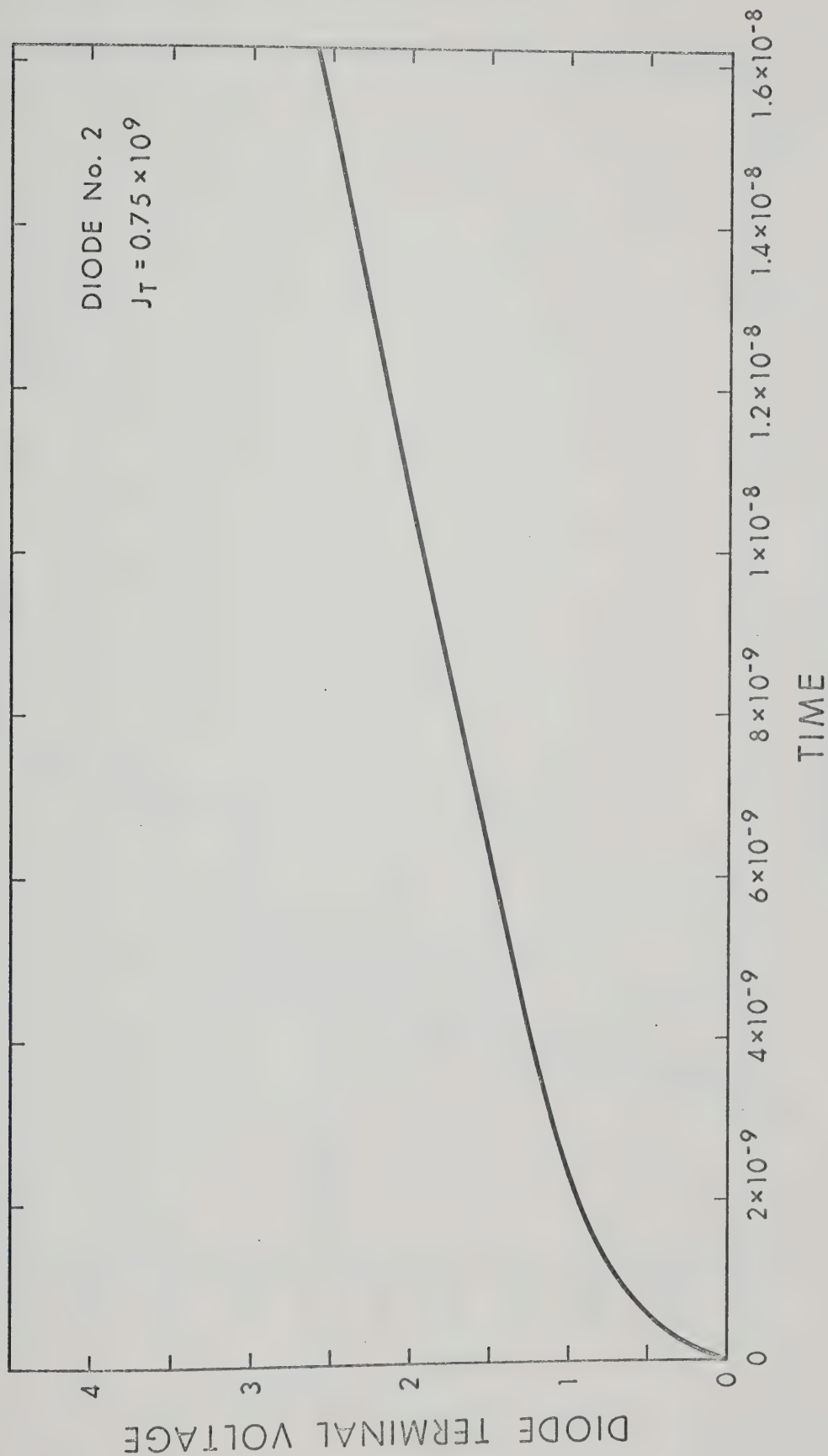


Fig. 8.8. Turn-on voltage response of diode No. 2 for the initial part of the turn-on transient.

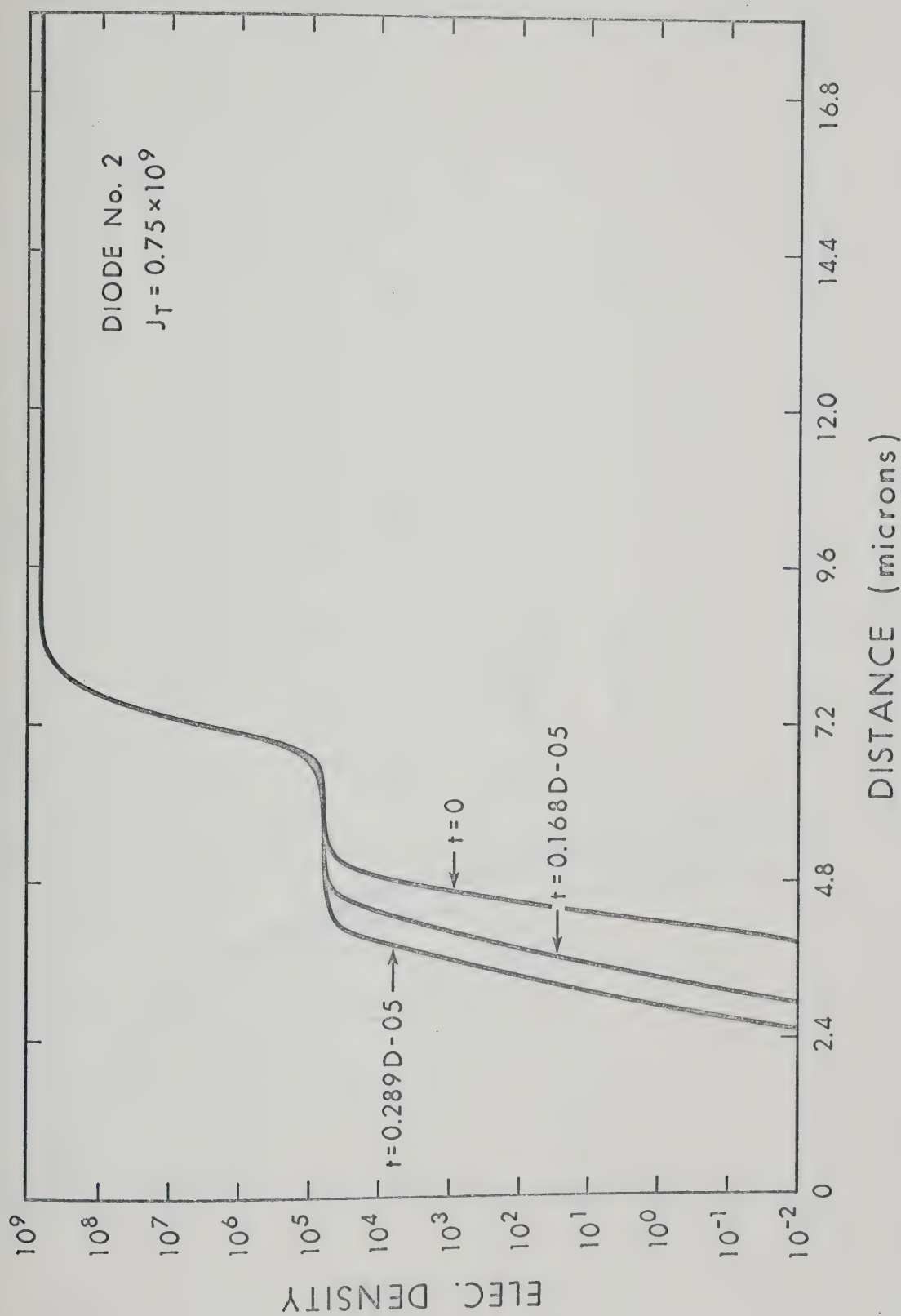


Fig. 8.9. Evolution of the electron density distribution in diode No. 2 during the turn-on transient.

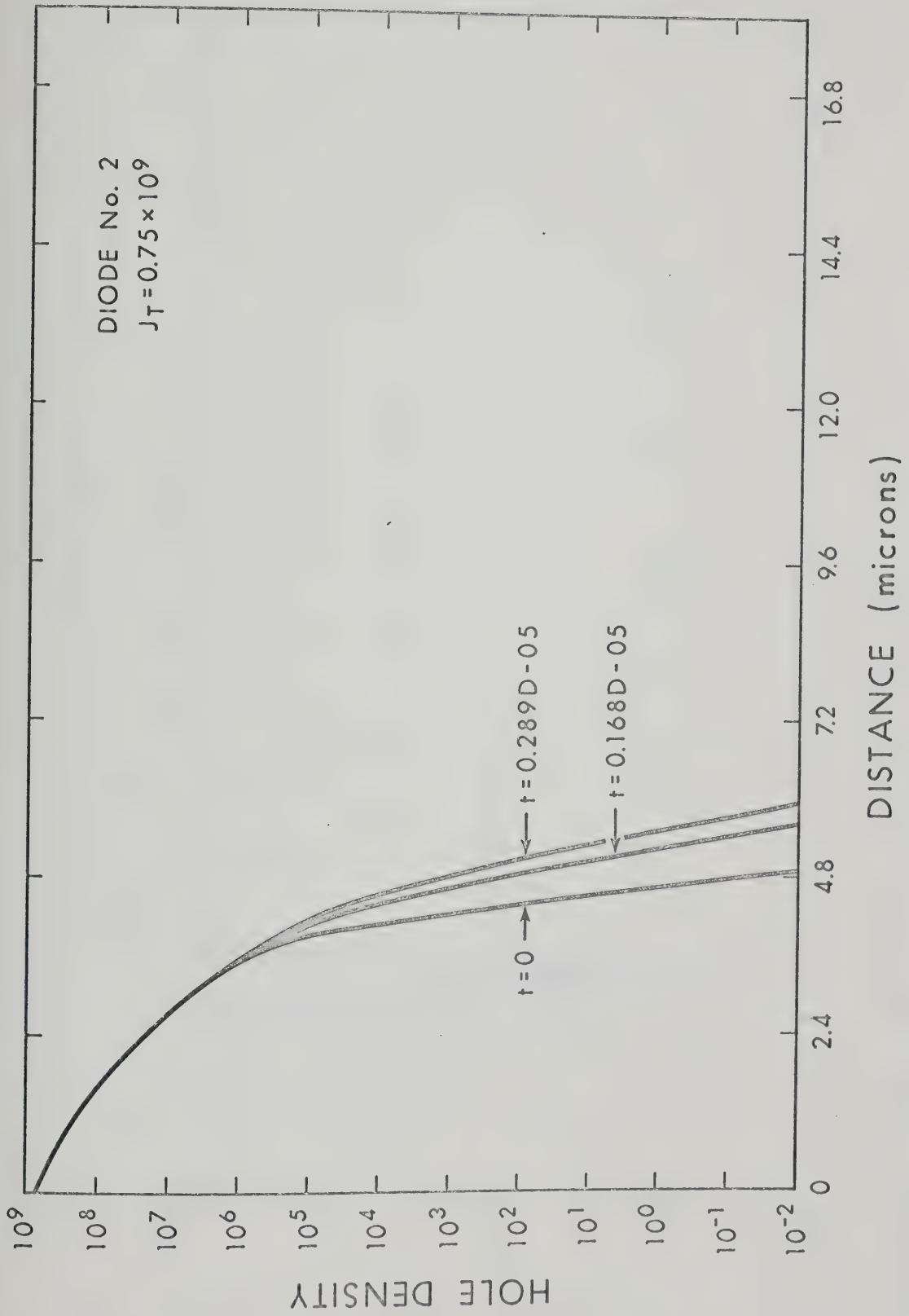


Fig. 8.10. Evolution of the hole density distribution in diode No. 2 during the turn-on transient.

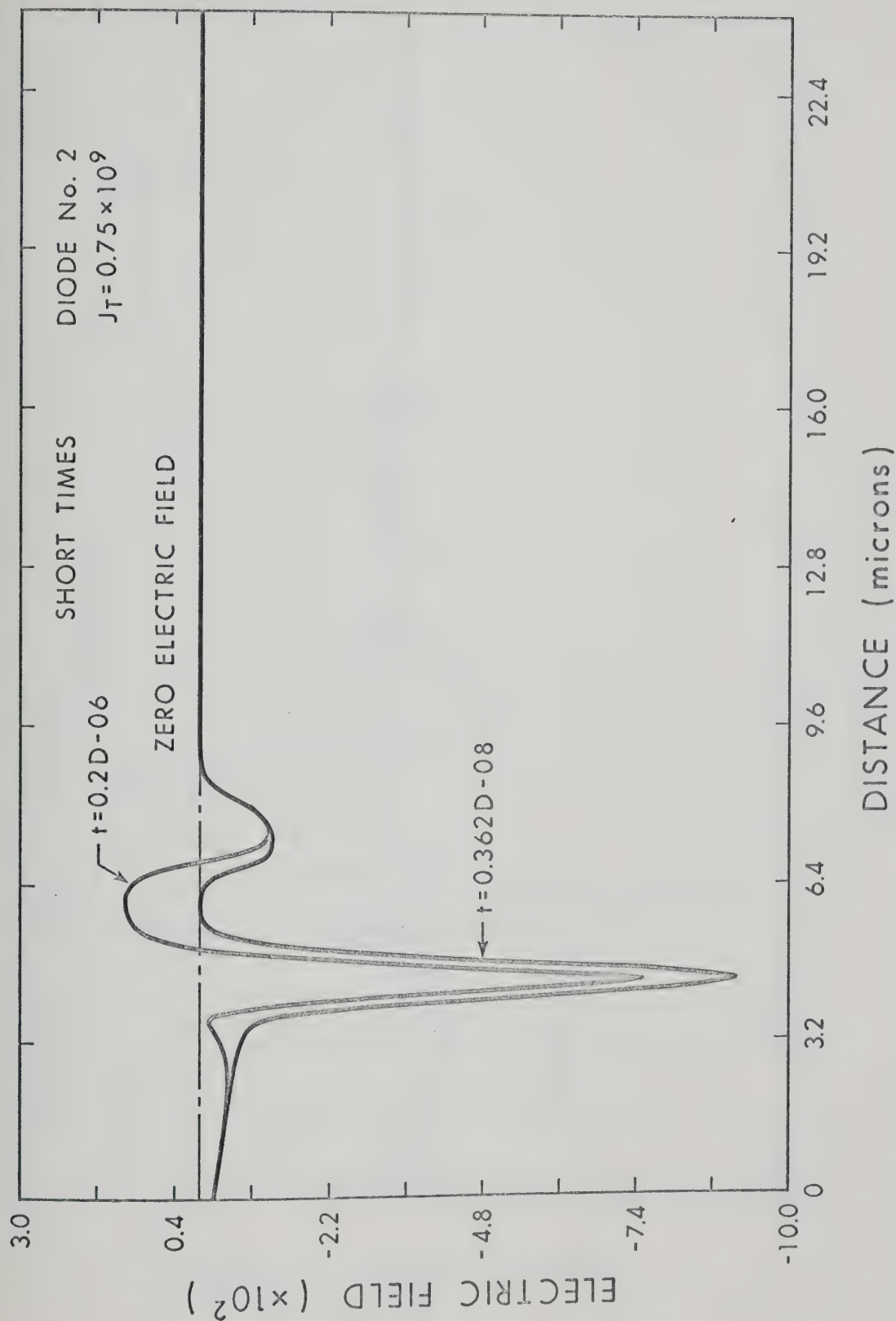


Fig. 8.11a. Evolution of the electric field distribution in diode No. 2 during the initial part of the turn-on transient.

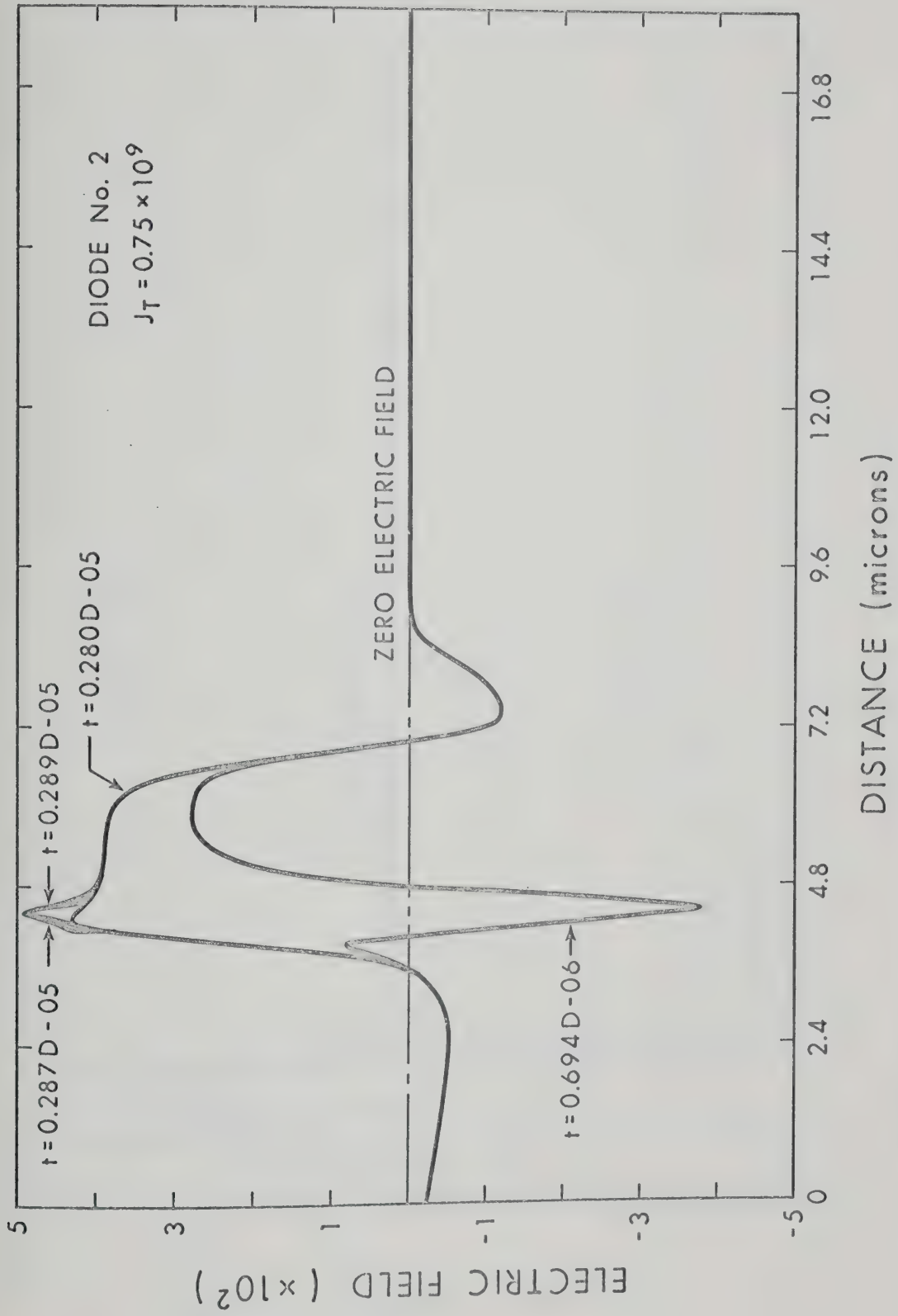


Fig. 8.11b. Evolution of the electric field distribution in diode No. 2 during the later part of the turn-on transient.

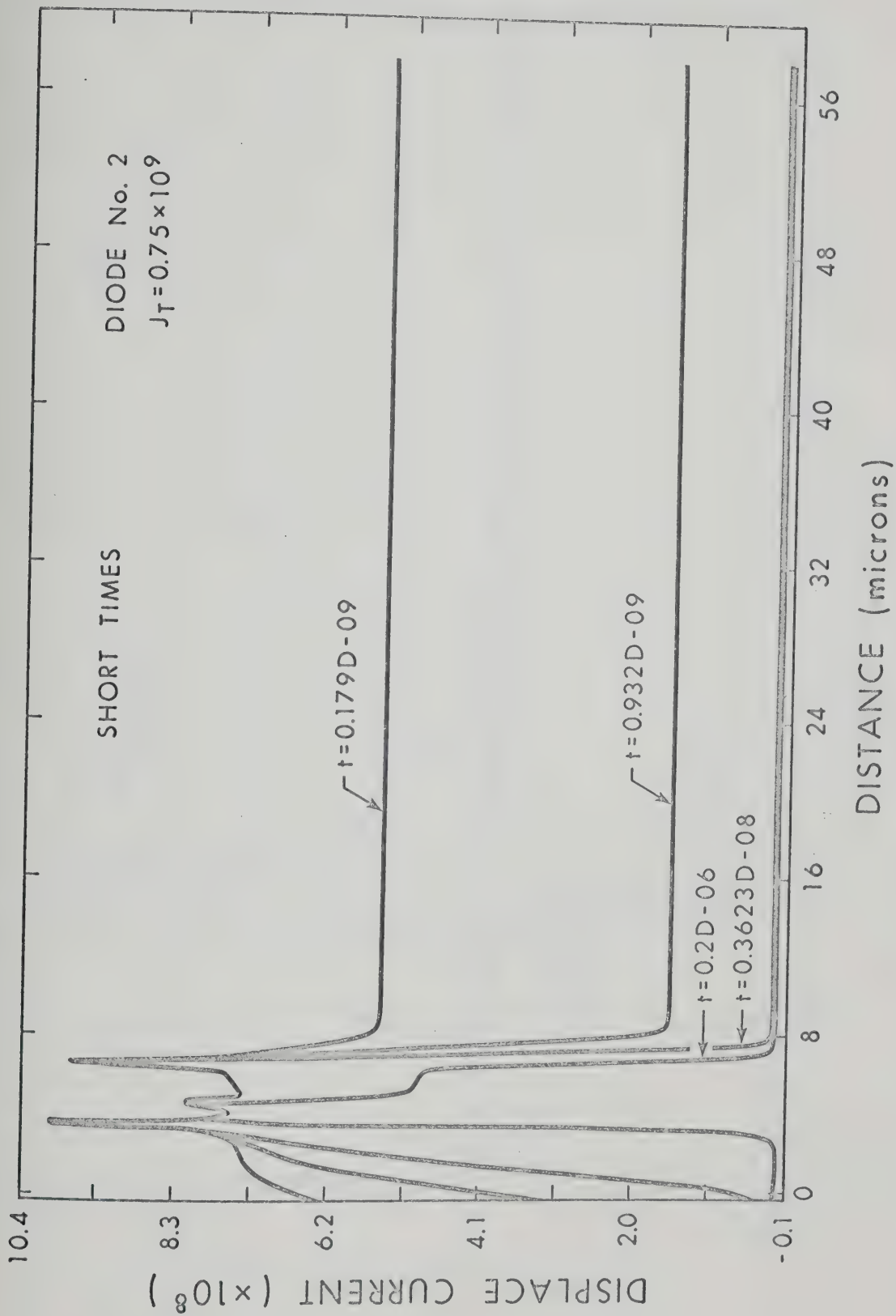


Fig. 8.12a. Evolution of the displacement current distribution in diode No. 2 during the initial part of the turn-on transient.

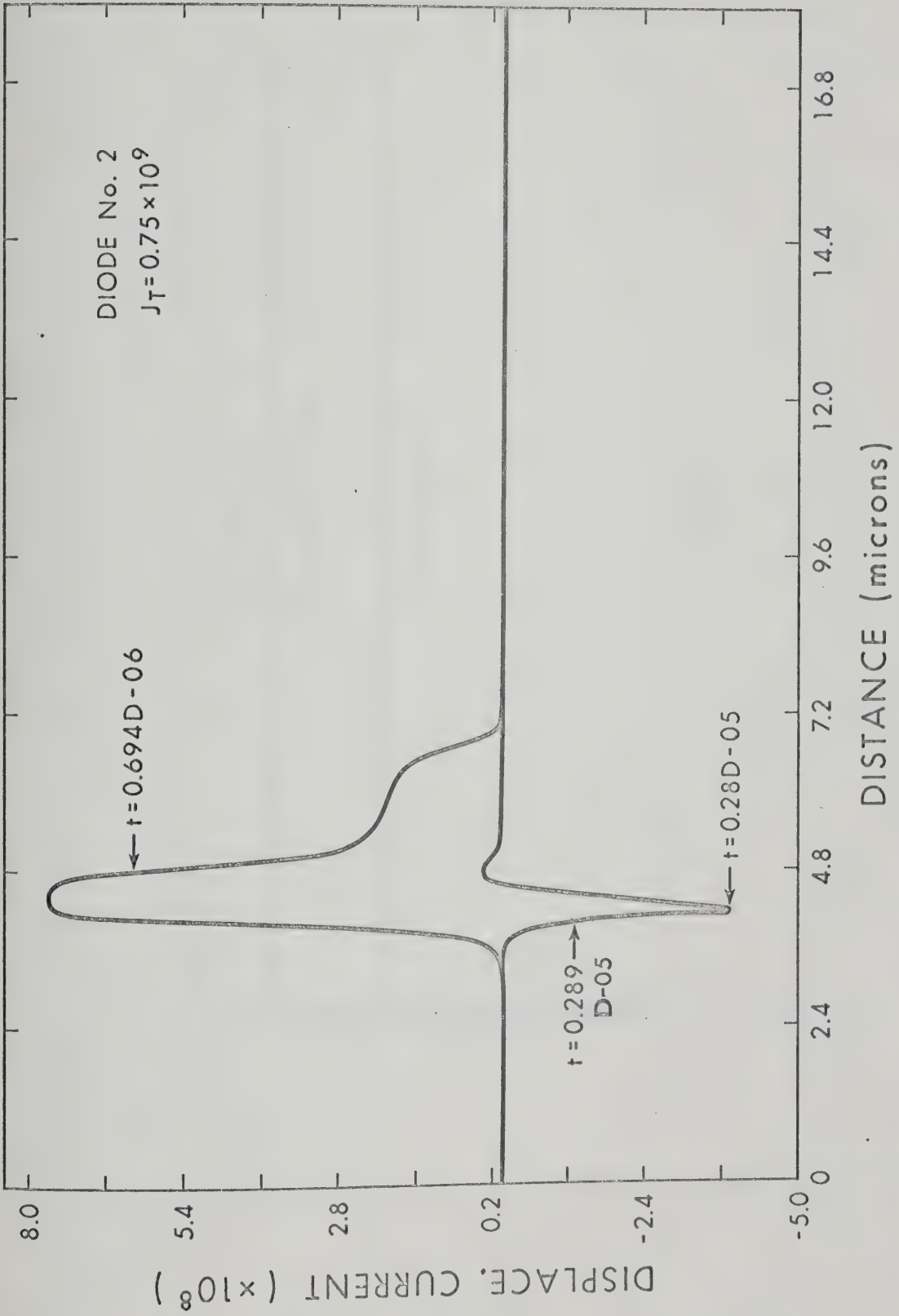


Fig. 8.12b. Evolution of the displacement current distribution in diode No. 2 during the later part of the turn-on transient.

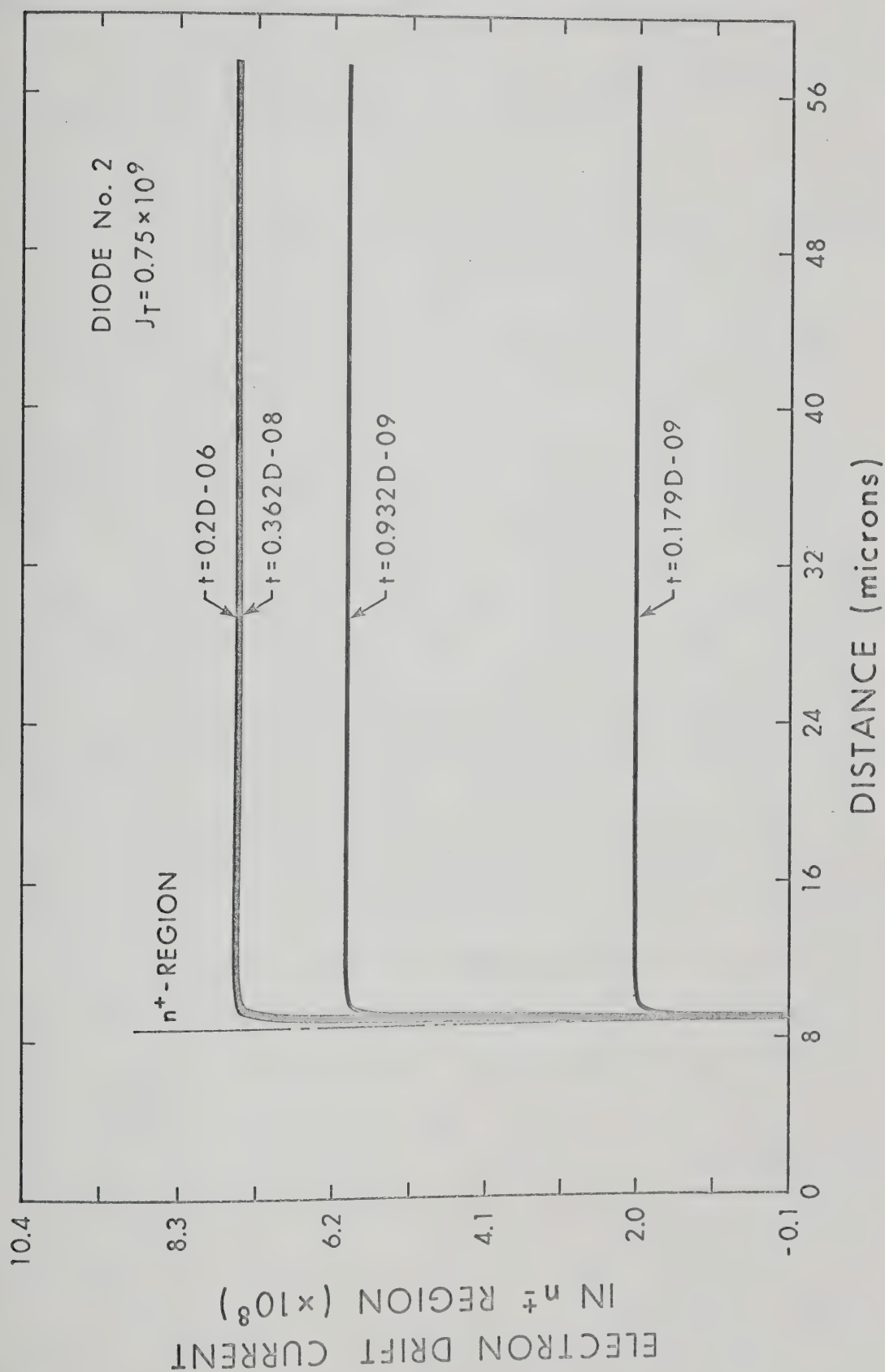


Fig. 8.13. Evolution of the electron drift current distribution in n^+ -region of diode No. 2 during the turn-on transient.

instants of time during the initial part of the transient. As is evident from Eqs. (8.12a) and (8.12b), displacement current features a basically different pattern in the n-region when compared to diode No. 1. The initial decrease of the displacement current, which corresponds to the build-up of the ohmic potential drop throughout the diode, is followed by an inversion of sign in the n-region and a subsequent decrease in the magnitude towards its steady-state zero value. The reversal of the direction of the displacement current flow is a consequence of the decrease of the voltage drop in a region whose conductivity is being modulated. The modulation initiates in the n-region at the edge of the transition region of the p^+-n junction and gradually spreads towards the n^+ -region. The conductivity is well apparent in the spatial distributions of the mobile carrier densities (Figs. 8.9 and 8.10). Due to smaller dielectric relaxation time, the displacement current, dominant in the initial stages, decreases markedly in the n^+ -region, though it is still dominant in the n-region. As shown in Fig. (8.13), the electron drift current replaces the displacement current in the n^+ -region. This is the consequence of the small electric field built up in the n^+ -region due to the flow of the current. Similar behaviour is exhibited by the p^+ -region. The electric field in the n-region exhibits an interesting behaviour (Figs. 8.11a and 8.11b). Initially the electric field is either negative or zero in this region. As the transient evolves in time, the electric field reverses its sign at the $n-n^+$ edge and becomes positive. This positive electric field region spreads towards the p^+ -region edge. At later time ($t \approx 0.28 \times 10^{-5}$) the whole n-region has electric field and even the transition region (p^+-n) exhibits a large positive electric field. But as the transient proceeds further in time,

the electric field at the p^+-n junction edge starts becoming less positive. At this point in the time domain, the decay of the terminal voltage towards its final steady-state value starts.

8.4 Conclusions

Diode No. 1 and diode No. 2 exhibit basically different terminal behaviour. The overall transient of diode No. 1 behaves some what similar to an RC circuit. Initial large conductivity of the semiconductor material on both sides of the p-n junction prevents conductivity modulation effects from becoming significant at the current density to which the diode is subjected. It is also shown that less than 5% of the holes stored for this current density under the steady-state conditions is injected in 2.2×10^{-10} seconds after the transient is initiated. The displacement current is dominant in the initial part of the transient throughout the diode. In a time of the order of two times the dielectric relaxation time of the substrate ($\approx 1.1 \times 10^{-16}$ sec.), the particle drift current takes over from the displacement current in the quasi-neutral bulk regions, but is still significant in the transition region. At later times, the minority-carrier injected across the junction become significant and the transient is governed by their flow. The steady-state value will thus be reached with a time constant of the order of the transit time of the holes in the n-region ($\approx 1.5 \times 10^{-6}$ sec.).

The overall transient of diode No. 2 behaves somewhat similiar to an RL circuit, the initial voltage being much greater than the steady-state voltage. The conductivity modulation effects in the high-resistivity n-region are mainly responsible for this behaviour. The

large forward current to which the diode is subjected, causes a high positive electric field to build up in the n-region. It later spreads to even the p^+-n junction transition layer. At later times (0.3×10^{-10} sec.), due to significant increases in the conductivity at the p^+-n junction edge, the positive electric field starts decreasing. At this point, the terminal voltage starts decaying towards its final value. This decay will be mainly governed by the flow of the mobile carriers in the n-region.

CHAPTER IX

LARGE-SIGNAL "TURN-OFF" RESPONSE

In this chapter, the computed results for both the internal and external behaviour of diode No. 1 and diode No. 2, when the device is "turned-off" with a current-limiting series resistance, are presented and briefly discussed.

9.1 Introduction

When a diode has been carrying current in the forward direction and a reverse-biasing potential is suddenly applied through a series resistance, the behaviour of the diode is called the "turn - off" response. We are interested in this phenomenon to study the recovery of the charge injected during the initial forward-biased condition. The purpose of the series resistance is to limit the initial reverse current which will start flowing instantly after the reverse-biasing potential is applied. The time required by the diode to recover its stored charge determines to a great degree the upper limit of the frequency at which a diode can be operated in the step-recovery mode.

A number of workers have studied this problem for a highly asymmetrical step p-n junction.^{9-13, 16} Their analysis has been mainly based upon the solution of a greatly simplified diffusion equation, which does not take into consideration the presence of the electric field. Muto et al.¹⁵ expanded the analysis for a graded-base diode and found it to have a faster response than a comparable uniform-base diode. Kennedy¹⁴ presented a second-order analysis taking into account various

recovery mechanisms which were neglected in the previous works mentioned above. In the analysis of Benda et al.¹⁷; a theory is developed for a p - s - n rectifier. The center high resistivity layer in diode No. 2 is very thin. Therefore, the theory of Benda et al.¹⁷ is not applicable as such and has to be modified.

In this chapter, the results for a "turn-off" transient for both diode No. 1 and diode No. 2 are presented. These results are based on our physical and mathematical model as discussed in Chapter III and Chapter IV. The details of the numerical solution are discussed in Chapter VI. All the quantities are displayed in normalised units, unless otherwise specified. (See Table 4.1)

9.2 Results for Diode No. 1

The parameters chosen for the switching circuit of Fig. (9.1) for diode No. 1 are as follows:

$$V_R = -20 \text{ volts}$$

$$V_F = +1 \text{ volt}$$

$$R = 10 \Omega$$

Figure (9.3) displays the diode terminal voltage for short times ($\approx 10^{-11}$ sec.) after the diode is subjected to the "turn-off" transient. At the time instant $t = 0^+$, a current $I(t=0^+) = \frac{V_R + V_F(t=0)}{R}$ is forced through the device, since its terminal voltage remains constant from $t=0$ to $t=0^+$. As soon as the current starts flowing, the build-up of ohmic drop in the quasi-neutral p and n regions becomes the dominant effect. The build-up of ohmic drop effectively takes place in a time constant of the order of the dielectric relaxation time of the n-region

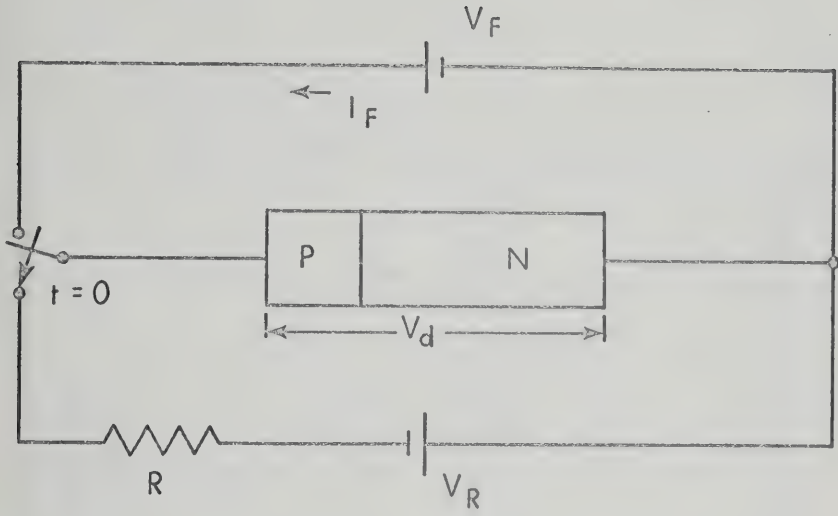


Fig. 9.1. Circuit model used for the study of the large-signal turn-off response of the diodes.

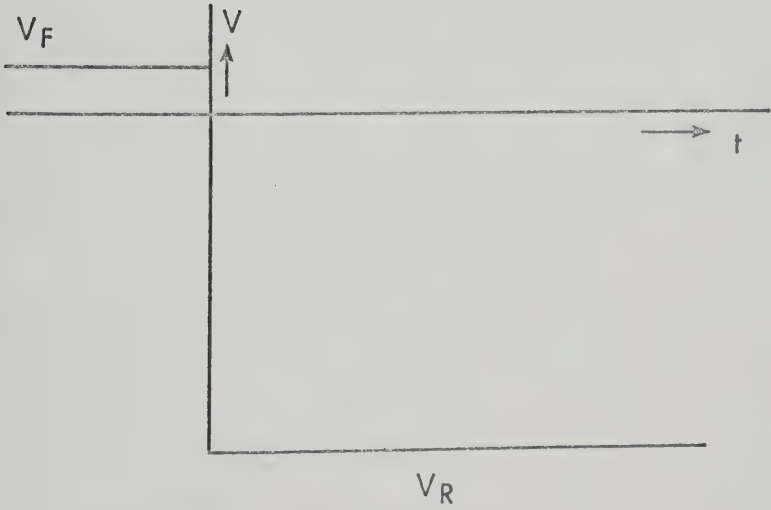


Fig. 9.2. Switching waveform applied to the diodes.

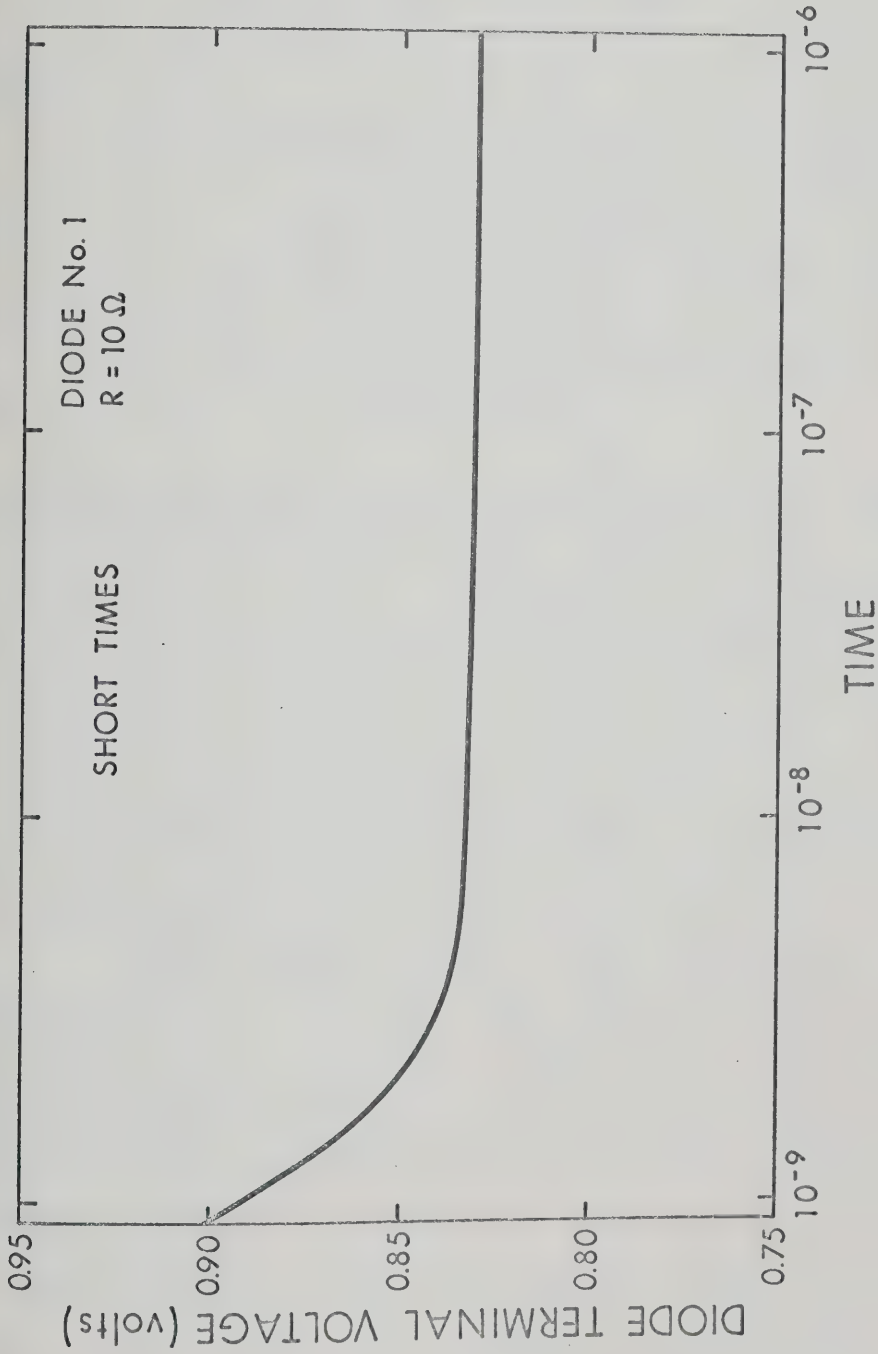


Fig. 9.3. Terminal voltage as a function of time during the initial period of the reverse transient for diode No. 1.

($\approx 1.1 \times 10^{-16}$ sec. for an average doping density of 10^{20} cm^{-3}). The approximate value of the ohmic drop in the n-region may be estimated as follows:

$$\Delta V \Big|_{\text{ohmic}} = \frac{\rho \ell}{A} (I(0) - I(t_1))$$

where

ρ = average resistivity of the device calculated from the steady-state considerations,

ℓ = approximate length of the n-region, and

$I(t_1)$ = value of the current once the ohmic drop is established.

The value of ΔV calculated for our case is about -0.1 volts, which is well in agreement with our computer result as displayed in Fig. (9.3). As the ohmic drop occurs very rapidly, the displacement current in the bulk regions is significant only over very short time intervals and is replaced by the majority-carrier drift currents. The majority-carrier current is the consequence of the presence of a small electric field in the bulk regions after the ohmic drop is established.

As the transient evolves in time, the particle currents become significant in the transition region and start extracting the injected holes and electrons from the very vicinity of the metallurgical junction. The departure of the minority-carriers from the vicinity of the metallurgical junction results in a build-up of the electric field in the transition region as shown in Fig. (9.4a). Figure (9.4b) displays the build-up of electric field throughout the diode and shows the presence of a small electric field in both the p- and n-regions. Since the

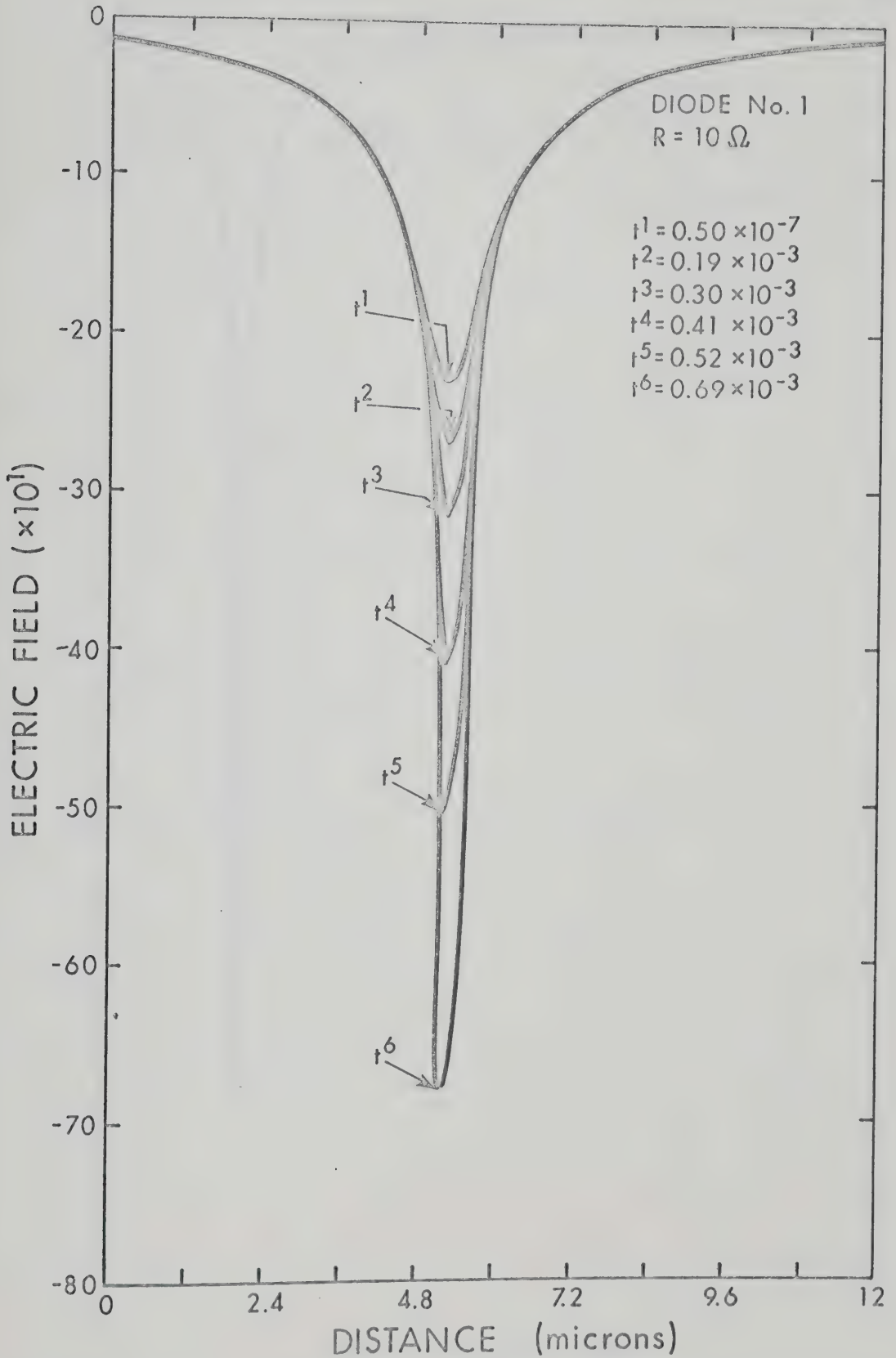


Fig. 9.4a. Evolution of the electric field in the vicinity of the junction during the initial period of the turn-off transient, for diode No. 1.

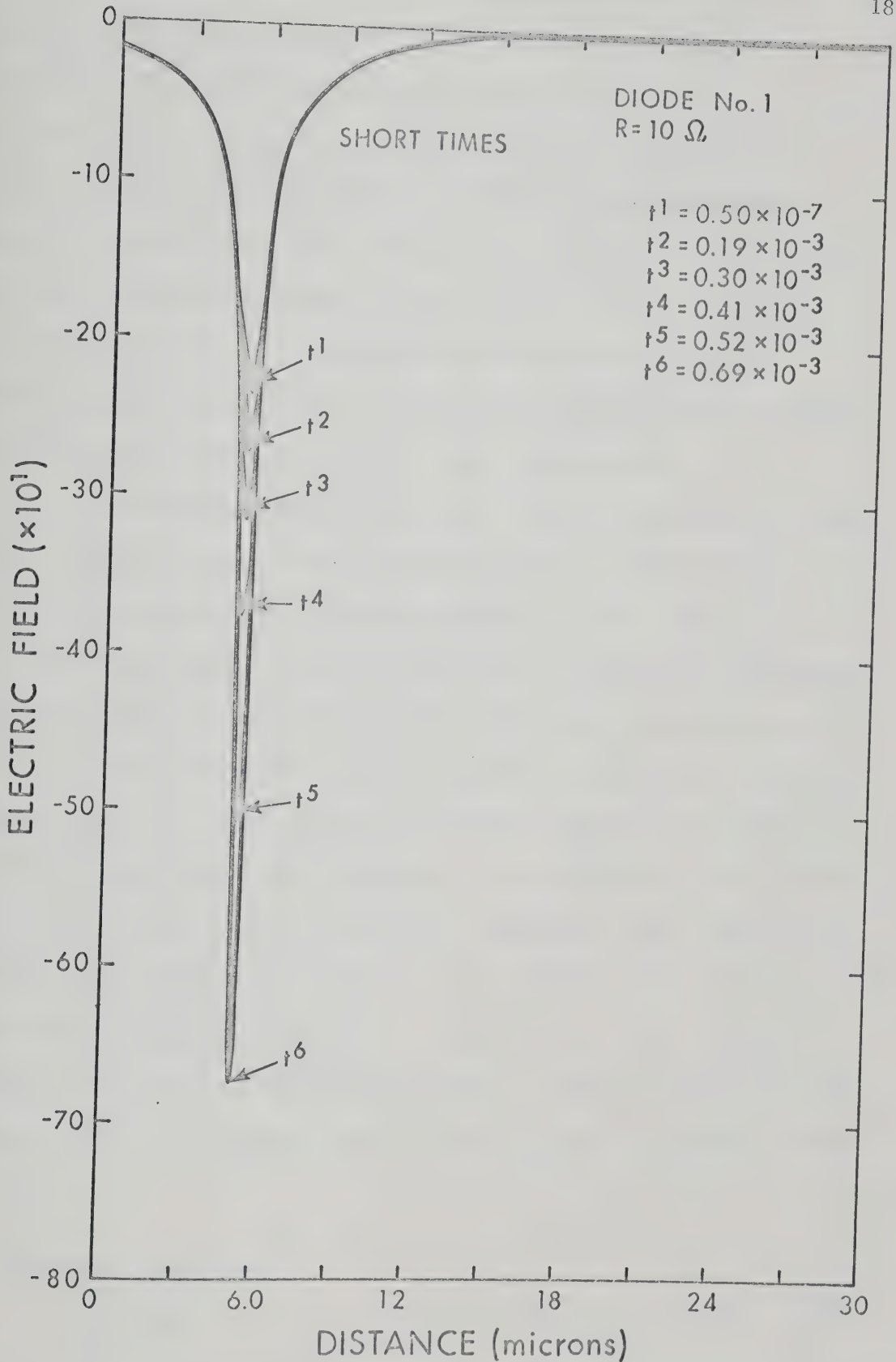


Fig. 9.4b. Evolution of the electric field throughout diode No. 1 during the initial period of the reverse transient.

density of the majority-carriers is much greater than the density of the minority-carriers, this small electric field gives rise to a very large majority-carrier drift current which almost accounts for the total current. The electron and hole current distributions throughout the diode for one particular time instant are plotted in Fig. (9.5). The fact that the majority-carrier current cannot be ignored in our case, renders the validity of the analytical models adopted for highly asymmetrical p-n junctions⁹⁻¹⁵ doubtful when applied to heavily doped, doubly-injecting diodes like the one under consideration.

Figure (9.6) displays the overall transient response for diode No. 1. The computations were discontinued after 0.2 microseconds, since we are only interested in times corresponding to the periodic times at microwave frequencies. After an initial drop, the terminal voltage and terminal current assume constant values. The spatial distributions of the hole density during the transient period are plotted in Fig. (9.7). Figures (9.8a) and (9.8b) display the spatial distributions of the electron density during the transient. The distribution of the carriers show the effect of electric field in the transition region which tends to accumulate carriers at the edge of the transition region in the quasi-neutral bulk regions, and deplete the region close to the external contacts. It may be stated that this effect tends to lengthen the time period in which the terminal current remains constant (constant current phase).

9.3 Results for Diode No. 2

The parameters chosen for the switching circuit of Fig. (9.1) for diode No. 2 are as follows:

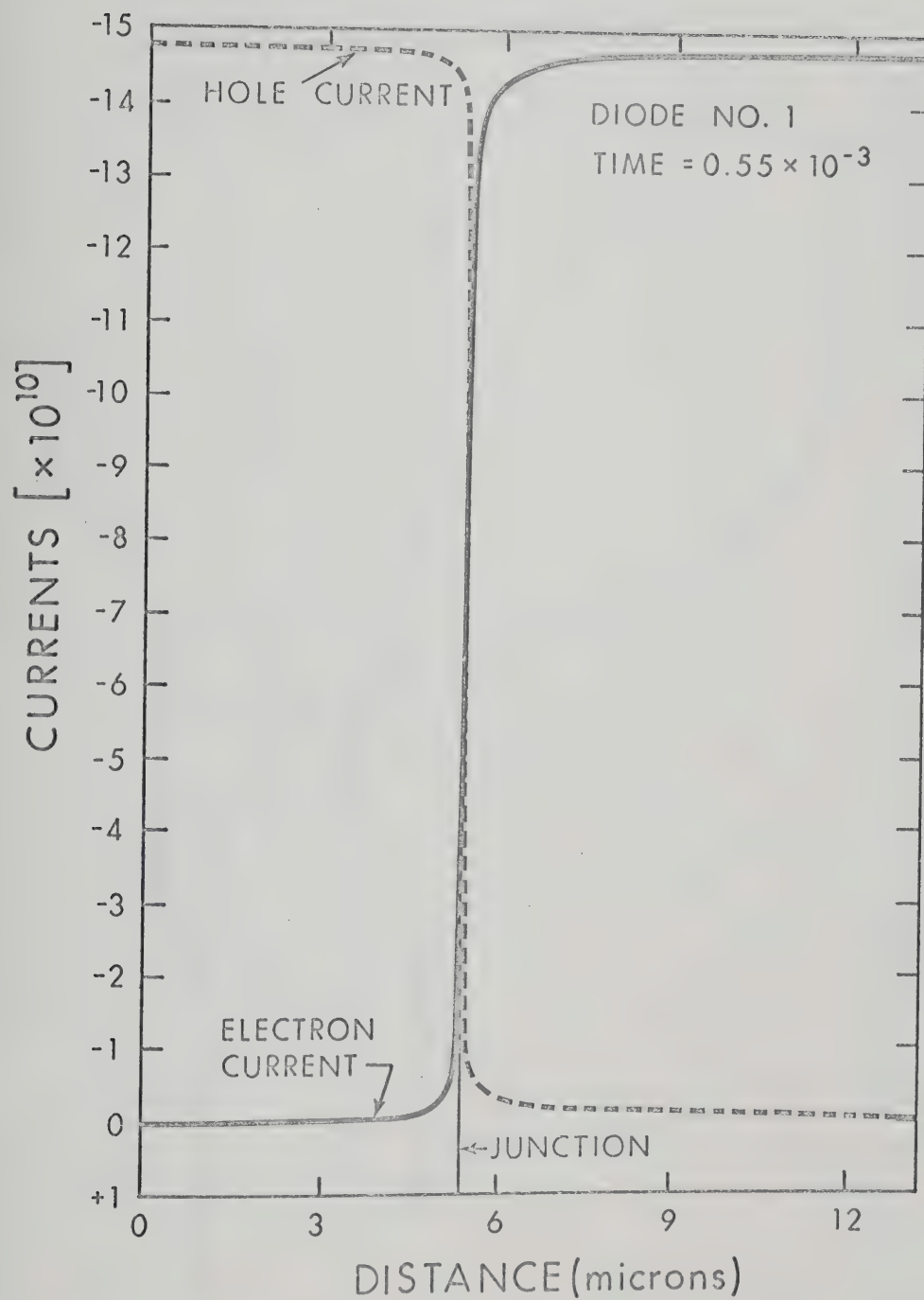


Fig. 9.5. Spatial distribution of hole and electron currents for a particular time instant ($= 0.55 \times 10^{-3}$) during the reverse transient, for diode No. 1.

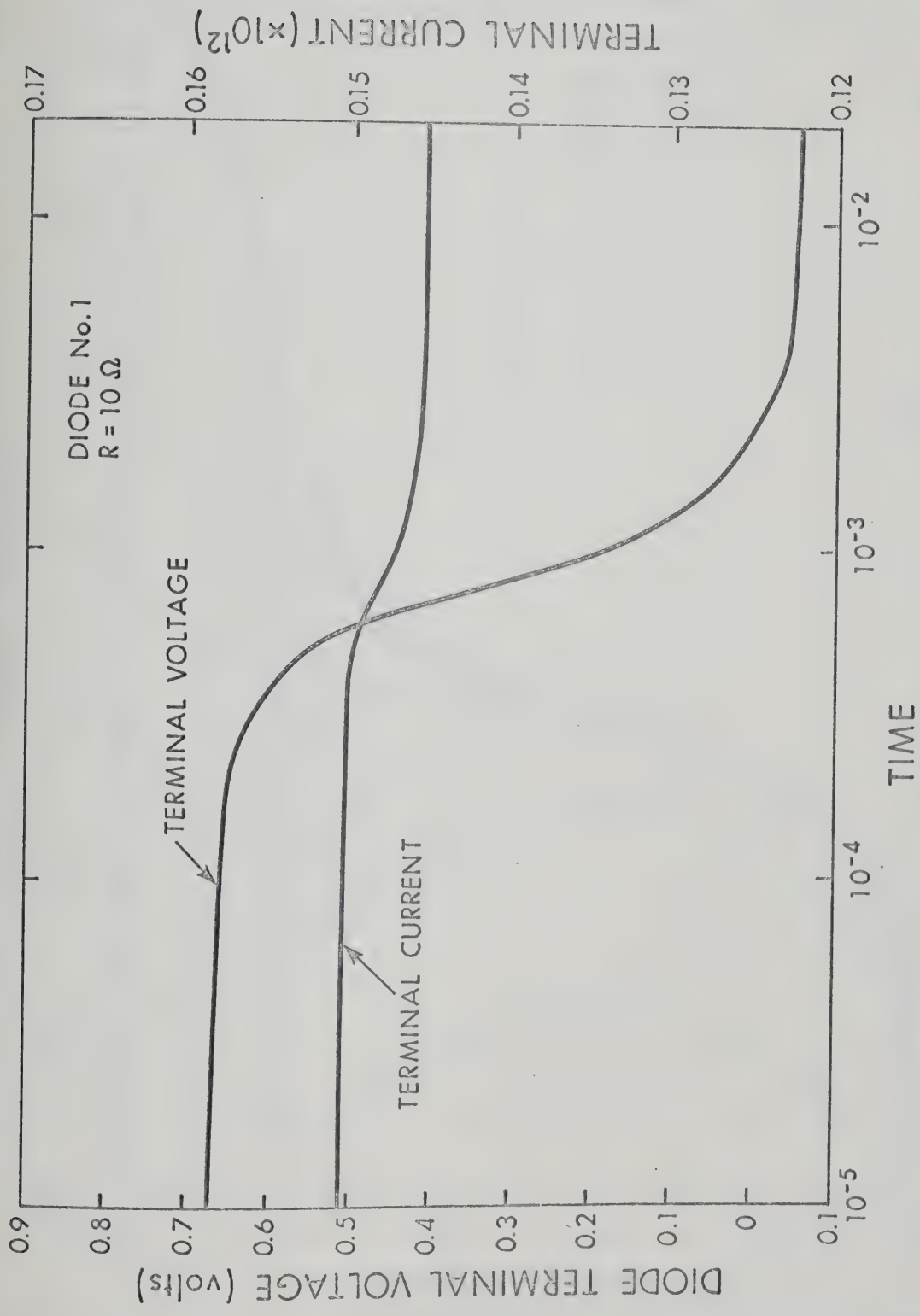


Fig. 9.6. Diode terminal voltage and current as a function of time during the reverse transient, for diode No. 1.

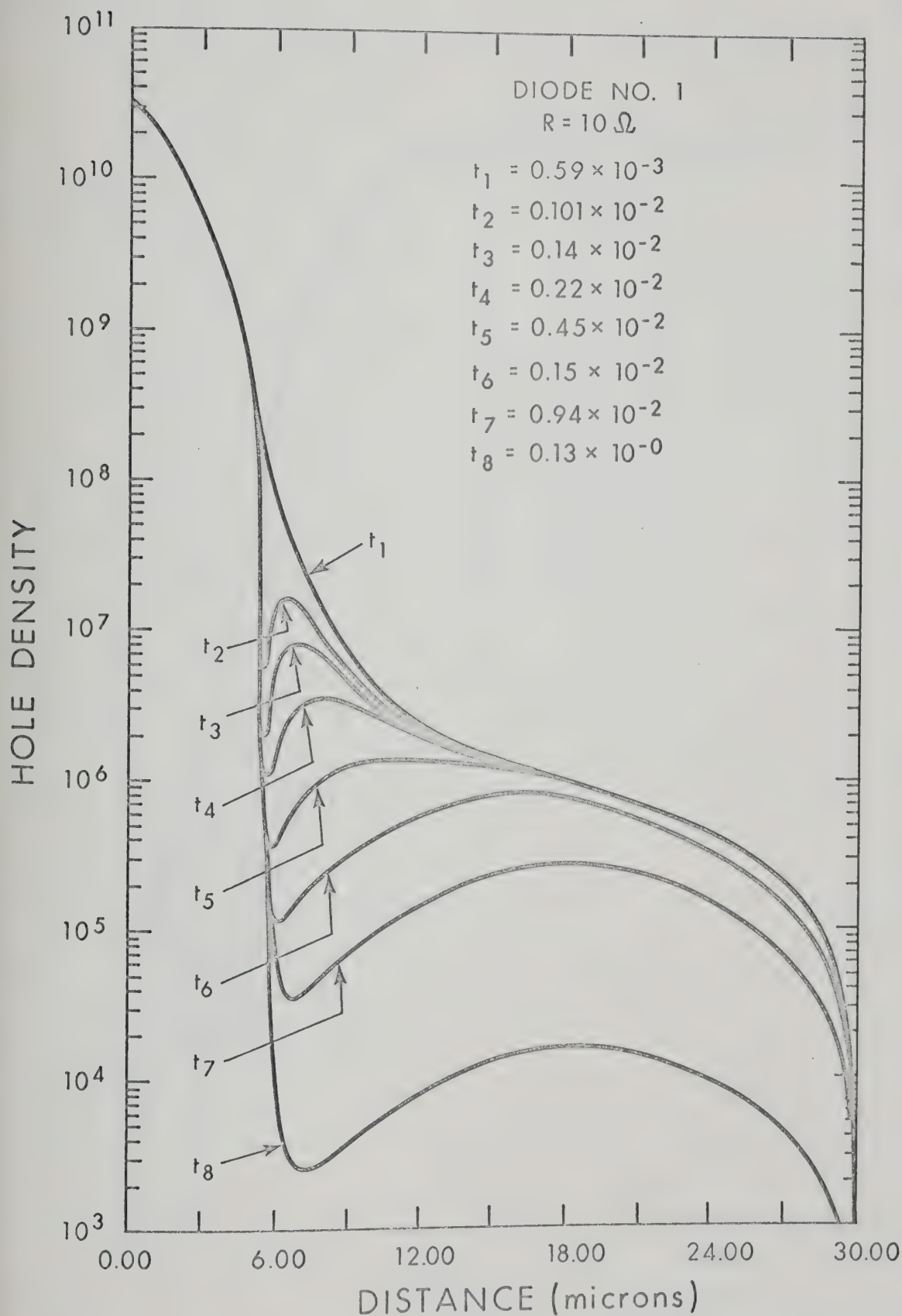


Fig. 9.7. Hole density distribution at various instants of time during the reverse transient, for diode No. 1.

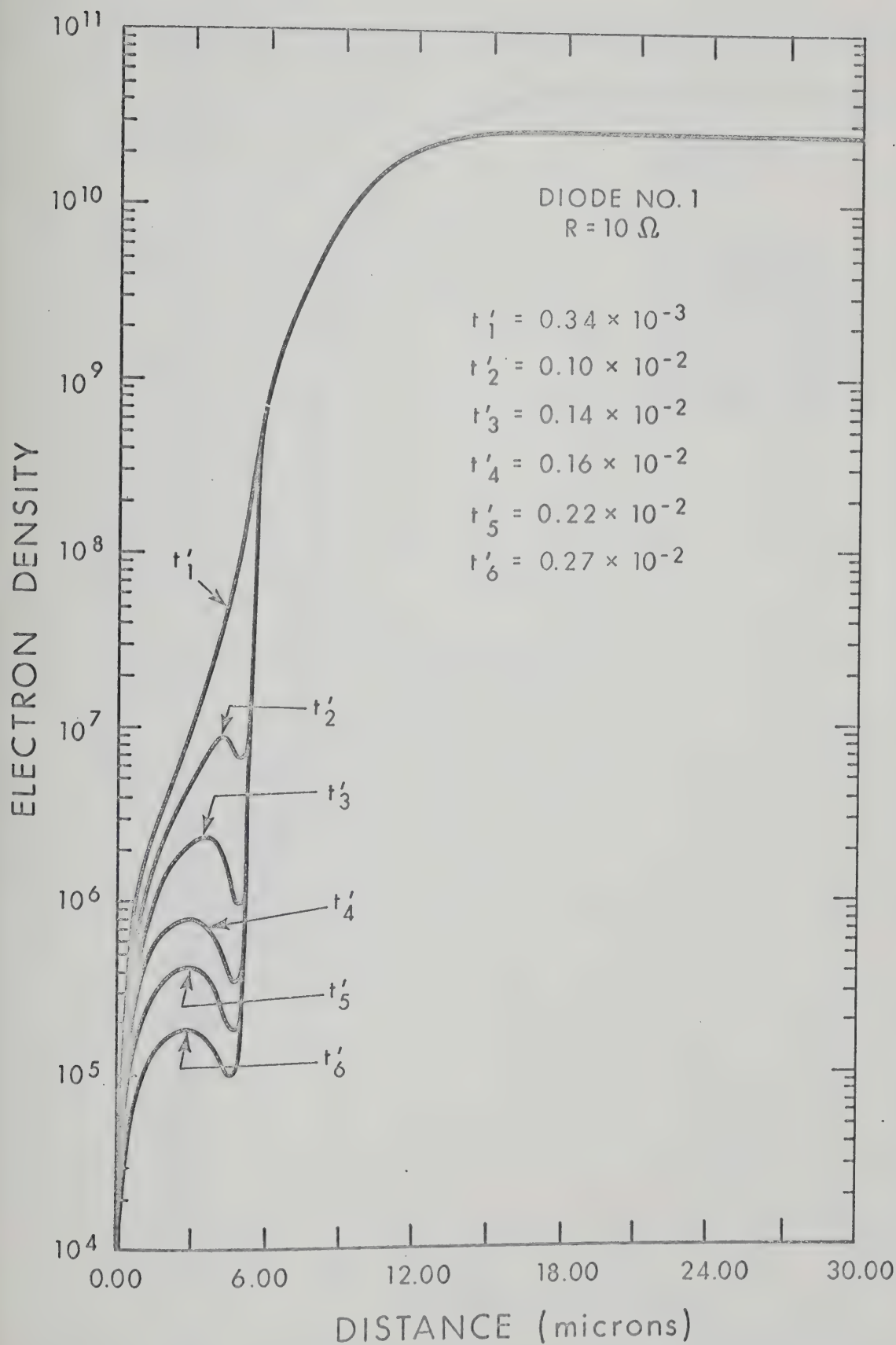


Fig. 9.8a. Electron density distribution at various instants of time during the reverse transient, for diode No. 1.

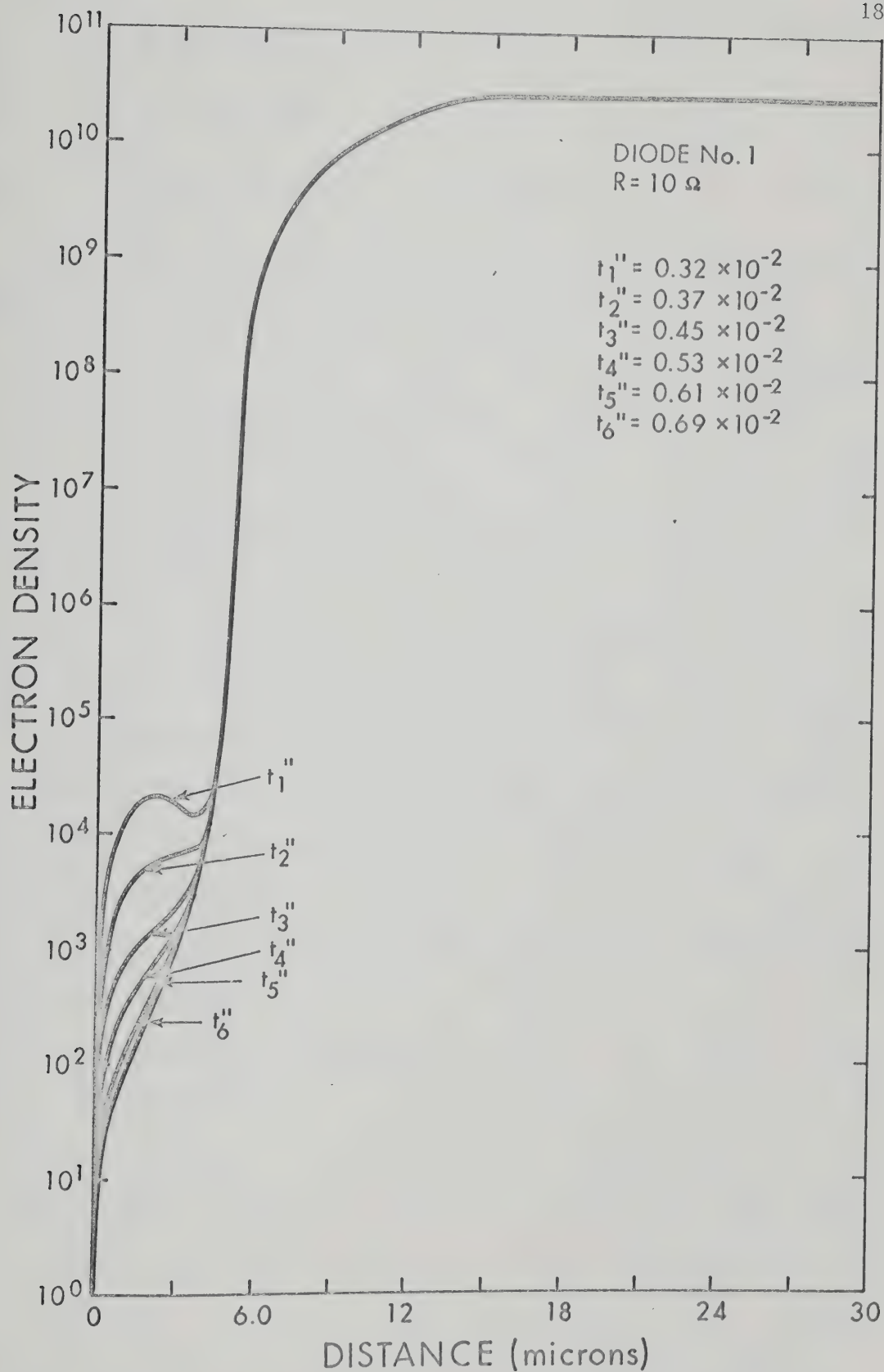


Fig. 9.8b. Electron density distribution at various instants of time during the reverse transient, for diode No. 1.

$$V_R = -5 \text{ volts}$$

$$V_F = 0.8 \text{ volts}$$

$$R = 10 \, \Omega$$

The initial part of the transient is marked by the build-up of the ohmic drop in the p^+ - and n^+ -regions and the center high-resistivity region. The build-up of the ohmic drop in all the three regions is governed by their respective dielectric relaxation times. The estimated average dielectric relaxation times, computed on the basis of charge distribution before the reverse biasing potential is applied are 6.25×10^{-13} sec., 2.2×10^{-12} sec. and 3.5×10^{-12} sec. for the n^+ -, n - and p^+ -regions, respectively. The initial part of the transient behaviour is depicted in Figs. (9.9) and (9.10). Figure (9.9) displays the terminal voltage and the terminal current for the initial part of the transient. Figure (9.10) shows the build-up of the electric field throughout the interior of the device. The hole and electron density distributions which are not significantly affected in a time of the order of 1.1×10^{-12} sec., are not plotted. The high reverse current caused by the applied reverse bias potential and limited by the external series resistance, is initially contributed by the displacement current. The build-up of the electric field gives rise to large hole and electron drift currents. These hole and electron currents become the major contributor to the total current within a time of the order of 0.2×10^{-12} sec. Such high particle drift currents start depleting the stored charge in the p^+ - n space-charge region. The depletion of the charge from the p^+ - n space-charge region reinforces the build-up of the electric field, which in turn causes the build-up of the terminal voltage and consequent decrease

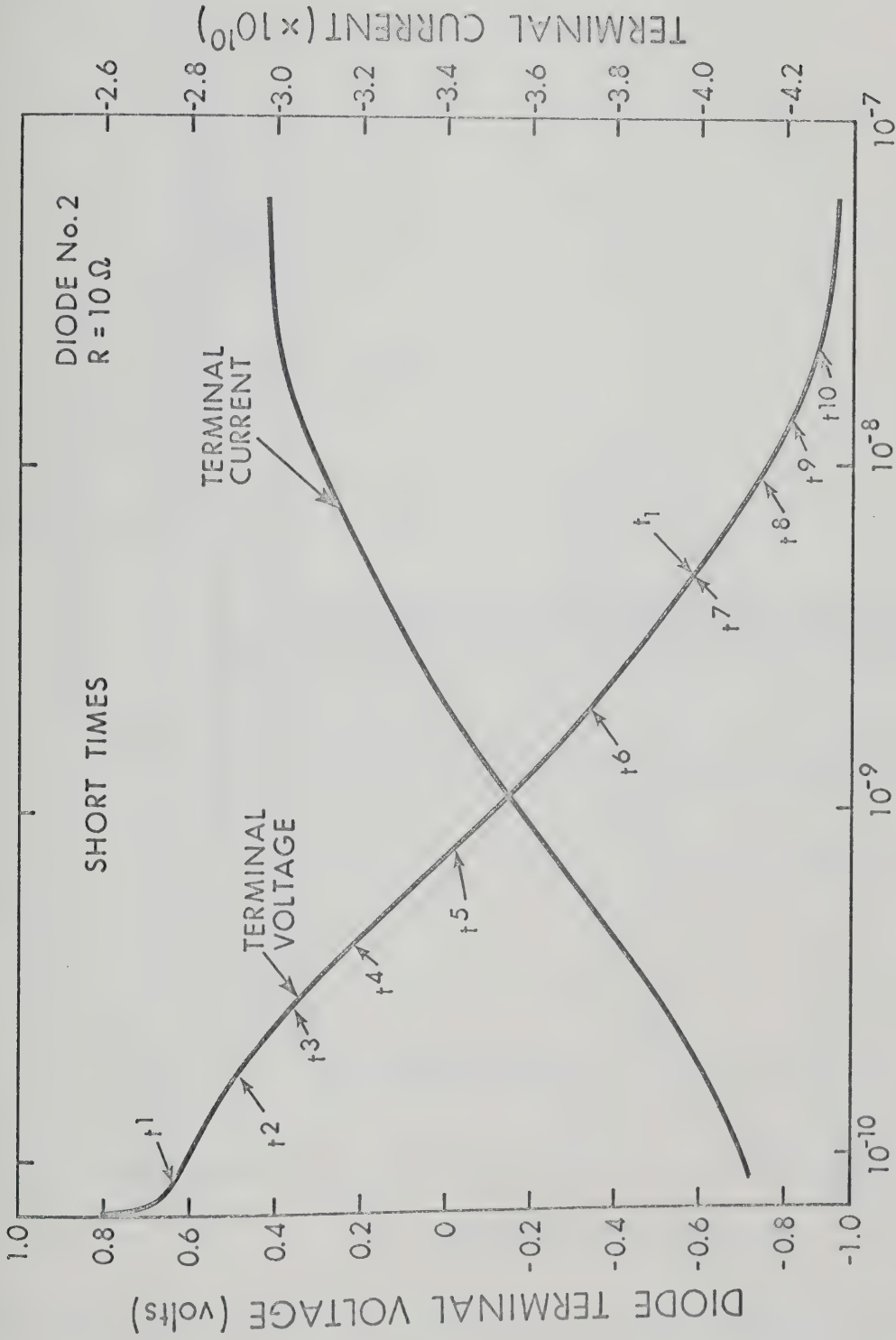


Fig. 9.9. Terminal voltage and current as a function of time during the initial period of the reverse transient, for diode No. 2.

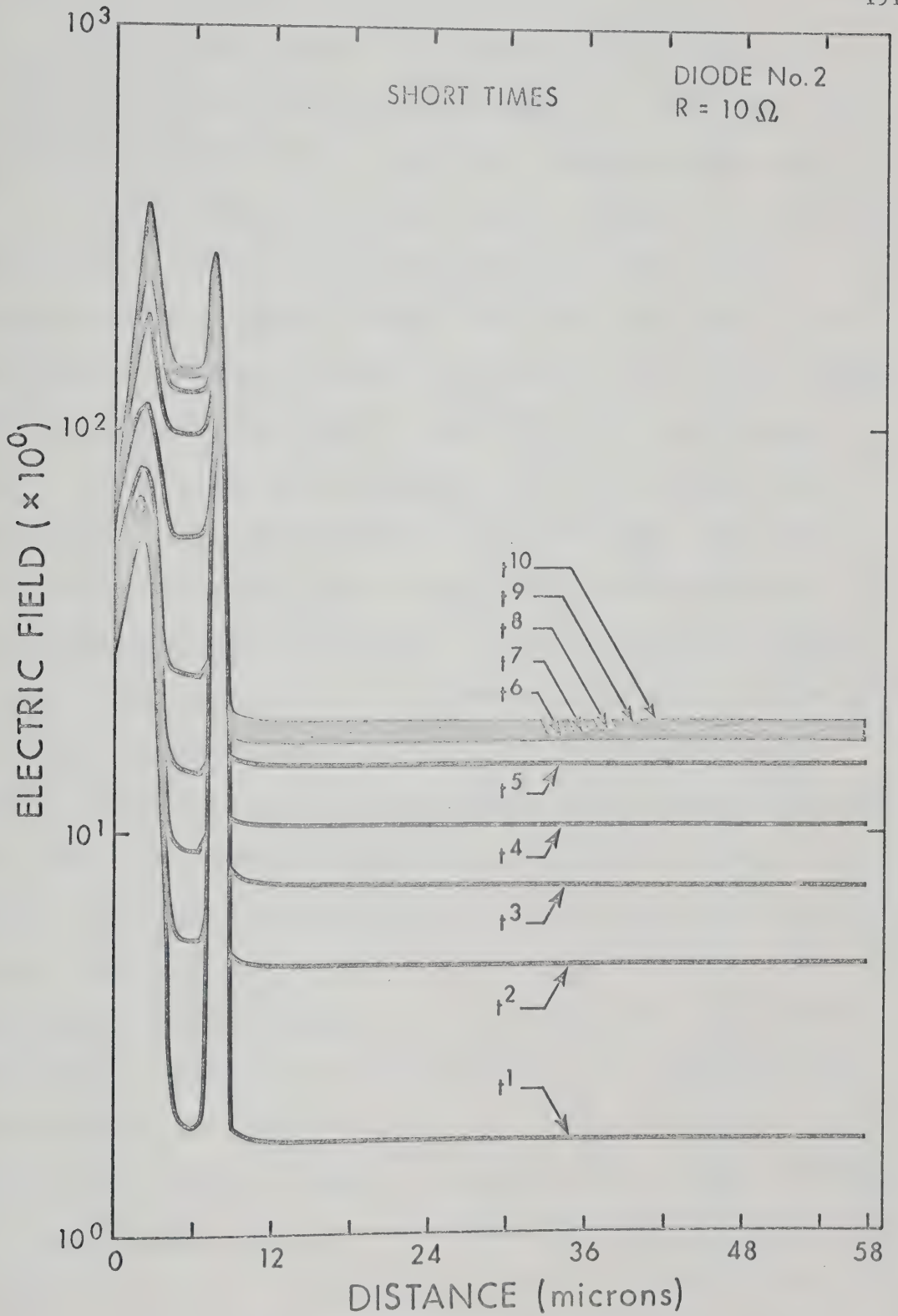


Fig. 9.10. Electric field distribution at various instants of time (values indicated in Fig. 9.9) during the initial period of the reverse transient, for diode No. 2.

in the reverse terminal current. The terminal current decreases to about 75% of its initial value in approximately 5.5×10^{-13} sec. The decrease in the terminal current causes the built-up electric field in the p^+ -, n - and n^+ -regions to decrease slightly. However, at the $p^+ - n$ junction, due to the depletion of the charge, the electric field continues to build up slowly. Figure (9.11) shows the overall response of the device. The reverse current and, therefore, the terminal voltage exhibit a relatively slower rate of change after the initial large build-up. The terminal current decreases to 25% of its initial value within 8×10^{-10} sec. Figures (9.12), (9.13) and (9.14) display the electric field, hole density and electron density distributions for various instants of time as indicated. Figure. (9.12) shows that the negative electric field at the $p^+ - n$ junction is the main contributor to the terminal voltage build-up. At the $n - n^+$ junction, the electric field first rises and then starts decreasing slowly. Figures (9.13) and (9.14) show increasing charge depletion in the vicinity of the $p^+ - n$ junction, but exhibit a slight accumulation in the vicinity of the $n - n^+$ junction. This behaviour of the hole and electron density is rather unexpected. It may be explained in the following manner. The present model considers the hole and electron mobility to be a strong function of the distance. The carrier mobility shows a large variation in the vicinity of the regions of different doping (see Figs. (7.13a), (7.13b), (7.13c) and (7.13d)). Moreover, the electric field in the vicinity of the regions of different doping is greater than in the rest of the device. The electric field in the n -region is higher than in the n^+ - and p^+ -regions due to the ohmic drop caused by the large reverse current through the device. As the transient proceeds, the reverse current

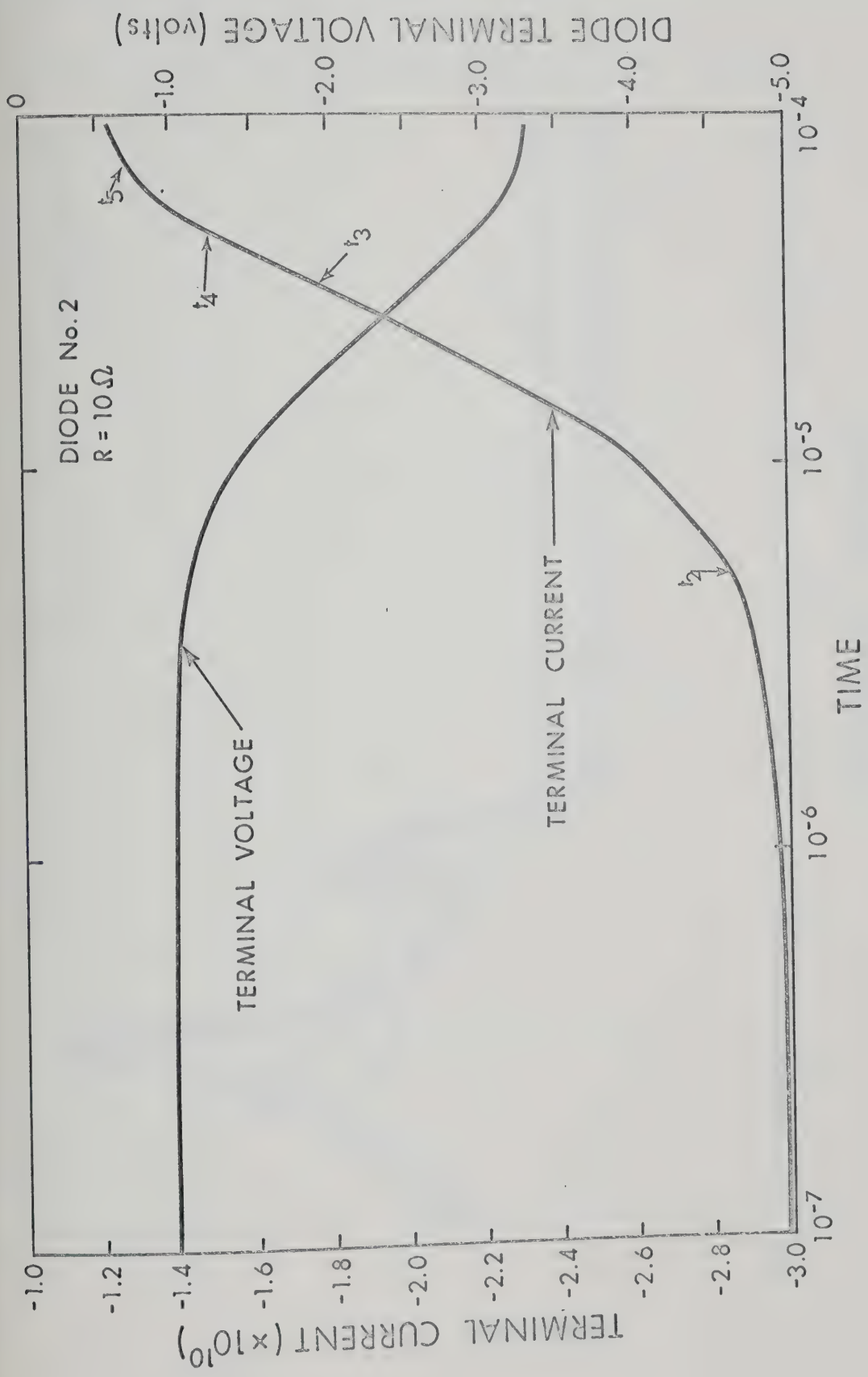


Fig. 9.11. Terminal voltage and current as a function of time during the reverse transient, for diode No. 2.

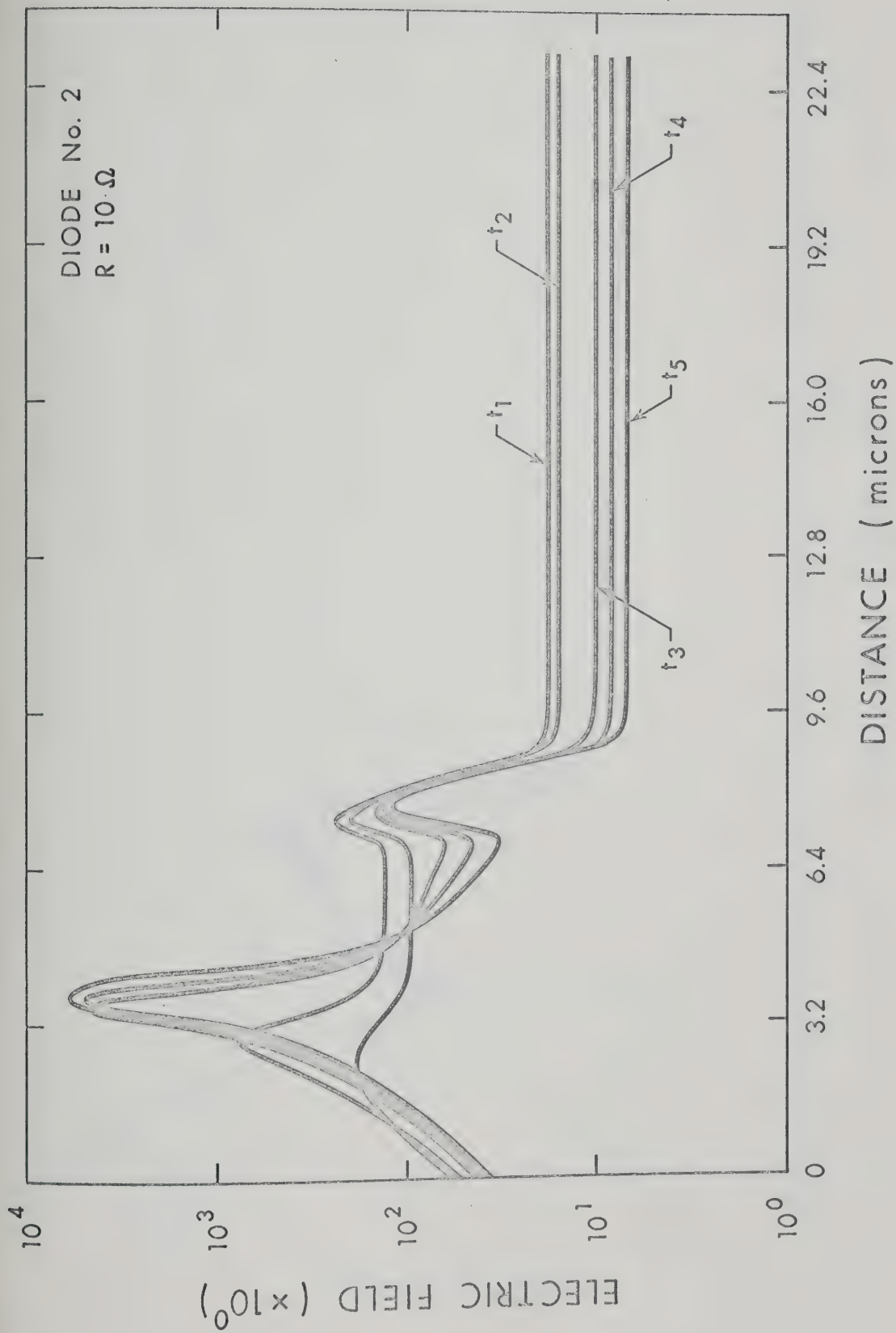


Fig. 9.12. Electric field distribution at various instants of time (values indicated in Fig. 9.11) during the reverse transient, for diode No. 2.

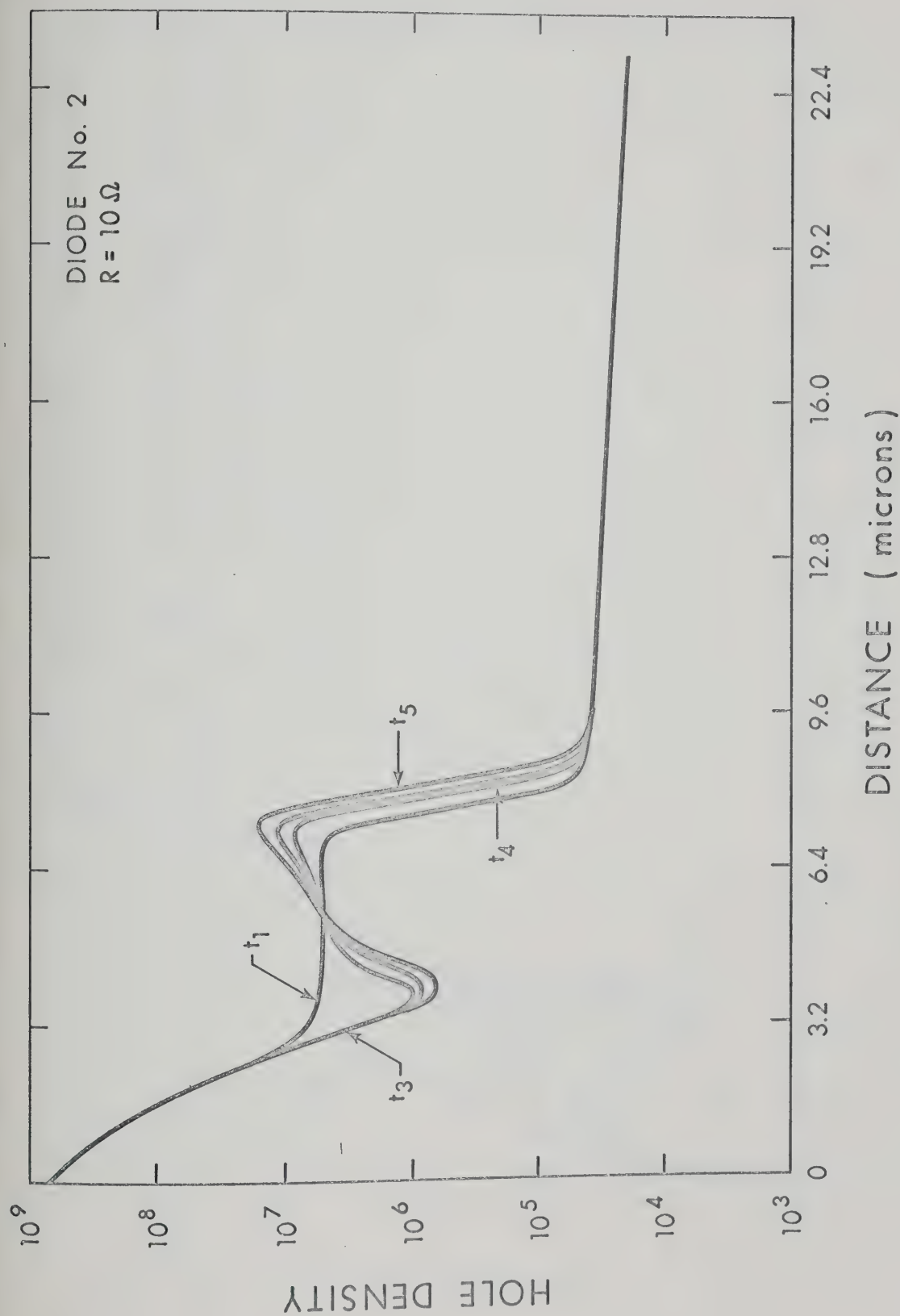


Fig. 9.13. Hole density distribution at various instants of time (values indicated in Fig. 9.11) during the reverse transient, for diode No. 2.

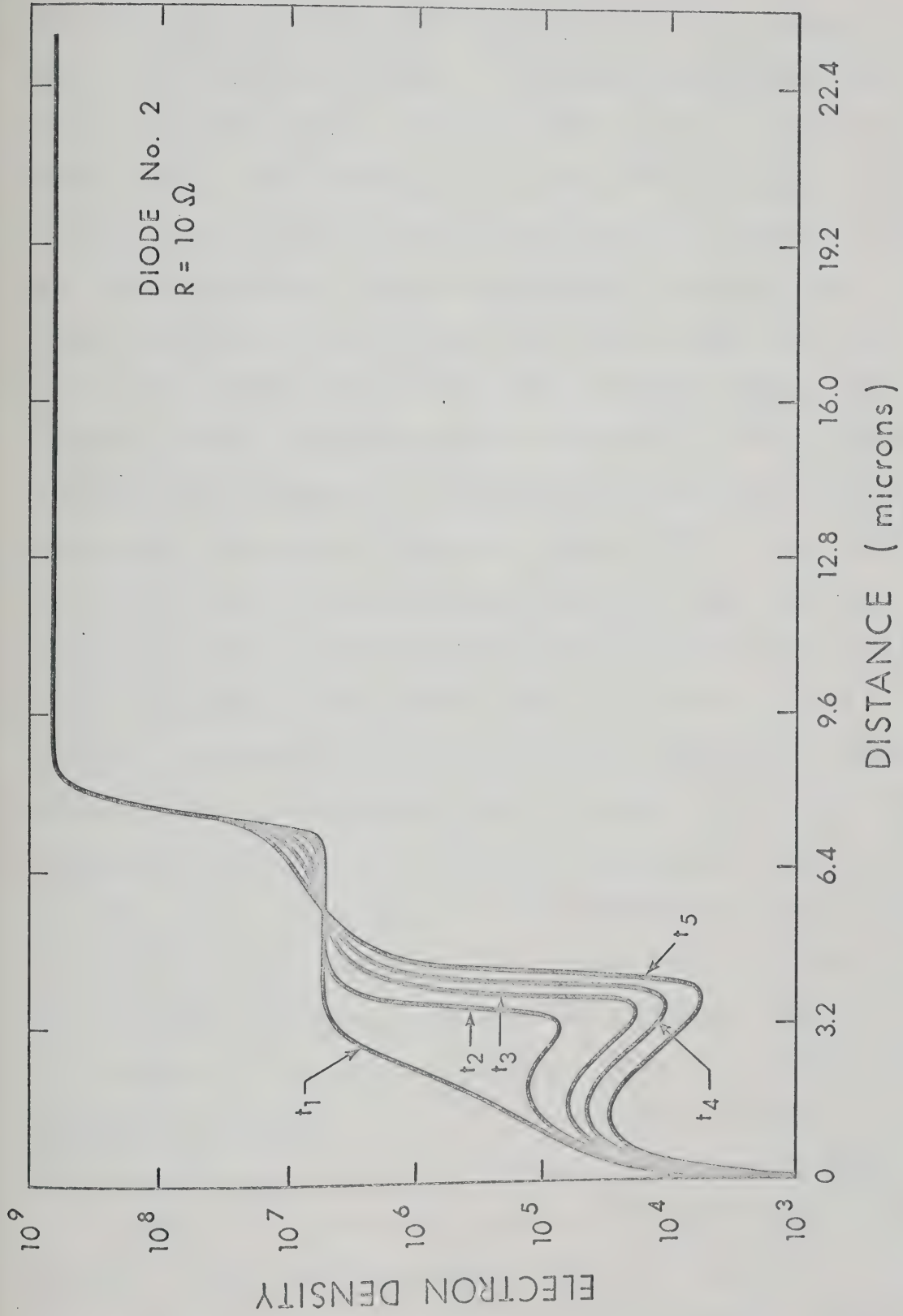


Fig. 9.14. Electron density distribution at various instants of time (values indicated in Fig. 9.11) during the reverse transient, for diode No. 2.

decreases and so does the negative electric field in the n-region. The current in the vicinity of the $n - n^+$ junction consists of both the hole and electron currents. The displacement current is relatively a small component and, therefore, can be ignored for the argument here. In the n^+ -region, current is mainly contributed by the majority carriers and the minority carrier current is negligible. In the n-region, current is made up of both the hole and electron current components. The electron current component being almost twice the hole current component. Figure (9.15) displays the distribution of both the hole and electron current components in and around the n-region for a particular time instant. Now let us examine what happens in the vicinity of the $n - n^+$ junction. The holes drifting towards the n-region under the influence of the small negative electric field in the n^+ -region, find a region of greater negative electric field in the vicinity of the $n - n^+$ junction, though the mobility has not changed. This region of greater electric field causes the hole current to increase due to a larger drift component. As the holes enter the edge of the n-region, the mobility increases and as a result the hole current magnitude further increases. When the hole reaches that part of the n-region where the electric field once again has a low value, the hole current decreases. This results in the accumulation of holes in the vicinity of the $n - n^+$ junction. As a consequence, a gradient of the hole concentrations is formed at the edge of the $n - n^+$ junction so as to support the terminal reverse current.

Now let us consider the electrons drifting towards the $n - n^+$ junction. As they reach the vicinity of the $n - n^+$ junction where large negative electric fields are present, the electron current increases due to a larger drift component caused by the electric field. When the

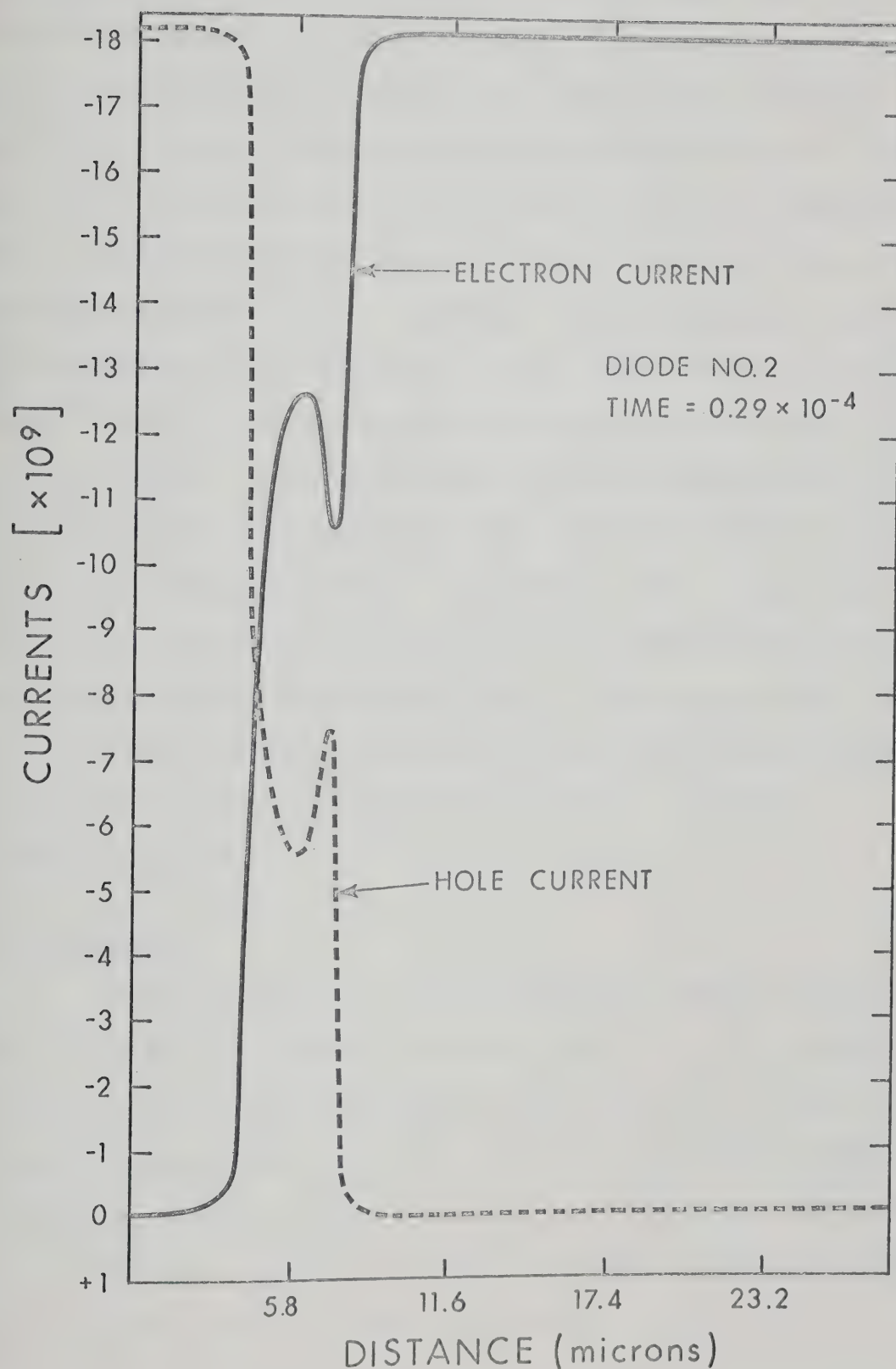


Fig. 9.15. Spatial distribution of hole and electron currents for a particular instant of time ($= 0.29 \times 10^{-4}$) during the reverse transient, for diode No. 2.

electrons cross to the n^+ -region part of the transition region, the mobility decreases, resulting in a decrease of the electron drift current. As the electrons travel a little further, they encounter a smaller electric field which results in making the electron drift current still smaller. The abrupt decrease in the mobility at the $n - n^+$ interface, thus, indirectly aids the electrons and the holes to accumulate in the neighbourhood of the $n^+ - n$ junction. The accumulation of both the holes and electrons in the vicinity of the $n - n^+$ interface results in a slight decrease in the electric field in the space-charge region at the $n - n^+$ interface. It may be mentioned that if the carrier mobilities are assumed constant throughout the device, the small charge accumulation at the $n - n^+$ interface would not be so obvious. This is one of the reasons that Benda et al.¹⁷ did not observe any charge accumulation in their analysis though they observed that the space-charge region at the $p^+ - n$ junction was mainly responsible for the voltage build-up across the device, and the space-charge region at the $n - n^+$ junction contributed little.

9.4 Conclusions

In this chapter, the 'turn-off' transient behaviour of diode No. 1 and diode No. 2 has been presented. The value of the current-limiting external series resistance has been chosen so as to enable the reverse recovery current to be much greater than the initial forward current. In the case of diode No. 1, the computations were terminated at 0.2×10^{-6} sec., since our interest is confined to times corresponding to the periodic times at microwave frequencies.

The reverse terminal current in diode No. 1 assumes a constant value after the initial decay due to the build-up of the ohmic drop. The presence of the electric field in the neighbourhood of the p-n junction helps maintain the 'constant current phase'. Moreover, the small electric field (positive) also 'pushes' the injected minority carriers from the regions close to the external contacts towards the space-charge region. This small positive electric field also gives rise to large majority-carrier drift currents in the bulk regions and these drift currents constitute the major part of the total current. Therefore, the majority carrier currents can no longer be ignored, as was done in the singly-injected diodes case. This effect that the minority-carrier current constitutes only a small portion of the total current, slows down the extraction of stored minority carriers compared to the case of the singly-injected diode.

In the case of diode No. 2, the space-charge region in the vicinity of the $p^+ - n$ junction plays the dominant role and behaves as a normal p-n junction under 'turn-off' transient conditions. The $n - n^+$ junction space-charge region has little effect. In the initial stages of the transient, it helps the terminal voltage to build-up, but at later times it shows a slight decrease in the electric field resulting from a small accumulation of the mobile-carriers. This unexpected behaviour may be attributed to the fact that the carrier mobility changes abruptly at the $n - n^+$ junction and there is an appreciable electric field present in the neighbourhood of the $n - n^+$ junction.

CHAPTER X

LARGE-SIGNAL, SINUSOIDAL EXCITATION RESPONSE

In this chapter, the computed results for the internal and external behaviour of diode No. 1 and diode No. 2 in a broadband, harmonic generating circuit are presented and briefly discussed.

10.1 Introduction

The broadband circuit of Fig. (10.1) is one of the simplest circuit configurations which can be employed for harmonic generation⁵⁷. The internal and external behaviour of the diodes in such a broadband circuit is analysed here. This circuit configuration is chosen to minimize the complexities of the external circuit and its interaction with the device. The analysis is based upon the numerical solution of the physical and mathematical model as discussed in Chapter III and Chapter IV. The details of the numerical solution are discussed in Chapter VI. The signal frequency is chosen to be 5 GHz, to reduce the computation time. However, lower microwave frequencies can be chosen at the expense of more computer time. The d.c. bias is assumed to be equal to 5 volts and the peak to peak value of the applied signal is assumed to be 12 volts. The load and source resistances (R_G and R_L) are assumed equal to 3.7 ohms. This value of resistance is within a factor of 5 of the computed series resistance of diode No. 1 at zero volts bias, (definition given in Chapter V).

Various quantities, such as electron and hole densities, electric field and diode terminal current and voltage are displayed in

normalised units, unless otherwise specified (see Table 4.1). Fourier analysis of the current and voltage waveforms yield the fundamental frequency contents and thus enables us to compute the large-signal impedance of the diodes at the generator frequency.

10.2 Results for Diode No. 1

The numerical solution for the diode behaviour in a broadband harmonic generating circuit of Fig. (10.1) is obtained here by applying both the reverse d.c. bias, and the a.c. signal simultaneously to the diode which is initially in thermal equilibrium. The results are obtained for the first five a.c. cycles. The terminal current, the terminal voltage and the applied signal as a function of time are displayed in Fig. (10.3). It is evident from Fig. (10.3) that the terminal response becomes almost repeatable in the time domain after the initial transient period ($\approx 1.1 \times 10^{-11}$ sec.). Detailed snap shots of the electric field, and the hole and electron density inside the diode during the fourth cycle are displayed in Figs. (10.4a), (10.4b), (10.4c) and (10.4d). Figure (10.5) gives the hole and electron densities for various time instants during the fourth cycle. Points to note are the following.

- (1) The electric field in the very vicinity of the metallurgical junction (1 to 2 microns on each side of the junction) controls the time-dependent behaviour of the device in this case. The electric field away from the junction (about 3 microns and more on each side of the junction) is small in magnitude; it thus contributes little to the time-dependent behaviour. The high electric field at the junction spreads into the bulk when the net applied voltage is negative and contracts back towards

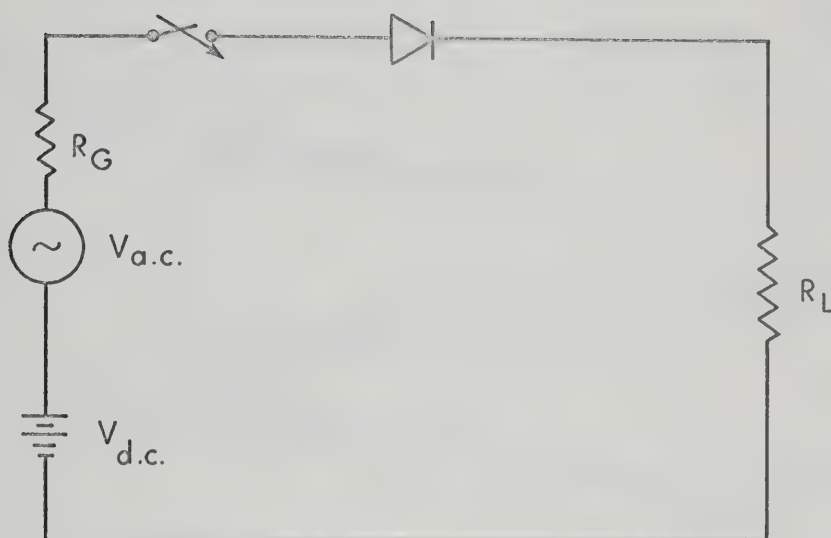


Fig. 10.1. Circuit model used for the study of the large-signal, sinusoidal excitation response of the diodes.

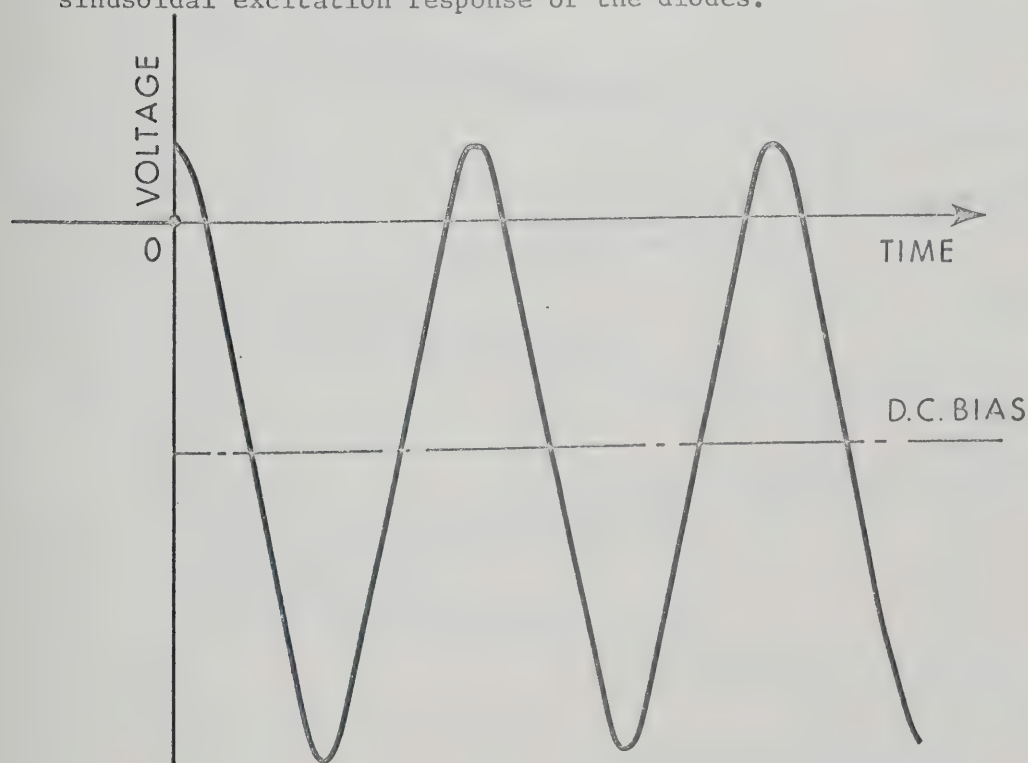


Fig. 10.2. Applied waveform in the circuit of Fig. (10.1).

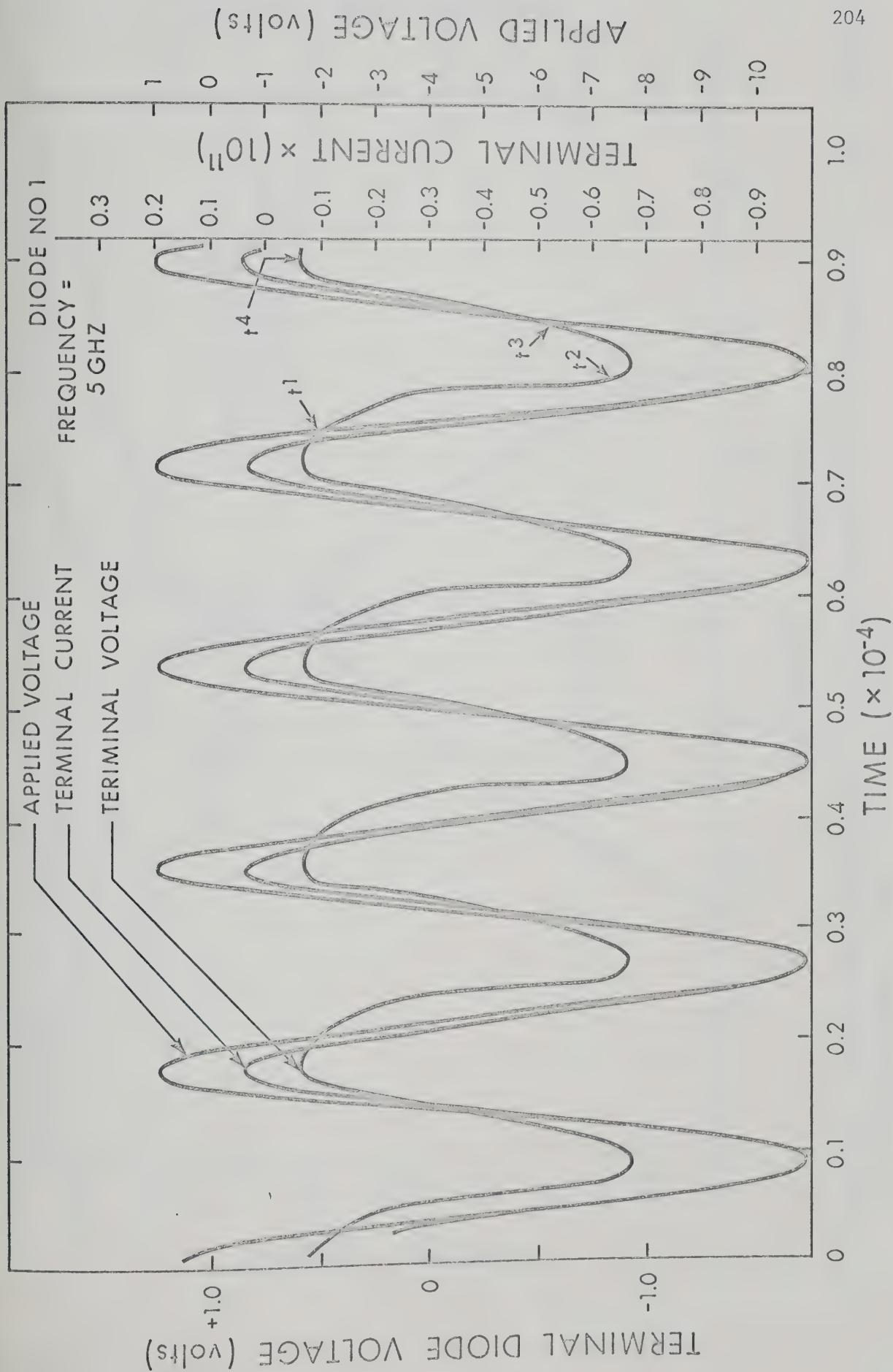


Fig. 10.3. Terminal voltage, applied voltage and terminal current versus time for the first five cycles after the signal is applied to diode No. 1.

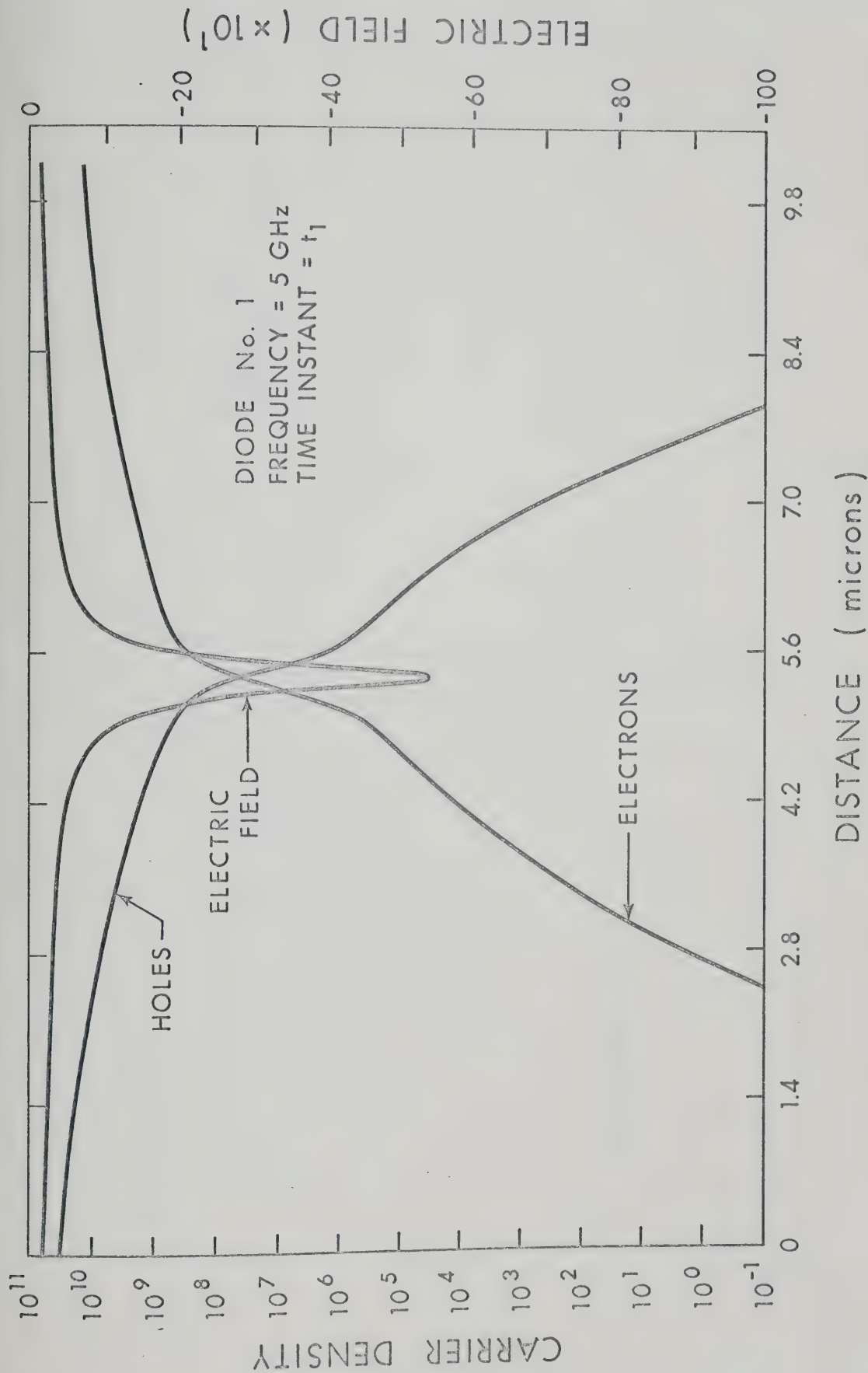


Fig. 10.4a. Spatial distribution of hole and electron densities and of electric field at time instant t_1 (value indicated in Fig. 10.3) for diode No. 1.

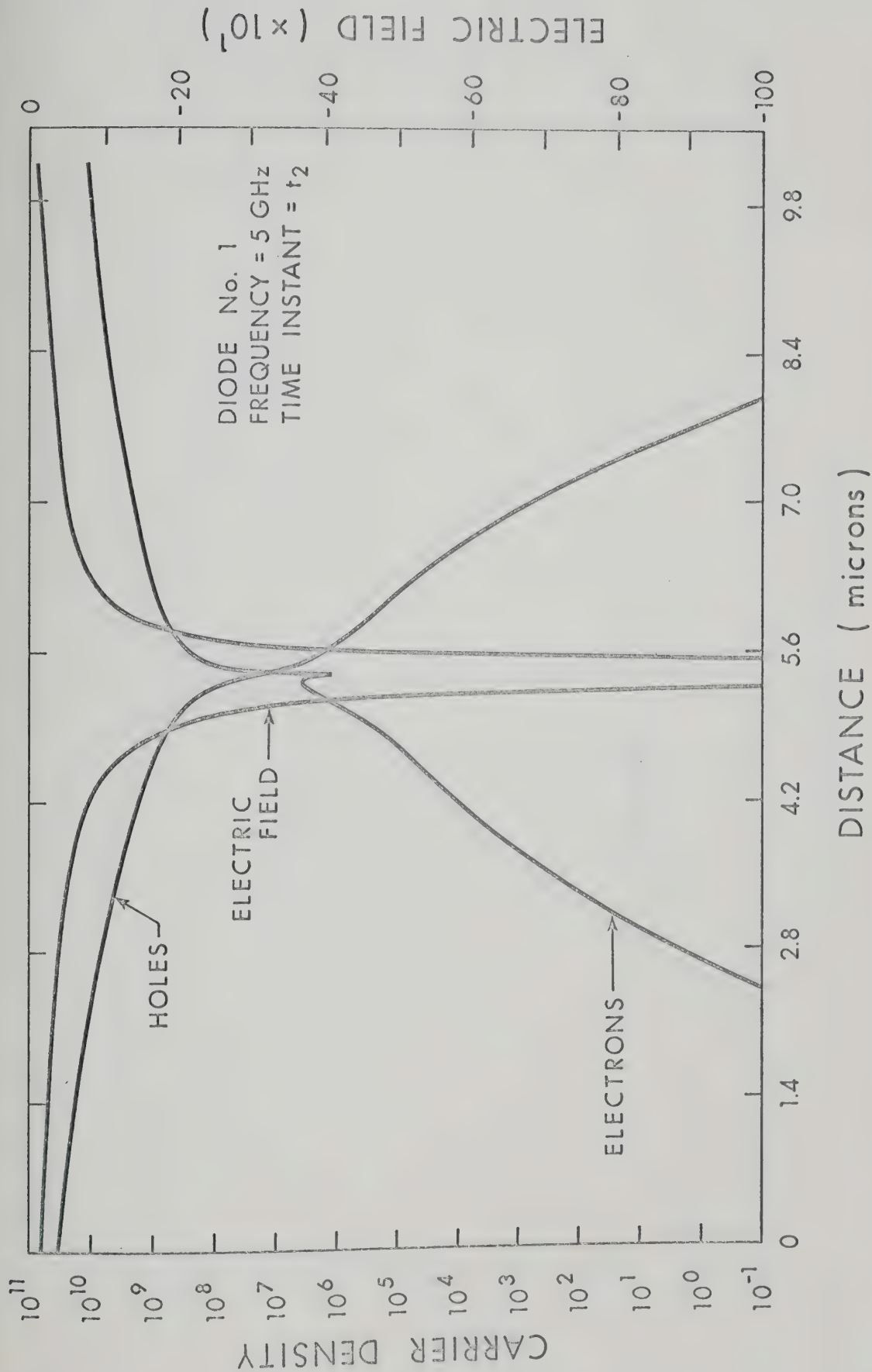


Fig. 10.4b. Spatial distribution of hole and electron densities and of electric field at time instant t_2 (value indicated in Fig. 10.3) for diode No. 1.

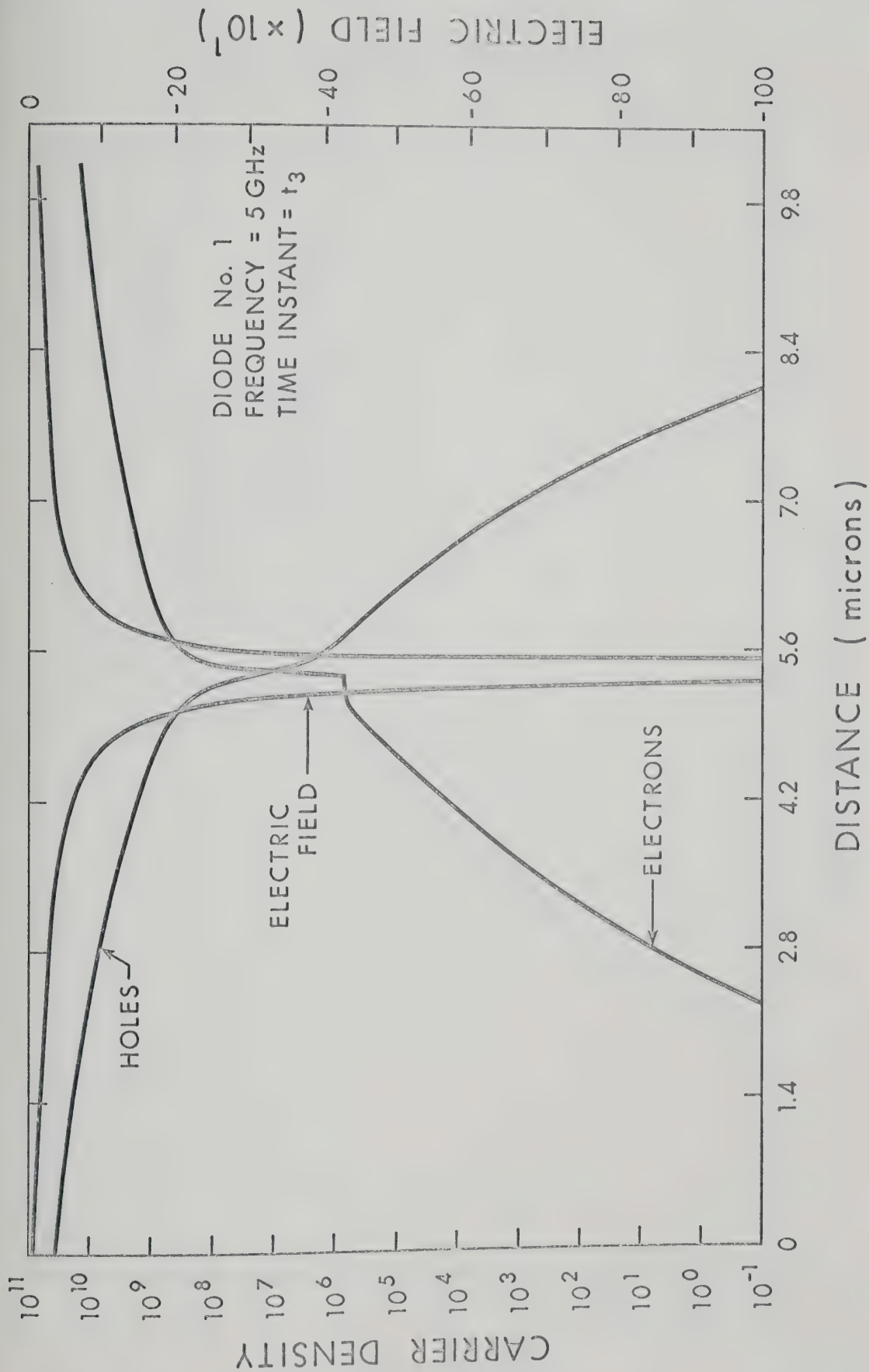


Fig. 10.4c. Spatial distribution of hole and electron densities and of electric field at time instant t_3 (value indicated in Fig. 10.3) for diode No. 1.

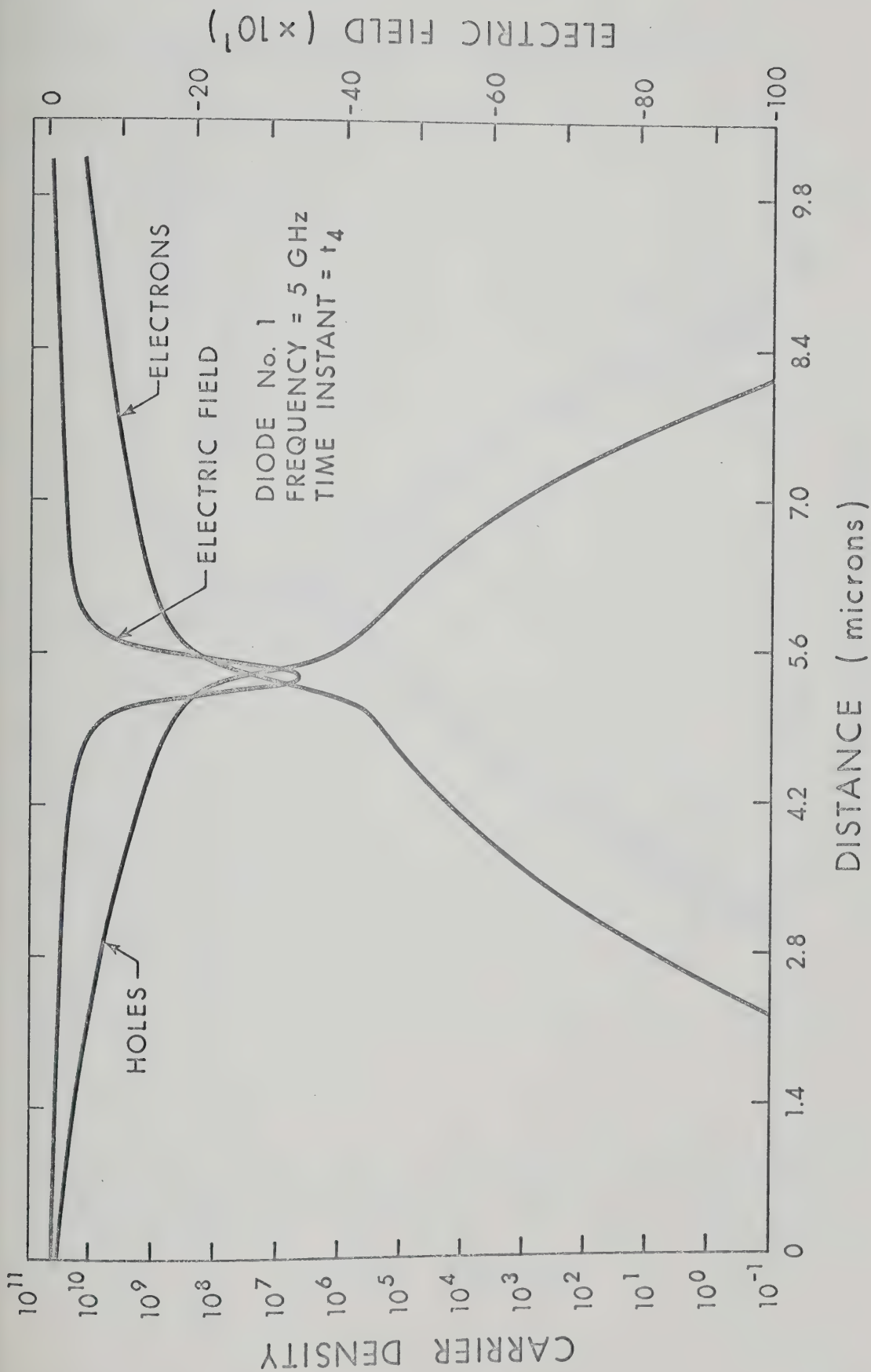


Fig. 10.4d. Spatial distribution of hole and electron densities and of electric field at time instant t_4 (value indicated in Fig. 10.3) for diode No. 1.

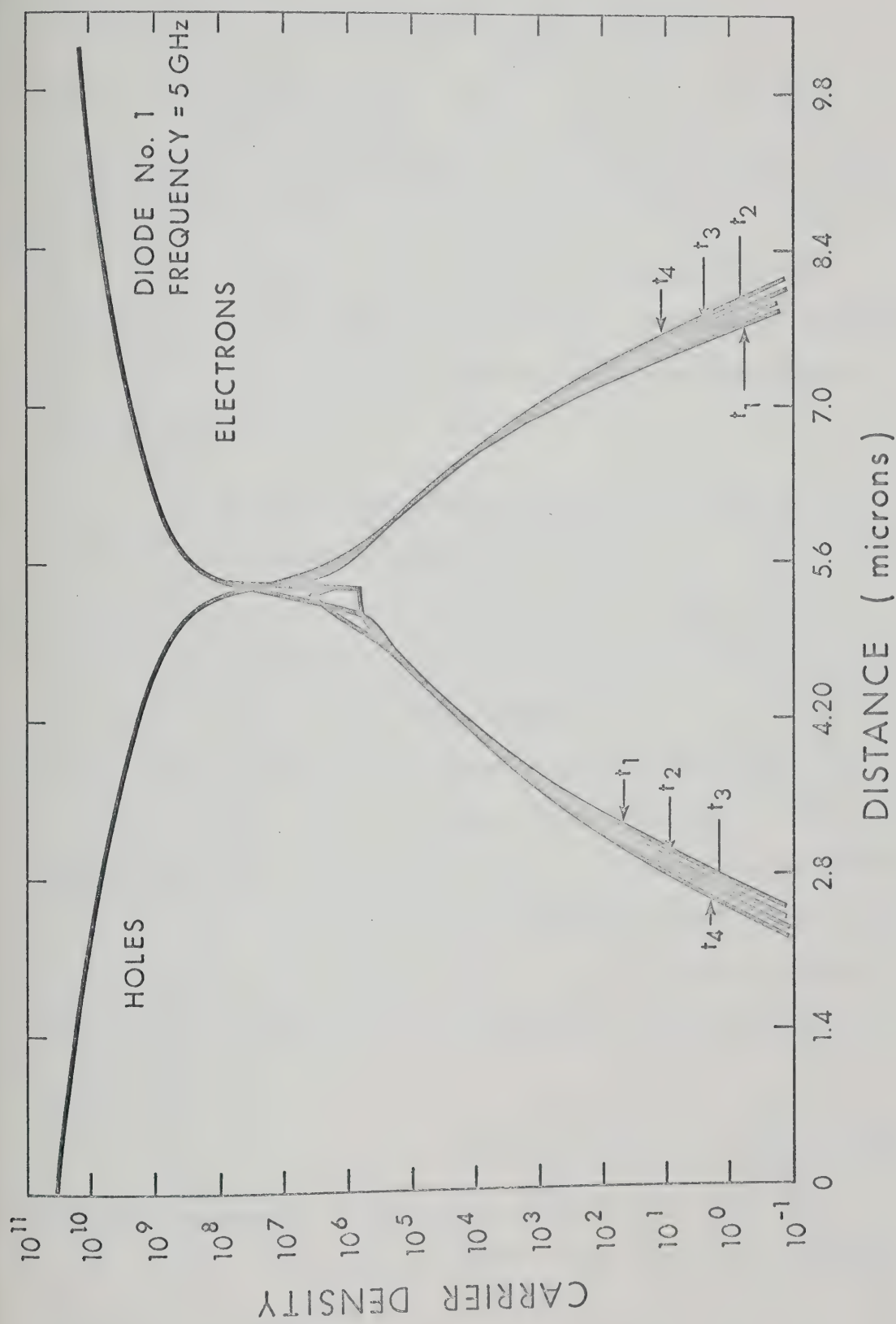


Fig. 10.5. Spatial distribution of hole and electron densities at various instants of time during the fourth cycle (values indicated in Fig. 10.3), for diode No. 1.

the junction when the net applied voltage is positive.

(2) The bulk regions exhibit large majority-carrier drift currents which account for almost the total current flowing. These current components result from the small electric field which is built in the bulk regions due to the flow of the large current. The displacement current is very small throughout the diode except in the very vicinity of the junction, where it contributes significantly to the total current.

(3) No significant recovery mechanism is exhibited for retrieving the injected minority-carriers which have moved relatively far away from the junction (2 microns or more). Large carrier concentration gradients here give rise to a forward particle current. The negative electric field here is small and does not give rise to a large reverse current, so that the minority-carrier currents have a net forward component. Thus, the carriers which are injected beyond the region of the high electric field tend to travel further towards the contacts rather than being retrieved during the reverse part of the cycle. However, the carriers present in approximately 1.5 microns width on each side of the junction are effectively retrieved during the reverse part of the cycle.

(4) The large-signal impedance of the diode is an effective value at the generator frequency obtained by the Fourier analysis of the terminal current and voltage waveforms. The value of the impedance obtained in the present case is $0.971 + j0.51$ ohms. This value of impedance, however, is not unique and depends upon the operating

conditions and the surrounding passive circuitry.

10.3 Results for Diode No. 2

The terminal current and voltage of the diode as a function of time are displayed in Fig. (10.6). Detailed results are computed for only one cycle after the initial transient vanishes because of the lengthy computer runs required to compute the results for a few more a.c. cycles. The results obtained for diode No. 1 show that the terminal response is almost repeatable once the initial transient has vanished. Detailed snap shots of the electric field, electron density and hole density as a function of distance during this a.c. cycle are displayed in Figs. (10.7a), (10.7b), (10.7c), (10.7d), (10.7e) and (10.7f). Figure (10.8) gives the terminal voltage and current as a function of time during the initial transient period. Points to note are the following.

(1) The electric field exhibits a large negative value in the n-region during the reverse part of the net applied voltage. However, during the forward part of the net applied voltage, an appreciable positive electric field is built-up in the n-region. Both the positive and negative electric fields built-up in the n-region during the a.c. cycle may be attributed to the ohmic voltage drop caused by the large current flow.

(2) The injected minority-carriers are kept well within the center n-region. The large negative electric field built-up in the n-region during the reverse part of the net applied voltage enables almost all of the injected minority-carriers to be retrieved.

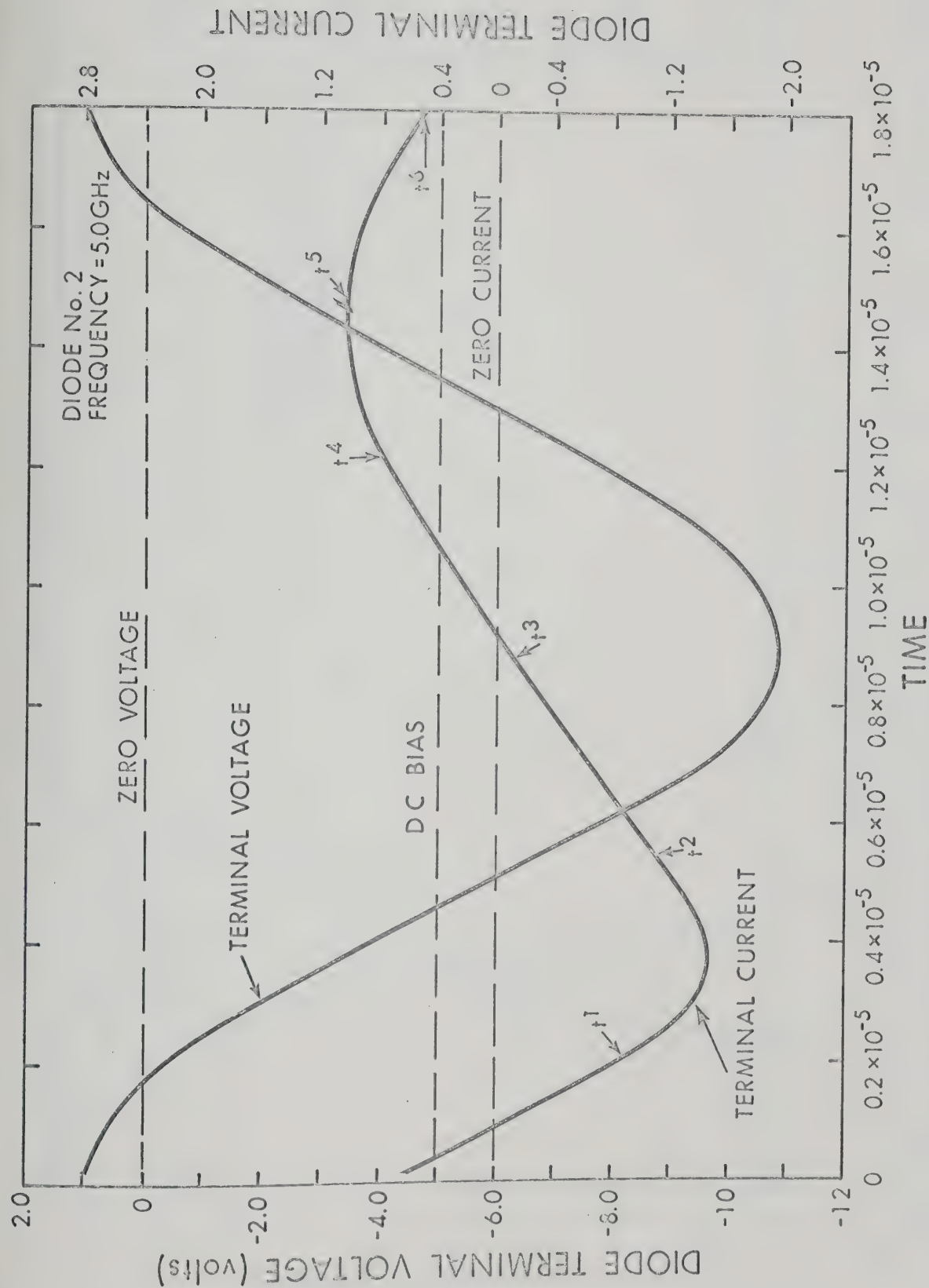


Fig. 10.6. Terminal voltage and current versus time for about the first cycle of the applied signal for diode No. 2.

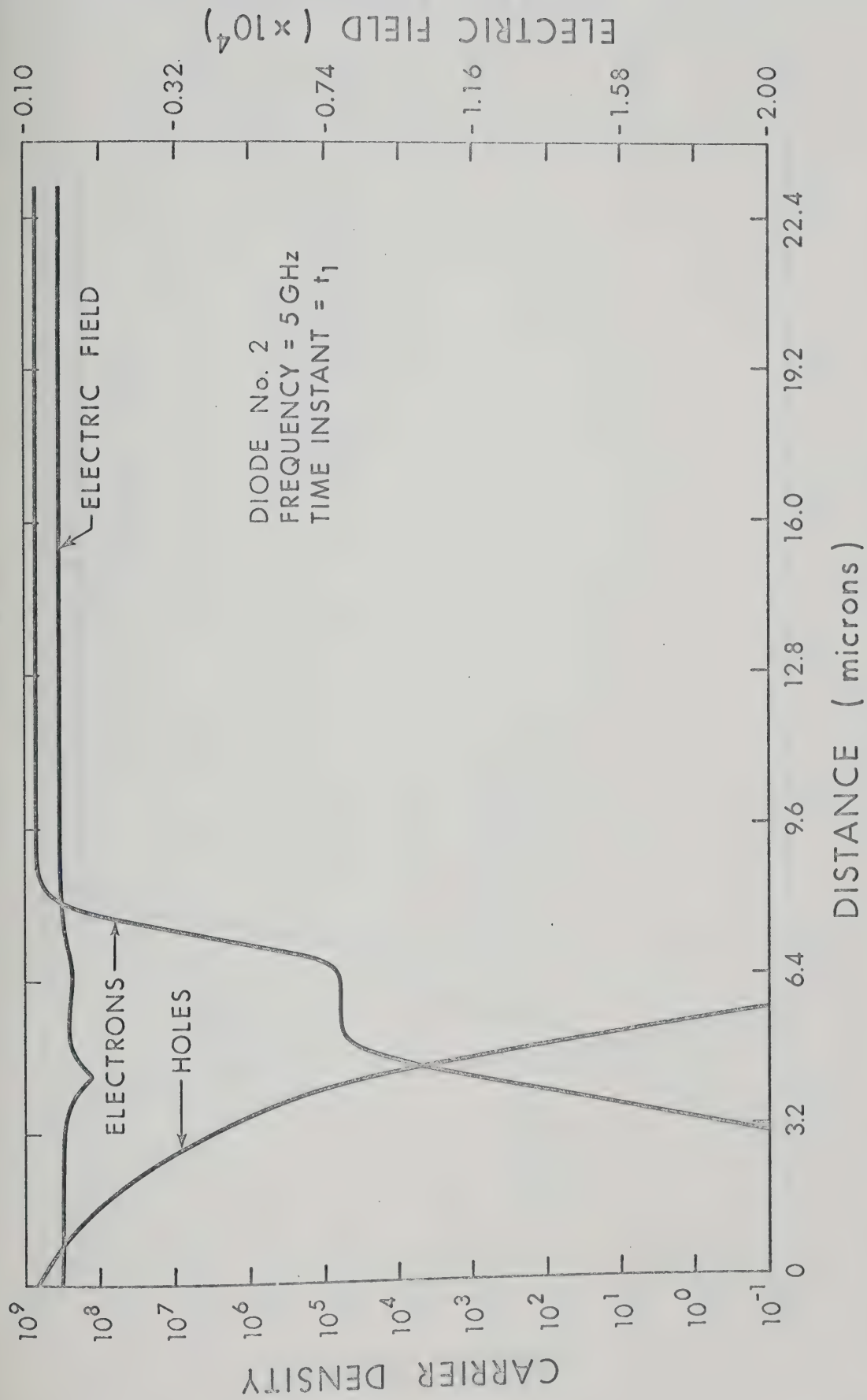


Fig. 10.7a. Spatial distribution of hole and electron densities and of electric field at time instant t_1 (value indicated in Fig. 10.6) for diode No. 2.

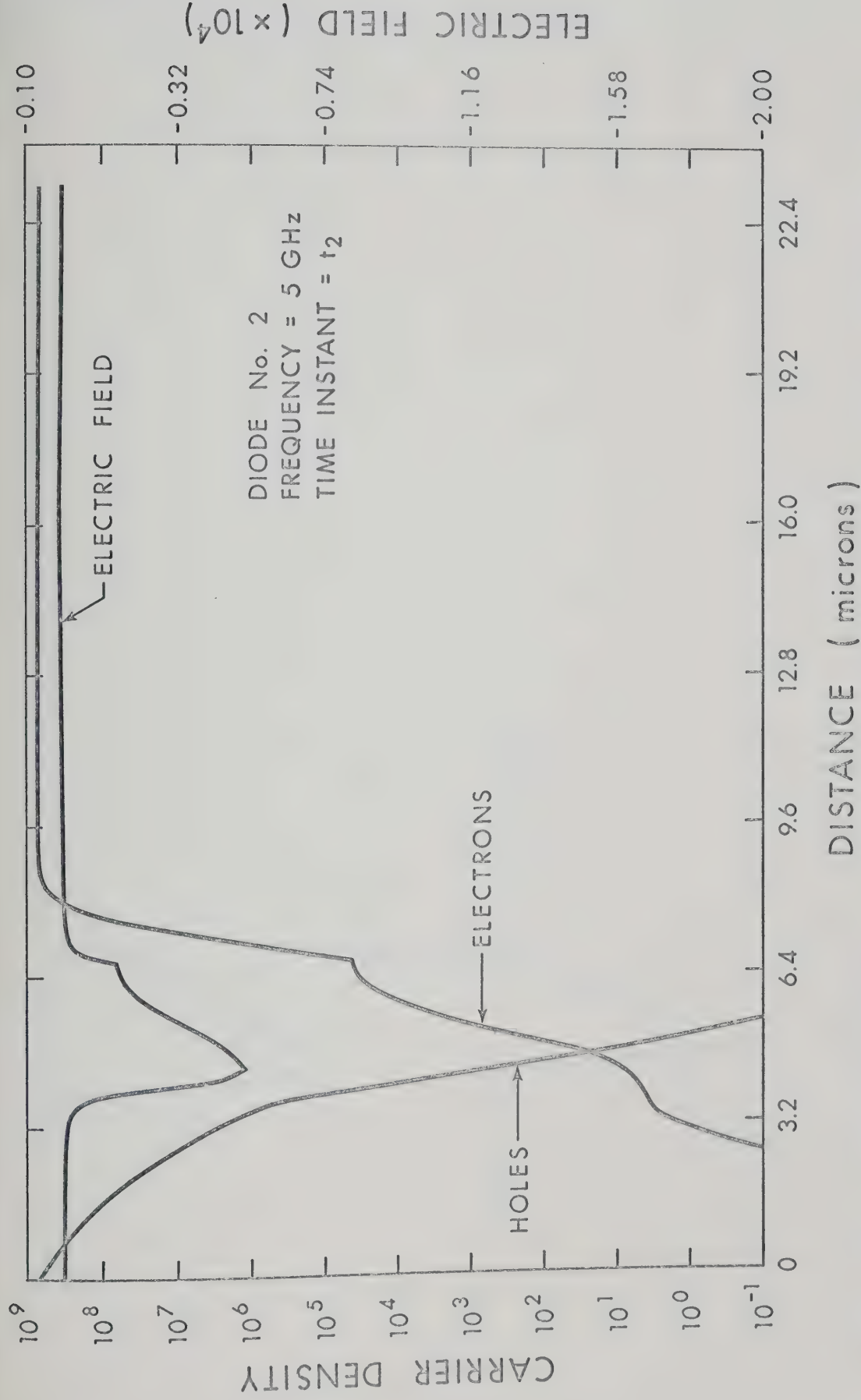


Fig. 10.7b. Spatial distribution of hole and electron densities and of electric field at time instant t_2 (value indicated in Fig. 10.6) for diode No. 2.

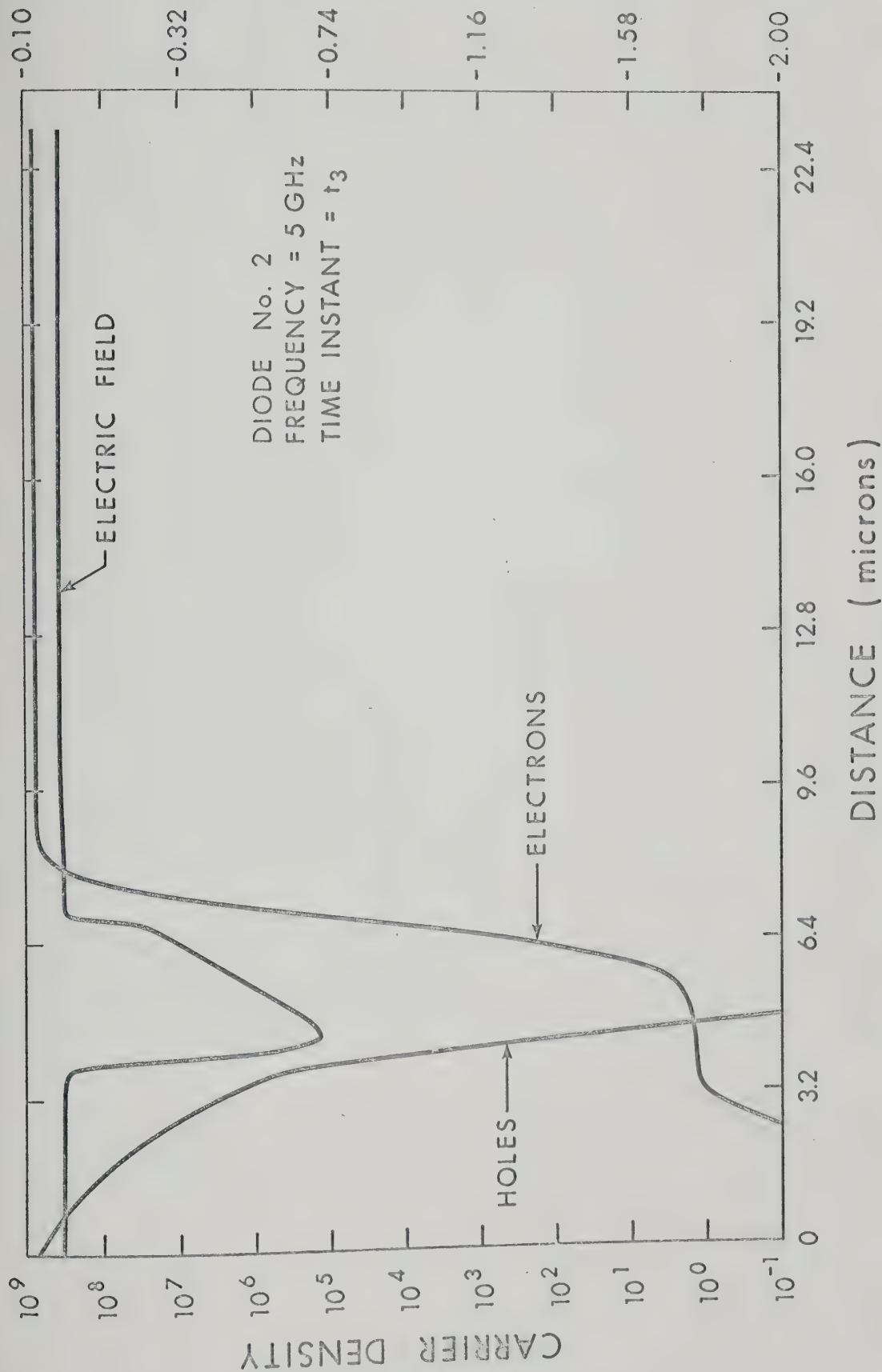


Fig. 10.7c. Spatial distribution of hole and electron densities and of electric field at time instant t_3 (value indicated in Fig. 10.6) for diode No. 2.

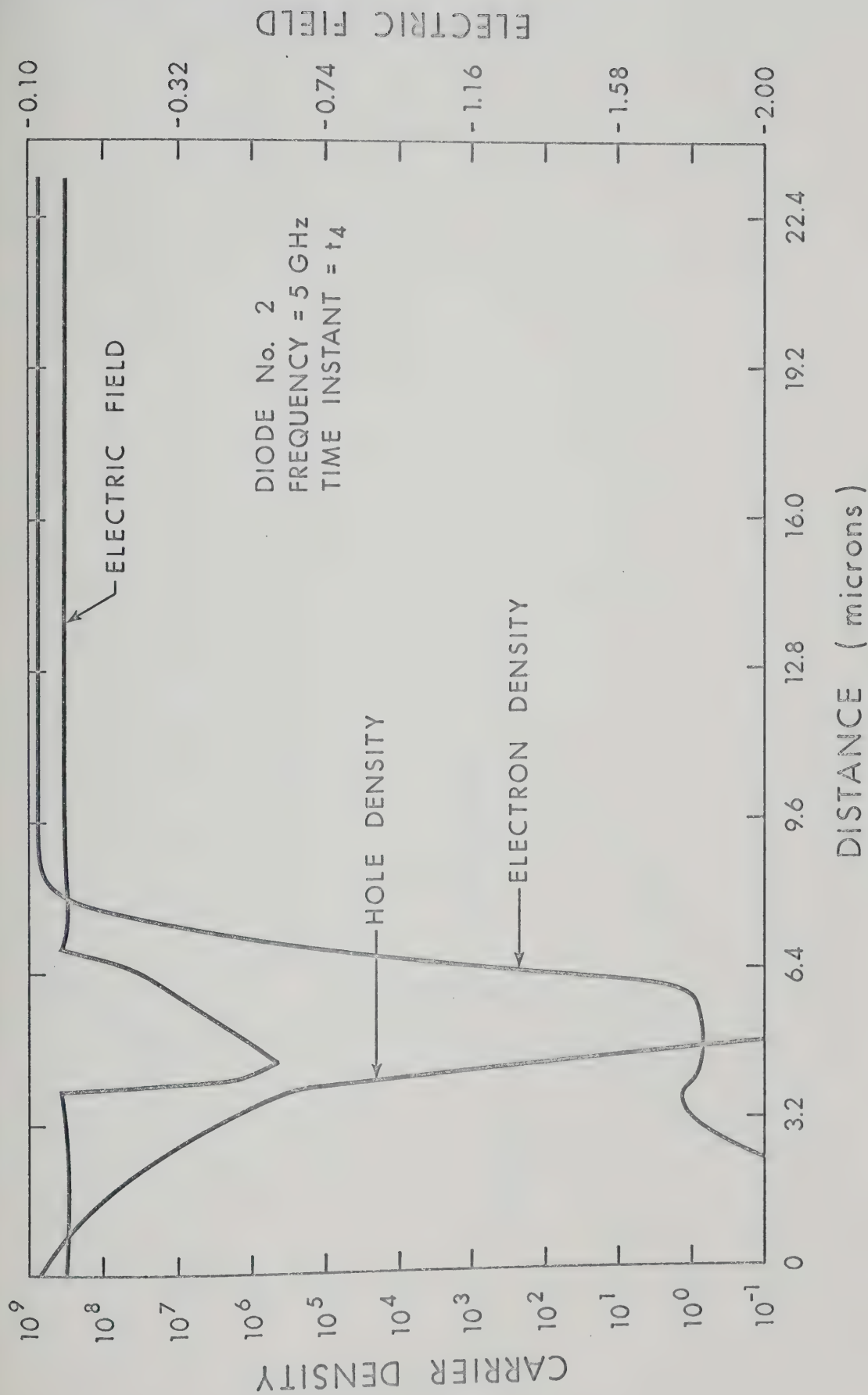


Fig. 10.7d. Spatial distribution of hole and electron densities and of electric field at time instant t_4 (value indicated in Fig. 10.6) for diode No. 2.

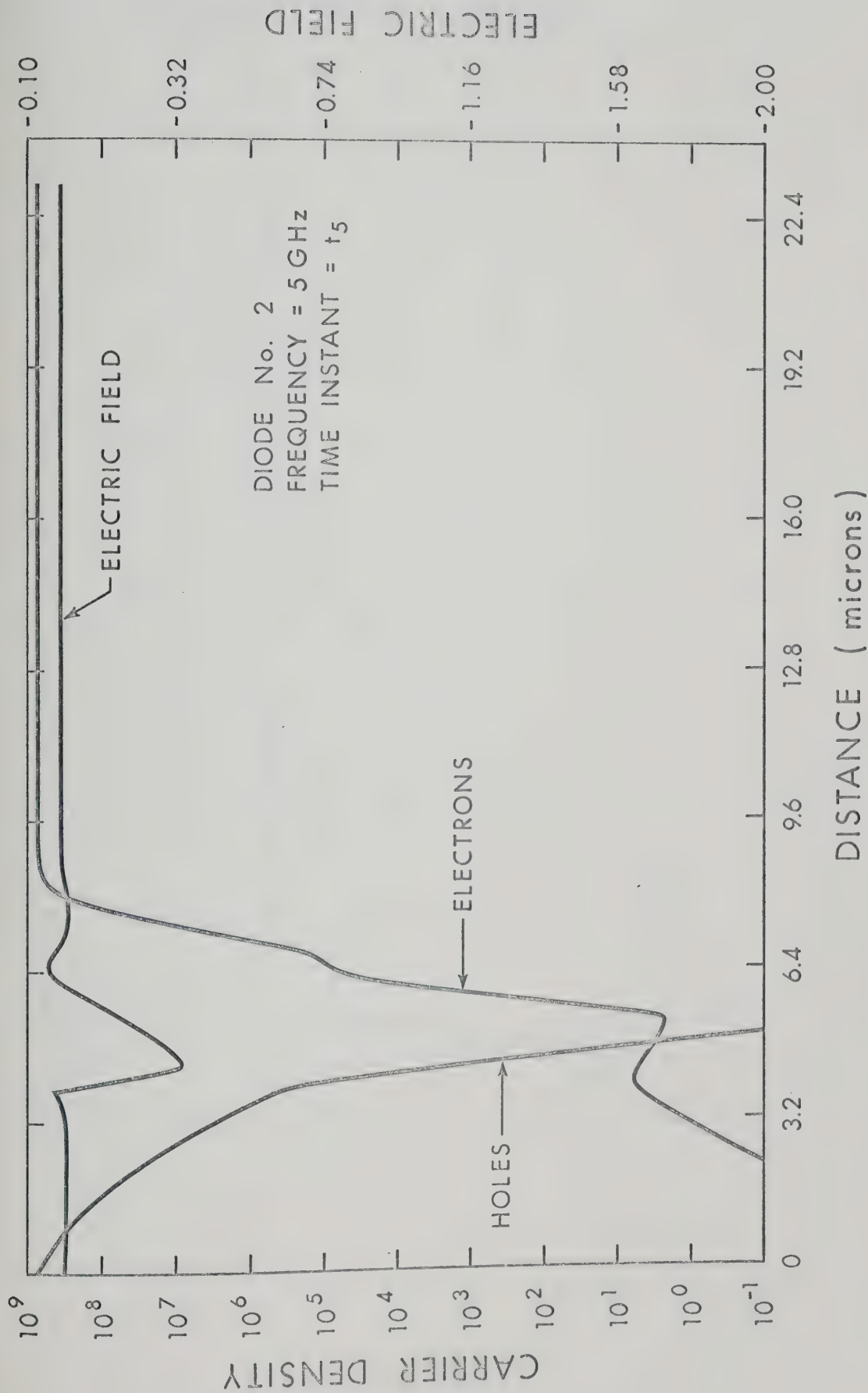


Fig. 10.7e. Spatial distribution of hole and electron densities and of electric field at time instant t_5 (value indicated in Fig. 10.6) for diode No. 2.

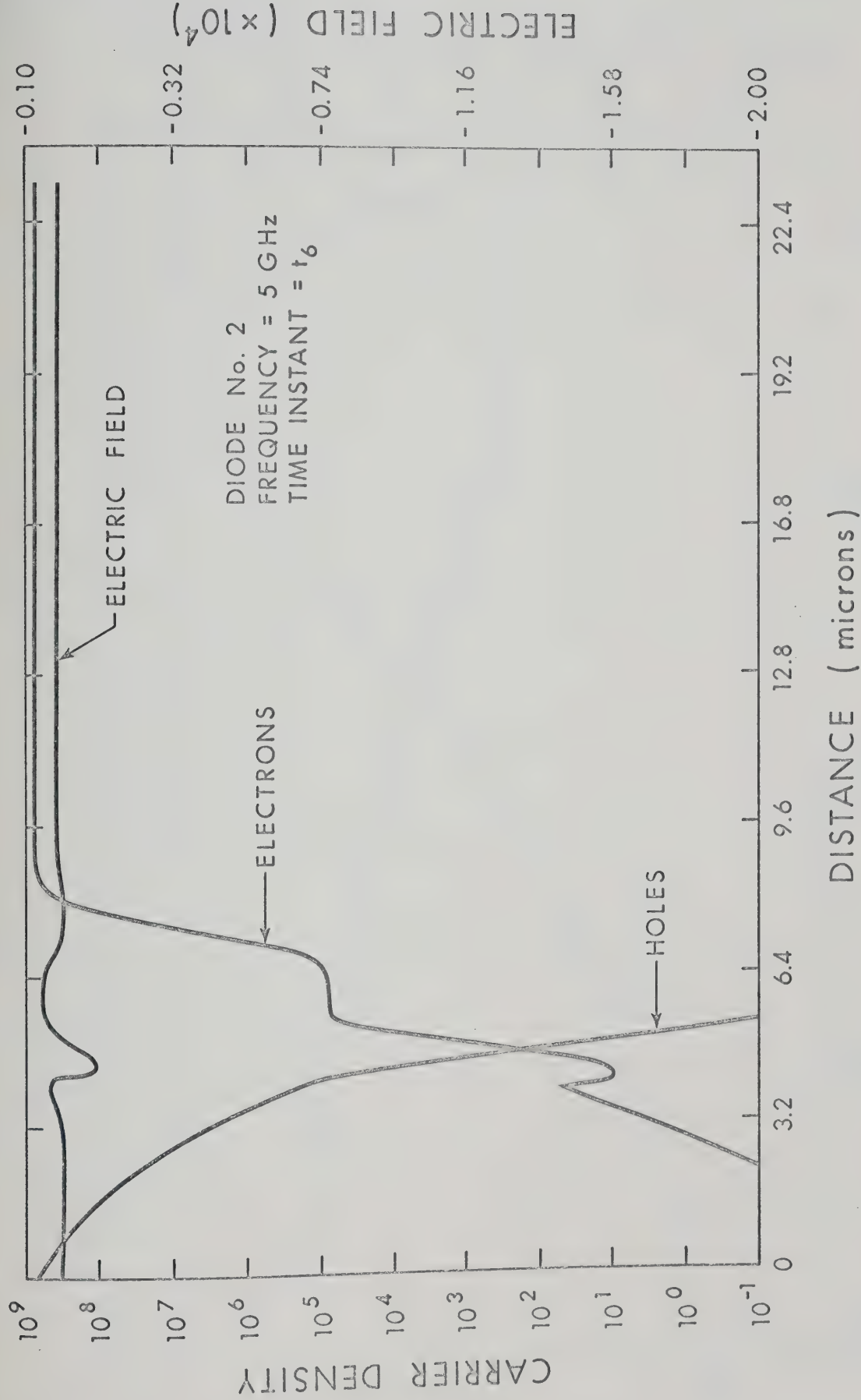


Fig. 10.7f. Spatial distribution of hole and electron densities and of electric field at time instant t_6 (value indicated in Fig. 10.6) for diode No. 2.

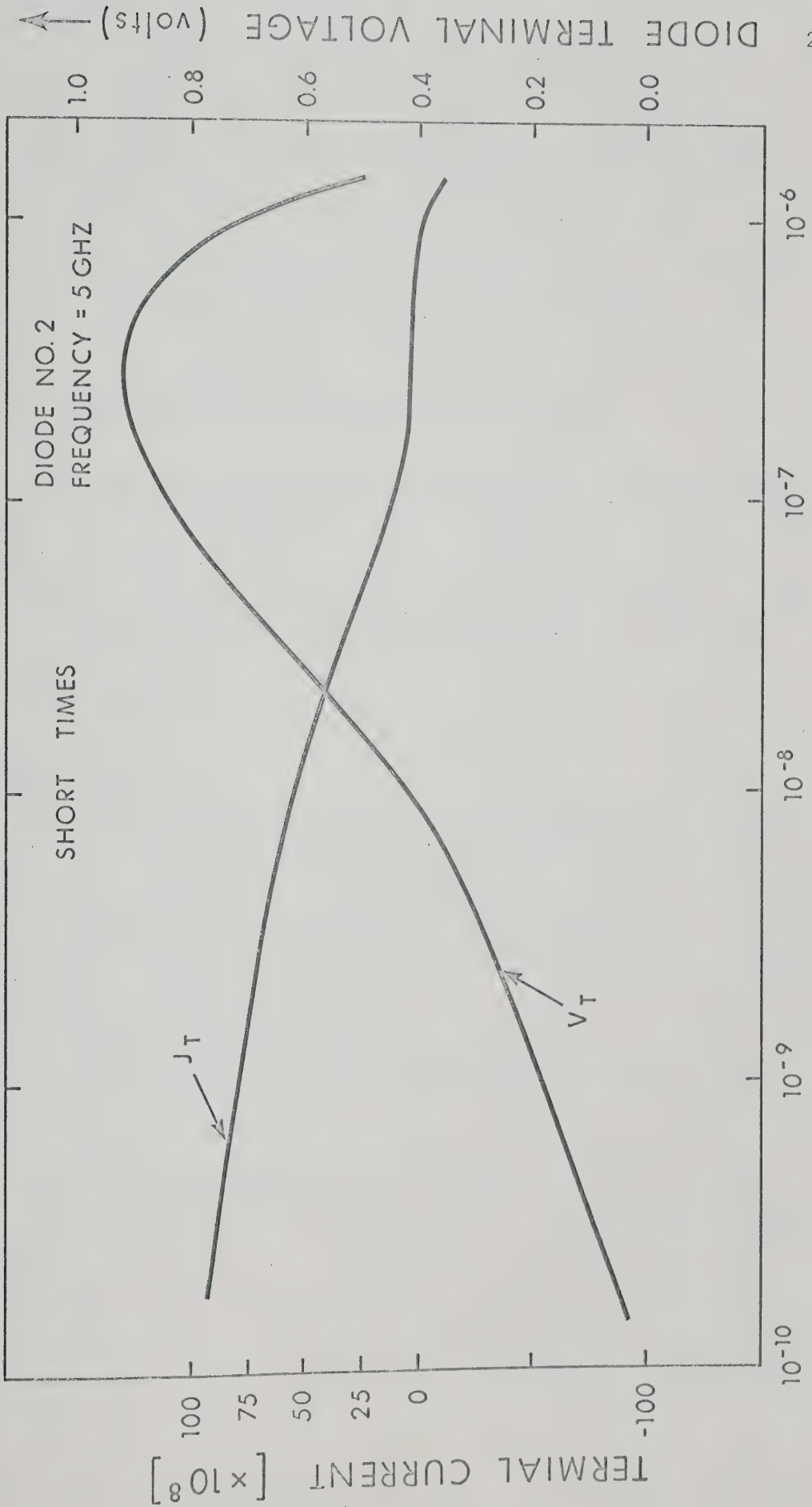


Fig. 10.8. Terminal voltage and current versus time for the initial transient period for diode No. 2.

(3) The bulk regions exhibit large majority-carrier drift currents which account for almost the total current flowing. These current components result from the small electric field which is built in the bulk regions due to the flow of a large current. The displacement current is relatively small in the p^+ - and n^+ -regions. In the n -region, the displacement current accounts for most of the total current and the particle currents are relatively small.

(4) The large-signal impedance of the diode at the generator frequency as defined in Section (10.2) is computed to be $46.102 + j374.96$ ohms. It may be stated again that this value of the impedance is not unique and depends upon the operating conditions and the surrounding passive circuitry.

10.4 Conclusions

The internal and external behaviour of diode No. 1 and diode No. 2 in a broadband harmonic generating circuit has been analysed. In the case of diode No. 1, no significant recovery mechanism is exhibited for the injected minority-carriers which have moved relatively far away from the junction (2 microns or more). In the case of diode No. 2 the injected minority-carriers are kept well within the center n -region. The large negative electric field present in the n -region during the reverse part of the net applied voltage, enables almost all of the injected minority carriers to be retrieved. The large-signal impedance of both diode No. 1 and diode No. 2 at the generator frequency shows an inductive character. This result indicates that the classical model of a varactor diode consisting of a series combination of a variable

capacitance and resistance may not always be valid and a variable inductance may be included in the equivalent circuit of a varactor.

CHAPTER XI

MICROWAVE MEASUREMENTS OF THE STATIC CHARACTERISTICS
OF A MICROWAVE VARACTOR

In this chapter, various techniques used to measure the static properties of a varactor, namely the series resistance and junction capacitance and hence static Q, are discussed. Measurements based upon these techniques are presented and compared. A commercially available step-recovery diode (Hewlett Packard No. 5082-0251) has been used.

11.1 Introduction

For most varactor applications at microwave frequencies, it is not adequate to rely on low frequency measurements of the varactors parameters; even parasitics may be frequency dependent. Besides, measurement of the series resistance at low frequencies is difficult and inaccurate. Microwave measurements are therefore necessary for varactor characterization. There are two basic methods of measurement presently applicable to waveguide-mounted varactors:

- (1) the transmission loss method due to DeLoach⁵⁸ with variations by Roberts and Wilson⁵⁹; and
- (2) relative impedance method due to Houlding⁶⁰ with variations by Harrison⁶¹ and Mavadatt⁶².

The transmission method^{58,59} requires mounting the diode in reduced-height waveguide and measuring the transmitted power near the series-resonant frequency. The method consists of either holding the bias fixed and varying the frequency⁵⁸ or holding the frequency fixed and

varying the bias⁵⁹. Due to the necessity of mounting the diode in waveguide, this method is limited in the range of junction capacitance and package inductance which may be resonated.

The relative impedance method^{60,61,62} requires matching the diode to a slotted line with a lossless tunable transformer. By changing the bias voltage and measuring the VSWR, the diode quality factor may be calculated by assuming a series resistance which does not vary with bias voltage. However, while measuring high quality varactors, the line loss and holder loss cause a large measurement error and correction for these additional losses is necessary. Sard⁶³ gave a new procedure to correct for these losses. However, this procedure is rather tedious and complex.

Another technique is presented here which considers the diode as a dielectric post mounted in the center of the waveguide. Various elements of the equivalent circuit⁶⁴ are determined by impedance measurements. These measurements are corrected to transform the impedance measured in a regular height slotted section to that in the reduced-height waveguide, in which the diode is mounted, using the procedure given by Oliner⁶⁵.

11.2 Dielectric Post Approach

11.2.1 Equivalent Circuit of the Diode in a Reduced-Height Waveguide

An account of the theory pertaining to the situation where the coaxial line presents an arbitrary impedance at the junction with the waveguide is given by Lewin⁶⁴, as shown in Fig. (11.1). For simplicity, the coaxial line in Fig. (11.1) is replaced by a lumped impedance Z_1 connected to the end of the perfectly conducting post, as shown in

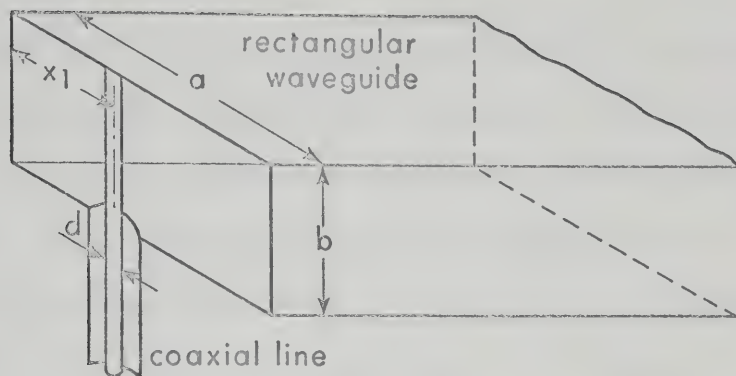


Fig. 11.1. Sectional view of junction between a rectangular waveguide (TE₁₀ mode) and coaxial line.

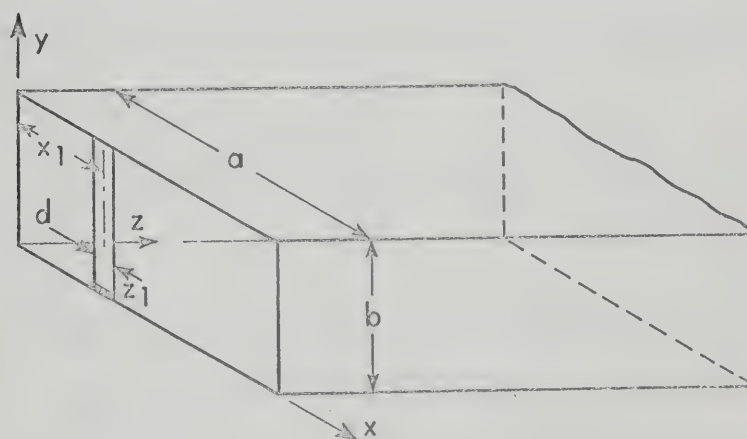


Fig. 11.2. Equivalent case of configuration shown in Fig. (11.1).

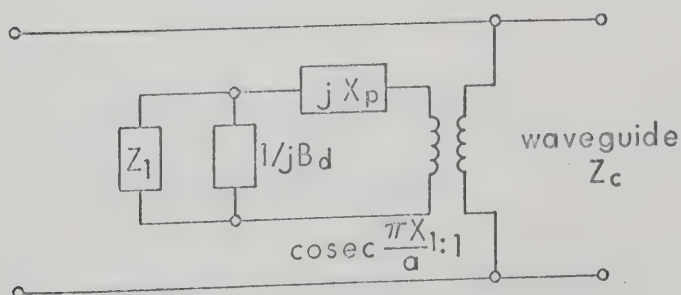


Fig. 11.3. Equivalent circuit for the configuration shown in Fig. (11.2).

Fig. (11.2). When a TE_{10} -mode electromagnetic wave is incident on a perfectly conducting post mounted in a waveguide, the incident electric field is cancelled at the surface of the post. Surface currents are set up on the post, and their radiation into the waveguide is responsible for the reflected wave that is set up. For a post of small diameter, that is, $\frac{\pi d}{a} \ll 1$, where d is the diameter of the post, the resulting effect is similar to that produced by a fictitious current filament located at the center of the post⁶⁴. A solution for the integral equation of current yields a value for the reflected wave which is dependent on and related to the impedance of the post as follows⁶⁴:

$$Z = Z_c \operatorname{cosec}^2 \frac{\pi x_1}{a} \left\{ \left(\frac{1}{Z_1} + \frac{1}{jB_d} \right)^{-1} + jX_p \right\} \quad \dots(11.1)$$

where

jB_d = capacitance susceptance term, and

jX_p = inductive reactance term.

In the course of actual numerical calculations, a value for the applicable waveguide characteristic impedance Z_c resulted in⁶³:

$$Z_c = 240 \pi \frac{b}{a} \left(\frac{\lambda_g}{\lambda} \right) \quad \dots(11.2)$$

where

λ_g = guide wave-length, and

λ = free space wave-length.

The capacitance contributing to jB_d was interpreted by Lewin⁶⁴ as the capacitance between the post and the walls of the waveguide as well as being due to the discontinuity at the junction of the coaxial line with

the waveguide. The post inductance for a perfectly conducting short-circuited post is given by⁶⁶:

$$jX_p = \frac{a}{2\lambda_g} \left\{ \log \left(\frac{4a}{\pi d} \sin \frac{\pi d}{d} \right) + S \right\} \quad \dots(11.3)$$

where

S = correction term, and

d = diameter of the post.

Figure (11.3) gives the circuit representation of Eq. (11.1).

Similarly, the impedance for the case of a dielectric post instead of a conducting post is obtained by replacing the electric field due to the filament current by an appropriate expression for the electric field. For a small diameter dielectric post, the post reactance jX_p' is given by^{66,67}:

$$jX_p' = \operatorname{cosec}^2 \frac{\pi x}{a} \left\{ j\omega \frac{\mu b}{2\pi} S_o + \frac{1/J_o^2(\pi d/\lambda)}{\frac{\pi d}{\eta b} j\sqrt{(\epsilon')} \frac{J_1\{\pi d\sqrt{\epsilon'}/\lambda\}}{J_o\{\pi d\sqrt{\epsilon'}/\lambda\}} - j\frac{\lambda d}{\eta b} \frac{J_1(\pi d/\lambda)}{J_o(\pi d/\lambda)}} \right\} \quad \dots(11.4)$$

where

J_o and J_1 = Bessel functions,

ϵ' = relative permittivity of the post material,

μ = permeability of the post material,

ω = frequency in radians per second, and

S_o = correction factor.

Using the explanation of Getsinger⁶⁷, the terms on the right side of Eq. (11.4) can be represented by a geometric reactance ωL_g of the post in the waveguide, the radial-line admittance of the dielectric post and the negative value of the radial line admittance ωC_d at the post radius, but with the post absent. If the admittance Y_t is complex, $-jX_p$ is replaced by a impedance Z_a .

$$Z_a = \text{cosec}^2 \frac{\pi x_1}{a} \left\{ j\omega L_g + \frac{1}{Y_t - j\omega C_d} \right\} \quad \dots(11.5)$$

These considerations lead to an equivalent circuit for a dielectric post mounted in a waveguide and terminated in a impedance Z_1 (i.e., coaxial cable, etc.). Figure (11.4) gives the complete equivalent circuit. At a given frequency, the real and imaginary parts of the post dielectric constant can be adjusted (conceptually at least) to provide any desired value of radial line admittance over the surface of the post. Let the dielectric post be replaced by a diode in a package consisting in part of an outer dielectric sleeve having the same diameter as the post and having the same radial line admittance over its surface. It would then be expected that the waveguide equivalent circuit for the dielectric post can also be used to represent the impedance of this new configuration with reasonable accuracy. If the diode is centrally mounted, which is the usual case, the transformer reduces to one with a unity turns ratio. The capacitance C_d is given by⁶⁷:

$$C_d = \frac{\pi d^2}{4h} \epsilon_o \quad \dots(11.6)$$

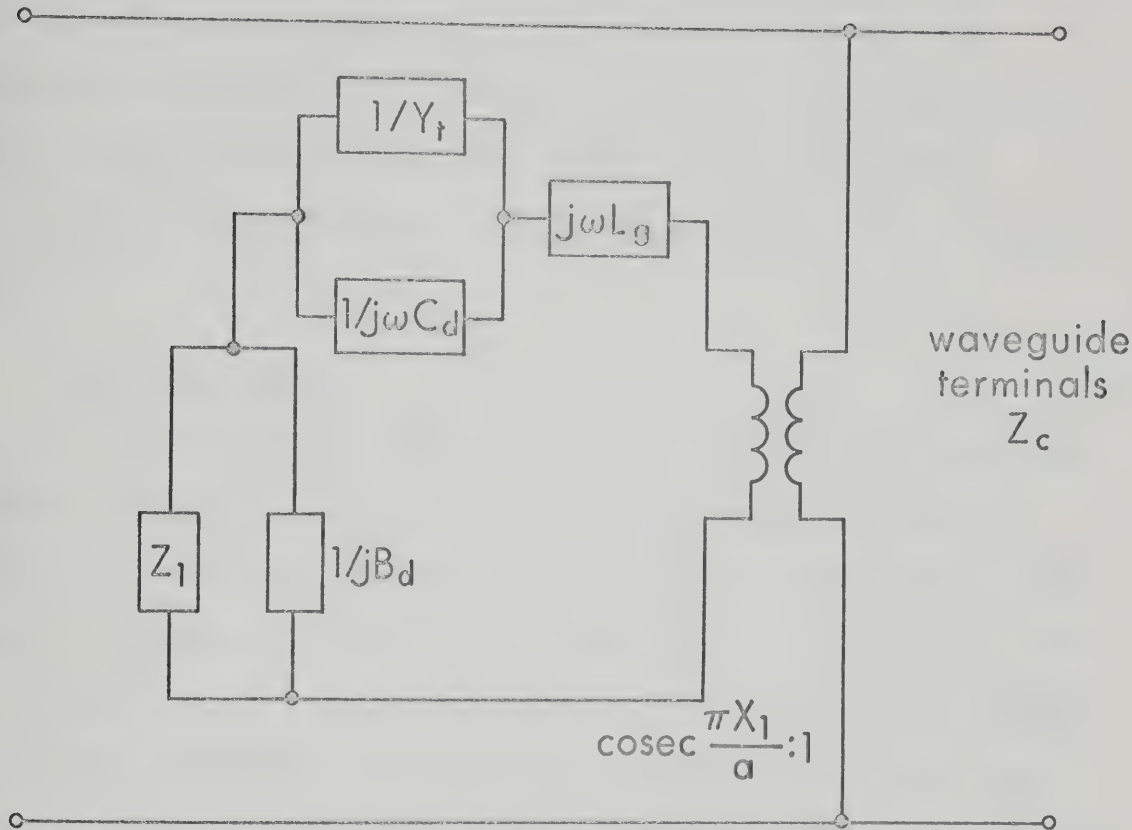


Fig. 11.4. Complete equivalent circuit for waveguide shunted by a small-diameter dielectric post and an impedance Z_1 presented by a coaxial line.

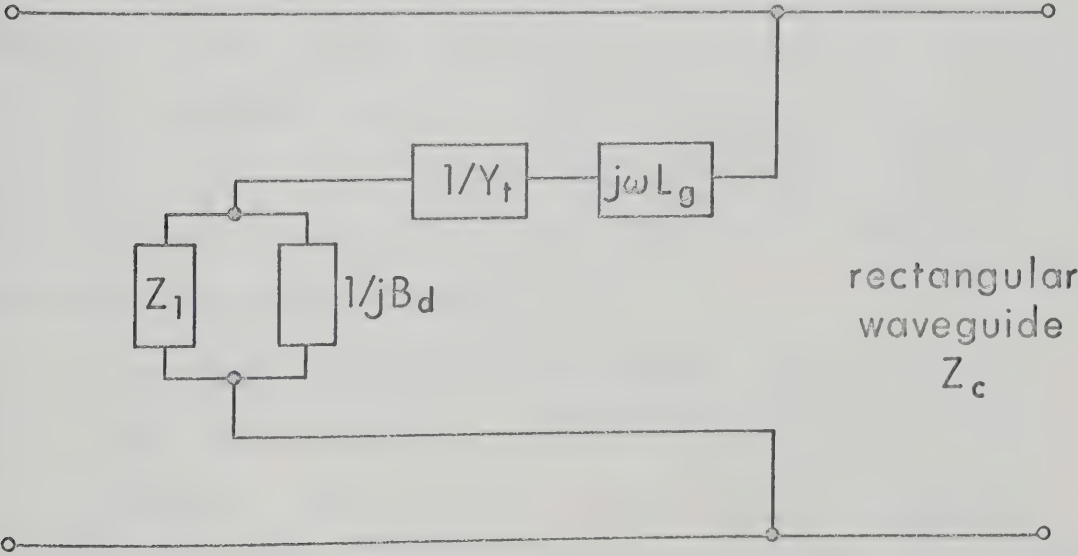


Fig. 11.5. Simplified equivalent circuit applicable for a centrally-mounted diode in the waveguide.

For a usual microwave diode, C_d is of the order of 0.02 pF. The presence of this parameter is ignored for our case as the capacitance to be measured is at least 20 times greater than C_d . Thus, the equivalent circuit reduces to a simplified circuit as shown in figure (11.5).

11.2.2 Measurements

To determine the packaged diode impedance from the equivalent circuit shown in Fig. (11.5), impedance measurements were made on a varactor diode mounted in a reduced-height rectangular waveguide whose height is chosen to be equal to the ceramic portion of the diode. Since no slotted line was available in reduced-height waveguide, measurements were made in a regular height waveguide (RGU/50) slotted line. The reduced-height diode mount was connected to the regular height waveguide by an impedance transforming section. The transformer used here was a quarter-wave stepped impedance transformer, which was theoretically designed to exhibit a return loss greater than 30 db all over the band. The actual transformer exhibited a return loss greater than 27 db over the frequency band of interest (6 - 8 GHz.) and 29 db for (6.35 - 6.9 GHz) along with 30 db at 6.4 and 6.7 GHz \pm 0.1 GHz, when two identical transformers were put back to back.

The reduced height diode mount is shown in Fig. (11.7). It uses a coaxial capacitor (more than 100 pF) to serve as a d.c. block and a r.f. by-pass. Steps were taken to ensure that the contacts at both ends of the diode package were practically lossless. Thin gallium washers were used to allow for small variations in the diodes dimensions. Both the diode mount and the impedance transformer were gold-plated to

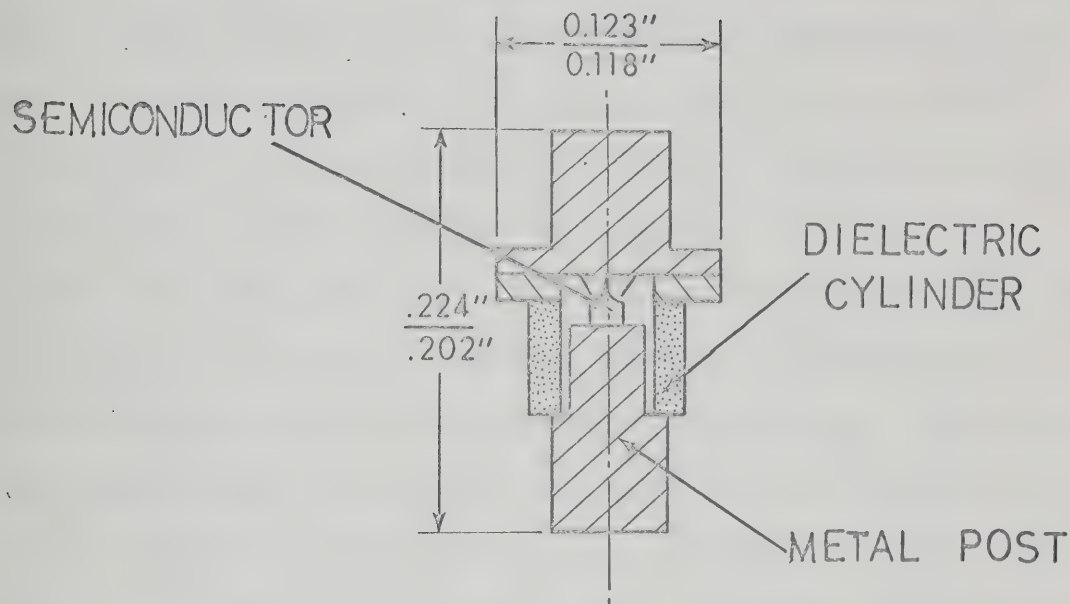


Fig. 11.6. Cross-section of a typical packaged varactor diode.

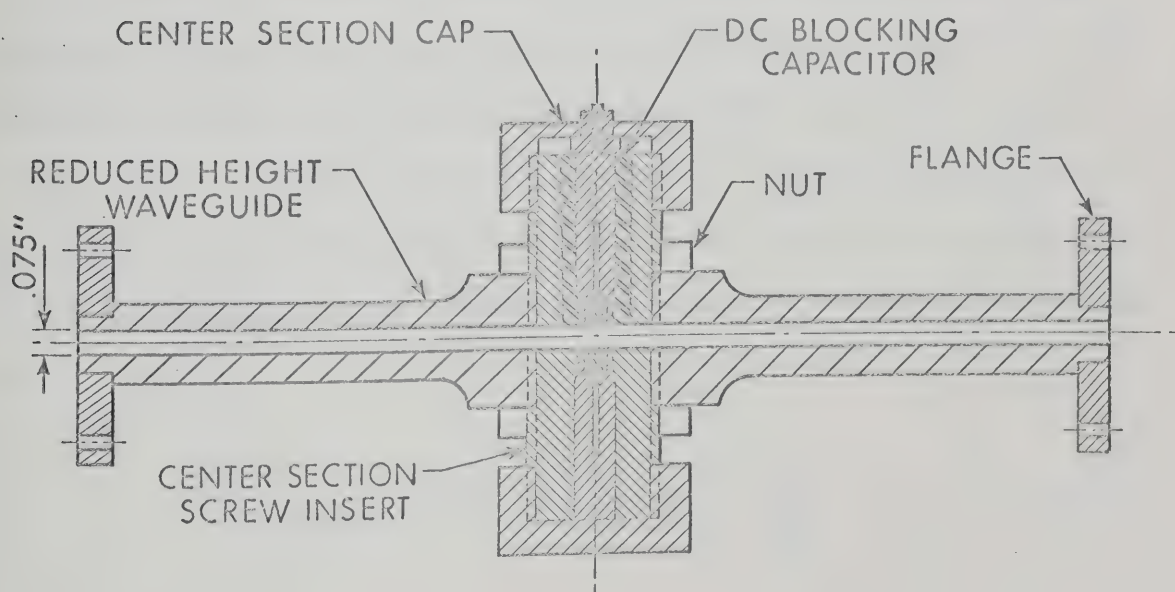


Fig. 11.7. The reduced-height rectangular waveguide diode mount.

minimize the losses.

First, the measuring system was calibrated to yield corrections for the discontinuity effects introduced by the impedance transformer, since the impedance measurements were made with a regular height slotted line. A procedure outlined by Oliner⁶⁵ allows correction of the measured data by means of a calibration curve. To obtain this calibration curve, positions of the voltage standing wave minima in the slotted line are accurately measured for various positions of an adjustable short circuit in the reduced-height section. These positions are closely spaced and readings must be taken over a distance of at least one-half of a guide wave-length at the frequency of the r.f. signal. From these measurements, a curve showing the difference between the position of the short circuit and the position of a minimum in the slotted line (both with arbitrary reference planes) as a function of the position of the slotted section is obtained. The calibration curve is strictly valid only for lossless terminations. However, Oliner⁶⁵ gave a procedure in which complex impedances can also be dealt with, using the same calibration curve and certain approximations. The applied equations then become⁶⁵:

$$D_{\text{corrected}} = \left[D + \Delta D \left\{ \frac{r_m^2 + 1}{r_m^2 - 1} \right\} \frac{\lambda_{gs}}{\lambda_{gd}} \right] \quad \dots(11.7)$$

$$r_{\text{corrected}} = r_m \left[1 + \frac{4\pi}{\lambda_{gd}} \left[\Delta D \right]^{1/8} \right] \quad \dots(11.8)$$

where

D = position of voltage minimum,

ΔD = correction available from calibration curve,

r_m = measured VSWR,

λ_{gs} = guide wave-length of moveable short,

λ_{gd} = guide wave-length of slotted line section,

$D_{\text{corrected}}$ = position of voltage minimum after correction,

$r_{\text{corrected}}$ = corrected value of VSWR, and

$\Delta D_{1/8}$ = correction available from calibration curve for
a position $D - \lambda_{gd}/8$.

A schematic of the experimental arrangement is shown in Figure (11.8). The experimental procedure was as follows: The position of the voltage minimum was noted for many closely-spaced positions of the adjustable short circuit in the reduced-height section. Readings were taken over a distance of more than one-half of a guide wave-length, at the frequency at which measurements were desired. The adjustable short circuit was placed at a distance $\lambda_g/2$ behind the position in which the diode is mounted. The diode and coaxial line were then removed and the resulting hole in the broad wall of the waveguide was closed by a gold-plated flat brass plate. The position of a reference voltage minimum in the slotted line was noted and corresponded to a short circuit at the plane of the diode. Then the adjustable short circuit was placed at a distance $\lambda_g/4$ behind the location at which the diode is mounted, thus corresponding to an open circuit at the plane of the diode. With this position of the short circuit, the VSWR and position of the minima was

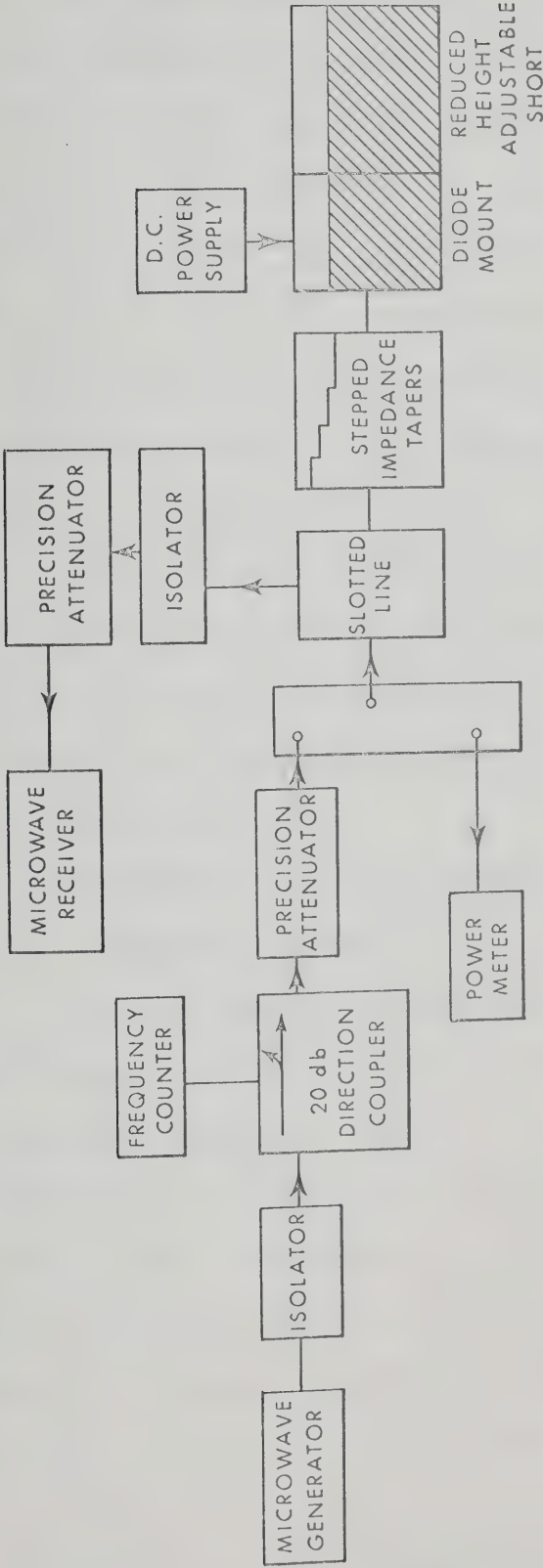


Fig. 11.8. Circuit arrangement used for measurements on waveguide mounted diodes.

noted when the coaxial line was reinserted with a highly conductive post of the same shape and size in place of the diode. The conducting post was then replaced with the diode, and the position of the voltage minimum and the VSWR were noted, the short circuit remaining in the same position. These readings were taken for various d.c. bias voltages applied to the diode. All these measurements were corrected as given in Eqs. (11.7) and (11.8). From the equivalent circuit given in Fig. (11.5), it is seen that the diode terminal impedance at any bias is readily calculated from the above measurements as the difference between the measured impedance of the assembly and the impedance of the system with a dummy diode substituted for the varactor. A calibration curve for a frequency of 6.757 GHz is shown in Fig. (11.9). Measurements* on the HP step-recovery diode No. 5082-0251 are listed in Table (11.1). The value of the characteristic impedance Z_0 , calculated from Eq. (11.2) is 53.8 ohms for this case.

11.2.3 Obtaining the Series Resistance from the Measured Terminal Impedance

The most commonly accepted equivalent circuit⁶⁷ of a varactor whose cross-section is as shown in Fig. (10.6) is as shown in Fig. (11.10), for the small signal case. For the measurements at the frequency considered here, fringing capacitance C_B can be neglected and the equivalent circuit simplifies to the circuit shown in Fig. (11.11). The value of the package inductance L_A and package capacitance C_A can be measured as outlined by Getsinger⁶⁷. However, to perform the measurements of L_A and C_A with sufficient accuracy, we need a set of

* Similar technique was applied to tunnel diodes by Scanlan⁶⁸.

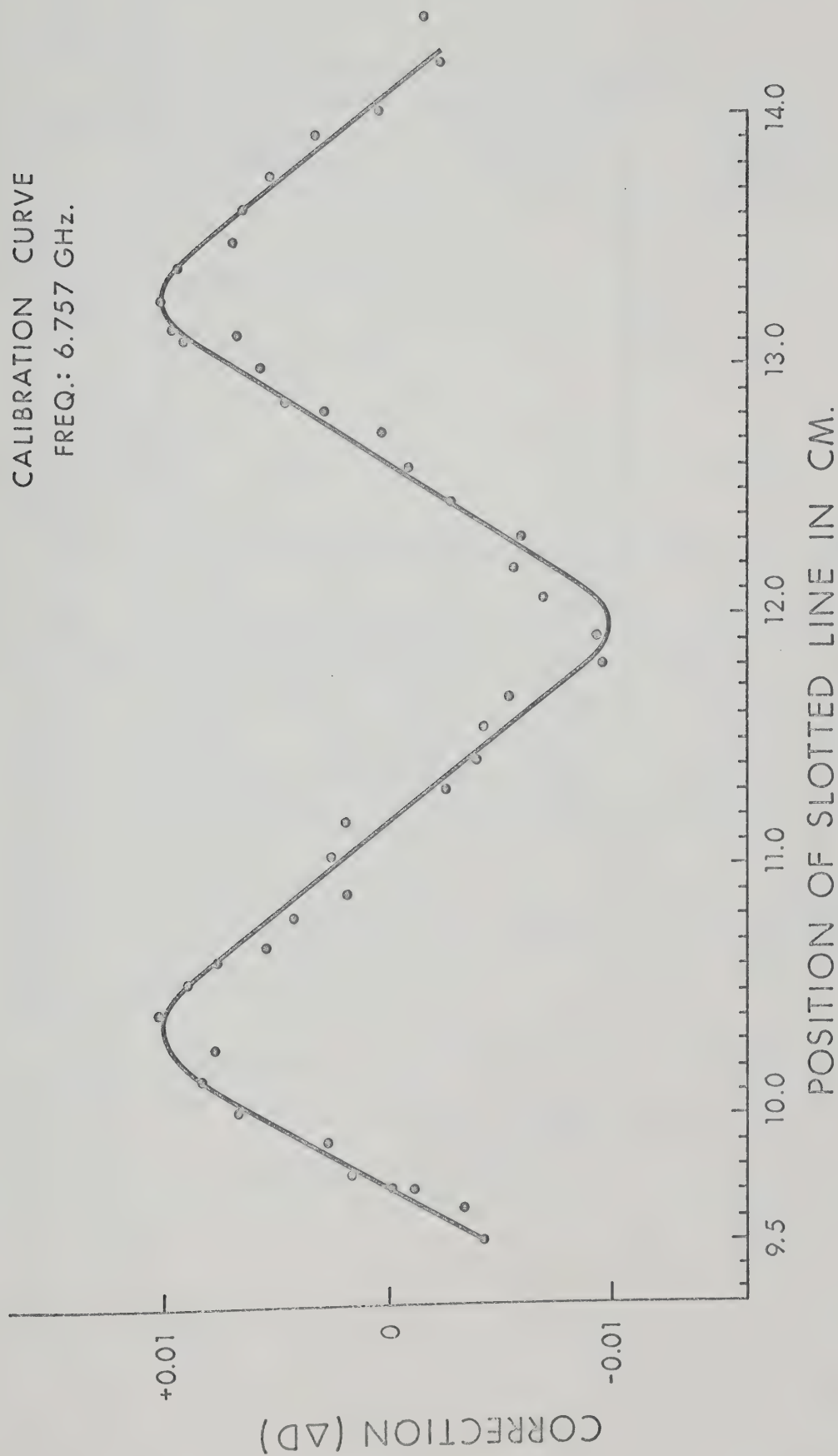


Fig. 11.9. Slotted-line calibration curve at 6.757 GHz.

Description	Corrected Relative Impedance	Relative Diode Terminal Impedance	True Diode Terminal Impedance
Brass Post Connected in Place of the Diode	0.030 + j0.482		
With Diode			
Bias (Volts) d.c.			
0.0	0.067 + j0.4	0.037 - j0.082	1.99 - j 4.4136
-3.0	0.058 + j0.185	0.028 - j0.297	1.501 - j15.97
-7.0	0.054 + j0.096	0.024 + j0.386	1.2912 - j20.766
-15.0	0.053 + j0.017	0.023 - j0.465	1.2374 - j25.01
+0.2	0.071 + j0.458	0.042 - j0.024	2.2596 - j 1.288
+0.4	0.079 + j0.497	0.049 + j0.015	2.6362 + j 0.8
+0.7	0.14 + j0.85	0.11 + j0.368	5.918 + j19.7984
+1.0	0.1 + j0.935	0.70 + j0.453	3.766 + j24.00

TABLE 11.1. TERMINAL IMPEDANCE OF STEP-RECOVERY DIODE

(HP. NO. 5082-0251) MEASURED BY THE

DIELECTRIC POST APPROACH.

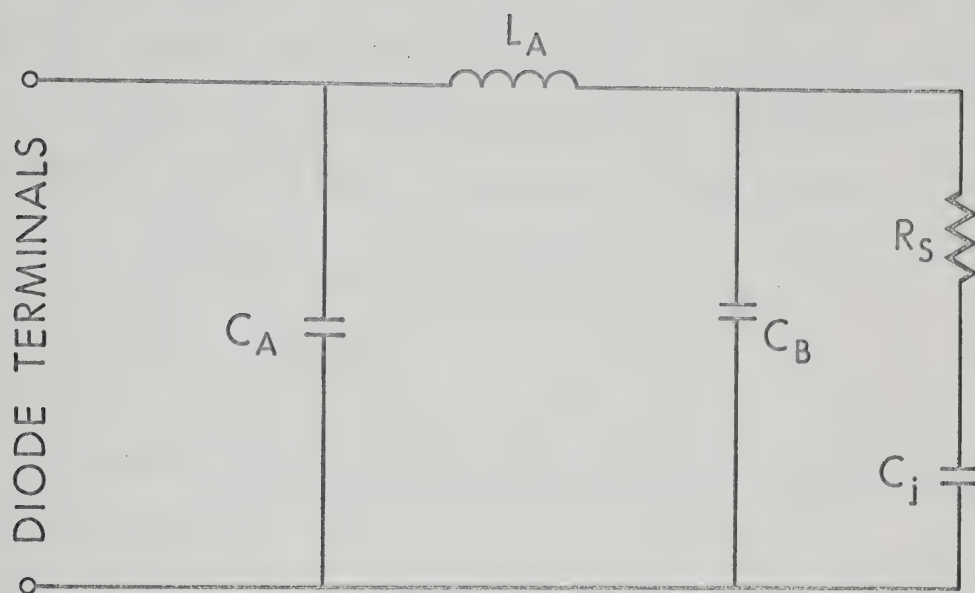


Fig. 11.10. Packaged varactor diode equivalent circuit at microwave frequencies.

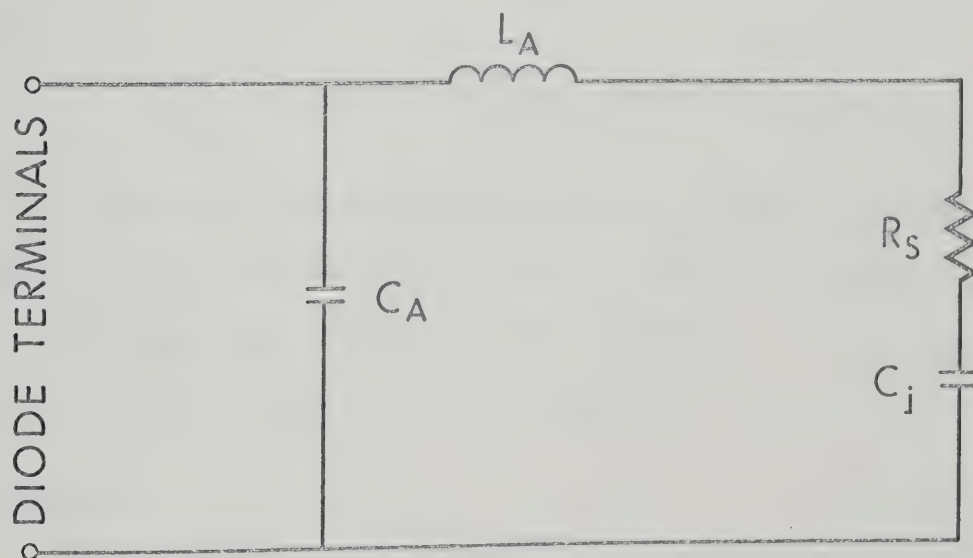


Fig. 11.11. Simplified equivalent circuit of packaged varactor diodes at lower microwave frequencies.

open and shorted diode packages so that statistical data can be collected from which a usable value of C_A and L_A can be chosen. Since we do not have a set of open and shorted diode packages, we needed to rely on the specifications supplied by the manufacturer for the package:

$$C_A = 0.20 \text{ pF}$$

$$L_A = 0.50 \text{ nH}$$

From the equivalent circuit of Fig. (11.11), we can write the following equation⁶⁷:

$$\frac{R_m}{R_s} = \frac{1}{\left\{ \left(1 + \frac{C_A}{C_j} - \omega^2 L_A C_A \right)^2 + \left(C_A^2 \omega^2 R_s^2 \right) \right\}} \quad \dots(11.9)$$

where

R_m = real part of the diode terminal impedance.

If it is assumed that the junction capacitance C_j at the measurement frequency has the same value as determined by the low frequency capacitance* measurements^{60,63}, R_s can be determined directly from Eq. (11.9), since we already know the value of L_A and C_A .

11.3 Results

The diode terminal capacitance, measured with a Boonton bridge using a small 1 MHz signal to minimise averaging effects, is displayed in Fig. (11.12) as a function of the bias voltage. From the equivalent

* This assumption is only valid for the reverse-bias and low forward-bias cases.

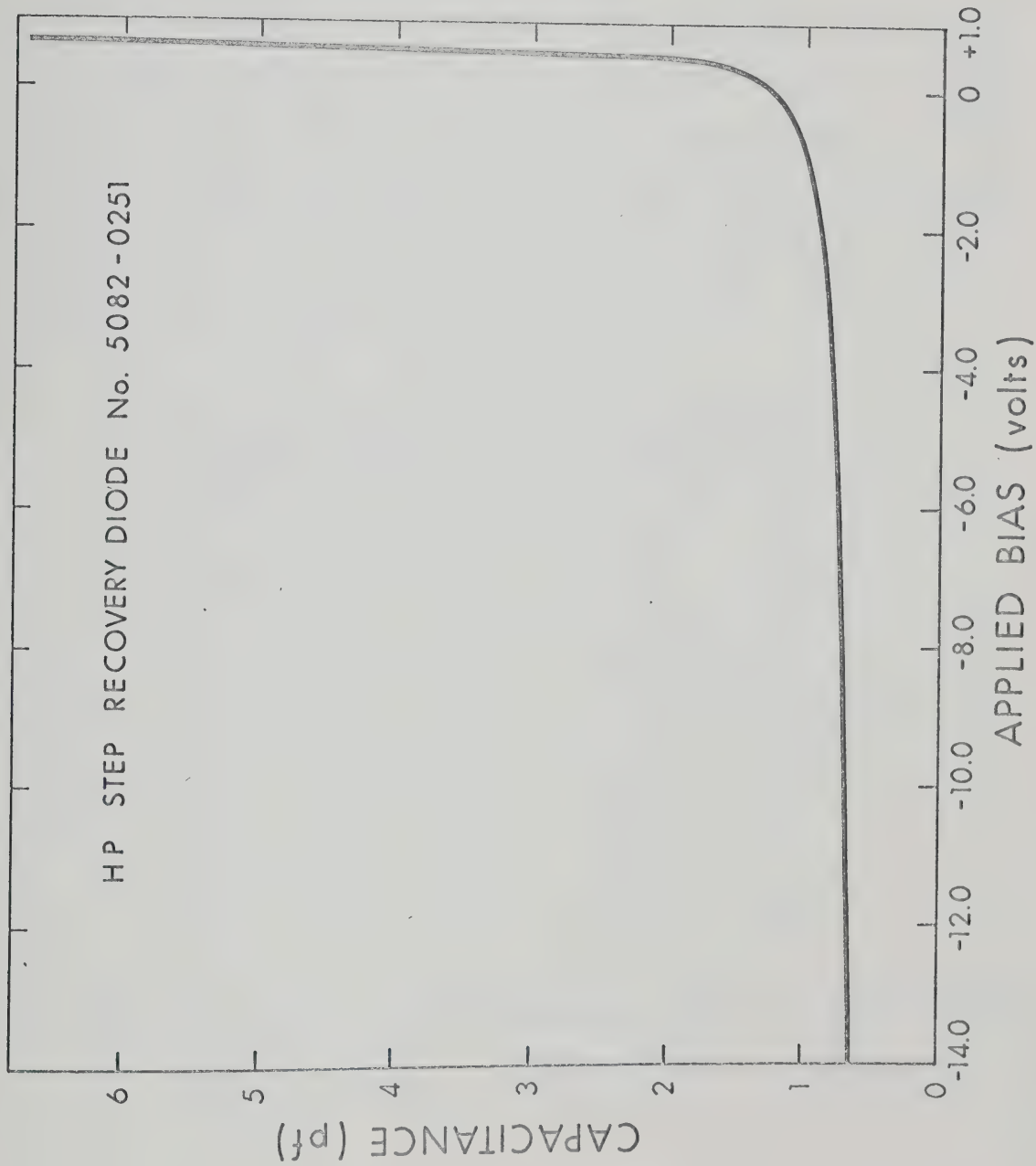


Fig. 11.12. Low-frequency terminal capacitance versus bias for the step recovery diode measured (HP. 5082-0251).

circuit of Fig. (11.11), this value of capacitance is almost equal to the value of $(C_A + C_j)$. If it is assumed that the junction capacitance C_j at the measurement frequency (6.757 GHz) has the same value as determined by the 1 MHz frequency measurements^{60,63}, the junction capacitance is determined from the measurements reported in Fig. (11.12), since we know the value of C_A (0.2 pF) as determined in Section (11.2.3). Equation (11.9) then yields the value of the series resistance R_s , since we know all the other parameters of the equivalent circuit. Table (11.2) lists the value of the series resistance R_s determined from Eq. (11.9) for various bias voltages.

Bias Voltage in volts d.c.	Series Resistance R_s in Ω
-15.0	1.572
-7.0	1.565
-3.0	1.710
0	2.149
+0.2	2.285
+0.4	2.410
+0.7	4.950

TABLE 11.2. THE VALUES OF SERIES RESISTANCE R_s FOR STEP-RECOVERY DIODE (HP. NO. 5082-0251) AS DETERMINED BY THE DIELECTRIC POST APPROACH.

Figures (11.13) and (11.14) give the static Q measurements at 6 GHz and 7 GHz, respectively, on the same diode using Harrison's⁶¹

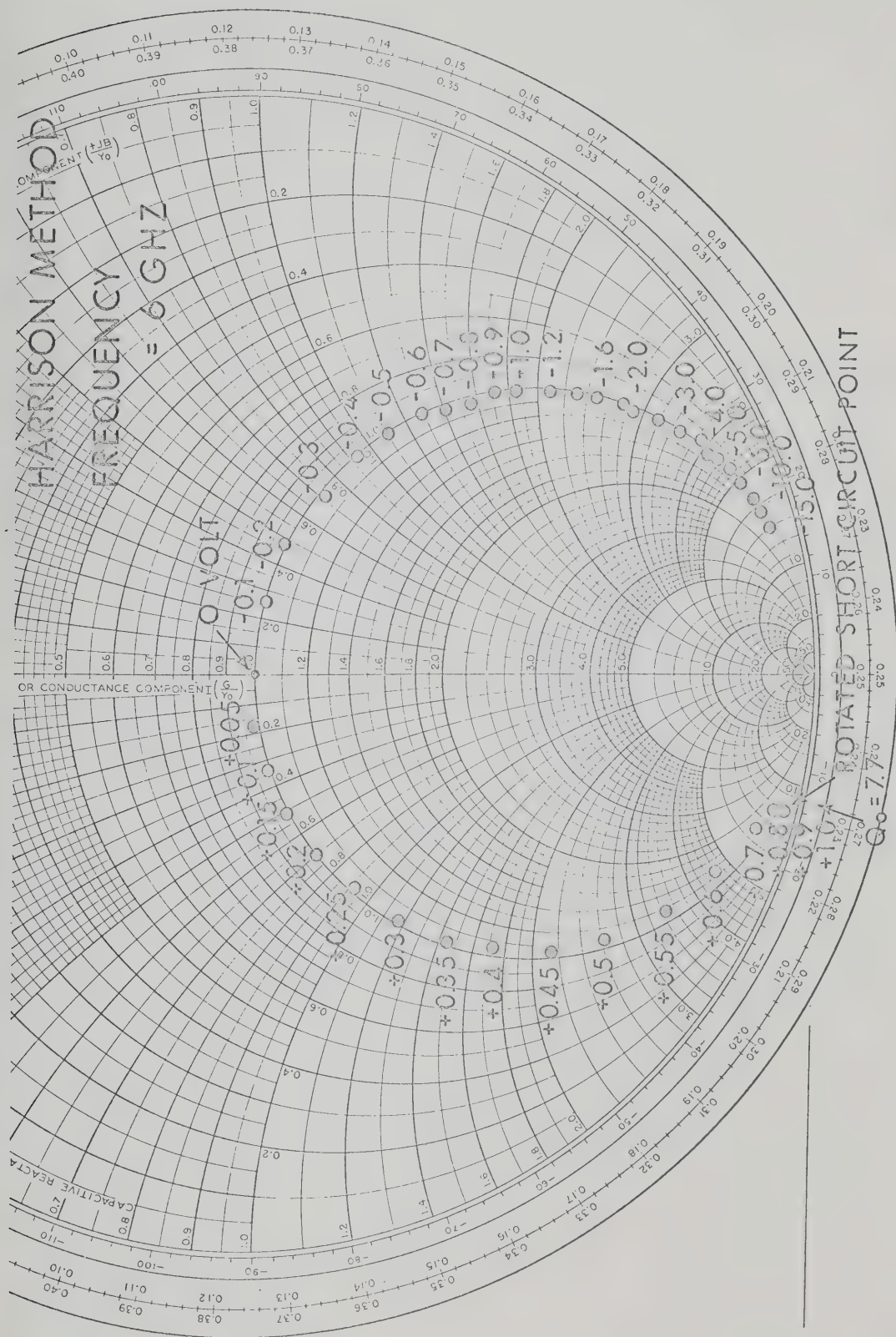


Fig. 11.13. Step-recovery diode (HP. 5082-0251) impedance for various bias voltages derived by Harrison's method at 6 GHz.

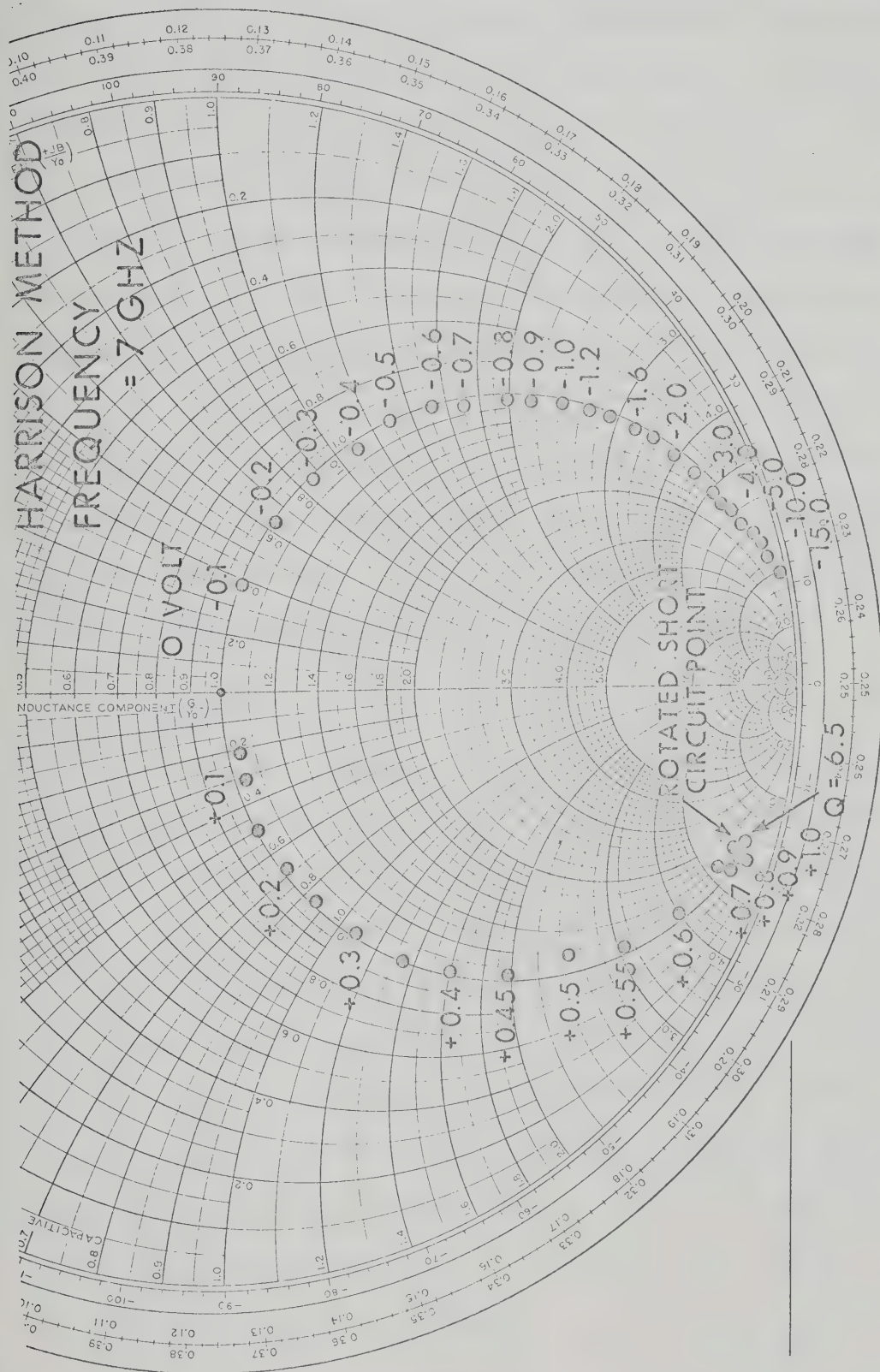


Fig. 11.14. Step-recovery diode (HP. No. 5082-0251) impedance for various bias voltages derived by Harrison's method at 7 GHz.

relative impedance method. A shorted diode package provided by Hewlett Packard Company is used to obtain the required short circuit reference. This method yields a static Q of 7.7 at 6 GHz and 6.5 at 7 GHz at zero volts bias for the diode under consideration. The static Q at zero volts bias for the diode as calculated by the dielectric post approach presented in Section (11.2) is equal to 8.756 at the measurement frequency of 6.757 GHz. Figure (11.15) compares the value of the capacitance as calculated for diode No. 2 for steady-state cases and the values of capacitance obtained for the step-recovery diode (HP. No. 5082-0251) from the Boonton bridge operating at 1 MHz. The values show an agreement for low forward-biases. The relatively large difference at high forward-bias may be attributed to the diffusion capacitance dependence upon the frequency⁴ of the measuring signal.

11.4 Conclusions

An improved procedure has been developed for measuring the static characteristics of a varactor diode. First, a theoretical circuit model for a varactor mounted in a reduced-height waveguide has been given. Then an experimental procedure for determining the parameters of this equivalent circuit has been described. This method takes into account the line loss and holder loss which are present in a practical measuring system. This method also yields directly the value of the series resistance R_s . The value of the static Q measured from this approach is higher than the one measured by Harrison's approach as the latter approach neglected line loss and holder loss, and thus assumes the measuring system to be lossless.

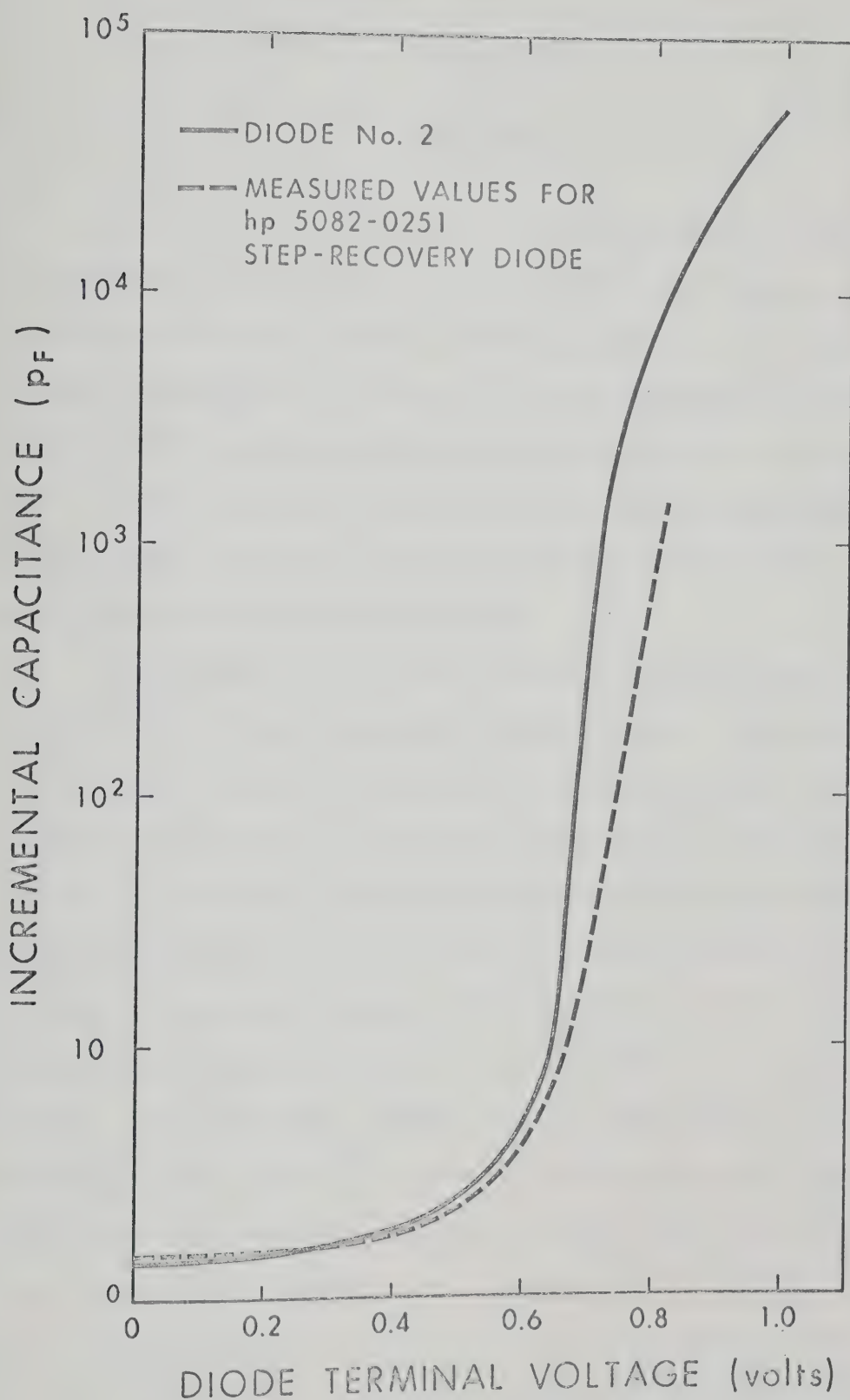


Fig. 11.15. Calculated incremental capacitance of diode No. 2 and low frequency terminal capacitance of step-recovery diode (HP. No. 5082-0251) as functions of forward-bias voltage.

CHAPTER XII

CONCLUSION

In this work, a computer-aided study of the electrical behaviour of microwave varactor diodes under static and dynamic large-signal conditions has been carried out. Numerical methods of solution have been used in preference to presently available analytical techniques because of the freedom available in the former approach in the choice of doping profile, generation-recombination law, mobility dependencies and injection level. Moreover, boundary conditions in this method are applied solely at the external contacts.

For purposes of this study, microwave varactors have been classified into two broad categories, namely varactor diodes and step-recovery diodes. The first category was taken to represent those diodes in which non-linearity of the junction capacitance in the reverse-bias condition is optimised. Diodes optimised for utilising the abrupt change of capacitance for voltage near the contact potential were taken to belong to the second category. Typical physical structures and doping profiles have been chosen to represent these two types of varactor. The steady-state solution has been obtained by an algorithm originally used by Gummel¹⁸ to solve the steady-state case for transistors. Time-dependent solutions have been obtained by finite difference methods originally used by DeMari²¹ for a simpler physical model of zero recombination and constant mobility. DeMari's algorithm has been extended to cover our physical model and was successfully

applied to the two different chosen diode structures; they exhibited a very different stability behaviour in their numerical solution, the step-recovery diode solution requiring more stringent procedures.

Four different forms of external excitation have been considered:

- (1) steady-state voltage excitation;
- (2) large-signal "turn-on" excitation;
- (3) large-signal "turn-off" excitation;
- (4) large-signal sinusoidal excitation in a broadband circuit.

Detailed results for the above mentioned cases have been presented and discussed in Chapters VII, VIII, IX and X. The results reflect the usefulness of numerical techniques for studying both the static and dynamic behaviour of these devices. These results also expose various inaccurate assumptions employed in much of the analytical work and in some cases, their inapplicability to the present device under the conditions studied.

An improved technique to measure the static characteristics of a varactor diode at microwave frequencies is reported in Chapter XI. The value of static Q obtained by this 'dielectric post approach' is higher than given by Harrison's method⁶¹ which neglects the circuit losses.

This investigation can be used as a basis for studies involving the device optimisation and optimisation of the device together with its embedding circuitry. A few examples are listed below:

- (1) the effect of doping concentration, width and gradient of the net doping profile at the boundaries of the center high resistivity region on the reverse-transient characteristics of step-recovery diodes;

(2) the dependence of large-signal impedance at the generator frequency upon signal amplitude and on frequency in a broadband circuit;

(3) the simulation of the circuit conditions when only certain frequencies are allowed to flow;

(4) the extension of the present one-dimensional model to two or three-dimensional cases to study complex geometry effects on the device behaviour;

(5) measurement of large-signal impedance of the device at microwave frequencies.

Several extensions of the computer model developed here come to mind and are listed below:

(1) The present numerical scheme may be extended to study the large-signal behaviour of the single-drift region ($p^+ - n - n^+$) avalanche diode, the double-drift region ($p^+ - p - n - n^+$) avalanche diode and microwave transistors;

(2) the present scheme may be extended to study the effect of multi-level carrier trapping and recombination on the behaviour of microwave semiconductor junction devices;

(3) the present scheme may also be extended to study the effect of temperature on the steady-state behaviour of microwave semiconductor junction devices.

REFERENCES

1. J. C. Irvin and T. P. Lee, Microwave Semiconductor Devices and their Applications, Part 3. New York: McGraw-Hill, pp. 149 - 190, 1969.
2. S. M. Sze, Physics of Semiconductor Devices. New York: Wiley, pp. 133 - 140, 1969.
3. P. A. Goud, "Solid State Power Sources," The Journal of Microwave Power, 2 - 3, p. 100.
4. W. Shockley, "The Theory of p-n Junctions in Semiconductors and p-n Junction Transistors," Bell Sys. Tech. J., vol. 28, pp. 435 - 489, July 1949.
5. N. H. Fletcher, "The High Current Limit for Semiconductor Junction Devices," Proc. IRE, vol. 44, pp. 862 - 872, June 1957.
6. C. T. Sah, "Effects of Electrons and Holes on Transition Layer Characteristics of Linearly-graded p-n Junctions," Proc. IRE, vol. 48, pp. 603 - 618, March 1961.
7. C. T. Sah, "The Spatial Variation of Quasi-Fermi Potentials in p-n Junctions," IEEE Trans. Electron Devices, vol. ED - 13, pp. 839 - 846, December 1966.
8. W. H. Ko, "The Forward Transient Behaviour of Semiconductor Junction Diodes," Solid-State Electron, vol. 3, pp. 59 - 69, January 1961.
9. W. H. Ko, "The Reverse Transient Behaviour of Semiconductor Junction Diodes," IRE Trans. Electron Devices, vol. ED - 8, pp. 123 - 131, March 1961.
10. R. H. Kingston, "Switching Time in Junction Diodes and Junction Transistors," Proc. IRE, vol. 42, pp. 1148 - 1154, May 1954.
11. E. L. Steele, "Charge Storage in Junction Diodes," J. Appl. Phys., vol. 25, pp. 916 - 918, July 1954.
12. B. Lax and S. F. Neustadler, "Transient Response of a p-n Junction," J. Appl. Phys., vol. 25, pp. 1148 - 1154, September 1954.
13. J. C. Henderson and J. R. Tillman, "Minority-Carrier Storage in Semiconductor Diodes," Proc. IEE, vol. 104B, pp. 318 - 333, January 1957.
14. D. P. Kennedy, "Reverse Transient Characteristics of a p-n Junction Diode Due to Minority Carrier Storage," IRE Trans. Electron Devices, vol. ED - 9, pp. 174 - 182, March 1962.

15. S. Y. Muto and S. Wang, "Switching Response of Graded-Base p-n Junction Diodes," IRE Trans. Electron Devices, vol. ED - 9, pp. 183 - 187, March 1962.
16. G. Grimsdell, "Diode Hole Storage and "turn-on" and "turn-off" time," Electronic Engineering, pp. 645 - 646, November 1958.
17. H. Benda, F. Dannhauser, A. Porst and E. Spenke, "Influence of Doping Concentration on Switching Process in p - s - n Rectifier," Solid-State Electron, vol. 10, pp. 1133 - 1147, December 1967.
18. H. K. Gummel, "A Self Consistent Iterative Scheme for One-Dimensional Steady-State Transistor Calculations," IEEE Trans. Electron Devices, vol. ED - 11, pp. 455 - 465, October 1964.
19. A. DeMari, "An Accurate Numerical Steady-State One-Dimensional Solution of the p-n Junctions," Solid-State Electron, vol. 11, pp. 33 - 58, January 1968.
20. D. P. Kennedy and R. R. O'Brien, "On the Mathematical Theory of the Linearly-Graded p-n Junctions," IBM J. Res. Dev., pp. 252 - 270, May 1967.
21. A. DeMari, "An Accurate Numerical One-Dimensional Solution of the p-n Junction Under Arbitrary Transient Conditions," Solid-State Electron, vol. 11, pp. 1021 - 1053, December 1968.
22. D. L. Scharfetter and H. K. Gummel, "Large-Signal Analysis of a Silicon Read Diode Oscillator," IEEE Trans. Electron Devices, vol. ED - 16, pp. 64 - 77, January 1969.
23. J. J. Chang and J. H. Forster, "Semiconductor Junction Varactors with High Voltage Sensitivity," IEEE Trans. Electron Devices, vol. ED - 10, pp. 281 - 287, July 1963.
24. J. L. Moll, S. Krakauer and R. Shen, "p-n Junction Charge Storage Diodes," Proc. IRE, vol. 50, pp. 43 - 53, January 1962.
25. S. Krakauer, "Harmonic Generation, Rectification and Lifetime Evaluation with the Step-Recovery Diodes," Proc. IRE, vol. 50, pp. 1665 - 1672, October 1962.
26. J. L. Moll and S. A. Hamilton, "Physical Modelling of the Step-Recovery Diode for Pulse and Harmonic Generation Circuit," Proc. IEEE, vol. 57, pp. 1250 - 1259, July 1969.
27. J. J. Chang and J. H. Forster, Unpublished Work.
28. K. Boltak, Diffusion in Semiconductors. New York: Academic Press, pp. 94 - 128, 1965.
29. C. T. Sah, R. N. Noyce and W. Shockley, "Carrier Generation and Recombination in p-n Junctions and p-n Junction Characteristics," Proc. IRE, vol. 45, pp. 1228 - 1243, September 1957.

30. W. Shockley and W. T. Read Jr., "Statics of Recombination of Holes and Electrons," Phys. Rev., vol. 87, pp. 835 - 852, September 1952.
31. R. N. Hall, "Germanium Rectifiers Characteristics," Phys. Rev., vol. 83, p. 228, July 1951.
32. V. Dolcan, "Effects of Spatial Dependence of Recombination Centers on I-V Characteristics of p-n Junctions," J. Appl. Phys., vol. 40, pp. 4095 - 4103, September 1969.
33. E. M. Conwell and V. F. Weisskopf, "Theory of Impurity Scattering in Semiconductors," Phys. Rev., vol. 77, pp. 388 - 395, February 1950.
34. E. J. Ryder, "Mobility of Holes and Electrons in High Electric Fields," Phys. Rev., vol. 90, pp. 766 - 769, June 1953.
35. J. C. Irvin, "Resistivity of Bulk Silicon and of Diffused Layers in Silicon," Bell Sys. Tech. J., vol. 41, pp. 387 - 410, March 1962.
36. D. M. Caughey and R. E. Thomas, "Carrier Mobilities in Silicon Empirically related to Doping and Field," Proc. IEEE, vol. 55, pp. 2192 - 2193, December 1967.
37. R. N. Hall, "Power Rectifiers and Transistors," Proc. IRE, vol. 40, pp. 1512 - 1518, 1952.
38. S. Chapman and T. G. Cowling, The Mathematical Theory of Non-Uniform Gases, Cambridge Eng.: Cambridge University Press, pp. 177 - 179, 1952.
39. N. R. Howard and G. W. Johnson, " $p^+ - i - n^+$ Silicon Diodes at High Current Densities," Solid-State Electron., vol. 8, pp. 275 - 284, 1965.
40. W. Shockley, Electrons and Holes in Semiconductors. New York: Van Nostrand, pp. 230 - 249, 1950.
41. F. Hermann, "The Electronic Energy Band Structure of Silicon and Germanium," Proc. IRE, vol. 43, pp. 1703 - 1732, December 1955.
42. John P. McKelvey, Solid-State and Semi-Conductor Physics. New York: Harper and Row, pp. 346 - 350, 1966.
43. W. Van Roosbroeck, "The Transport of Added Current Carriers in a Homogenous Semiconductor," Phys. Rev., vol. 91, pp. 282 - 285, July 1953.
44. J. L. Moll, Physics of Semiconductors. New York: McGraw-Hill, pp. 62 - 67, 1964.
45. R. V. Overstraeten and W. Nyuts, "Use of Space-Charge Approximation as a Trial Solution in the Computation of Potential Distributions in Semiconductor Devices," Electronics Letters, vol. 5, pp. 646 - 647, December 11, 1969.

46. W. T. Weeks, "Interpolation Data for your Computer," Electronic Design, vol. 16, pp. 198 - 203, August 15, 1968.
47. E. Forsythe and W. Wasow, Finite Difference Methods for Partial Differential Equations. New York: Wiley, pp. 88 - 139, 1960.
48. K. S. Kunz, Numerical Analysis. New York: McGraw-Hill, 1957.
49. P. Lax and R. Richtmyer, "Survey of Stability of Linear Finite-Difference Equations," Comm. Pure Appl. Math., vol. 9, pp. 267 - 295, May 1956.
50. F. John, "On Integration of Parabolic Equations by Difference Methods," Comm. Pure Appl. Math., vol. 5, pp. 155 - 211, May 1952.
51. K. Wilbrod, "Causes of Instabilities in Numerical Integration Techniques," International J. Computer Math., vol. 2, pp. 123 - 142, April 1968.
52. A. Ralston and H. S. Wilf, Mathematical Methods for Digital Computers, vol. I, New York: Wiley, pp. 135 - 144, 1967.
53. L. Fox, Numerical Solution of Ordinary and Partial Differential Equations, London: Pergamon Press, pp. 230 - 242, 1962.
54. A. DeMari, "Accurate Numerical Steady-State and Transient One-Dimensional Solutions of Semiconductor devices," Technical Report, Electrical Engineering Department, California Institute of Technology, Pasadena, California, 1967.
55. H. K. Gummel, "Hole-Electron Product of p-n Junctions," Solid-State Electron., vol. 10, pp. 209 - 212, March 1967.
56. D. A. Kleinman, "The Forward Characteristics of a p - i - n Diode," Transistor Technology, vol. 2, New York: Van Nostrand, pp. 115 - 127, 1958.
57. D. Leenov and A. Uhlir, "Generation of Harmonic and Subharmonics at Microwave Frequencies with p - n Junction Diodes," Proc. IRE, vol. 47, pp. 1724 - 1729, October 1959.
58. B. C. DeLoach, "A New Microwave Measurement Technique to Characterize Diodes and an 800 GHz cutoff Frequency Varactor at zero Volt Bias," IEEE Trans. Microwave Theory and Techniques, vol. MTT - 12, pp. 15 - 20, January 1964.
59. D. A. E. Roberts and K. Wilson, "Evaluation of High Quality Varactor Diodes," Radio and Electronic Engineer, vol. 31, pp. 277 - 285, May 1966.
60. N. Houlding, "Measurements of Varactor Quality," Microwave Journal, vol. 3, pp. 40 - 45, January 1960.

61. R. I. Harrison, "Parametric Diode Q Measurements," Microwave Journal, vol. 3, pp. 43 - 46, May 1960.
62. R. Mavaddat, "Varactor Diode Q Factor Measurements," Journal of Electronics and Control, vol. 15, pp. 51 - 54, July 1963.
63. E. W. Sard, "A New Procedure for Calculating Varactor Q From Impedance vs Bias Measurements," IEEE Trans. Microwave Theory and Techniques, vol. MTT - 16, pp. 849 - 860, October 1968.
64. L. Lewin, "A Contribution to the Theory of Probes in Waveguide," Proc. IEE, vol. 105, pp. 109 - 116, October 1957.
65. A. A. Olinear, "The Calibration of Slotted Section for Precise Microwave Measurements," Rec. Sci. Instrum., vol. 25, pp. 13 - 20, 1954.
66. N. Marcuvitz, Waveguide Handbook. New York: McGraw-Hill, 1951.
67. W. J. Getsinger, "A Packaged and Mounted Diode as a Microwave Circuit," IEEE Trans. Microwave Theory and Techniques, vol. MTT - 14, pp. 58 - 67, February, 1966.
68. J. O. Scanlan, "Characterisation of Waveguide Mounted Tunnel Diodes," Proc. IEE, vol. 114, pp. 1844 - 1849, December 1967.

APPENDIX A

AUTOMATICALLY ADJUSTABLE SELECTION OF
DISCRETIZATION MESH SIZE IN THE TIME DOMAIN

It is desired to achieve an automatic adjustment of time step size subject to the requirement of maintaining constant errors, throughout the time domain, in our numerical solution of time-dependent cases as reported in Chapter VI. In the procedure adopted in Chapter VI, only numerical differentiations are present. The total error introduced by such operations may be regarded as a sum of truncation and round-off errors. For a decrease in the step size and an increase in the order of interpolation scheme used, the former type of error decreases whereas the latter increases. For the present case, round-off errors may be usually considered negligible since double precision arithmetic is employed. This is a consequence of practical restrictions on both the order of the numerical scheme and the minimum step size that may be used (limited by memory size and computation time). The effort will then be towards achieving a constant truncation error throughout the time domain.

The Taylor expansion about a point $t = t_k$ of a continuous function $f(t)$ with continuous derivatives is considered:

$$f(t) = f(t_k) + (t - t_k) \left. \frac{df}{dt} \right|_{t=t_k} + \frac{1}{2!} (t - t_k)^2 \left. \frac{d^2f}{dt^2} \right|_{t=t_k} + \dots \quad \dots (A.1)$$

If a two-point formula is used to approximate the first derivative at the point $t = {}_k t$, such as

$$\left. \frac{df}{dt} \right|_{t={}_k t} \approx \frac{{}_{k+1} \Delta f}{{}_{k+1} \Delta t} \quad \dots (A.2)$$

where

$${}_{k+1} \Delta f = f({}_{k+1} t) - f({}_k t)$$

$${}_{k+1} \Delta t = {}_{k+1} t - {}_k t$$

and is inserted in the expansion (A.2) evaluated at the point $t = {}_{k+1} t$, one obtains:

$$f({}_{k+1} t) \approx f({}_k t) + \frac{1}{2} ({}_{k+1} \Delta t)^2 \left. \frac{d^2 f}{dt^2} \right|_{t={}_k t} + \dots \quad \dots (A.3)$$

If higher order contributions of Eq. (A.3) are neglected, the term

$${}_k \epsilon = \frac{1}{2} {}_{k+1} \Delta t {}_k f''$$

where

$${}_k f'' = \left. \frac{d^2 f}{dt^2} \right|_{t={}_k t}$$

represents the error introduced in the approximation (A.2). The relative error is then defined as the ratio ${}_k \epsilon / \frac{{}_{k+1} \Delta f}{{}_{k+1} \Delta t}$. The above may be repeated for a sequence of adjacent points ${}_k t$ ($k = 1, 2, 3, \dots$), and the requirement of maintaining a constant magnitude of the relative error at each point may be specified. In this case the following relation must hold:

$$\left| \frac{(\Delta t_k)^2}{\Delta f_k} \frac{f''_{k-1}}{f''_k} \right| = \left| \frac{(\Delta t_{k+1})^2}{\Delta f_{k+1}} \frac{f''_k}{f''_{k+1}} \right|$$

or

$$\Delta t_{k+1} = \sqrt{\frac{f''_{k-1}}{f''_k} \frac{\Delta f_{k+1}}{\Delta f_k}} \Delta t_k, \quad (k=1,2,3, \dots) \quad \dots (A.4)$$

which represents a relationship between consecutive steps in terms of local increments and curvatures of the function $f(t)$.

In the case of interest, the magnitude of the time step Δt_{k+1} at the next instant of time may be approximately predicted with the knowledge of quantities only available for times $t = t_k$ if the expression (A.4) is modified to the following form

$$\Delta t_{k+1} = \sqrt{\frac{f''_{k-2}}{f''_{k-1}} \frac{\Delta f_k}{\Delta f_{k-1}}} \Delta t_k, \quad (k=3,4,5, \dots) \quad \dots (A.5)$$

It is apparent that the sizes of the initial three time steps (Δt_k , $k=1,2,3, \dots$) must be independently specified, and the size of the fourth (and following ones) may be predicted by the relation of Eq. (A.5). Instants of time for which the argument of the square root of Eq. (A.5) exceeds the permissible range become singular points. These are likely to occur during the evolution of a transient solution and are easily taken care of by specifying the upper and lower bounds for the ratio of the consecutive steps and for the magnitude of the step size. These, as well as the initial three steps, must be chosen with regard to the total number of instants of time that may be allowed and to the rate of convergence of the iterative procedure, very much dependent upon the

step size.

Although a time step adjustment of the described type is not very accurate, it appears satisfactory from any practical point of view, also in consideration of the insignificant computation load required and by the observation that the selection of the time step is by no means critical.



EX LIBRIS
BIBLIOTHECAE
HISTORICAE

B29967